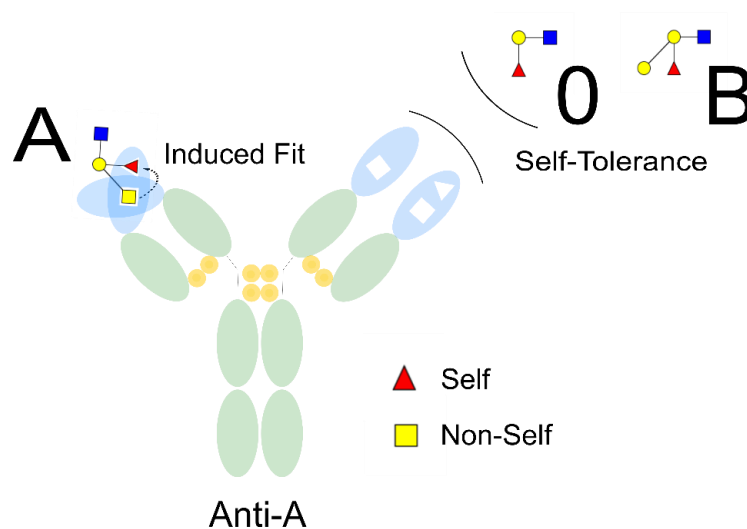

A Binding Model for Anti-Carbohydrate Antibodies

Thesis

submitted on October 24, 2018 in fulfillment of the requirements of the degree *Dr. rer. nat.* of the Department of Chemistry, Faculty of Sciences, University of Hamburg



by

Tim Raiber

from Oststeinbek

Hamburg, 2018

This thesis was performed under the guidance of Prof. Dr. E. Spillner at the Institute for Biochemistry and Molecular Biology from 2011 to 2015.

First Reviewer: Prof. Dr. B. Meyer

Second Reviewer: Prof. Dr. H. Schwalbe (University of Frankfurt)

Date of the Disputation: March 29, 2019

Type I hypersensitivities to CCDs are echo and smoke of an ancient glycan war, which was brought under control of DC-SIGN.

But here and there it is still smoldering.

I. List of Publications

Plum, M., Michel, Y., Wallach, K., Raiber, T., Blank, S., Bantleon, F. I., Diethers, A., Greunke, K., Braren, I., Hackl, T., Meyer, B., Spillner, E., *Close-up of the Immunogenic α 1,3-Galactose Epitope as Defined by a Monoclonal Chimeric Immunoglobulin E and Human Serum Using Saturation Transfer Difference (STD) NMR*. J. Biol. Chem., 2011. **286**(50): p. 43103-43111.

II. Table of Contents

1.	Contributions	1
1.1.	Own Work	1
1.2.	Third-Party Contributions	1
1.3.	Technical Support	1
1.4.	Acknowledgment	2
1.5.	Statement in Lieu of an Oath	2
2.	Abstract	3
3.	Zusammenfassung	4
4.	Introduction	5
4.1.	Introduction into the Concept of Allergy	5
4.1.1.	Serum as “Carrier of Immunity”	5
4.1.2.	Serum Sickness as an <i>Allergic</i> Response to Animal Serum – the Concept of <i>Allergy</i> is Developed	6
4.1.3.	Allergy is Classified into Types of Hypersensitivity	8
4.1.3.1.	Type I Hypersensitivity	8
4.1.3.2.	Type II Hypersensitivity	10
4.1.3.3.	Type III Hypersensitivity	10
4.1.3.4.	Type IV Hypersensitivity	11
4.2.	α 1-3 Core Fucose in the Context of Type I Hypersensitivity	11
4.2.1.	“De l’Action Anaphylactique de Certains Venins”	11
4.2.2.	Surprising Implication of a “Periodate-Sensitive and Heat-Stable” Antigen in Type I Hypersensitivity	13
4.2.3.	“Specific Interaction of IgE Antibodies with a Carbohydrate Epitope of Honey Bee Venom Phospholipase A ₂ ”	14
4.2.4.	Phospholipase A ₂ as a Combatant of the Glycan War	15
4.2.5.	“Fucose α 1,3-Linked to the Core Region of Glycoprotein N-Glycans Creates an Important Epitope for IgE from Honeybee Venom Allergic Individuals”	19
4.2.6.	“Fucose-Containing Conjugates Bind Only Weakly to Anti-Bee Venom”	19
4.3.	Introduction to Antibodies	20
4.3.1.	Structural Characteristics of Antibodies	20
4.3.2.	Adaptive Immunity by Clonal Selection	24
4.3.3.	Technique of Antibody Phage Display	24
5.	Aim of the Study	26
5.1.	Molecular Insight into the Cross-Reactivity of α -1,3 Core Fucose	26
6.	Results	28
6.1.	Access to Honeybee Venom CCD Fragments	28
6.1.1.	Synthesis of Fuc α 1-3GlcNAc	28

6.1.2.	A Proposed Mechanism for a LiClO ₄ -Promoted Chemical Glycosylation as a Heterogeneous Variant of Pocker's "Electrostatic Catalysis"	37
6.1.3.	Synthesis of Fuc α 1-3GlcNAc with Linker for Immobilization on a Pan	40
6.1.4.	Synthesis of Fuc α 1-3(Fuc α 1-6)GlcNAc	42
6.1.5.	Synthetic Manipulations of the Core Fucose Epitope	43
6.1.6.	Establishment of the Model System anti-TNT scFv-IgE 2.18 / RDX for the Analysis of Cross-Reactivities	44
6.2.	Analysis of the Interaction between Honeybee Venom CCD Fragments and Phage Display-Derived Monoclonal Anti-HRP Antibodies	47
6.2.1.	STD NMR Spectroscopy	47
6.2.1.1.	Spin Diffusion Experiments with Antibodies Prepared Way to STD NMR Spectroscopy	47
6.2.1.2.	Application of STD NMR Spectroscopy to Fragment-Based Drug Discovery	49
6.2.1.3.	Fundamental Principles of STD NMR Spectroscopy	49
6.2.1.3.1.	Nuclear Overhauser Effect	49
6.2.1.3.2.	Spin Diffusion	52
6.2.1.3.3.	Pulse Sequence	53
6.2.1.4.	STD NMR Results	54
6.2.1.4.1.	Persisting False-Positive STD NMR Results	55
6.2.1.4.2.	Negative Control Revealed Fatal Error	56
6.2.1.4.3.	STD Effects of CCD Fragments Statistically Insignificant	68
6.2.1.4.4.	STD Artefacts Probably Caused by Power Spill-Over due to Non-Calibrated Gaussian Pulse	79
6.2.2.	SPR Spectroscopy	83
6.2.2.1.	Fundamental Principles of SPR Spectroscopy	83
6.2.2.2.	SPR Results	85
6.2.3.	X-Ray Crystallography of Co-Crystals	87
6.2.3.1.	Fundamental Principles of X-Ray Crystallography	87
6.2.3.2.	Evaluation of Co-Crystal Data	89
6.2.4.	Molecular Modeling	94
6.2.4.1.	Fundamental Principles of Molecular Modeling	94
6.2.4.2.	Molecular Docking Reproduced Co-Crystal	97
6.2.4.3.	Man α 1-6 Constitutes an Important Fragment of the Epitope	99
6.2.4.4.	V _H and V _L Domains Internally Cross-Linked by the Two Glyco Valences Fuc α 1-3 and Man α 1-6	100
7.	Discussion	105
7.1.	Trapped in the Quicksand of STD NMR Artefacts	105
7.1.1.	STD NMR Spectroscopy Ended up Building Edifices on Sand	105
7.1.2.	An Artefact is an Incorrect Rejection of the Null Hypothesis	105
7.1.3.	Phage Display Study Misguided by STD NMR Artefacts	106
7.1.4.	STD NMR Artefacts Caused by Irradiation Anomalies	106
7.1.5.	Method Validation Guidelines	108
7.2.	Study Suffered from Confirmation Bias	109
7.3.	A Co-Crystal with Questionable Information Value	111
7.3.1.	Missing Crossroad Between Phage Display and Synthesis of CCD Substructures	111

7.3.2.	Docking Confirms Co-Crystal Data and Identified Fuc α 1-3GlcNAc as a Weak Binder	111
7.4.	Postulate of a Two-Glyco-Valences Binding Model	112
7.4.1.	Findings of This Study in Harmony with Findings of a Previous Study by Hypothesis of a Two-Glyco-Valences Binding Model	112
7.4.2.	Hypothesis II. Two-Glyco-Valences Recognition is a Logical Consequence of Self-Tolerance to Le ^x and sLe ^x	114
7.4.3.	Hypothesis III. Blood Groups are Natural Vaccination Gaps in the Population, which Break the Vicious Circle of the Red Queen Effect	115
7.4.4.	Hypothesis IV: Two-Glyco-Valences Binding Model Explains Self-Tolerance to Blood Group 0	116
7.4.5.	Hypothesis V. Anti-CCD Antibodies are a Logical Consequence of Antigen Capture by the Innate Receptor DC-SIGN	118
8.	Outlook	120
8.1.	Test of Binding Hypothesis	120
8.2.	Subjection of STD NMR Spectroscopy to Quality Assurance	120
9.	Experimental Section	121
9.1.	Materials and Methods	121
9.2.	Rabbit Immunization Experiment	122
9.3.	STD NMR Experiments	122
9.3.1.	Set-up of a Typical STD NMR Experiment	122
9.3.2.	Preparation of STD NMR Samples	123
9.4.	SPR Experiments	124
9.5.	Sitting Drop Vapor Diffusion Crystallization	126
9.6.	ELISA Experiments	126
9.6.1.	Activity ELISA of HMM5 against HRP	126
9.6.2.	Competition ELISA of Solute Nitro Compounds against TNP-BSA	127
9.7.	Access to Honeybee Venom CCD Fragments	128
10.	Supplemental Information	157
10.1.	¹ H-Check Sheet for STD NMR Samples	157
10.2.	DNA Sequences of Monoclonal Anti-HRP Antibodies and HRP C	160
10.3.	Hazard and Precaution Statements	164
10.4.	<i>Curriculum Vitae</i>	167
11.	References	168

III. List of Abbreviations

AAL	<i>Aleuria aurantia</i> agglutinin
Ac	acetyl
Anc. Gr.	Ancient Greek
APC	antigen presenting cell
AQ	acquisition time ($AQ = TD \times DW$)
a.u.	arbitrary unit
BADMA	benzaldehyde dimethylacetale
BBI	broadband inverse (<i>i.e.</i> , the inner coil is optimized for ^1H observation while the outer coil is tunable over a frequency range that permits decoupling of nuclei between ^{31}P and ^{15}N)
BBO	broadband observe (<i>i.e.</i> , the inner coil is optimized for observation of nuclei between ^{15}N and ^{31}P while the outer coil is optimized for ^1H decoupling)
BCR	B-cell receptor
Bn	benzyl
BSA	bovine serum albumin
BWA	buckwheat agglutinin
CCD	cross-reactive carbohydrate determinant
CD	cluster of differentiation
CDR	complementarity determining region
CFA	complete Freund's adjuvant
C_H	heavy chain
CIC	circulating immune complex
C_L	light chain
COSY	correlation spectroscopy
CRD	carbohydrate recognition domain
CTL	cytotoxic T lymphocyte
d	doublet
Da	Dalton
DAST	Diethylaminosulfur trifluoride
DCM	dichloromethane
DC-SIGN	dendritic cell-specific ICAM-grabbing non-integrin (ICAM = intercellular adhesion molecule)
DMF	N,N-dimethylformamide
DMSO	dimethyl sulfoxide
DNT	2,4-dinitrotoluene
DW	dwell time (time between acquisition of two successive data points)
EDC	N-ethyl-N'-(3-dimethylaminopropyl)-carbodiimide
EA	ethyl acetate
ELISA	enzyme-linked immunosorbent assay
eq.	equivalents; equation
ESI	electrospray ionization
Fab	antigen binding fragment
FID	free induction decay
FT	Fourier transform
HBV	honeybee venom
HEL	hen egg-white lysozyme
HHH1	phage display-derived monoclonal antibody which has been selected against <u>H</u> RP for three rounds
HMBC	heteronuclear multiple-bond correlation
HMM5	phage display-derived monoclonal antibody which has been selected against <u>H</u> RP (first round) and <u>M</u> UXF conjugate (second and third round)
HRP	horseradish peroxidase
HSA	human serum albumin
HSQC	heteronuclear single-quantum correlation
Ig	immunoglobulin
IL	interleukin
Lat.	Latin
LB	line broadening
LDN	LacdiNAc (GalNAc β 1-4GlcNAc)

Le ^x , Le ^y	Lewis x, Lewis y
LOB, LOD, LOQ	limit of blank/determination/quantification
LPS	lipopolysaccharide
Me	methyl
MeOH	methanol
MHC	major histocompatibility complex
m.p.	melting point
MS	mass spectrometry; molecular sieve
MUXF ³	M = mannose, U = unoccupied, X = xylose, F = fucose (at 3-position of GlcNAc)
MWCO	molecular weight cut-off
NBS	N-Bromosuccinimide
n.d.	not detected; not determined
NHS	N-hydroxysuccinimide
NMR	nuclear magnetic resonance
NOESY	nuclear Overhauser enhancement spectroscopy
n.r.	not resolved
NS	number of scans
OD	optical density (<i>i.e.</i> , absorbance)
o.n.	overnight
PAGE	polyacrylamide gel electrophoresis
PBS	phosphate buffered saline
PE	petroleum ether
PEG	polyethylene glycol
PL	phospholipase
pNPP	<i>para</i> -nitrophenyl phosphate
ppm	parts per million (Hz/MHz)
PRR	pattern recognition receptor
q	quartet
RAST	radio-allergo-sorbent test
RDX	Royal Demolition Explosive
R _f	ratio of fronts
rpm	rounds per minute
r.t.	room temperature
RU	response unit
s	singlet
scFv	single chain variable fragment
SDS	sodium dodecyl sulfate
S/N	signal-to-noise ratio
SPR	surface plasmon resonance
STD	saturation transfer difference
t	triplet
TBI	triple resonance broadband inverse (The inner NMR coil is double tuned to observe ¹ H and a further nucleus (<i>e.g.</i> , ¹³ C) for decoupling. The outer NMR coil is provided with a BB tuning system and can be used to simultaneously decouple any nucleus in the BB range.
TCR	T-cell receptor
TD	time domain (number of data points, which constitute the FID signal, a higher value for TD increases resolution, but also increases acquisition time, TD × NS = size of the spectrum)
TEA	triethylamine
TLC	thin-layer chromatography
TLR	toll-like receptor
TNBS	2,4,6-trinitrobenzenesulfonic acid
TNP	2,4,6-trinitrophenyl
TNT	2,4,6-trinitrotoluene
TOCSY	total correlation spectroscopy
Tris	tris(hydroxymethyl)aminomethane
UV	ultraviolet
vt	virtual triplet
v/v	volume per volume
WGA	wheat germ agglutinin
w/v	weight per volume

IV. Symbol and Text Nomenclature for Representation of Glycan Structures

The symbol and text nomenclature follow the recommendations of the *Nomenclature Committee of the Consortium for Functional Glycomics*.

Symbol nomenclature (color version):

Circles: Hexoses

Squares: N-Acetyl hexosamines

Diamonds: Acidic sugars

-  Galactose (Gal)
-  Mannose (Man, M)
-  N-Acetylglucosamine (GlcNAc)
-  N-Acetylgalactosamine (GalNAc)
-  Fucose (Fuc, F)
-  Xylose (Xyl, X)
-  N-Acetylneuraminic acid (Neu5Ac)
-  N-Glycolylneuraminic acid (Neu5Gc)

Text nomenclature:

The committee recommends a *modified IUPAC condensed* text nomenclature (linear or 2D),

e.g.,  $\xrightarrow[\beta]{4}$  = GalNAc β 1-4GlcNAc (= LacdiNAc, LDN).

V. Code of Amino Acids

Amino Acid	Three-Letter Code	One-Letter Code
<i>Nonpolar</i>		
Alanine	Ala	A
Valine	Val	V
Leucine	Leu	L
Isoleucine	Ile	I
Proline	Pro	P
Phenylalanine	Phe	F
Tryptophan	Trp	W
Methionine	Met	M
<i>Polar</i>		
Glycine	Gly	G
Serine	Ser	S
Threonine	Thr	T
Cysteine	Cys	C
Tyrosine	Tyr	Y
Asparagine	Asn	N
Glutamine	Gln	Q
<i>Acidic</i>		
Aspartic acid	Asp	D
Glutamic acid	Glu	E
<i>Basic</i>		
Lysine	Lys	K
Arginine	Arg	R
Histidine	His	H

1. Contributions

1.1. Own Work

Intensive work has been carried out to gain access to glyco structures for analyzing their interactions with anti-carbohydrate antibodies. From inconsistent STD NMR data, I concluded that the measurements should be double-checked on another spectrometer. This check showed no spectrometric response, not even by sweeping the irradiation frequency. No binding signals were detectable by SPR spectroscopy either. To investigate this issue, I carried out a negative control STD NMR experiment together with the NMR service on the originally used spectrometer. This control showed peaks not generated by the sample but by the spectrometer itself (*i.e.*, artefacts). Due to this disconfirming evidence, I re-evaluated all STD NMR data and developed two statistical tests, which are able to evaluate such data. Having re-evaluated co-crystal data of the same ligand and receptor, I carried out molecular docking experiments with differently extended ligand fragments and harmonized all aforementioned re-evaluations by developing a binding model, which postulates a *necessary linkage of two contact points*. Hence, fragments representing either one or the other contact point show no binding signals (*e.g.*, no STD effects). The spectrometer operators and data interpreters are identified in the figure captions.

1.2. Third-Party Contributions

Antibody Phage Display (HHH1, HMM5)	J. Eckenberger, M. Plum, E. Spillner
Co-Crystallization (HMM5 / Fuc α 1-3GlcNAc)	L. Tjerrild (<i>University of Aarhus</i>)
Co-Crystal Structure (pdb- and ccp4-file)	G. R. Andersen (<i>University of Aarhus</i>)
STD NMR Experiments (~240 ser-files) Antibodies / Saccharides December, 2012 – May, 2015	M. Fölsing, T. Hackl, B. Meyer

1.3. Technical Support

STD NMR test data HSA / Trp + sucrose	F. Schumann (<i>Bruker BioSpin</i>)
MestReNova 10.0, <i>Strategies for Assignment</i>	M. Perez (<i>Mestrelab</i>)
Immobilization of Fuc α 1-3GlcNAc	V. Uzunova (<i>Biacore</i>)

1.4. Acknowledgment

I am very much obliged to E. Spillner for the possibility to work on this topic. I am particularly grateful to M. Plum for providing the monoclonal antibodies HHH1 and HMM5. STD NMR data of HSA/Trp were kindly provided by *Bruker BioSpin*. This research was supported by a scholarship from the *Roland und Elfriede Schauer-Stiftung*.

1.5. Statement in Lieu of an Oath

I hereby confirm that I have performed this thesis on my own and that I have not used any other media or materials than the ones referred to in this thesis. Furthermore, I confirm that this thesis has not, even in extracts, been submitted for another examination.



Hamburg, October 24, 2018, Tim Raiber

2. Abstract

Analysis of the Interaction between Honeybee Venom CCD Fragments and Anti-CCD Antibodies

In allergy diagnostics, cross-reactive carbohydrates (CCDs) may cause false-positive results. At the molecular level, the interactions between CCDs and anti-CCD antibodies are poorly understood. The study at hand provides insight into the interaction between the fragment Fuc α 1-3GlcNAc and phage display-derived anti-CCD antibodies. With polyclonal anti-HRP antiserum, the fragment Fuc α 1-3GlcNAc showed weak STD effects. Conversely, with mAbs, the same fragment showed no STD effects. To recognize this, a negative control had to unmask inconsistent STD NMR interpretations as artefacts. Literature suggests that these artefacts may have been caused by power spill-over. Thereupon, the STD data were statistically re-evaluated by defining a limit of detection, which considers the signal-to-noise ratio. As a result, all epitope maps were rated as statistically insignificant. However, co-crystal data facilitated an insight into the complementarity between the HMM5 Fab antibody pocket and the α 1-3 core fucose and showed that only the heavy chain is involved in the binding. Especially the amino acids Y31, N32, T52 and Y99 mediate van der Waals forces to hydrophobic regions of the disaccharide and contribute to a stabilization on the CDR interface with aromatic side chains. Apart from the acetamido function of GlcNAc, only the fucose unit contributes to this stabilization. A molecular docking experiment reproduced the binding very well and identified the HMM5 Fab as a low-affinity antibody. Docking experiments involving extended glyco structures explain the apparent contradiction of non-binding properties found in STD NMR and SPR experiments and binding properties found in the co-crystal and suggest a minimal motif with Man α 1-6 and Fuc α 1-3 as necessary valences. Docking of extended glyco structures indicates that a cross-linking of the V_H and V_L chain is mediated by these two glyco valences. Due to the original immune function of the T_H2 response, this binding hypothesis applies to parasite-associated glyco patterns, too. Since the immune system must distinguish whether the subunit Fuc α 1-3GlcNAc belongs to self- or non-self antigens, the study presented here interprets the role of blood groups (Le^x, sLe^x, AB0) from a new perspective and links it with type I hypersensitivities to CCDs.

3. Zusammenfassung

Analyse der Interaktion zwischen CCD-Fragmenten des Honigbienengifts und monoklonalen anti-CCD-Antikörpern

In der Allergie-Diagnostik können kreuzreaktive Kohlenhydrat-Determinanten (CCDs) zu falsch-positiven Befunden führen. Auf molekularer Ebene sind die Wechselwirkungen zwischen CCDs und anti-CCD-Antikörpern noch weitgehend unverstanden. Die vorliegende Arbeit untersucht daher die Beiträge einzelner CCD-Fragmente zur Kreuzreaktivität. Das Fragment $\text{Fuc}\alpha 1\text{-3GlcNAc}$ zeigte mit polyklonalem anti-HRP-Serum schwache STD-Effekte. Mit monoklonalen Antikörpern zeigte dieses Fragment hingegen keine bindenden Wechselwirkungen. Um zu dieser Erkenntnis zu gelangen, mußte allerdings erst hanebüchene STD-NMR-Interpretationen der Daten entzogen werden, indem eine Negativ-Kontrolle sie als Artefakte entlarvte, die vermutlich durch Leistungsüberstrahlung verursacht wurden. Im Rahmen einer Neubewertung wurde eine Bestimmungsgrenze definiert, die das Signal-Rausch-Verhältnis berücksichtigt. Zwar wurden daraufhin alle Epitopkarten als statistisch insignifikant gewertet, aber Kokristall-Daten ermöglichten trotzdem einen Einblick in die Komplementarität der HMM5-Fab-Antikörper-Bindungstasche zur $\alpha 1\text{-3-Core-Fucose}$ und zeigten, dass nur die schwere Kette in die Bindung involviert ist. Besonders die Aminosäuren Y31, N32, T52 und Y99 tragen zur Stabilisierung der $\alpha 1\text{-3-Core-Fucose}$ auf der CDR-Schnittstelle bei, wobei aromatische Seitenketten eine Schlüsselrolle spielen. Docking-Experimente reproduzierten die Bindung und identifizierten HMM5-Fab-Antikörper als einen niedrig-affinen Antikörper. Auf diese Weise verifizierten die Modeling-Ergebnisse die Kokristall-Daten und erklärten gleichzeitig die nicht-bindenden Eigenschaften der monoklonalen Antikörper, die mit STD-NMR- und SPR-Experimenten festgestellt wurden. Daraus wurde eine Bindungshypothese entwickelt, die $\text{Man}\alpha 1\text{-6}$ und $\text{Fuc}\alpha 1\text{-3}$ als für eine Bindung notwendige Valenzen postuliert, da sie eine Kreuzvernetzung von V_H - und V_L -Kette vermitteln. Da $\text{Fuc}\alpha 1\text{-3GlcNAc}$ zu einem Epitopmuster parasitärer Nematoden gehört und daher vom Immunsystem des Wirts von Selbstantigenen, die auch $\text{Fuc}\alpha 1\text{-3GlcNAc}$ enthalten (Le^x , sLe^x , AB0), unterschieden werden muss, wird die Rolle der Blutgruppen-Determinanten neu interpretiert und in Zusammenhang mit Typ I-Hypersensitivitäten gegen CCDs gebracht.

4. Introduction

4.1. Introduction into the Concept of Allergy

4.1.1. Serum as “Carrier of Immunity”

In the **19th century**, the modern bacteriology was founded. Henle, Koch and Löffler found a causative relationship between a microbe and a disease.^{1,2,3} To identify the causative agent of a particular disease, four criteria were established:² (i) “The pathogen must be present in all cases of the disease.” (ii) “The pathogen must be isolated from the diseased host and grown in pure culture.” (iii) “The pathogen from the pure culture must cause the disease when inoculated into a healthy, susceptible laboratory animal.” (iv) “The pathogen must be reisolated from the new host and shown to be the same as the originally inoculated pathogen.”

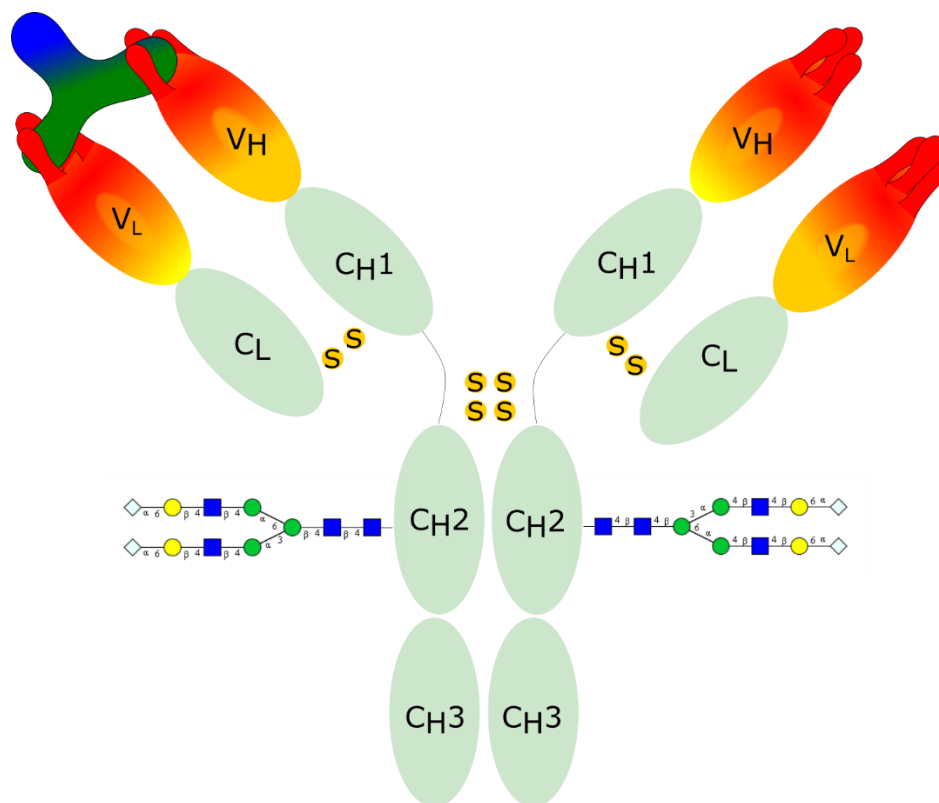


Fig. 1: Equine anti-diphtheria toxin antibody (“diphtheria antitoxin” from serum horses) with two Fc glycosylations. The glycans show terminal Neu5Gc residues, which are recognized by human IgG antibodies. At least two Fc Neu5Gc termini are required for binding to human anti-Neu5Gc antibodies.⁴ The discrimination between Neu5Gc and Neu5Ac gave rise to serum sickness at diphtheria patients who were treated with “diphtheria antitoxin” from serum horses. The serum sickness antigen is referred to as Hanganutziu-Deicher antigen.⁵

Vaccines against many infections were developed, but diphtheria, an infection mostly children died from, remained still incurable. Von Pettenkofer pointed to the importance of hygiene for prevention of epidemics.⁶ Behring and Kitasato (*Institute for Hygiene, Berlin*) recognized serum as the “carrier of immunity” and developed an anti-diphtheria serum therapy.⁷ An equine

anti-diphtheria toxin antibody is illustrated in fig. 1. The implication of the Fc glycosylation is described later. Since **1894**, diphtheria patients have been treated with horse serum-derived diphtheria antitoxin. The mortality rate decreased immediately. In **1901**, Behring received the Nobel Prize in Medicine “for his work on serum therapy, especially its application against diphtheria, by which he has opened a new road in the domain of medical science and thereby placed in the hands of the physician a victorious weapon against illness and deaths”. With the prize money, he founded the Behring Werke, where immunized horses provided large quantities of serum (fig. 2).

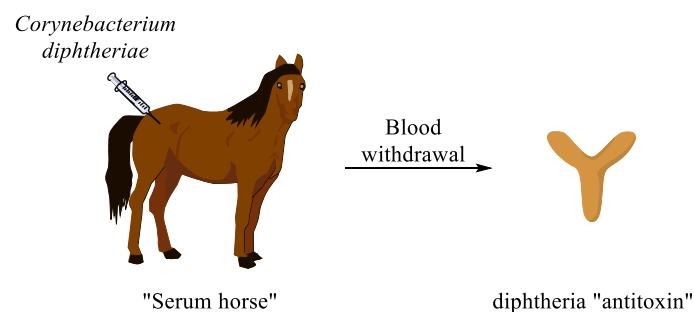


Fig. 2: Blood withdrawal from an immunized horse („serum horse“) for the production of “diphtheria antitoxin”. The diphtheria toxin is an AB-toxin (61 kDa) consisting of an A-domain (21 kDa; depicted as blue protein proportion in fig. 1), which is connected by several disulfide bridges with a B-domain (40 kDa; green). It is an exotoxin (i.e., secreted by the bacterium). The genetic code for the toxin is provided by phages. Passive vaccinations have cured many infected patients at the turn of the century at **1900**.

It is notable that the mammalian immune system is not as efficient as that of evolutionary ancient species like crocodiles or alligators.⁸ But active vaccinations, which are based on the cross-reactivity of vaccines with pathogenic antigens, improve its efficacy. These were developed by Jenner at the example of pus-derived cowpox vaccines (from Lat. *vacca* = cow) in **1796** and optimized by Ehrlich (tetanus toxoids) in **1897** and Salk (formaldehyde inactivated poliomyelitis viruses) in **1954**.

4.1.2. Serum Sickness as an *Allergic Response to Animal Serum* - the Concept of *Allergy is Developed*

“After diphtheria antitoxin came into general use in the treatment of diphtheria in **1894**, the occurrence of exanthems, joint pains, etc., following the injection began to be reported.”⁹ Von Pettenkofer (*Institute for Hygiene, Munich*) suggested to von Pirquet that “a study of incubation time would furnish an important clue to the concept of immunity”.¹⁰ In **1905**, the pediatricians von Pirquet and Schick stated the following about the time course of “serum sickness” in a patient (fig. 3): “(i) The formation of circulating antibodies is delayed after administration of serum. (ii) There is a similar delay in the onset of the symptoms of serum sickness. (iii) A

second, later injection of serum leads to a drop in the amount of circulating antibodies and a more rapid onset of symptoms. (iv) The reaction is specific, as using a different serum for the second does not incite the same accelerated response. (v) Although small doses of serum injection stimulate antibody formation, they do not result in clinical symptoms.”¹¹ Fig. 3 shows the time course in terms of horse serum (Pirquet’s “allergen”), antibody and “toxic body” formation. The latter was suggested as a “toxic physiological product” formed by “a chemical interaction between the horse serum and the antibodies of the vital (that is, immune) reaction”. This suggestion corresponds to the modern concept that an immune complex deposited at blood vessel walls activates the complement system.¹²

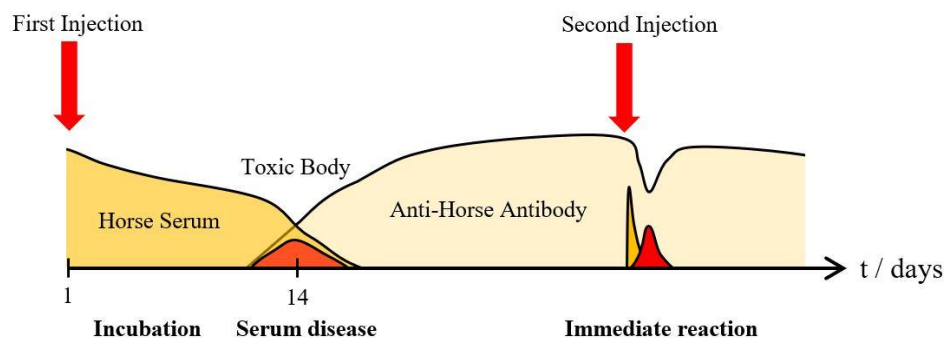


Fig. 3: Horse serum (Pirquet’s “allergen”) and antibody titer as a function of time. The term “toxic body” indicates the formation of an immune complex eliminating the allergen and causing the symptoms of serum sickness. Though Pirquet’s documentation is brilliant it remained unrewarded. Adopted from von Pirquet (1911).¹³

During this so-called classical way of complement activation, the complement proteins C3a and C5a are released as pro-inflammatory mediators. In addition, “C5a is a highly potent chemotaxin, and it stimulates the release of hydrolytic granular enzymes, bioactive lipids, and superoxide anions from neutrophils.” In contrast, “C3a is a chemotaxin for eosinophils but not for neutrophils.” Thus, the “toxic body” proposed by von Pirquet and Schick is a “biologic response to complement-derived anaphylatoxins C3a and C5a” and, as indicated in fig. 3, gives rise to the clinical manifestation of the serum sickness, especially to joint pain. Hence, von Pirquet and Schick recognized serum sickness as an *allergic* response to animal serum (from Anc. Gr. $\alpha\lambda\lambda\omicron\varsigma$ $\epsilon\rho\gamma\omicron\varsigma$ = altered reactivity) and in 1910, both authors proposed the full mechanism of serum sickness.¹⁴ The formation of immune complexes is typical for type III allergic reactions. This response occurs when the antigen reacts in the tissue space with potentially precipitating antibodies, mainly IgM, forming micro precipitates in and around small vessels, causing secondary damage to cells. If the antigen is present in excess, soluble immune complexes are formed and further deposited in the endothelial lining of blood vessel walls, fixing complement and causing local inflammation. Immune complexes are primarily

deposited in the lung, joints, kidneys and the skin. Tissue injury is initiated by the local inflammation response, involving activation of the complement. Various cells, such as macrophages, neutrophils and platelets, are subsequently attracted to the deposition site and further contribute to the tissue damage.

4.1.3. Allergy is Classified into Types of Hypersensitivity

Immunology is the science of self-non-self-discrimination. In case of hypersensitivities (*i.e.*, allergic and autoimmune responses), these discriminations are carried out imperfectly. Hypersensitivities are immune reactions of the adaptive immune system (T_H and B cells) against evolutionary new antigens. As a consequence, the reaction is not that precise than that of the innate immune system (TLRs), which reacts against evolutionary conserved structures (*e.g.*, TLR4 against LPS). Hence, hypersensitivities are inappropriate and/or excessive immune reactions, which occur as a side-effect of the body's capacity to reject foreign invasion, particularly pathogens. In **1963**, Coombs and Gell classified hypersensitivity diseases into four major categories upon underlying causes: immediate (type I), antibody-mediated (type II), immune complex-mediated (type III) and cell-mediated (type IV) hypersensitivity.¹⁵ Type IV is further subdivided into two subtypes. Nowadays, the validity of the classification is discussed.¹⁶ In contrast to symptoms and antibody titers, *cytokine patterns* and complement proteins are a direct and characteristic fingerprint of a hypersensitivity.

4.1.3.1. Type I Hypersensitivity

In type I hypersensitivity, an allergen (mistaken for a parasite-derived antigen) is phagocytized by an APC which then migrates into the next lymph node to present a fragment of this allergen to T_H0 cells, whereupon these T_H0 cells differentiate into T_H2 cells since this is determined by the cytokine IL-4 (clonal expansion; fig.s 4 and 5). These T_H2 cells activate B cells by secretion of IL-2, IL-4 and IL-5 to differentiate into antibody producing plasma cells (fig. 4), followed by a class switch from IgG/M to IgE. IgE antibodies then binds to the $Fc\epsilon$ receptors of mast cells (tissue) and basophils (blood). Mast cells and basophils coated by IgE are now sensitized against the allergen. A later exposure to the allergen will result in a cross-linking of the IgE antibodies and a secretion of vasoactive amines, such as histamine (degranulation). IL-4, IL-9 and IL-13 induce goblet cell hyperplasia and promote mucus production. Besides, T_H2 - and mast cell-derived cytokines (IL-3, IL-5, GM-CSF) stimulate eosinophils and leukocyte recruitment, giving rise to a delayed reaction (2 to 4 h after exposure). Symptoms are relieved

by antihistamines (binding to histamine receptors) and Omalizumab (binding to IgE). In immunotherapy, immune tolerance is build up by exposition to increased amounts of allergen.¹⁷

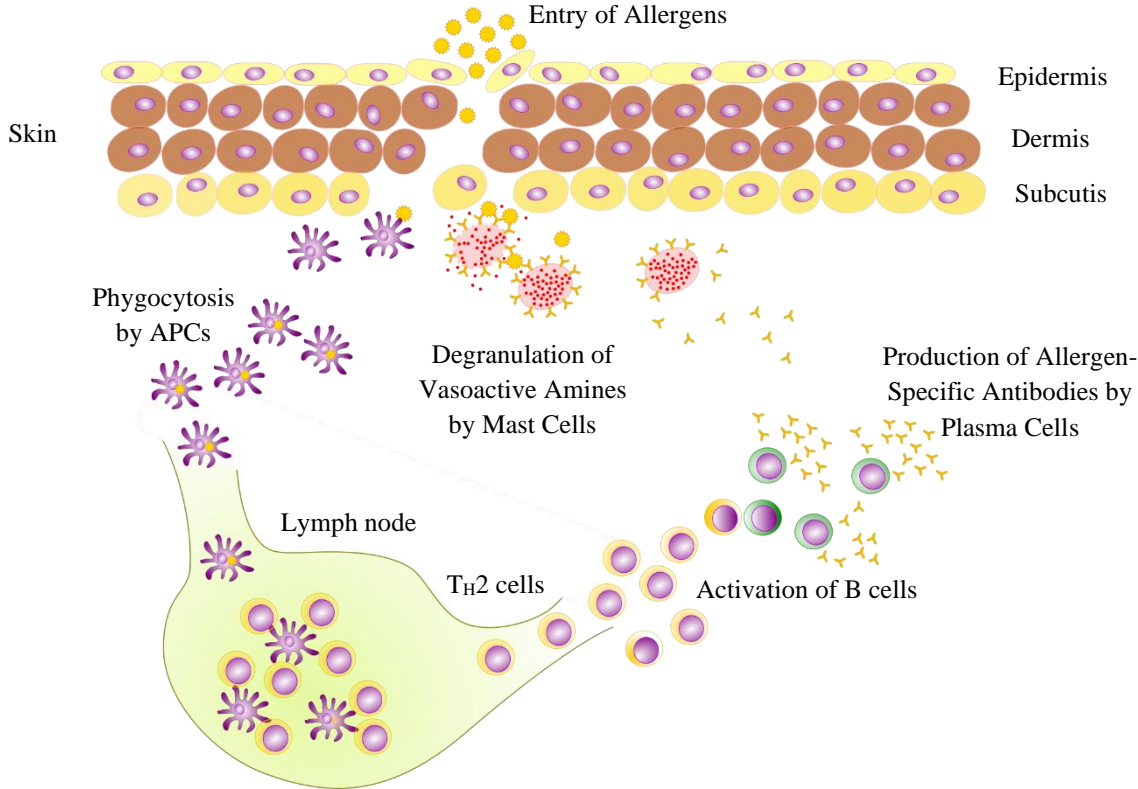


Fig. 4: Pathomsm of hypersensitivity type I. Its steps are exposition to an allergen, sensitization, production of allergen-specific IgE antibodies, re-exposition to the allergen, cross-linking of IgE antibodies followed by mast cell degranulation, which gives rise to allergy symptoms. The activation of B cells is illustrated in fig. 5.

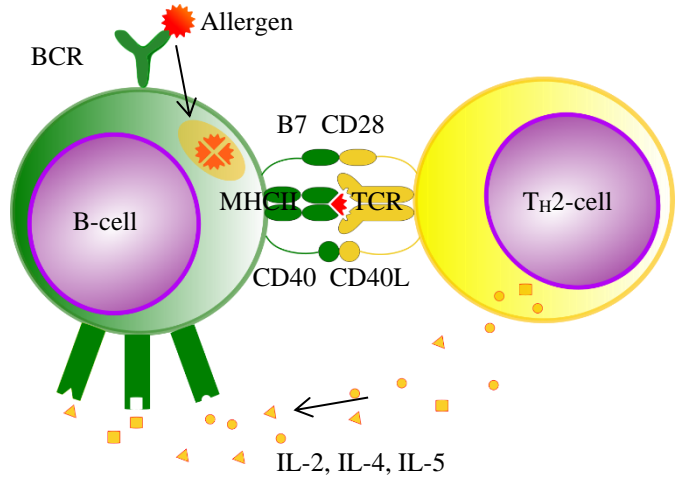


Fig. 5: Interaction between B and Th2 cell. The B cell binds allergen and presents phagocytosed allergen fragments (red) on the top of an MHC II complex (yellow) to a Th cell. The first signal is the binding of the TCR (green) to the MHC II complex and the second signal is the binding of CD28 to B7.

Independently, Emanuel and Strachan developed a hygiene hypothesis, which states that a lack of early childhood exposure to infectious agents, symbiotic microorganisms (such as the gut flora or probiotics), and parasites increases the susceptibility to type I hypersensitivities by

suppressing the natural development of the immune system.^{18,19} In particular, the lack of exposure is thought to lead to defects in the establishment of immune tolerance. The reason for this is that allergies are a misfiring of a defense against parasites like helminths.²⁰ Accordingly, the cytokine patterns are equally expressed.²¹

4.1.3.2. Type II Hypersensitivity

In type II hypersensitivity, autoreactive IgG antibodies bind to somatic cells (“self”) which display antigens on their surface (adsorbed, possibly as part of an infection with a pathogen). This activates the complement system (C1-C9) in the way that C1q binds to the Fc γ region of IgG and C3b to the cell surface. These tagged cells are then recognized by natural killer (NK) cells and macrophages *via* Fc γ RIII (CD16) and C3bR, resulting in phagocytosis. The anaphylatoxins C3a and C5a induce degranulation of mast cells and basophils. An important example is drug-induced autoimmune hemolytic anemia.²² Antibody-dependent cell-mediated cytotoxicity is utilized in antitumor therapy with monoclonal antibodies, such as Trastuzumab against breast cancer.

4.1.3.3. Type III Hypersensitivity

Type III hypersensitivity is mediated by circulating immune complexes (CICs) which precipitate on blood vessel walls, causing inflammation and tissue damage. In contrast to type II, in type III, the complexes are such small that they are less attractive to macrophages and are not cleared as quickly than tagged cells are cleared in type II hypersensitivity. Thus, they proceed circulating and reach blood supplied tissues like kidneys, where blood is being filtered, and joints, where plasma is being filtered producing synovial fluid. Typically, the CICs bind to the basement membrane and activate the complement system (C1-C9). The anaphylatoxins C3a, C4a and C5a are released, resulting in an increase of vascular permeability (*i.e.*, fluid leaks into surrounding tissue) and causing an edema. Besides, the anaphylatoxins act as chemokines, meaning they recruit other cells like neutrophils to the site of inflammation. The neutrophils degranulate lysosomal enzymes and reactive oxygen species, which cause tissue necrosis and vasculitis. Thus, if CICs precipitate in the kidney, this may cause glomerulonephritis, and if they precipitate in the joints, this may cause arthritis. An example for a type III hypersensitivity is serum sickness.²³ It has been reported after treatment of diphtheria, rabies or cancer with equine and murine antisera or monoclonal antibodies.²⁴ Another example is the Arthus reaction, which has been reported after vaccinations containing diphtheria and tetanus toxoid.²⁵

4.1.3.4. Type IV Hypersensitivity

Type IV hypersensitivity is classified into two subtypes (T_H1 or autoreactive CTL mediated immune response). $CD4^+$ T_H1 cells recognize antigens presented by APCs, which have been migrated into lymph nodes. These APCs (*e.g.*, macrophages) secrete IL-12, which stimulates the proliferation of further T_H1 cells. These secrete IL-2 and IFN- γ stimulating macrophages (positive feedback loop). Stimulated autoreactive CTLs attack somatic cells. This way is taken in autoimmune diseases like celiac disease.²⁶ In celiac disease, the tight junctions of the intestine lumen become unsealed in response to the release of zonulin by enterocytes. As a result, gluten fragments are able to pass the lumen, are phagocytized by macrophages and presented as modified gluten in complex with MHC I (HLA DQ2 or 8) to T_H1 cells. These T cells stimulate CTLs to attack enterocytes.

4.2. α 1-3 Core Fucose in the Context of Type I Hypersensitivity

4.2.1. “De l’Action Anaphylactique de Certains Venins”

In **1901**, Richet and Portier discovered anaphylaxis as they exposed two dogs to weak doses of sea anemone *Physalia physalis* actinotoxin, which is a yet uncharacterized toxin, and then repeated the injection at various time intervals.²⁷ The dogs did not react with any symptoms, but if the injections were repeated after 2 or 3 weeks with an “equally weak dose”, then “violent toxic symptoms” followed and the dogs died. In **1913**, Richet proposed two factors that were necessary and sufficient to cause an anaphylactic reaction: “increased sensitivity to a poison after previous injection of the same poison, and an incubation period necessary for this state of increased sensitivity to develop.”²⁸ Since its discovery, *Hymenoptera* venom has revealed as a most common causative agent of anaphylaxis. Other causative agents are implicated, too (*e.g.*, β -lactam antibiotics and local anesthetics). According to the *Federal Statistical Office*, in 3.5 % of the German population an insect sting causes systemic reactions. Around 20 cases of death per year are caused due to anaphylaxis as a consequence of insect sting. In Germany, wasps are responsible for most of the insect stings (wasps: 69.5 %; bee: 17.4 %, hornet: 5.5 %, bumblebee: 0.4 %).²⁹ In *Hymenoptera* venom allergy, about 75 % of detected *in vitro* double positivity to wasp and honeybee venom is ascribed to specific IgE directed against CCDs. Anaphylaxis after European hornet stings is nearly always due to cross-reactivity against *Vespula* venom.³⁰ Basophil activation is strongly affected by CCDs.³¹ The composition of *Hymenoptera* venoms has been elucidated in detail.³² A bee injects around 100 μ g venom (pH 4.5 to 5.5). The major component of honeybee venom is melittin (Api m4; from Anc. Gr.

μελιττα = bee; 50 % of dry weight), which is a cationic polypeptide consisting of 26 amino acids (2.8 kDa) and forms pores in cell membranes resulting in release of K^+ ions and cell death. Since melittin is not glycosylated, it is not responsible for cross-reactivity due to CCDs. The dipeptidyl peptidase IV (DPP IV; 2 % of dry weight) is cross-reactive due to its sequence homology (54-56 %) and CCDs (Api m5 and Ves v3, both 100 kDa and 5-7 glycosylation sites). It cleaves promelittin to melittin. The second most frequent component is PLA₂ (Api m1; 12 % of dry weight) which is a glycoprotein (17 kDa) that catalyzes the hydrolytic cleavage of phospholipids (*i.e.*, cell membranes). Since it is monoglycosylated, it is not responsible for cross-reactivity based on carbohydrates. A cross-linkage requires at least 2 glycosylated sites. Because of that, Api m1 is a specific marker for the diagnosis of bee venom allergy. The phospholipase of *Vespidae* cleaves at *sn*2 (Ves v1 = PLA₂). Because it is not glycosylated, Ves v1 is a specific marker for the diagnosis of wasp venom allergy. Phospholipases A₂ are also present in viperine venoms, acting as anti-coagulants and platelet aggregation inhibitors (*i.e.*, hemotoxins). Most of them are unglycosylated. The rare cases of glycosylated PLA₂ coincide with the glycosylation patterns of bee venom.³³ Phospholipases in elapids just play an inferior role. The venom of the most elapids acts as neurotoxin (immobilization of the prey). Apamin is an 18 amino acid peptide neurotoxin (2-3 % of dry weight). It is the smallest neurotoxin polypeptide known, and the only one that passes the blood-brain barrier. Its target organ is the central nervous system. Here it inhibits small-conductance Ca^{2+} -activated K^+ channels in neurons. Hyaluronidase (Api m2, 2 % of dry weight, 45 kDa) cleaves hyaluronan, *i.e.*, the linear polymer $(-4GlcA\beta 1-3GlcNAc\beta 1-)_n$, which is an important substance in the extracellular matrix. By digesting the connective tissue, hyaluronidase acts as a spreading factor, what means that the other venom compounds become distributed in the tissue. Hyaluronidase is able to cross-link IgE antibodies because of its 2 glycosylation sites. It cross-reacts with the hyaluronidase from *Vespula vulgaris* (Ves v2, 43 kDa), which is at least two-fold glycosylated and the amino acid sequence corresponds with 53 %. Mast cell degranulating peptide (MCD; 2 % of dry weight) is a cationic peptide consisting of 22 amino acid residues. Without being glycosylated, this peptide causes release of histamine from mast cells. Serum of a patient who reacts both against bee and wasp venom is tested with HRP to detect CCD specific IgE antibodies.

4.2.2. Surprising Implication of a “Periodate-Sensitive and Heat-Stable” Antigen in Type I Hypersensitivity

In 1981, Aalberse *et al.* (Central Laboratory of the Netherlands Red Cross Blood Transfusion Service) have reported that “IgE in some human sera reacted with an antigen present in a large number of unrelated foods: potato, spinach, wheat, buckwheat, peanut, honey, and others.³⁴ The antigen, which was periodate-sensitive and heat-stable, was also found in pollen. Even more surprisingly, these antibodies often reacted *in vitro* with bee and vespid venom and were sometimes apparently induced by *Hymenoptera* stings.” A RAST analysis showed a cross-reactivity pattern for a serum derived from a 15-year-old girl hypersensitive against honeybee (“serum A”). (“Serum A was obtained from a girl born in 1964. In August 1979 she was stung on her foot by an insect, presumably a honeybee; this caused a large local reaction that lasted for 2 days.”) As a positive control, a serum obtained from a rabbit inoculated with HBV was used (anti-HBV). For comparison, a serum obtained from a rabbit inoculated with BWA was used (anti-BWA). As a negative control, serum obtained “from a rabbit injected with CFA” only was used (anti-CFA). Serum A shows 30 % of “bound radioactivity” for HBV. Surprisingly, serum A cross-reacts with a lot of plant extracts. The strongest cross-reactivities are detected in case of rice (29 %), *Dactylis glomerata* (29 %) and potato (28 %). Additionally, sera obtained from two beekeepers after stinging by honeybees were analyzed by HBV and buckwheat RAST: “These results indicate that bee stings can apparently induce IgE antibodies to vegetable foods, such as buckwheat; the IgE antibody titer of serum from subject W. A. toward buckwheat was considered lower than to HBV.” Based on these findings, Aalberse *et al.* discussed the following three key questions:

- i. “Is the IgE binding caused by IgE antibodies to an *antigen*?”
- ii. “Is the polyspecificity of serum P caused by *multiple sensitizations* or by *cross-reacting* IgE antibodies?”
- iii. “Are these IgE antibodies *clinically relevant*?”

First, Aalberse *et al.* stated that “IgE binding *seems* to lack specificity” and brought forward a “lectin hypothesis”: “Might not the IgE binding, *e.g.*, to Sepharose-coupled potato or buckwheat extracts, be caused by lectins in these extracts that bind IgE *via* its carbohydrate side-chains? In support of this lectin hypothesis is the finding that some gums, notably tragacanth gum are potent inhibitors of the buckwheat or potato RAST.” But the authors concluded that “the results of direct RAST experiments, as opposed to the above-mentioned RAST inhibition experiments, indicate that the component responsible for the IgE binding is

periodate sensitive” and substantiated this conclusion with the findings that first, the induction of IgE antibodies by bee stings “is difficult to reconcile with the lectin hypothesis”, and second, the immunization of the rabbits “with a buckwheat preparation or a HBV fraction *induced antibodies with a crossreactivity pattern closely similar to that of the IgE antibodies*”. Regarding the second key question, the authors concluded “that the IgE binding to potato or buckwheat is most likely caused by IgE antibodies that specifically bind to some ubiquitous antigen. The periodate susceptibility and the affinity to Con-A lead us to believe that this antigen or determinant is most likely a *carbohydrate*. We provisionally refer to this material as a CCD.” The authors even speculated about “hydroxyproline-rich plant glycoproteins” as “likely candidates” and cited an article published by Allen *et al.* in 1978.³⁵ Based on the state of knowledge of their time and despite no N-glycan or α -1,3-fucosylation is mentioned in that reference - since these determinants are elucidated later - they opened the door to a wide research field, forming the term “cross-reactive carbohydrate determinant”, albeit under lack of knowledge of its structure. The third key question was negated by the authors in the following way: “Our hypothesis is that *these IgE antibodies react with an antigenic determinant consisting of some carbohydrate side-chain present in a number of different glycoproteins found mainly in plants*. For some reasons – possibly continuous desensitization *via* oral exposure – *this IgE antigen system will rarely, if ever, trigger mast cells or basophils*. If further investigation should substantiate this hypothesis, it would be logical to disregard antibodies to this “allergen” for diagnostic purposes. In the RAST, this can be accomplished in principle by preabsorption of sera with BWA or a similar preparation but complete absorption may be difficult to achieve.” However, Aalberse *et al.* linked the field of type I hypersensitivity to the field of plant glycoproteins and pioneered the structural elucidation of these CCDs.

4.2.3. “Specific Interaction of IgE Antibodies with a Carbohydrate Epitope of Honey Bee Venom Phospholipase A₂”

In 1986, Weber *et al.* have shown that crude PLA₂ from honeybee venom is composed of 12 % unglycosylated PLA₂ and 88 % glycosylated PLA₂.³⁶ The glycosylated fraction contains two glycoforms, *i.e.*, one with a complete N-glycan and the other with a “lack of either 3- or 6-linked mannosyl residues and terminal N-acetylglucosamine.” One year later, the same group showed that “IgE from 11 of 14 bee venom allergy sera exhibited significantly higher, and in two cases exclusive, affinity to *glycosylated* phospholipase.”³⁷ In RAST inhibition experiments using phospholipase coupled to discs, five of the sera were completely inhibited by

glycopeptide at 0.1 mg/mL; four sera were partially inhibited and two sera could not be inhibited. Glycoasparagine, lacking all amino acids except the carbohydrate-linking asparagine, inhibits IgE-binding to glycopeptide discs up to 100 %. These data clearly demonstrate that *an oligosaccharide* of a structural type frequently found in glycoproteins *can represent an epitope which is recognized by IgE antibodies from allergic patients*, which are specifically directed against the parent glycoprotein.” In detail, the results indicate that the *sera can be classified into three groups* (i.e., no, partial or complete inhibition by PLA₂).

4.2.4. Phospholipase A₂ as a Combatant of the Glycan War

The diversity of glycans is large (fig.s 7-17). They are not so much specifically detectable by antibodies, which may underly cross-reactivities due to structural resemblance of the glycans, but rather by lectins (table 1). Hence, lectins are predestinated for control experiments. For instance, AAL shows a β -propeller folding with six blades with five ones bearing fucose binding sites. In each of them, fucose is stabilized by tryptophan, glutamic acid and arginin.³⁸ The structure of plant N-glycans was elucidated by Ishihara *et al.* at the example of stem bromelain in **1979** (fig. 8).³⁹ Its extended variant MMXF³ was characterized by Yang *et al.* at the example of HRP in **1996** (fig. 9). This structure consists of a core C (fig. 7), which is α -1,3 fucosylated and β -1,2 xylosylated. HRP is a glycoprotein with several isotypes and is heterogeneously glycosylated.⁴⁰ The α -1,6 fucosylated variant (MMXF⁶) occurs in snails.⁴¹ The non-xylosylated variants of the α -1,3 fucosylated N-glycan occur in insect venoms and were elucidated by Kubelka *et al.* at the example of PLA₂ in **1993** (fig. 9).⁴² Extended variants occur in helminths like *S. mansoni* (fig.s 10 and 11) and induce a T_H2 response upon infection.⁴³ By mimicking Le^x (fig.s 10 and 11), the host's immune response is reduced to such an extend that the parasite can escape.^{44,45,46,47} Such host-parasite relationships have a competitive character: Hosts require glycans for critical cellular functions (*e.g.*, secretion, stabilization, adhesion), but must constantly vary them to evade glycan-binding pathogens.⁴⁸ This leads to three Red Queen effects (fig. 6). Another immunogenic substituent is sialic acid, which occurs in mammals as Neu5Gc and, due to a dysfunctional mutation of the Neu5Ac hydroxylase encoding gene, as Neu5Ac in humans. It is believed that sialic acid plays a decisive role in enabling neurotransmission between neurons. Human anti-Neu5Gc antibodies give rise to serum disease.⁴⁹

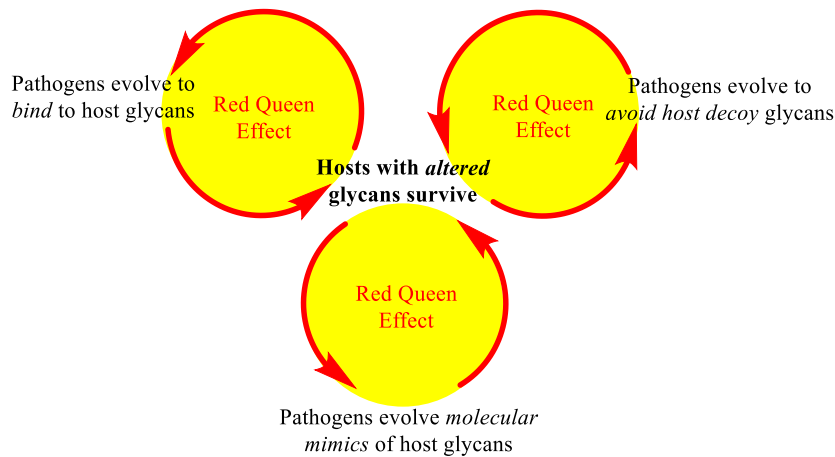
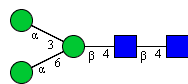


Fig. 6: Evolutionary forces are driving the diversification of glycans. Each circle represents a vicious cycle driven by a Red Queen effect: While set against evolving pathogens in a constantly changing environment, hosts must constantly adapt and evolve in order to survive. The Red Queen effect was first described by van Valen who took the illustration from Carroll’s “Through the Looking-Glass” when the Red Queen says to Alice, “Now, here, you see, it takes all the running you can do, to keep in the same place.”^{50,51} Diagram adapted from Varki (2009).

The blood groups were discovered by Landsteiner in **1923** and share Gal β 1-4GlcNAc as a common structure.⁵² Their potential protective role was described by Gagneux and Varki in **1999**, who also found an evolutionary pattern for the occurrence of the α Gal blood group, that is that the loss of α Gal in the complete lineage of Old World monkeys is “accompanied by complement-fixing antibodies directed against the same structure”. The α Gal epitope was found on a deer-infecting nematode species and gives rise to type I hypersensitivities to lone-star tick saliva, porcine heparin or heart valves and Cetuximab.^{53,54,55}



Core C

Fig. 7: The basic structure of N-glycans is referred to as core C.⁵⁶ It is attached to asparagine.



Fig. 8: N-Glycans of plants.

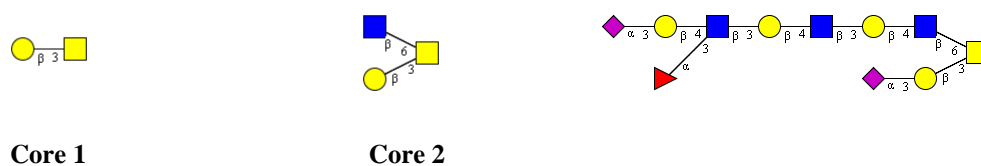


Fig. 15: Mammalian O-glycans are attached to serine or threonine (core 1, core 2 and O-glycan bearing fucosylated and sialylated lactosamines).



Fig. 16: Blood group determinants.



Fig. 17: Lewis antigens Le^x and sLe^x. sLe^x is important for leucocyte recruitment by selectins and is expressed on the endothelium. Both antigens play a role during inflammation and homing to lymph nodes.

Table 1: Lectins and their ligand motifs. Since glycan patterns are specifically recognized by lectins, lectins are suitable positive controls for anti-carbohydrate antibodies.

Lectin	Lectin Abbreviation	Ligand motif	K _D
<i>Galanthus nivalis</i> agglutinin	GNA	gp120 (HIV), Man α 1-3Man	\sim 0.33 nM (gp120) ⁵⁷
Wheat germ agglutinin	WGA	GlcNAc β 1-4GlcNAc	\sim 1.6 μ M (chitin) \sim 46 μ M (chitobiose) (Angulo <i>et al.</i> , 2010)
<i>Aleuria aurantia</i> agglutinin	AAL	Fucose and all binding positions of fucose	\sim 0.16 mM (fucose) ⁵⁸
For comparison:	2G12 (only carbohydrate-directed monoclonal antibody against HIV)	gp120 (HIV)	\sim 10 nM ⁵⁹
	Streptavidin	Biotin	\sim 1 fM ⁶⁰

4.2.5. “Fucose α 1,3-Linked to the Core Region of Glycoprotein N-Glycans Creates an Important Epitope for IgE from Honeybee Venom Allergic Individuals”

In 1993, a short time after the elucidation of the N-glycan of the PLA₂ in honeybee venom, Altmann *et al.* reported on „122 sera with appreciable levels of IgE antibodies directed against bee venom“ with “34 sera exhibited significant amounts of glycan-reactive IgE.⁶¹ These sera cross-reacted with the N-glycan from the plant glycoprotein bromelain.” “Since *defucosylated* bromelain glycopeptides or glycopeptides containing a Man₃GlcNAc₂ oligosaccharide were *not recognized* by most of these sera”, the authors concluded “that α 1,3-fucosylation of the innermost N-acetylglucosamine residue of N-glycoproteins forms an IgE-reactive determinant” and ascribed great importance to the core α -1,3-fucosylation: “This structural element is frequent in glycoproteins from plants, and it occurs also in insects. It is suspected to be one of the major causes of the broad allergenic cross-reactivity among various allergens from insects and plants.”

4.2.6. “Fucose-Containing Conjugates Bind Only Weakly to Anti-bee Venom”

In 2011, Collot *et al.* published that immobilized F³ and F³F⁶ core fragments show extremely low ELISA binding signals with anti-bee venom, anti-HRP and patient sera (fig. 18).⁶²

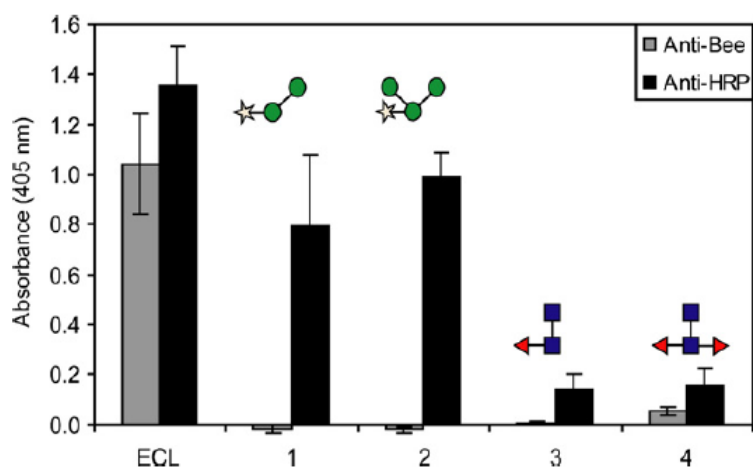


Fig. 18: “ELISA with anti-bee venom and anti-horseradish peroxidase antisera. Microtiter wells were coated with streptavidin followed by biotinylated Erythrina cristagalli lectin (ECL, as a positive control) or compounds **1** (MUX fragment), **2** (MMX fragment), **3** (monofucosylated F³ core fragment) and **4** (difucosylated F³F⁶ core fragment) at 5 μ g/mL. ‘Blank corrected’ results of the average of two independent duplicate assays are presented (total $n = 4$, with standard deviations); structures of the oligosaccharide fragments are shown according to the nomenclature of the Consortium for Functional Glycomics. BSA-MUXF³ was used to coat one set of lanes as a positive control, whereas biotinylated ECL was shown not to bind BSA-blocked plates unless streptavidin was used to coat the wells (data not shown).”

4.3. Introduction to Antibodies

4.3.1. Structural Characteristics of Antibodies

In **1959**, Porter demonstrated that papain cleaves the Ig molecule into three pieces of approximately equal size (45 kDa).⁶³ Two of these pieces retain the ability to bind to an antigen and are therefore referred to as Fab fragments for “fragment antigen binding”. Since these fragments can bind to but cannot precipitate the antigen, they must be monovalent – they possess only one binding site each. At least two binding sites are needed for precipitation, presumably to bridge two antigen molecules. The complete Ig molecule, which can both bind to and precipitate an antigen, is bivalent (*i.e.*, it contains two binding sites). The fragment produced by papain digestion differs from the two Fab fragments in that it can be crystallized. Porter therefore referred to it as Fc for “fragment crystallizable”. Since crystals are formed easily only from identical molecules, the crystallization of Fc fragments indicates that the fragments do not vary much from antibody to antibody. By the same token, the inability to crystallize Fab fragments or the whole Ig molecule suggests that they are responsible for most of the antibody variability and heterogeneity. Pepsin digestion breaks the Fc fragment into several oligopeptides, leaving the rest of the molecule intact. The remaining large fragment has a molecular weight approximately double that of one Fab fragment, indicating that it exhibits two binding sites, and is therefore referred to as F(ab)₂. The two enzymes thus act on approximately the same region of the Ig molecule, but one splits the molecule on one side and the other on the other site of the disulfide bond that holds the two Fab fragments together. In **1960**, Edelman demonstrated that treatment of the Ig molecule with mercaptoethanol, an agent that breaks disulfide bridges, reduces the size of the molecule, apparently by dissociating it into its subunits. Subsequent studies revealed the existence of four such chains in each molecule, two with molecular weights of about 53 kDa each and another two with molecular weights of about 22 kDa each. The two larger chains have been denoted with H for “heavy” and the two smaller with L for “light”. Mercaptoethanol treatment of Fab fragments yields two chains from each fragment – one that has the molecular weight of an L chain, and another (referred to as the Fd fragment simply because d is the next letter in the alphabet) that is slightly heavier than the L chain. On the basis of this information, in **1962**, Porter proposed a model of the Ig molecule that proved to be essentially correct.⁶⁴ According to this model, the molecule consists of four polypeptide chains – two identical H chains and two identical L chains – held together by disulfide bridges (fig. 19). The first immunoglobulin polypeptide to be sequenced completely was an L chain of a Bence-Jones protein. A comparison of the sequence of two different L

chains revealed that the two chains were identical, starting with the amino acid in position 107 at the C terminal of the molecule, and totally different from the N terminal to the residue in position 106. The L chain could thus be divided into two segments – a variable (V) region, showing wide variation in amino acid sequence from one molecule to another, and a constant (C) region.⁶⁵

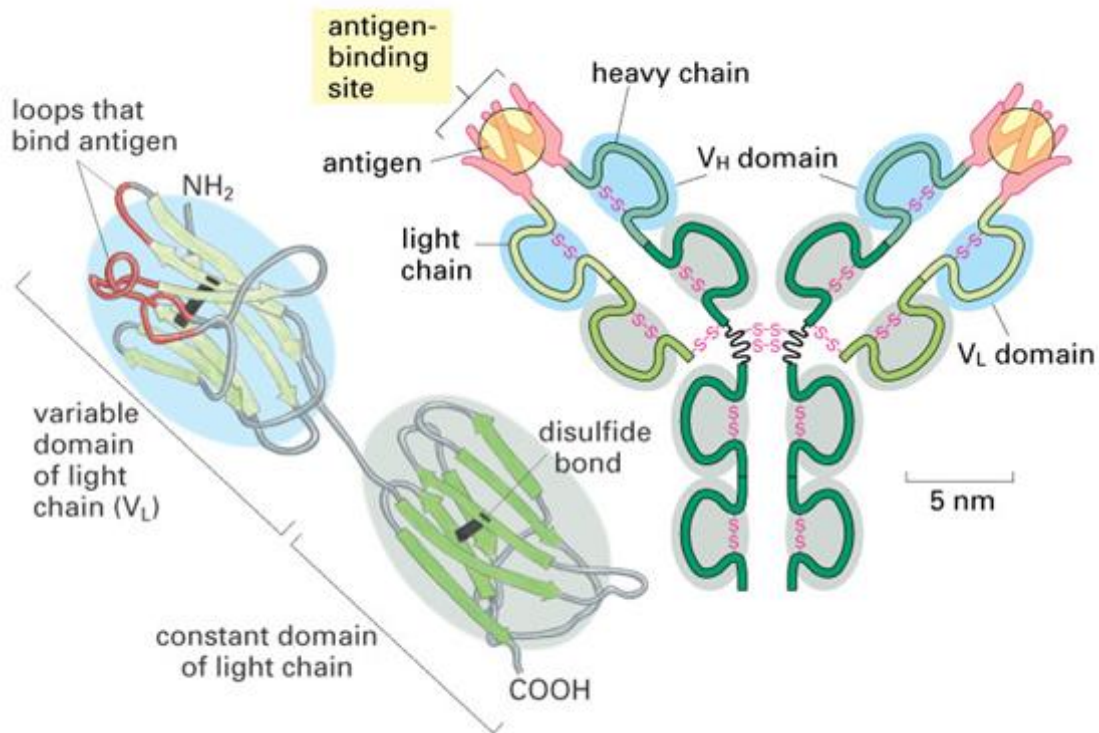


Fig. 19: Basic structure of antibodies. An antibody is a homodimer. The N-terminal chains of the heavy and light chain work together to form a binding site consisting of loops. The V_L and V_H domains are highly variable in their amino acid sequence forming a unique antigen-binding site, the so-called paratope. The hypervariable regions that form the antigen-binding site are therefore also called complementarity-determining regions (CDRs). The mechanism for antigen-binding is the induced fit mechanism at the CDR. The hinge region is a segment of the C_H chains. Since antigens are able to have epitopes at non-adjacent sites, the hinge region is critical for the flexibility of the antibody, thus allowing the two antigen-binding sites to act independently. The L chain comprises 2 domains and the H chain can have either 4 or 5 domains. Each domain is around 110 amino acids in length, comprised of two β -sheets, linked by a disulfide bridge. Illustrator: anonymous.

Edelmann demonstrated that similar regions existed in the heavy chain. To distinguish them, those in the light chain are denoted with V_L and C_L and those in the heavy chain with V_H and C_H . Following the sequencing of an entire Ig molecule by Edelmann in **1969**, it appeared that each Ig polypeptide chain could be divided into domains, each domain consisting of approximately 110 to 120 amino acids (10 to 12 kDa).⁶⁶ Since these domains are homologous to each other, antibodies apparently have been evolved from gene duplication. Alignment of the different domains reveals that any of them shares around 30 % of their amino acids. Each

light chain consists of two domains, one in the V and the other in the C region, whereas each heavy chain consists of four domains, one V_H and three C_H (C_{H1} , C_{H2} , C_{H3}). Since papain is an enzyme of broad specificity for peptide bonds, the fact that it cleaves only one peptide bond indicates that the others are inaccessible. Probably, the domains are folded into globules so that the whole antibody consists of 12 globules. These globules are folded around intrachain disulfide bridges, of which each homology region contains at least one. In contrary, the region in which disulfide bridges are formed between the two heavy chains is quite unfolded and highly flexible. Hence, such an arrangement allows the arms of the Fab fragments to move in relation to each other. Due to this swivel function, the unfolded segment is referred to as *hinge region*.

Mammalian antibodies are homodimers with each monomer consisting of a light and a heavy chain (fig.s 20A and B). Light and heavy chain are connected by at least one disulfide bridge. The antigen-binding site is formed where a heavy chain variable domain (V_H) and a light chain variable domain (V_L) come close together. An scFv antibody consists of the smallest functional antigen-binding domain (25 kDa, fig. 20C). In contrast, *Camelidae* and *Chondrichthyes* express single-domain antibodies (fig.s 20D and E).

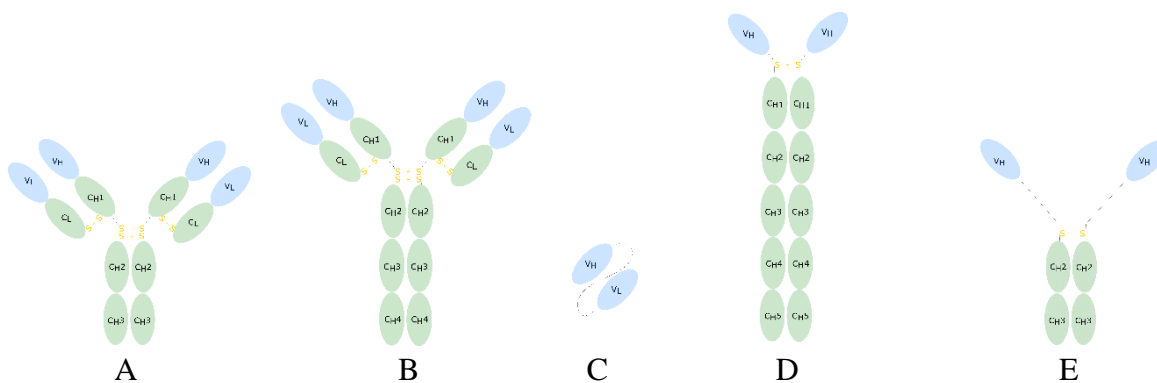


Fig. 20: Structural characteristics of antibodies. IgG (A), IgE (B), scFv (C), V_H H (camelids, D), IgNAR (cartilaginous fishes, E).

The antigen binding region of camelids and cartilaginous fishes is just half the size of an scFv-antibody (12 kDa). Nevertheless, the shark single-domain antibody V region is even able to bind to lysozyme.⁶⁷ Sharks and other cartilaginous fishes are the phylogenetically oldest living organisms that rely on antibodies as part of their adaptive immune system. Secretory IgA (sIgA) is designed as anti-microbial defense, so-called mucosal immunity. It is a homodimer, which is stabilized by a J chain and a secretory component, and is secreted by plasma cells under the endothelium (fig. 21A).

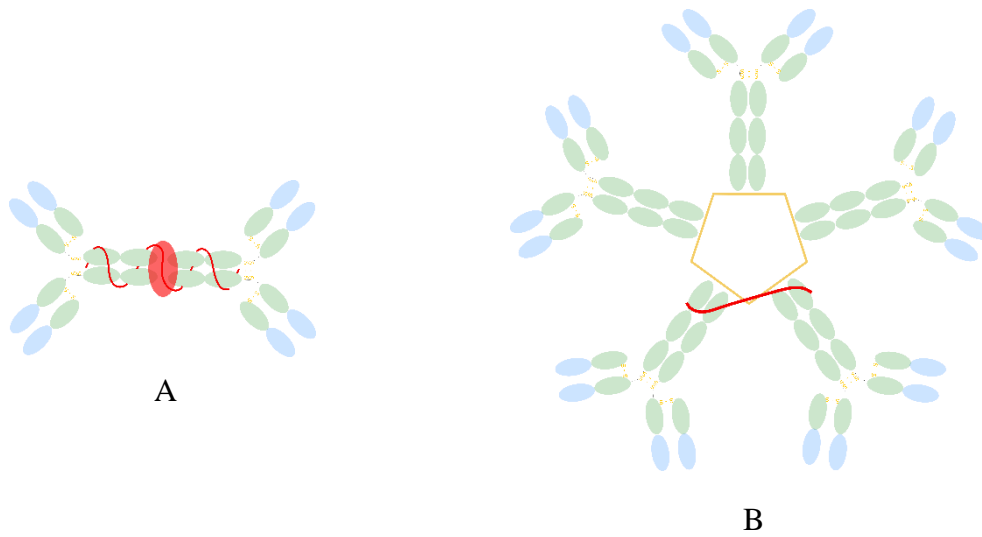


Fig. 21: Structural characteristics of sIgA (A) and IgM (B) antibody. sIgA is a homodimer stabilized by a J chain (red helix) and a secretory component (red ellipse). IgM is a homopentamer of IgE stabilized by disulfide bridges (yellow) and a J chain (red).

It must pass the endothelium to reach the mucosa of the respiratory and genital tract as well as of the digestive system. For this passage, a dimerization is necessary to prevent binding of the Fc fragment to Fc receptors on endothelial cells. Moreover, the secretory component protects from digestive enzymes. Besides, IgA is present in the mother's milk to provide the born child with so-called passive immunity. All naïve B cells carry (monomeric) IgM on their surface. It is the first responder of the humoral immune system and activates the complement cascade by fixation of complement factors. IgM mediates phagocytosis of antigens because macrophages carry many complement receptors on their surface. Its concentration in the blood serum is very low due to the fixation on mast cells and eosinophils. For an increased avidity, secreted IgM forms a homopentamer, which is stabilized by a J chain (fig. 21B). IgM has low affinity but high avidity because it has ten weak binding sites for antigen as opposed to the two stronger binding sites of IgG and IgE with higher binding affinities. IgG is the dominant Ig class in the blood serum (10 mg/mL) and in the extracellular liquid. It is the only Ig that is able to pass the placenta from the mother to the unborn child. In this way, the mother provides the unborn child with a so-called passive immunity. The most important function of IgG is neutralization of antigens to prevent their binding to target structures.

4.3.2. Adaptive Immunity by Clonal Selection

In 1959, Burnet proposed the *clonal selection theory* which is still the central paradigm of adaptive immunity.⁶⁸ Without prior antigen contact, the BCR and TCR repertoire emerges from V-DJ recombination. In case of infection, this repertoire is selected against the pathogen resulting in a clonal expansion. The repertoire can be calculated from the number of genes present in the segments (table 2). An adaptive immune response simulated *in vitro* is referred to as antibody phage display and was invented by Smith in 1985.

Table 2: V-DJ recombination resulting in a possible BCR diversity of $\sim 2 \cdot 10^6$ and TCR diversity of $\sim 5.8 \cdot 10^6$ for $\alpha\beta$ and 2160 for $\gamma\delta$.

Segment	BCR			TCR			
	Heavy chain	Light chain		α	β	γ	δ
		κ	λ				
D	25	0	0	0	2	0	3
J	6	5	4	61	13	5	3
V	40	40	30	70	52	12	4
$D \times J \times V$	6000	200	120	4200	1352	60	36

4.3.3. Technique of Antibody Phage Display

In 1985, Smith demonstrated the display of peptides on the filamentous phage by fusing the peptide of interest onto gene III.⁶⁹ He stated that this method “could be a useful way of obtaining antibodies against restricted determinants or of producing vaccines of medical or veterinary interest.” A single-chain variable fragment (scFv) is not actually a fragment of an antibody, but instead is a fusion protein of the variable regions of the heavy (V_H) and light chains (V_L) of immunoglobulins, connected by a short linker peptide of ten to about 25 amino acids. The linker is usually rich in glycine for flexibility, as well as serine or threonine for solubility, and can either connect the N-terminus of the V_H with the C-terminus of the V_L , or *vice versa*. This protein retains the specificity of the original immunoglobulin, despite removal of the constant regions and the introduction of the linker. These molecules were created to facilitate phage display, where it is highly convenient to express the antigen-binding domain as a single peptide. Such scFv antibodies have many uses (*e.g.*, flow cytometry, immunohistochemistry, and as antigen-binding domains of artificial T cell receptors). Unlike monoclonal antibodies, which are often produced in mammalian cell cultures, scFv antibodies are most often produced in bacterial cell cultures, such as *E. coli*. The steps of phage display procedure are as follows: Total mRNA is prepared from a cell source (*e.g.*, spleen) and this RNA is transcribed reversely to cDNA. An isotype-specific PCR is carried out for V_H and V_L in order to construct scFv. The

overlapped fragments are inserted into a phagemid vector (*e.g.*, pHEN2). The DNA encoding an antibody is ligated into the pIII or pVIII gene, encoding either the minor or major coat protein, respectively. The phagemid vector is then transferred to *E. coli* cells, such as TG1 or XL1-Blue, either chemically or by electroporation. Upon infection with a helper phage, the phages are released from the *E. coli* cells. This step is referred to as rescue of phages. By immobilizing a relevant target to the surface of an immunotube, phages that display antibodies that bind to this target will remain, while non-binding phages are removed by washing. Those that remain can be eluted (*e.g.*, by TEA) and used to reinfect *E. coli* cells. The repeated steps are referred to as panning.

5. Aim of the Study

5.1. Molecular Insight into the Cross-Reactivity of α -1,3 Core Fucose

Cross-reactive carbohydrate determinants (CCDs) are an issue in allergy diagnosis, where about a fifth of all patients displays IgE antibodies against Asn-linked oligosaccharides (N-glycans) containing α 1,3-linked core fucose.⁷⁰ The study at hand aims to gain insight into the interaction between anti-CCD antibodies and α -1,3 core fucose towards an improved understanding of cross-reactivities in insect venom allergy. As shown by F. Altmann, the α 1-3 core fucose is an important molecular feature. But Collot *et al.* have shown that CCD fragments exhibit low affinities (fig. 18). Thus, an amplification of antibody binding affinity is mandatory for the success of this study. This can be realized by antibody phage display, involving biopanning with $\text{Fuc}\alpha$ 1-3GlcNAc as a target (fig. 22 and 24). The phage affinities of each round shall be monitored by STD NMR spectroscopy.

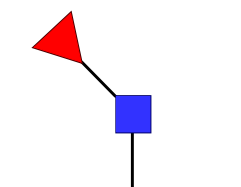


Fig. 22: The immobilized minimal motif $\text{Fuc}\alpha$ 1-3GlcNAc as biopanning target.

By reducing complexity to the reactive subunits (*i.e.*, α 1-3 core fucose and anti- α 1-3 core fucose scFv antibody), the study shall shed light on the molecular causes of false-positive results. To obtain a big picture of the respective immune reactivities, the fragments shown in fig. 23 shall be synthesized and tested.

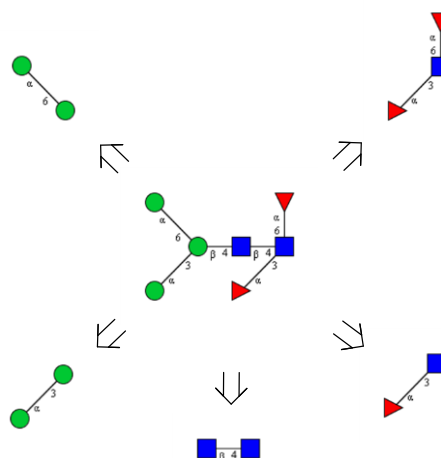


Fig. 23: Explosion diagram of a N-glycan typical for insect venom glycosylations. The shown fragments are targets of synthesis. This fragment-based approach was chosen to facilitate an unambiguous assignment of STD effects to the ring protons.

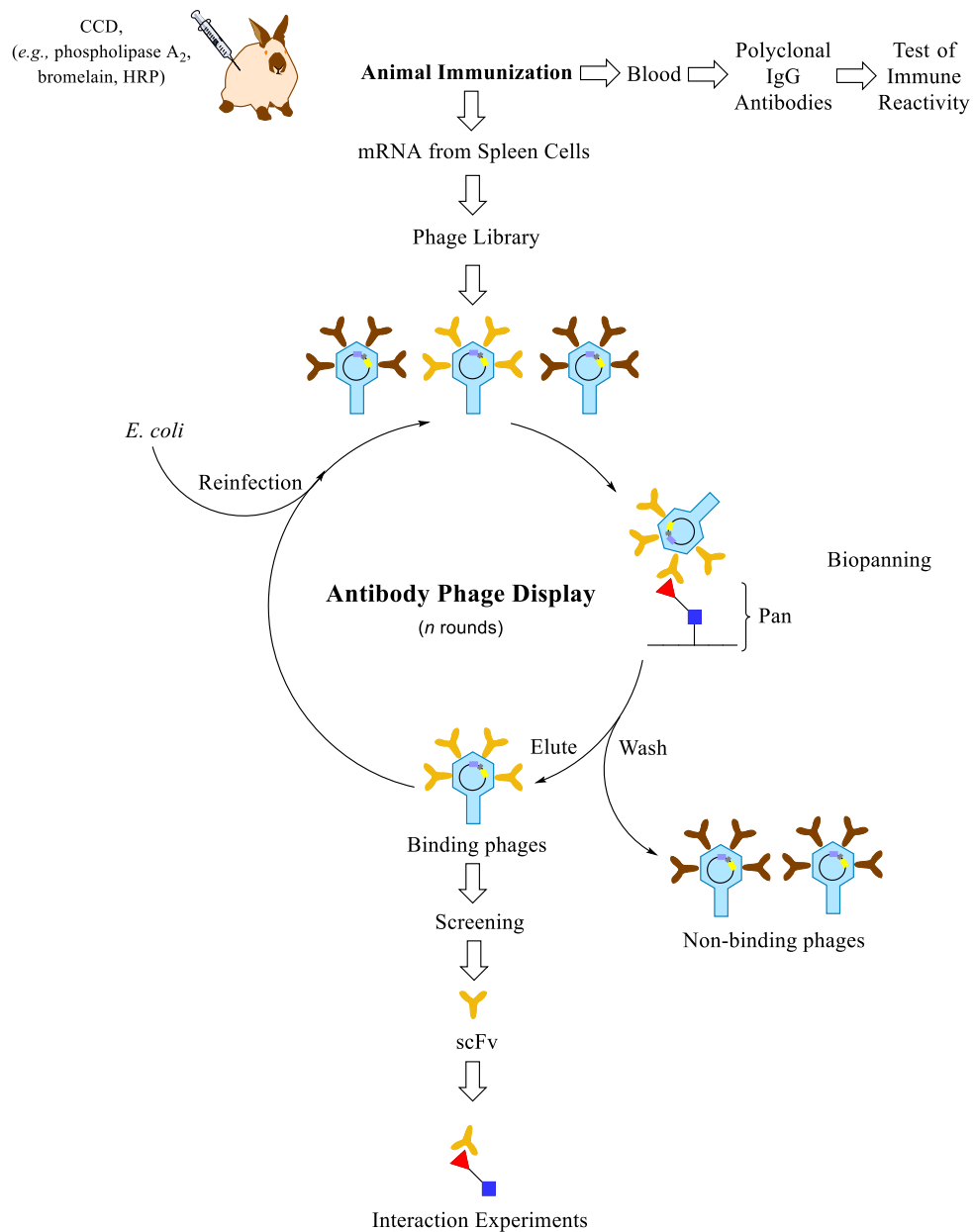
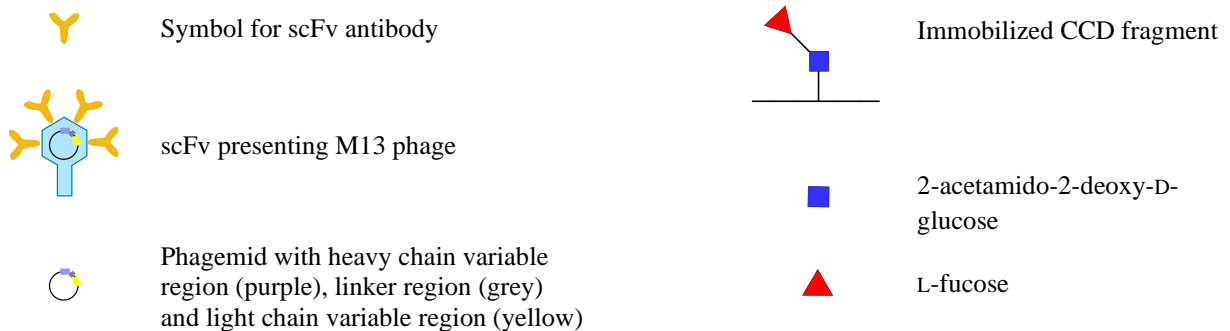


Fig. 24: Antibody phage display with selection against Fuc α 1-3GlcNAc as an essential step. Spleen cells from an immunized animal should be extracted to obtain mRNA encoding the information of the immune response. The isolated mRNA is transcribed reversely to cDNA and inserted into a phagemid. Beforehand, anti-CCD rabbit serum should be tested for immune reactivity against the minimal motif Fuc α 1-3GlcNAc (e.g., by STD-NMR).

Legend:

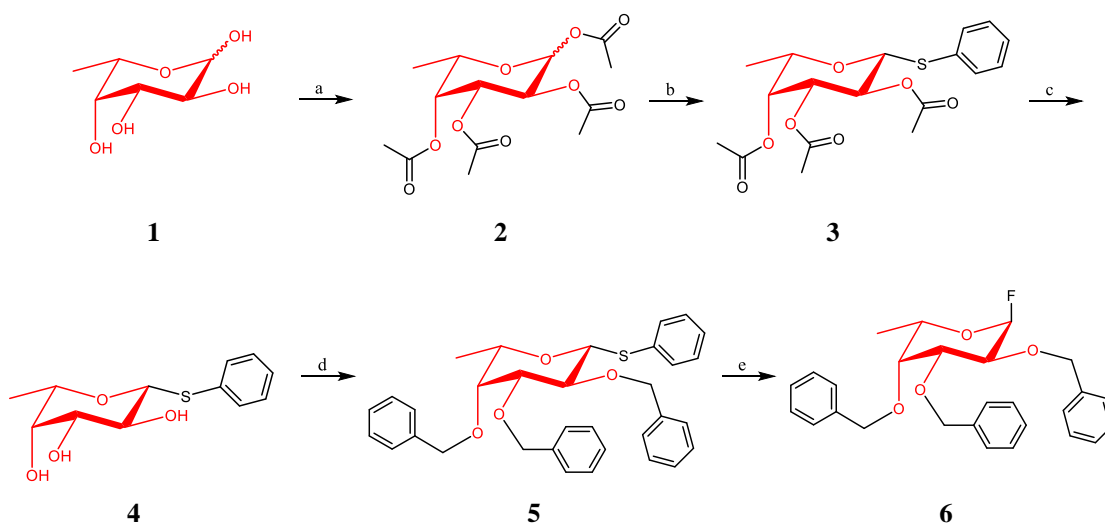


6. Results

6.1. Access to Honeybee Venom CCD Fragments

6.1.1. Synthesis of Fuc α 1-3GlcNAc

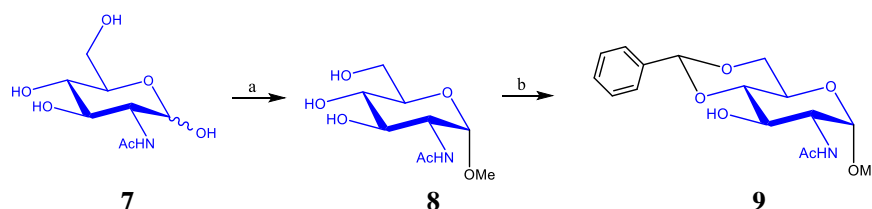
In order to provide vast amounts of the CCD fragment Fuc α 1-3GlcNAc, a chemical donor/acceptor approach was chosen. Since immune reactivity of polyclonal anti-HRP IgG against Fuc α 1-3GlcNAc should be tested by STD NMR spectroscopy before starting phage display, the synthesis route was started with a Fischer glycosylation of 2-acetamido-2-deoxy- α/β -D-glucose yielding GlcNAc α 1-OMe as a thermodynamic main product in order to avoid a double (α/β) STD NMR data set. The methyl glycoside was protected at 4,6-position with benzaldehyde dimethylacetale according to Demchenko (scheme 2). L-Fucose (**1**) was peracetylated, converted to the phenyl 1-thio glycoside **3**, deacetylated and perbenzylated (scheme 1). Compound **5** was crystallized as β -anomer, exclusively. These crystals were used for the preparation of fluoride **6** according to Nicolaou. Due to its sensitivity to hydrolysis, the fluoride was used immediately after its preparation.



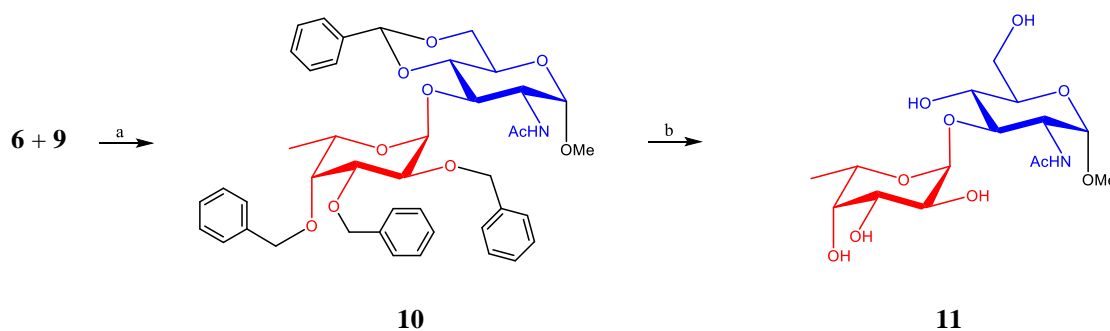
Scheme 1: Reagents and conditions: (a) Py/Ac₂O 2:1, r.t., o.n., 86 %; (b) PhSH, r.t., o.n., 61 %; (c) NaOMe, MeOH, pH 9.5, r.t., o.n., 75 %; (d) DMF, NaH, 0 °C, 1 h; 15 % TBAI, 9 eq. BnBr, 83 %; (e) DAST, NBS, DCM, 0 °C, 5 h, 73 %.^{71,72,73,74,75}

The disaccharide **10** was synthesized by chemical glycosylation according to Böhm and hydrogenated yielding target compound **11** (scheme 3). In order to obtain valid interaction data, the quality of the tested ligand was assured as follows: It was purified by biogel chromatography and its purity has been proven by ¹H NMR (fig.s 26-28). The ESI MS spectrum shows a peak

at m/z 404.154(2) for the molecular ion adduct $[M + Na]^+$ (fig. 25). The identity of the disaccharide has been proven by comparison of the specific rotation with the literature. Due to caramelization at ~ 245 °C and carbonization at ~ 257 °C, a melting point could not be determined though given by the literature (m.p. 276-277 °C). An evidence of a glycosylation at 3-position is delivered by HSQC (fig. 30).



Scheme 2: Reagents and conditions: **(a)** MeOH, Dowex 50W-X8, reflux, 6 h, 70 %; **(b)** BADMA, CSA, ACN, reflux, 20 min, 70 %.^{76,77}



Scheme 3: Reagents and conditions: **(a)** LiClO_4 , CsF, MS 4 Å, DCM, r.t., 24 h, 81 %; **(b)** H_2 , Pd/C, MeOH, r.t., o.n., 88 %.^{78,79}

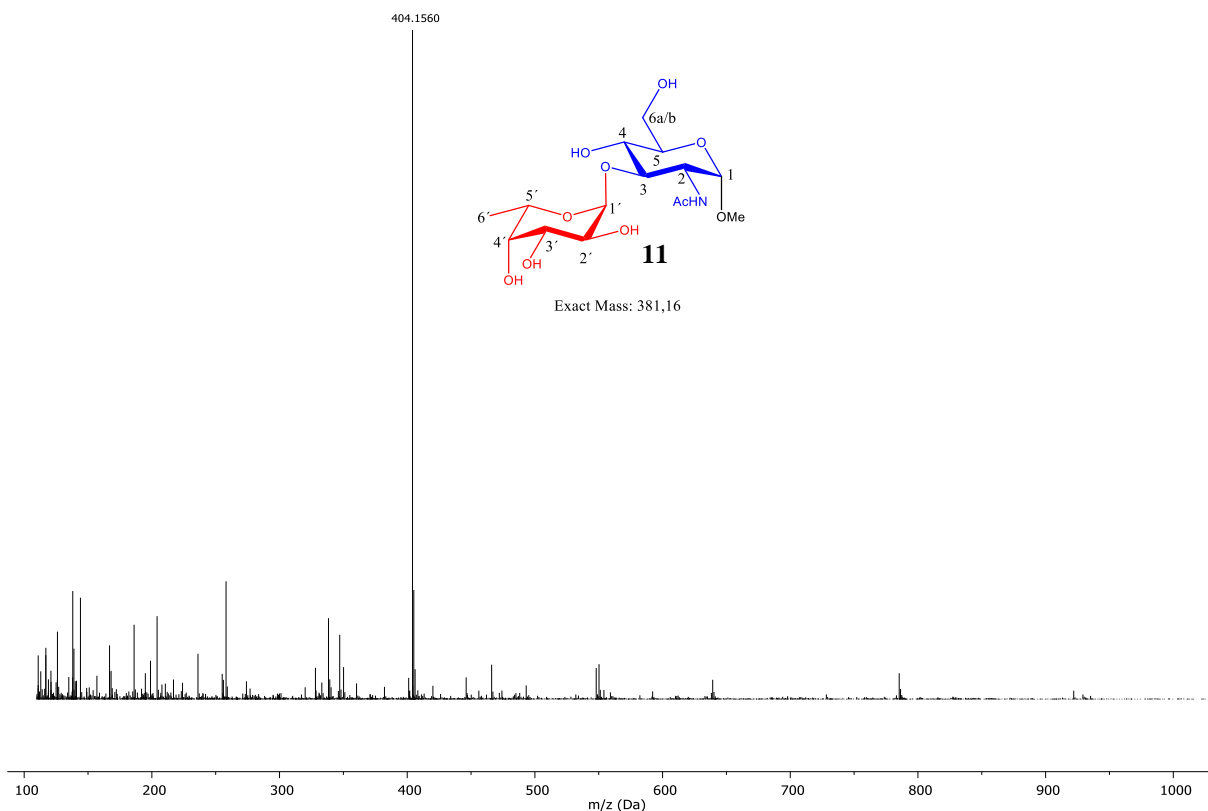


Fig. 25: ESI-TOF-MS spectrum of Fuc α 1-3GlcNAc α 1-OMe with a peak at m/z 404.156(0) for the molecular ion adduct $[M + Na]^+$ (Agilent 6224, positive mode, range of measurement 110-3200 m/z , direct injection). MS operator: D. Gellert, MS interpreter: T. Raiber.

NMR Interpretation Commentary: The ^1H NMR spectrum was recorded on a Bruker *AVANCE I 400* NMR spectrometer equipped with a 5 mm BBO probe head and the 2D NMR spectra were recorded on a Bruker *DRX 500* NMR spectrometer equipped with a 5 mm BBI probe head. For processing and analysis of the NMR data, Mnova 10.0 was used. The ^1H spectrum was processed with an LB value of -0.60 Hz. The NMR assignment starts with the unequivocal carbonyl C atom of the acetamido group (174.4 ppm, fig. 29), which in the HMBC spectrum couples weakly across the nitrogen atom with H-2 (4.11 ppm, fig. 31). The H-2 signal is shifted to higher frequencies due to the electron-withdrawing (-M, *i.e.*, deshielding) effect of the acetamido group and shows a characteristic splitting pattern (dd) with a small coupling constant to H-1 (3.6 Hz, cis-coupling to H-1) and a bigger one to H-3 (10.5 Hz, trans-coupling to H-3). Additionally, H-2 couples in the HMBC spectrum with C-3. C-3 is strongly shifted to high frequencies (78.3 ppm) because of the fucosyl moiety at the adjacent O-3. A coupling between H-2 and C-1 was not detected. In the HSQC spectrum, C-3 is connected to H-3 at 3.80 ppm (fig. 30). Due to the adjacent 2-acetamido group, C-2 is strongly shifted to low frequencies (53.2 ppm), what is a general feature of GlcNAc

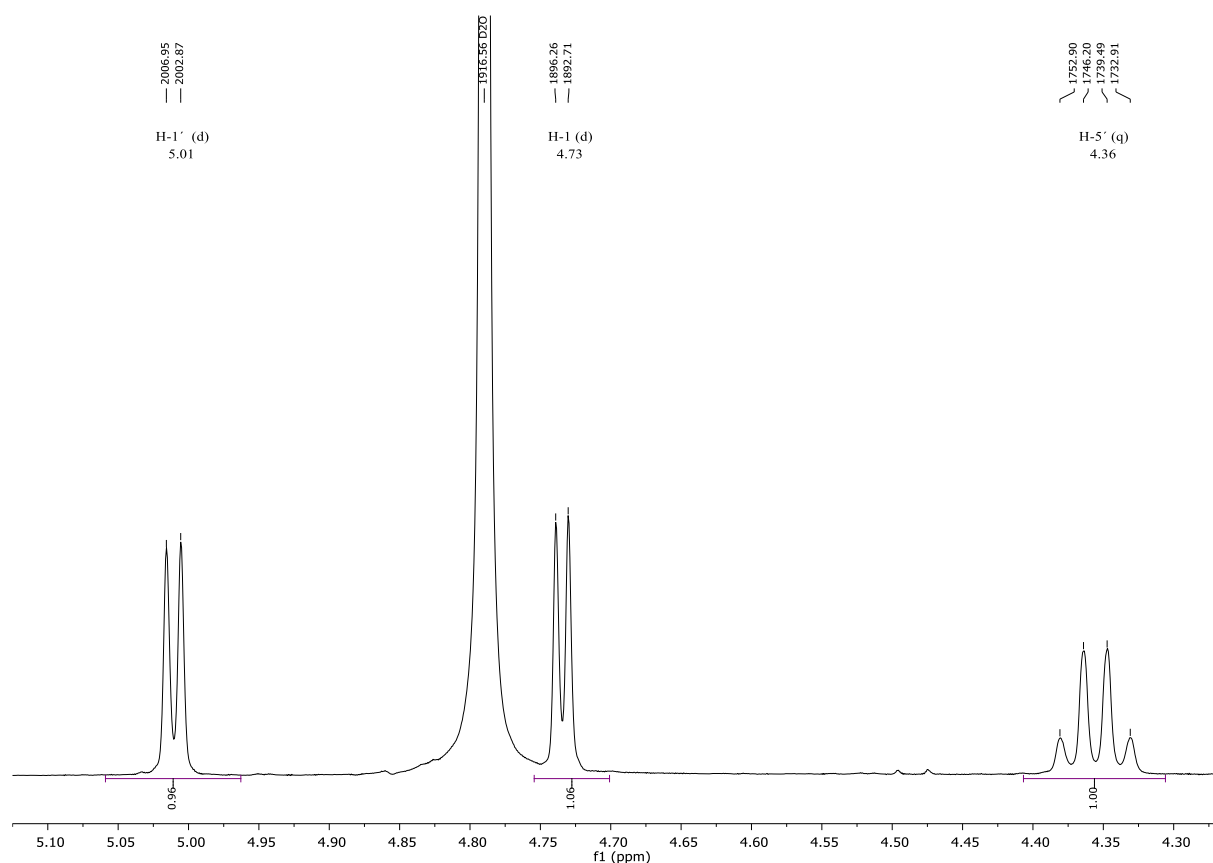


Fig. 26: High frequency proton signals of Fuc α 1-3GlcNAc α 1-OMe (**11**). Here, the anomeric protons H-1' (5.01 ppm, d, $J_{1',2'} = 4.1$ Hz) and H-1 (4.73 ppm, d, $J_{1,2} = 3.6$ Hz) as well as the ring proton H-5' (4.36 ppm, dq~vq, $J_{4',5'} < 1$ Hz, $J_{5',6'} = 6.6$ Hz) are detected. NMR interpreter: T. Raiber.

compounds - and couples in the HMBC spectrum with H-3. By HMBC, the coupling of both anomeric protons, H-1' and H-1, with C-3 is very well detectable. Furthermore, both anomeric protons couple with their related C-5 partner across the ring oxygen (C-5 71.8 ppm, C-5' 66.8 ppm) and H-2' couples to C-3' like H-2 to C-3, see above (fig. 31). Of particular interest - especially with regard to the aim of this study - is the vicinal coupling constant $^3J_{1',2'}$ of the anomeric proton of the fucosyl moiety, which indicates with 4.1 Hz an α -configuration in good agreement with the Karplus' relationship for $^3J_{\text{e}a} \approx 2$ to 5 Hz ($\phi = 60^\circ$; for comparison: $^3J_{1',2'}$ of the β -anomer equals 7.8 Hz; fig. 26). Due to the deoxygenized C-6' atom, H-6' is remarkably shifted to low frequencies (1.19 ppm) and occurs as a doublet with a vicinal coupling constant of 6.6 Hz as a result of its coupling with H-5' (fig. 28). In the HMBC spectrum, it couples across two σ -bonds with C-5' (66.8 ppm) as well as across three σ -bonds with C-4' (fig. 31). Since C-4' shows the same chemical shift as C-5 (71.8 ppm), further assignments are not trivial. Thus, it is stated that both, H-1 and H-4 couple to C-5. Due to the very small coupling constant $J_{4',5'} < 1$, the H-5' signal splits into a virtual quartet (dq~vq), and is shifted to higher frequencies (4.36 ppm) due to the proximity of H-5' to the ring oxygen (fig. 26).

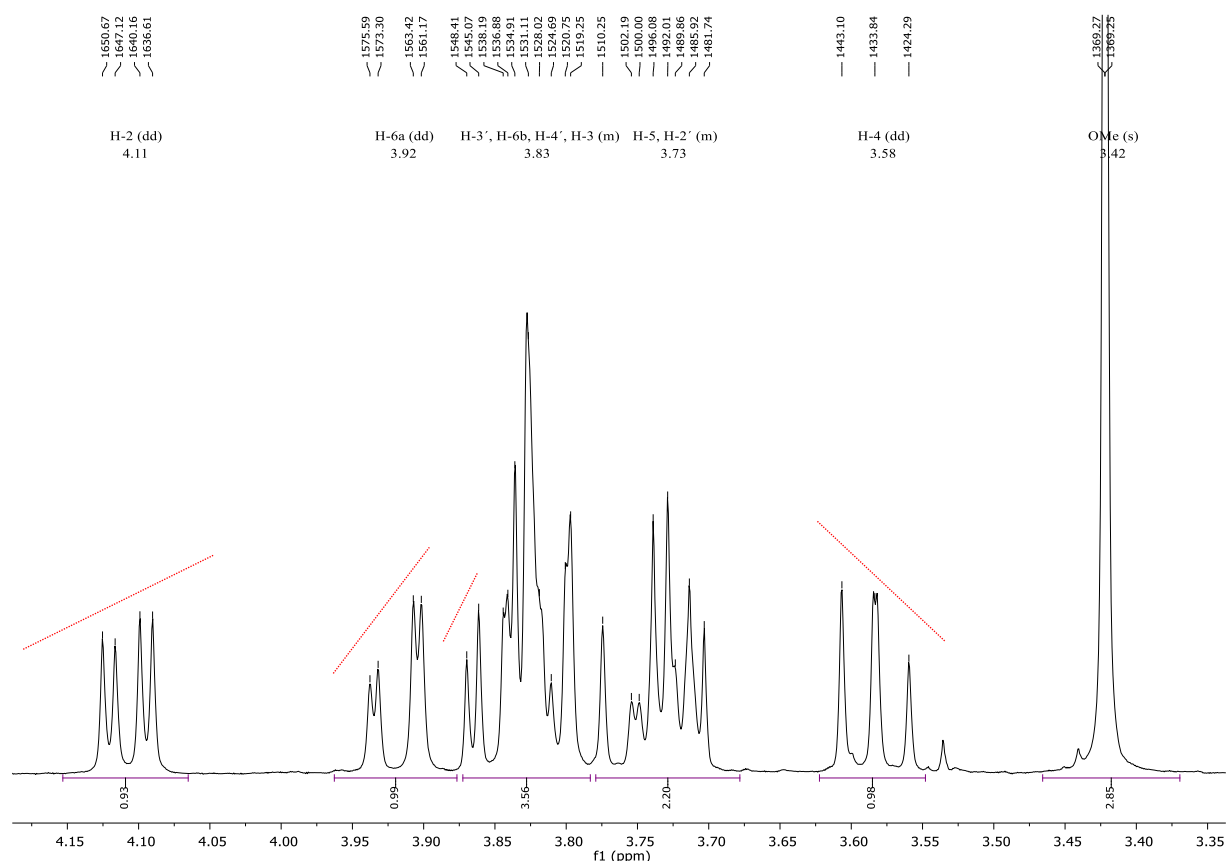


Fig. 27: ^1H NMR section of Fuc α 1-3GlcNAc α 1-OMe (**11**) in which most of the ring proton signals appear. The sections 3.88-3.68 ppm and 3.76-3.68 ppm are characterized by interferences of ring proton signals, their assignments are commented below. The dotted lines indicate roof effects characteristic of higher-order coupling systems, but the spectra are interpreted as approximately first-order. NMR interpreter: T. Raiber.

The distinction between H-4' (3.81 ppm) and H-3' (3.85 ppm) was performed by H,H-COSY and TOCSY spectra. In the TOCSY spectrum, H-1' couples with a proton at 3.85 but not at 3.81 ppm (fig. 33). The left part of the H-3' signal is separated from the multiplet, giving access to the vicinal coupling constant $^3J_{3',4'}$ with a value of 3.3 Hz (fig. 27). The peaks at 3.74 and 3.71 ppm reveal $^3J_{2',3'}$ as 10.2 Hz, completing the information about the trans/cis conformation of H-3'. A NOESY spectrum could not provide unambiguous information about a conformational preference, but the cross-peak at 3.80 ppm / 5.01 ppm (H-3 / H-1') supports the information about a 3-glycosylation (fig. 34). In this regard, the signal group between 3.88 ppm and 3.60 ppm was deconvoluted to avoid an incorrect assignment (fig. 35).

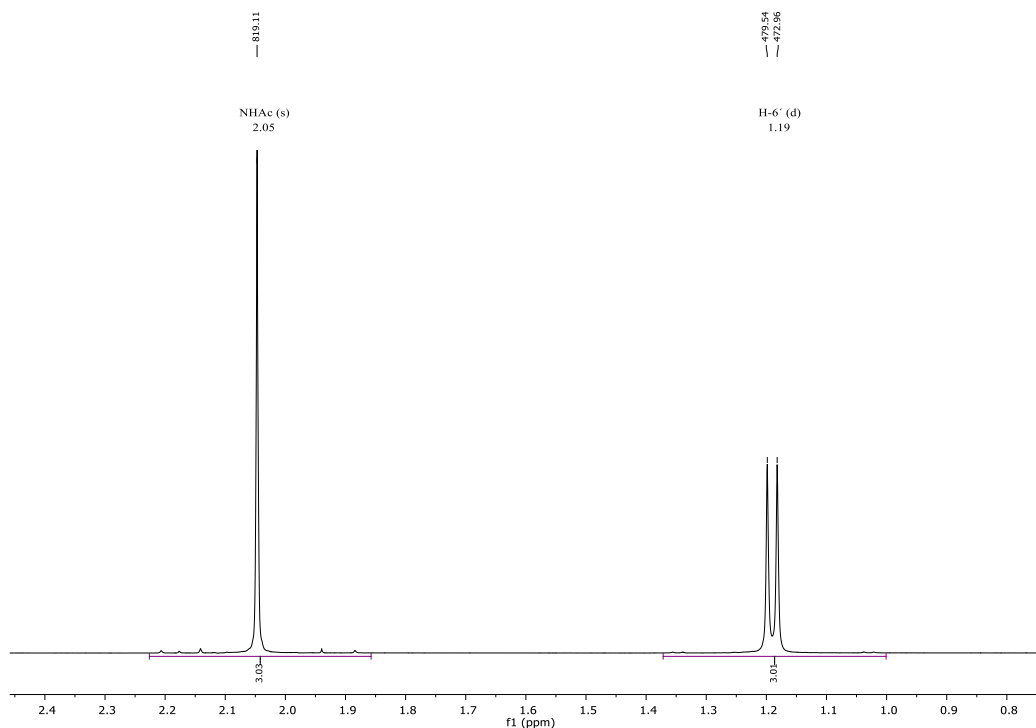


Fig. 28: Low frequency proton signals of Fuc α 1-3GlcNAc α 1-OMe (**11**). Here, the methyl group of the acetamido group (2.05 ppm, s) and H-6' (1.19 ppm, d, $J_{5',6'} = 6.6$ Hz) are detected. The remarkable shift of the H-6' signal to low frequencies is commented below. NMR interpreter: T. Raiber.

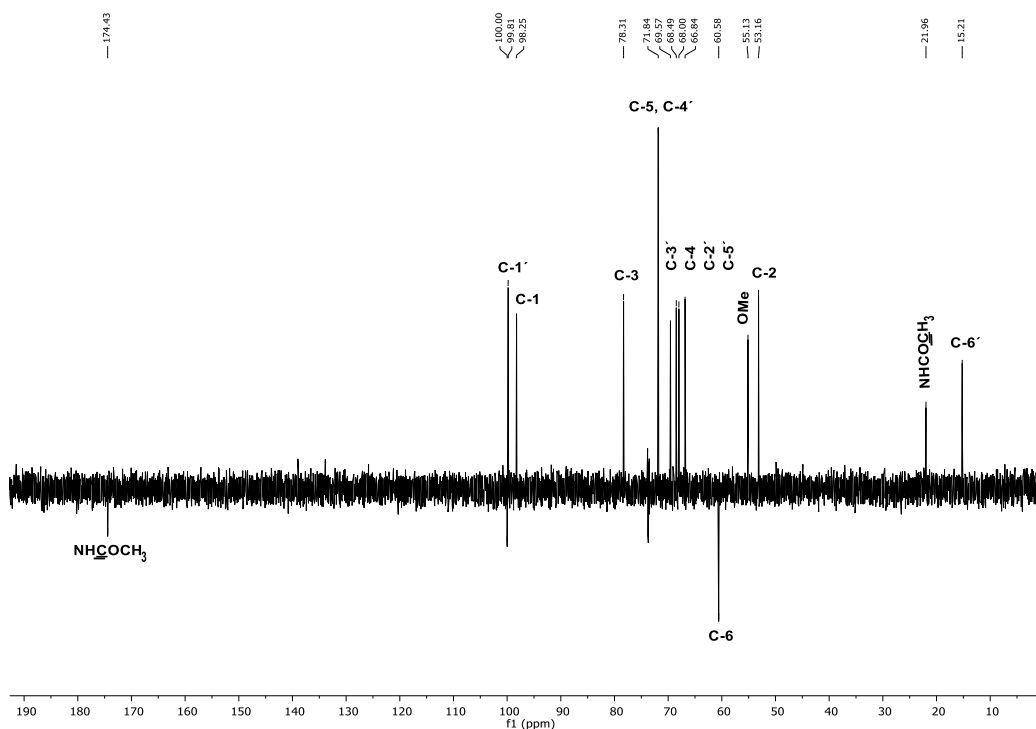


Fig. 29: APT spectrum of Fuc α 1-3GlcNAc α 1-OMe (**11**) (positive: CH, CH₃; negative: CH₂, quaternary carbon atoms). Due to 3-glycosylation, the C-3 signal is remarkably shifted to high frequencies (78.3 ppm). Bruker DRX 500 NMR spectrometer, ¹³C = 125.76 MHz, 5 mm PABBI probe head, *jmod*, AQ 1.09 s, NS 320, TD 64 k, 65 mg / 650 μ L D₂O. NMR interpreter: T. Raiber.

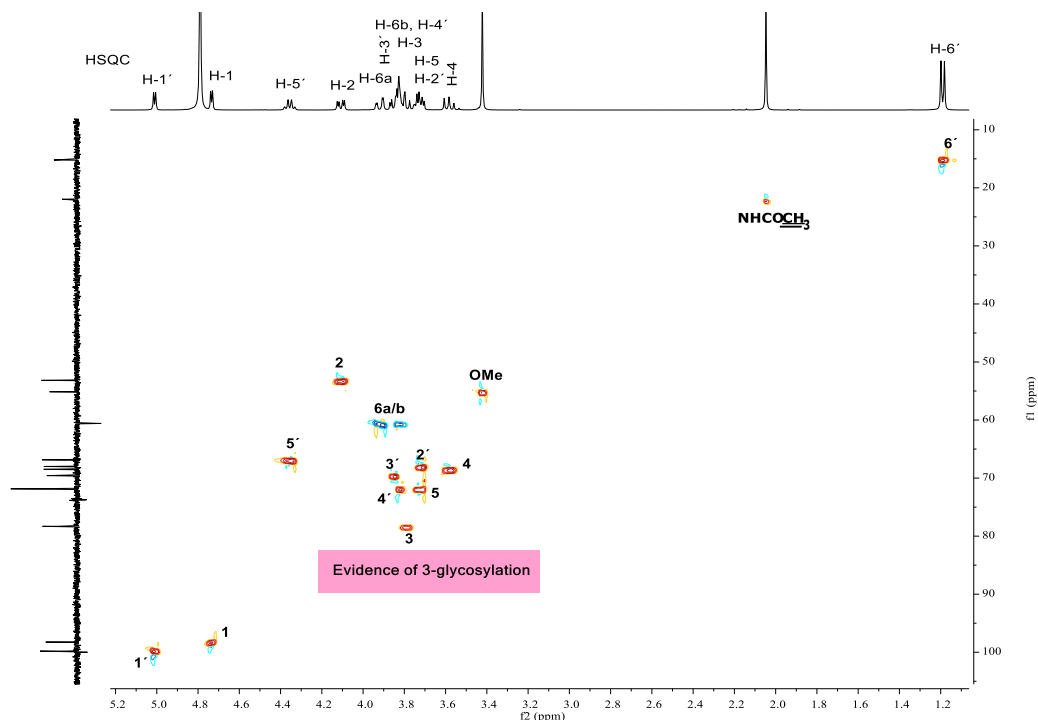


Fig. 30: HSQC spectrum of Fuc α 1-3GlcNAc α 1-OMe (**11**). Due to glycosylation, C-3 is remarkably shifted to high frequencies. The data are processed with ZF (up to 2 k) and LP (Zhu-Bax). Bruker DRX 500 NMR spectrometer, ^{13}C = 125.76 MHz, 5 mm PABBI probe head, *hsqcedetgp*, AQ 167 ms, NS 4, TD 1 k, 65 mg / 650 μL D $_2$ O. NMR interpreter: T. Raiber.

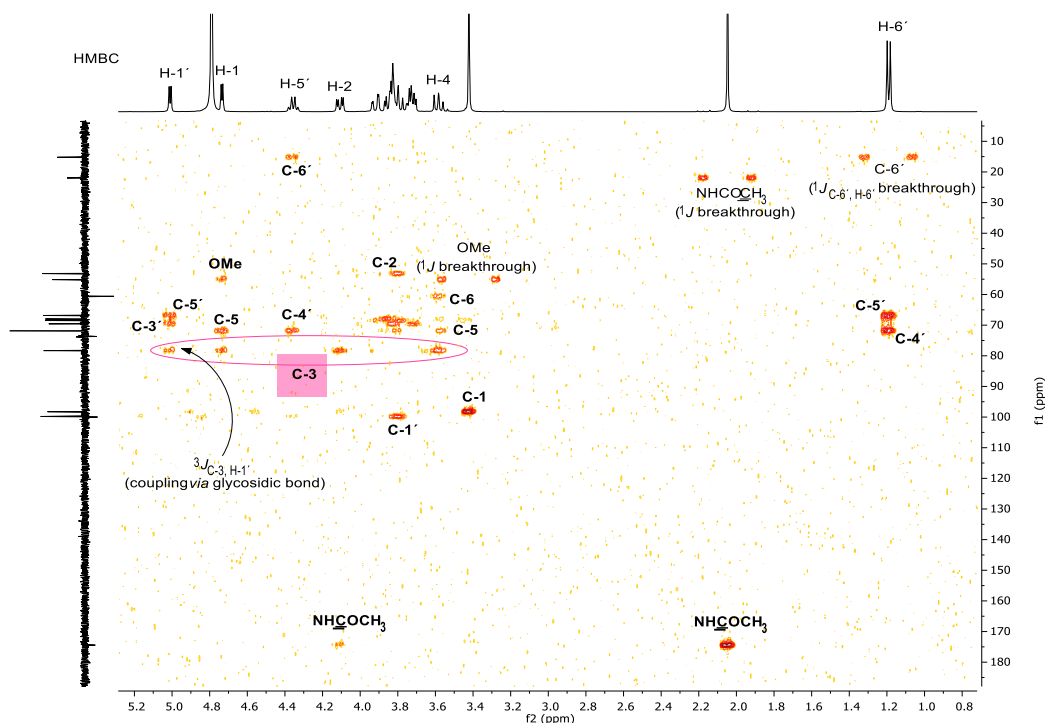


Fig. 31: HMBC spectrum of Fuc α 1-3GlcNAc α 1-OMe (**11**). A vicinal coupling *via* the glycosidic bond (between C-3 and H-1') is detected. Bruker, DRX 500 NMR spectrometer, ^{13}C = 125.76 MHz, 5 mm PABBI probe head, *hmbcgplndqf*, AQ 669 ms, NS 8, TD 4 k, 65 mg / 650 μL D $_2$ O. NMR interpreter: T. Raiber.

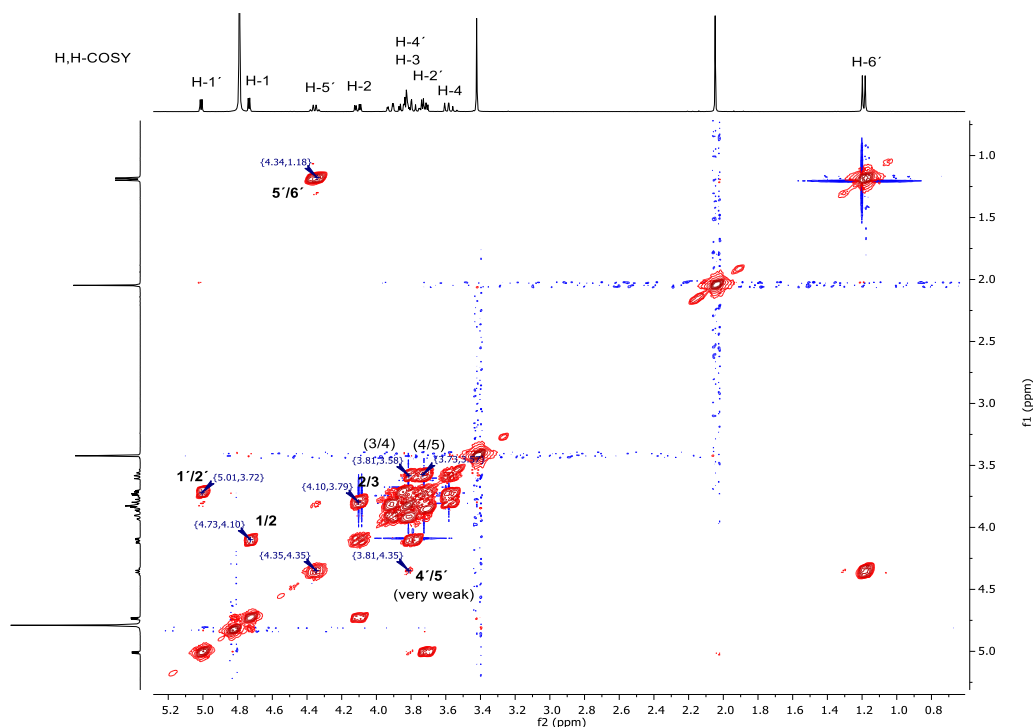


Fig. 32: H,H-COSY spectrum of Fuca1-3GlcNAc1-OMe (**11**). The baseline was corrected automatically with Whittaker smoother (Mnova 10.0). Especially the assignment of H-2 and H-2' is facilitated by H,H-COSY. In contrast to the strong $J_{5',6'}$, the coupling between H-5' and H-4' is very weak. The threshold is set very low in order to make this cross-peak visible. Bruker, DRX 500 NMR spectrometer, ^1H = 500.13 MHz, 5 mm PABBI probe head, *cosyqf90*, AQ 334 ms, NS 4, TD 2 k, 65 mg / 650 μL D₂O. NMR interpreter: T. Raiber.

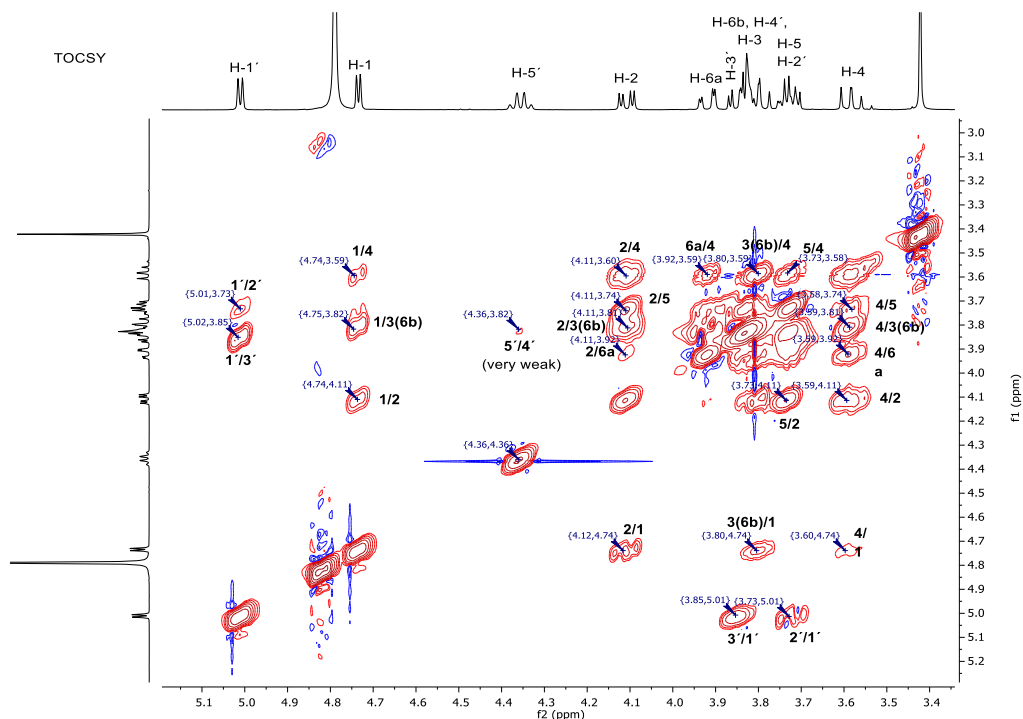


Fig. 33: Section of TOCSY spectrum of Fuca1-3GlcNAc1-OMe (**11**). The TOCSY spectrum facilitates the distinction of H-3' (3.85 ppm) from H-4' (3.81 ppm). Bruker, DRX 500 NMR spectrometer, ^1H = 500.13 MHz, 5 mm PABBI probe head, *mlevph*, AQ 334 ms, NS 8, TD 2 k, 65 mg / 650 μL D₂O. NMR interpreter: T. Raiber.

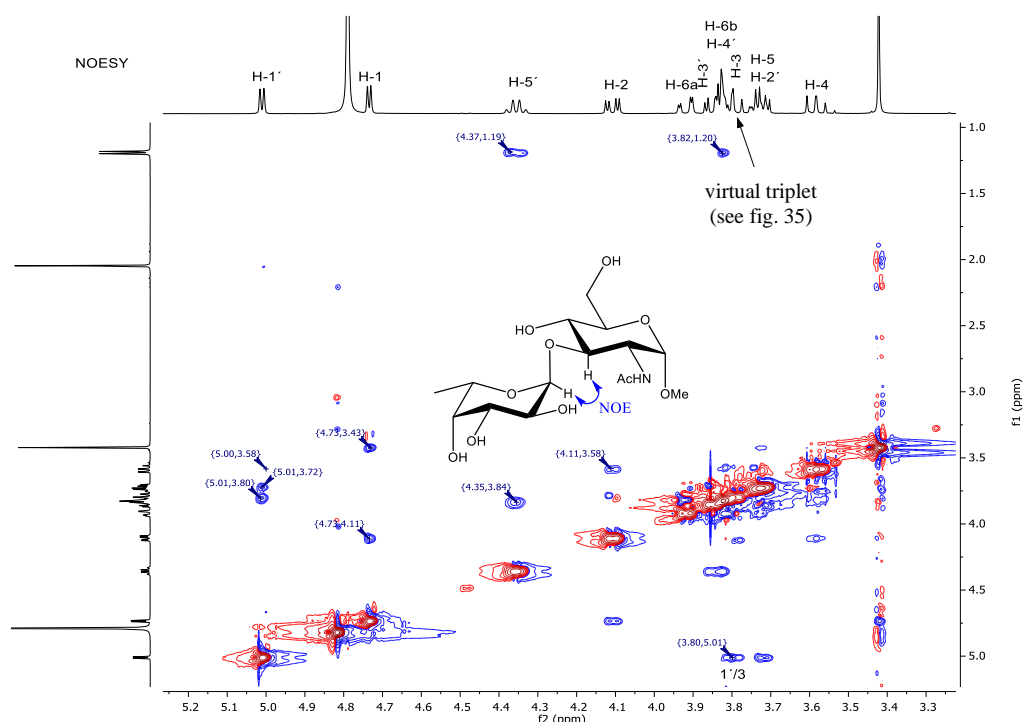


Fig. 34: NOESY spectrum of Fuc α 1-3GlcNAc α 1-OMe (**11**). The baseline was corrected automatically with Whittaker smoother (Mnova 10.0). The cross-peak at 3.80 ppm / 5.01 ppm (H-3 / H-1') supports the information about a 3-glycosylation. The spectrum is not able to indicate any conformational preferences. Bruker, DRX 500 NMR spectrometer, ^1H = 500.13 MHz, 5 mm PABBI probe head, *noesyph*, AQ 669 ms, NS 16, TD 4 k, 65 mg / 650 μL D $_2$ O. NMR interpreter: T. Raiber.

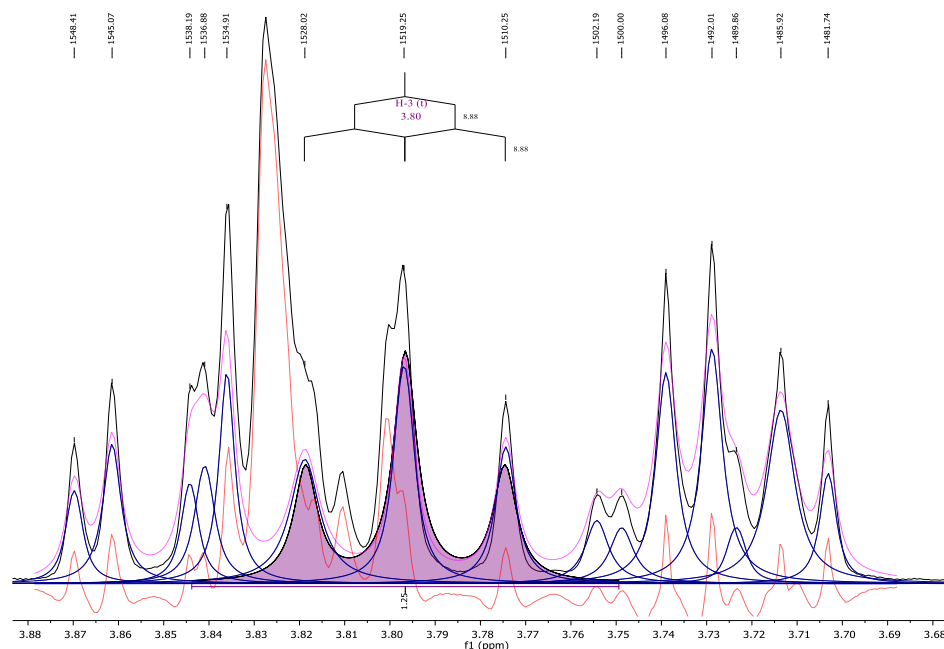
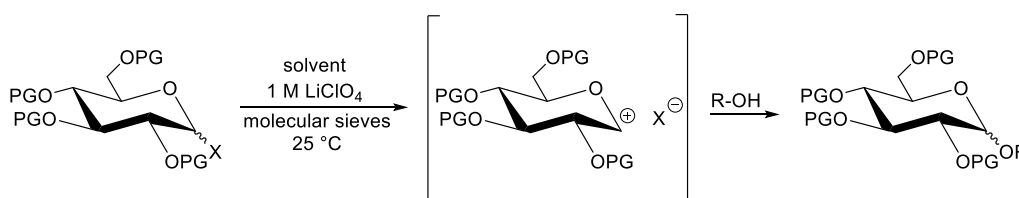


Fig. 35: Deconvolution by Mnova 10.0 reveals the *complete* virtual triplet centered at 3.80 ppm with a vicinal coupling constant of 8.9 Hz; blue: *peak*, orange: *residue*, magenta: *sum*. At 3.80 ppm / 5.01 ppm the NOESY spectrum shows a cross-peak (fig. 34). Deconvolution of the ^1H NMR signal group confirms the assignment of this cross-peak to H-3 / H-1'. NMR interpreter: T. Raiber.

6.1.2. A Proposed Mechanism for a LiClO₄-Promoted Chemical Glycosylation as a Heterogeneous Variant of Pocker's "Electrostatic Catalysis"

Glycosyl fluorides were introduced by Mukaiyama *et al.* in 1981 and can be activated by SnCl₂ as Lewis acid.^{80,81} In 1994, Waldmann *et al.* successfully transferred lithium perchlorate from Diels-Alder reactions to the field of chemical glycosylation and established it to activate glycosyl fluorides, suggesting an S_N1 mechanism with a glycosyl cation as an intermediate, which is stabilized by a counter ion X⁻ (Scheme 4).⁸² For this type of glycosylation, 1,6-anhydro pyranoses have been observed as side products.⁸³ It is generally known that an α-glycoside product predominates because it will be favored by the anomeric effect.^{84,85} However, the exact function of LiClO₄ is not clear. In this regard, it seems to be indicated to reconsider the predominant factors which might drive this glycosylation.

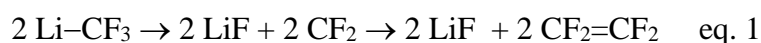


Scheme 4: Chemical glycosylation “without addition of promoters or reagents to form the O-glycosides”. This schematic mechanism lacks an explanation of the exact function of LiClO₄.

Grieco *et al.* established lithium perchlorate in Diels Alder reactions - where Li⁺ binds to Lewis basic sites on the dienophile - and found that 5.0 M LiClO₄ in Et₂O accelerate the reaction rate accelerations by compressing the reactants in the same manner as external pressure (by confining solute movement in the ionic medium).^{86,87} Lithium perchlorate is known for its remarkable solubility in polar organic solvents like diethyl ether (113.7 g / 100 g solvent). Hence, in Diels-Alder reactions, lithium perchlorate participates as a *solute* and is able to unfold its Lewis acid properties. But “no detectable solubility of lithium perchlorate” was found “in pure hydrocarbons or in chlorinated hydrocarbons”.⁸⁸ This leads to the conclusion that LiClO₄ catalyzed Diels-Alder reactions in diethyl ether are subjected to totally different reaction principles than LiClO₄-promoted glycosylations in dichloromethane.

Pocker *et al.* analyzed the role of lithium ions in many reactions and found that LiClO₄ in Et₂O catalyzes the ionization of triphenylmethyl chloride and hydrogen chloride.^{89a-g} The catalysis was shown to be essentially electrostatic in nature and to arise from the capacity of [Li⁺(OEt₂)_m,ClO₄]_n ion pair aggregates to promote the ionization process.” *t*-Butyl chloride was shown to ionize by forming “ionic aggregates” like the “triple ion” Cl⁻Li⁺ClO₄⁻ and a “quadruple ion intermediate” (CH₃)₃C⁺Cl⁻Li⁺ClO₄⁻.

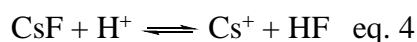
Based on this information, a mechanism could be postulated (scheme 5): First, the solvated fucosyl fluoride contacts a LiClO₄ particle by an ion-dipolar interaction (I). A similar scenario was described by Pocker *et al.* for “dipolar molecules and lithium ions”. The polarity between anomeric carbon and its fluoro substituent should be around 1.41 D. The high fluorophilicity of a lithium ion rather than its low Lewis acidity comes into play (II) and activates the fucosyl donor.⁹⁰ Such driving force is known from perfluoroalkyl lithium compounds, which are predestinated to fragment by α- and β-elimination (eq.s 1 and 2), respectively, to difluorocarbene due to the possibility to form LiF (high lattice energy of 1039 kJ/mol).⁹¹



The formation of LiF on the surface of the particle might give rise to an electrostatic catalysis since the transfer of fluoride anions charges the particle. This might be imagined as particle sites covered with fluoride anions. Thus, the glycosyl cation is stabilized on the negatively charged particle surface but still remains solvated by dichloromethane (III). Analogously to Pocker, eq. 3 shows a “quadrupole ion” with a glycosyl instead of a *t*-butyl cation and a fluoride instead of a chloride anion.

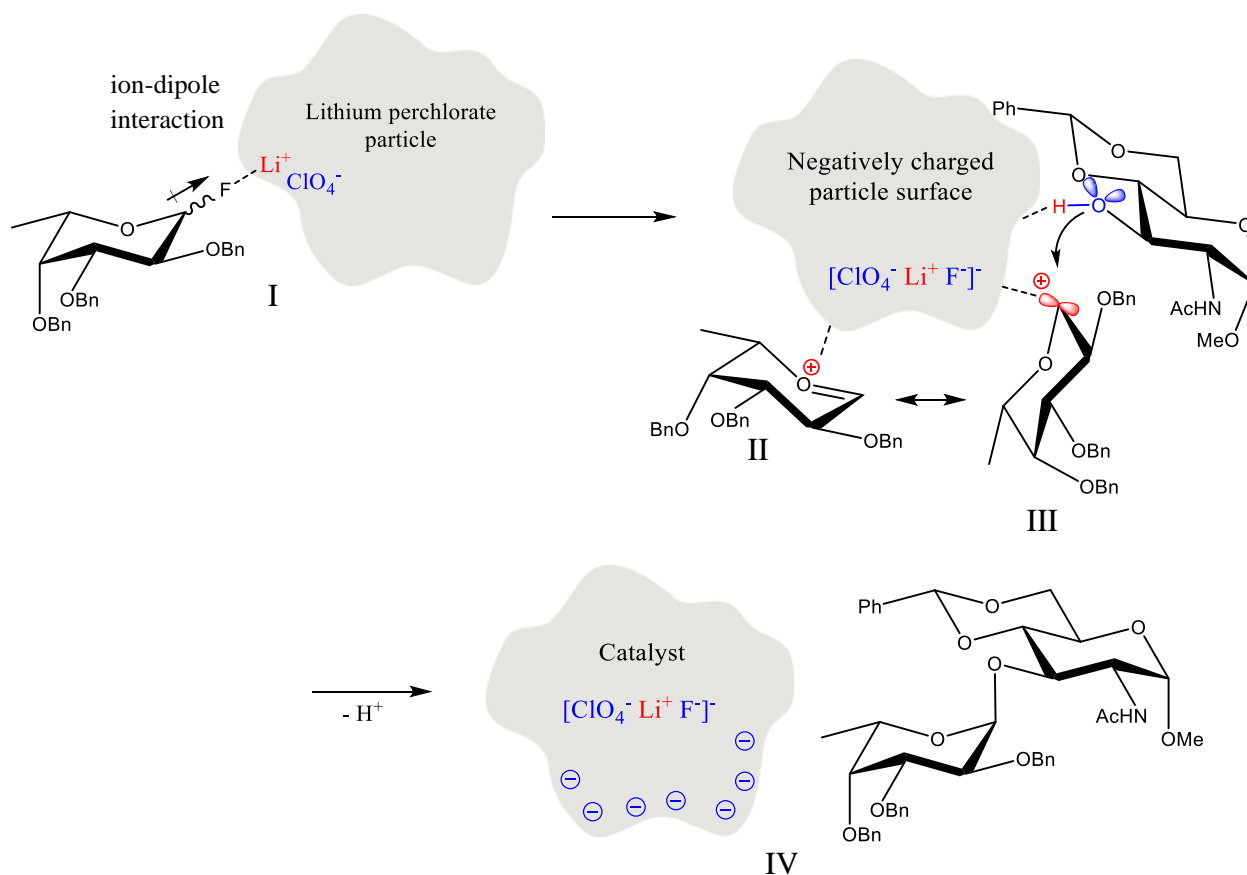


This may be described as an electrostatic adsorption of the glycosyl cation. The anomeric center is nucleophilically attacked by a glycosyl acceptor from the α-half space favored by the anomeric effect (III) and followed by desorption of the α-glycoside (IV). To maintain mild conditions, CsF works as an acid scavenger. It is moderately basic because HF is a weak acid (eq. 4).



Following the logic of this proposal, a particle size, once charged, retains its charge because of the high lattice energy of LiF. Such superficial ionic aggregate might be formulated as multiple ion Glycosyl⁺₁[F⁻_mLi⁺_n(ClO₄⁻)_n]^{m-}. By that, an electrostatic catalysis might be unfold since the charge m- should grow with every further donor activation. Since mass transfer of donor molecules from the bulk phase to particle surface should depend on charge-to-surface ratio, increasing LiClO₄ concentrations should decrease the catalytic effect, exactly this was observed by Waldmann, at 1 M, catalysis unfolds ideally, whereas at 3 to 5 M, 1,6-anhydro pyranose is formed. The adsorbed donor (*i.e.* the donor in its activated state) cannot be found by the solvated acceptor, and thus converts into 1,6-anhydro pyranose. Hence, equally increasing

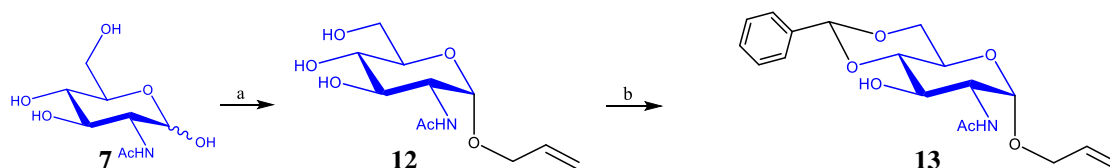
concentrations of both LiClO_4 and donor should in principle maintain catalysis, at least until other effects, such as viscosity, will influence the system. Pores, such as appearing in zeolites, seem to play no role in the case of LiClO_4 .⁹²



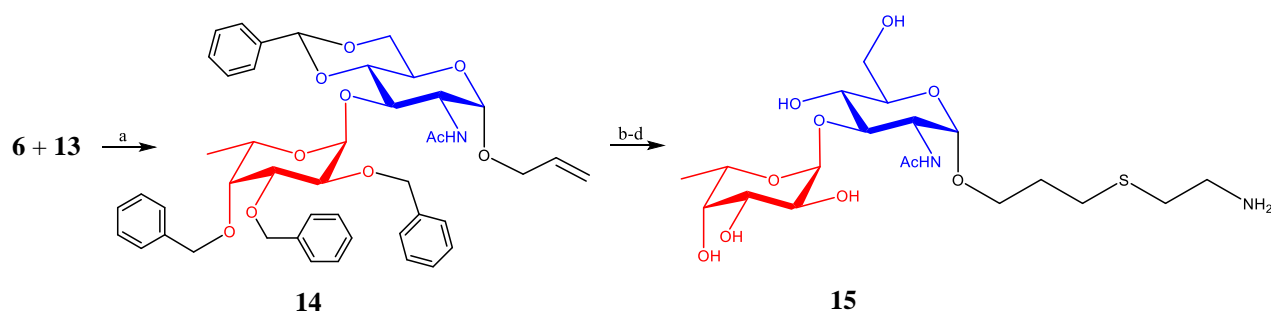
Scheme 5: Proposal of a reasonable glycosylation mechanism ($\text{S}_{\text{N}}1$) via a heterogeneously promoted activation of fucosyl fluoride by lithium ions with formation of lithium fluoride precipitate as driving force (I), stabilization of the resulting glycosyl cation by electrostatic adsorption on the negatively charged particle surface forming an "ionic aggregate" (II), a nucleophilic attack from α -half space by the glycosyl acceptor (III) and desorption of the resulting α -glycoside (IV). It suggests that there is no high internal solvent pressure in chemical glycosylations in dichloromethane. Instead, it states that LiClO_4 powerfully promotes the ionization of glycosyl fluorides by heterogeneous electrostatic catalysis.

6.1.3. Synthesis of Fuc α 1-3GlcNAc with Linker for Immobilization on a Pan

The allyl glycoside **14** was synthesized accordingly and modified according to Auzanneau and Pinto to introduce an amino group (schemes 6- and 7). The ESI MS spectrum showed the molecular ion of target compound **15** (fig. 36) and the ^1H NMR spectrum a characteristic pattern of triplets belonging to the methylene groups of the linker (fig. 37). Compound **15** can be conjugated to polystyrene, BSA or biotin.



Scheme 6: (a) Allyl alcohol, Dowex 50W-X8, reflux, 6 h, 70 %; (b) BADMA, CSA, ACN, reflux, 20 min, 70 %.



Scheme 7: Reagents and conditions: (a) LiClO₄, CsF, MS 4 Å, DCM, r.t., 24 h, 76 %; (b) HOAc, reflux, 20 min; (c) HS-(CH₂)₂-NH₂, H₂O, r.t., o.n.; (d) H₂, Pd/C, r.t., o.n.; 28 % over 3 steps.⁹³

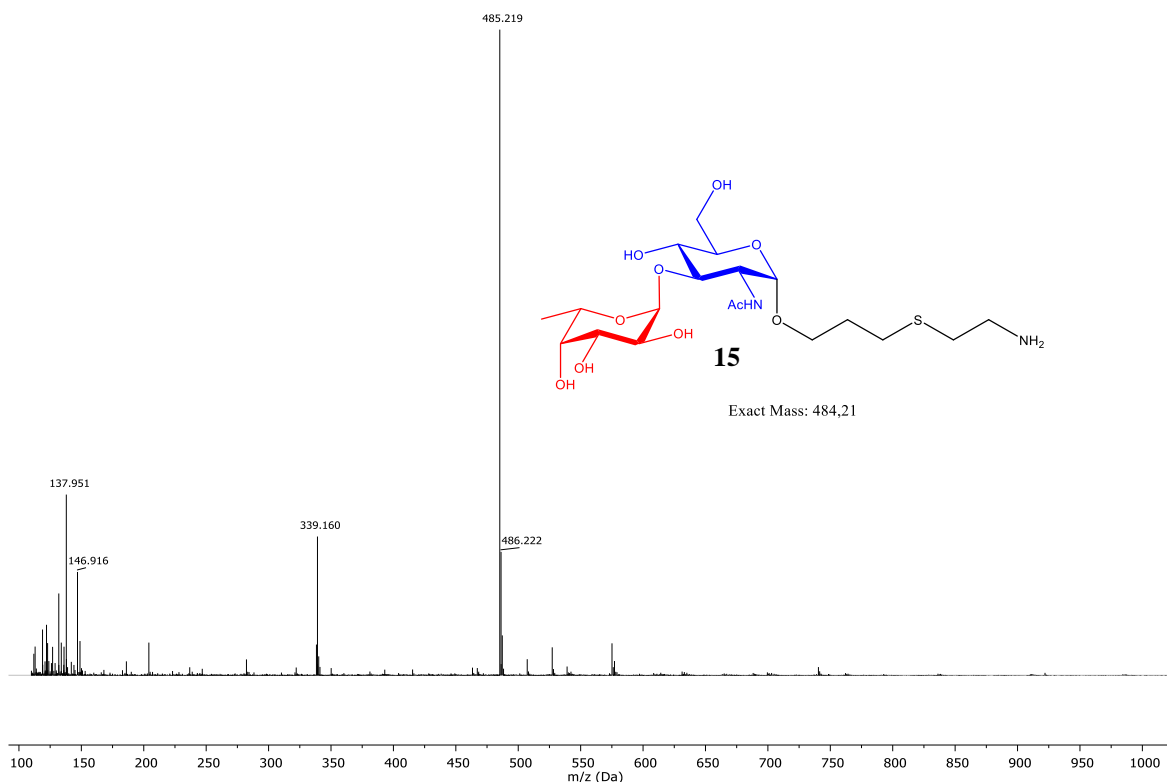


Fig. 36: ESI MS spectrum of 3-(2-aminoethylthio)propyl 2'-acetamido-2'-deoxy-3'-O- α -L-fucopyranosyl- α -D-glucopyranoside (**15**). MS operator: D. Gellert, MS interpreter: T. Raiber.

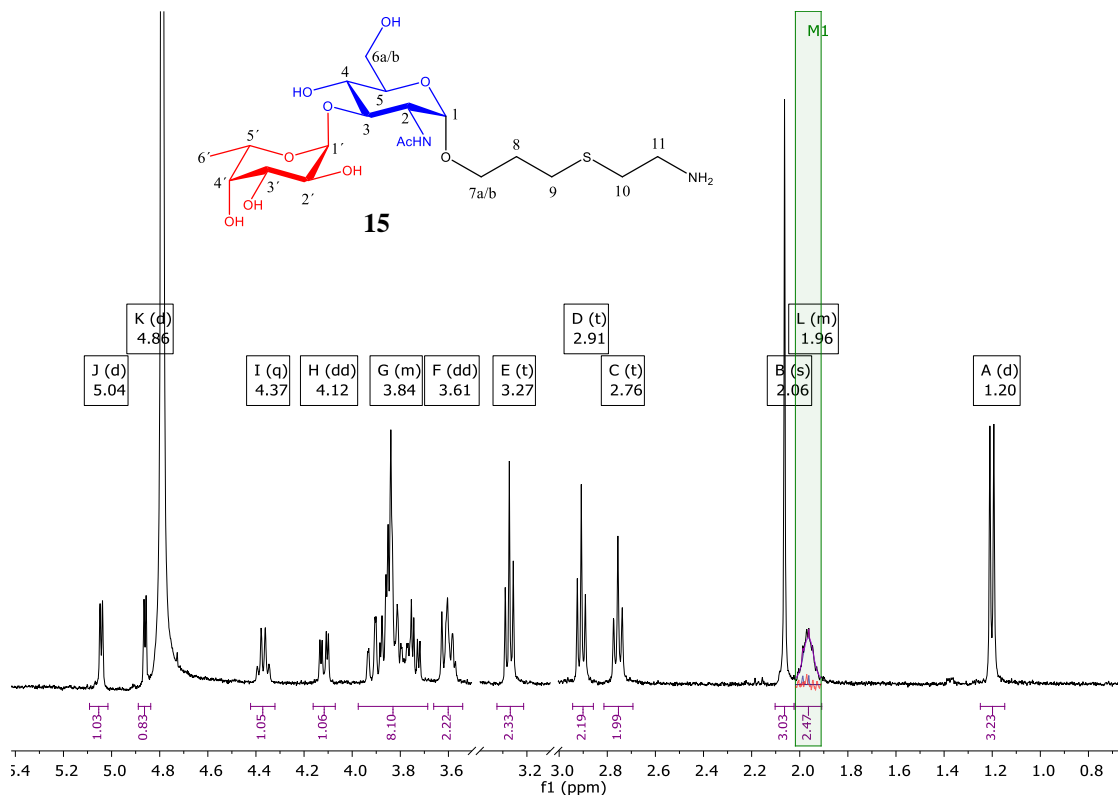
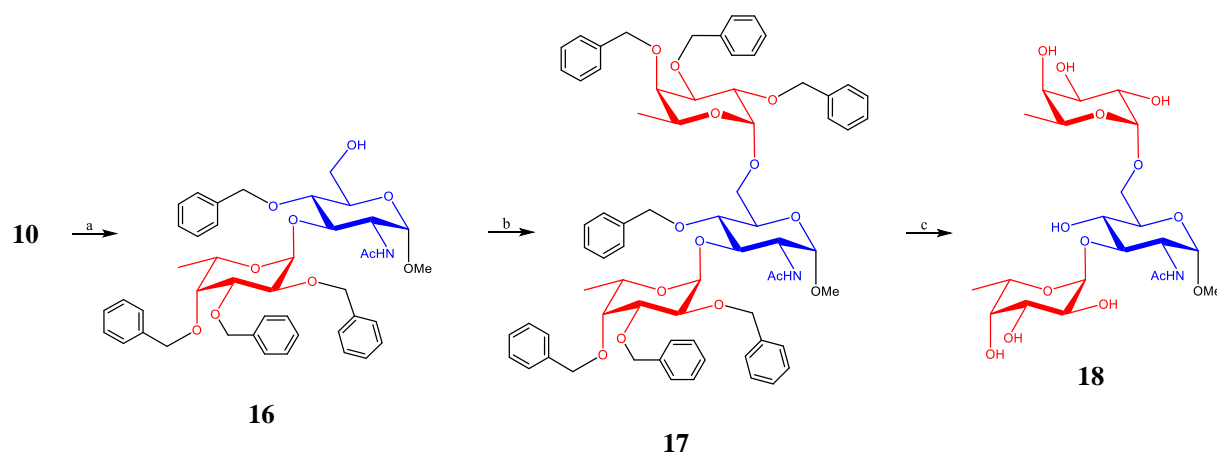


Fig. 37 : ^1H NMR spectrum of 3-(2-aminoethylthio)propyl 2'-acetamido-2'-deoxy-3'-O- α -L-fucopyranosyl- α -D-glucopyranoside (**15**) for immobilization (panning step). NMR interpreter: T. Raiber.

6.1.4. Synthesis of Fuc α 1-3(Fuc α 1-6)GlcNAc

To investigate the importance of the regioisomeric fucosyl residues, the trisaccharide Fuc α 1-3(Fuc α 1-6)GlcNAc was synthesized based on the disaccharide **10**. This precursor was deprotected at 6-position of GlcNAc according to Liptak, and the subsequent reactions were carried out as described above (scheme 8). The ^1H NMR spectrum shows three doublets at low field (anomeric protons) and two doublets at high field (H-6 of fucosyl residues) (fig. 38).



Scheme 8: Reagents and conditions: (a) $\text{LiAlH}_4\text{-AlCl}_3$, diethyl ether, reflux; (b) LiClO_4 , CsF, dichloromethane, donor, r.t.; (c) H_2 , Pd/C, methanol, r.t., 19 % over 3 steps.⁹⁴

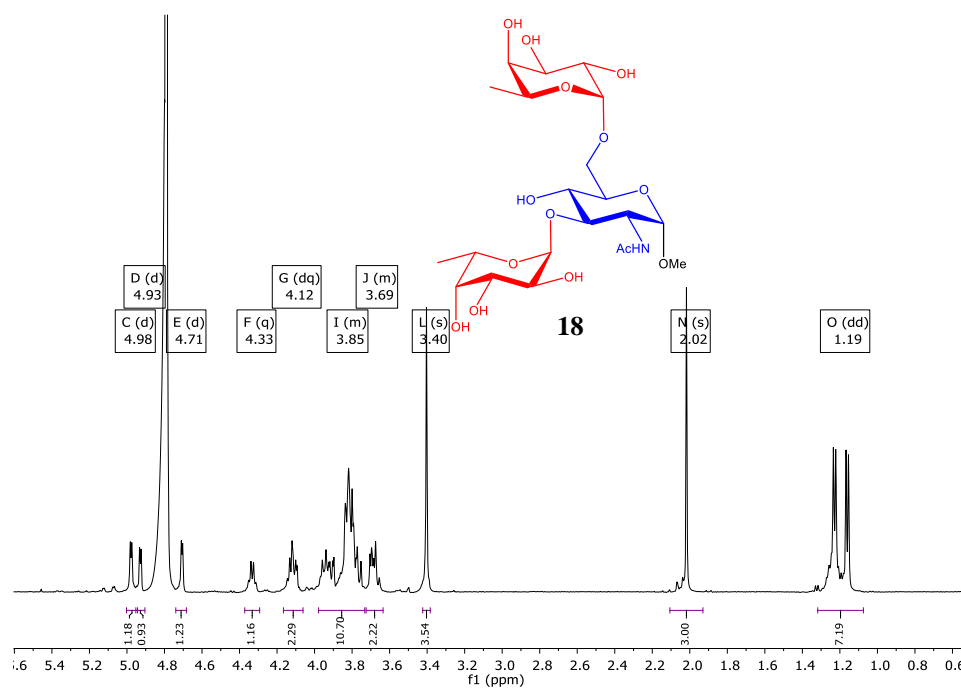
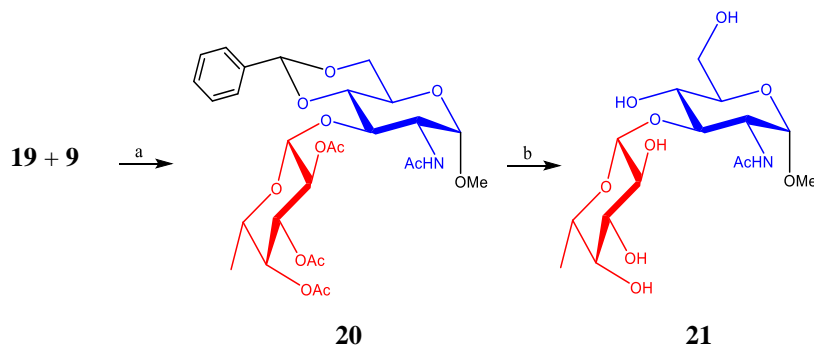


Fig. 38: ^1H NMR spectrum of Fuc α 1-3(Fuc α 1-6)GlcNAc α 1-OMe (**18**). NMR interpreter: T. Raiber.

6.1.5. Synthetic Manipulations of the Core Fucose Epitope

In order to evaluate the importance of α -configuration, the β -anomer **21** was synthesized according to Kartha *et al.* (scheme 9, fig. 39). Furthermore, β -Fuc α 1-3GlcNAc was synthesized analogously to α -Fuc α 1-3GlcNAc (see above; data not shown).



Scheme 9: Synthesis of Fuc β 1-3GlcNAc α -1OMe (**21**). Reagents and conditions: (a) Iodine, potassium carbonate, dichloromethane, r.t., o.n., 17 %; (b) HOAc, reflux, 20 min; (c) NaOMe, methanol, r.t., o.n., 81 % (over 2 steps).⁹⁵

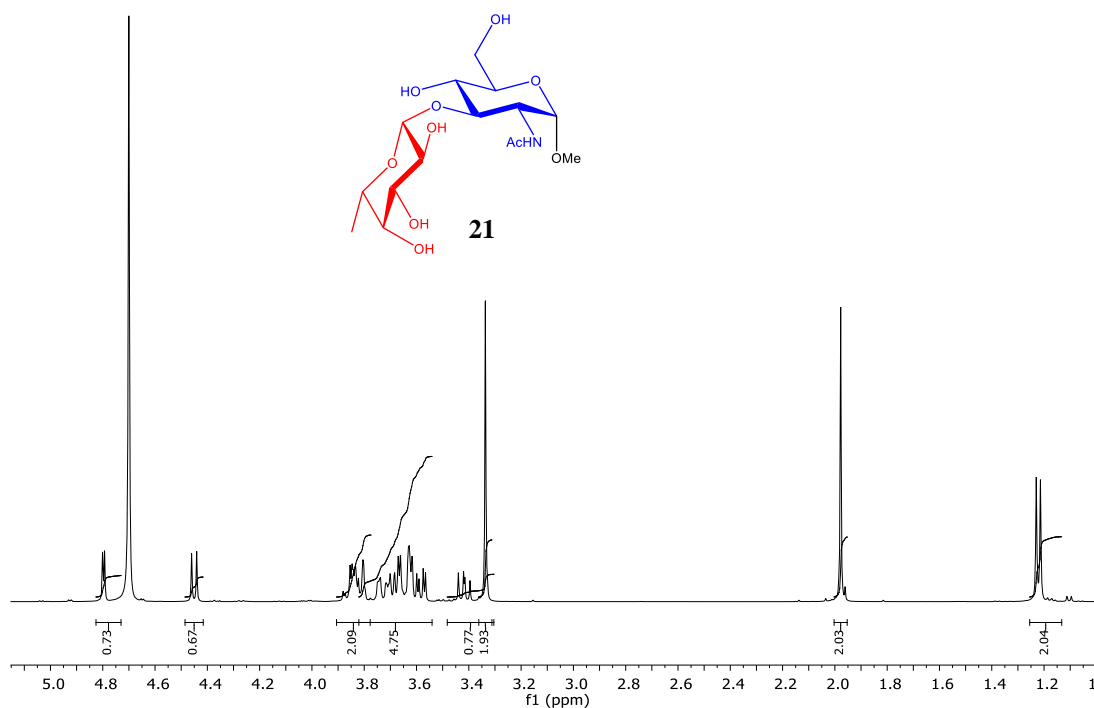


Fig. 39: ^1H spectrum of Fuc β 1-3GlcNAc α -1OMe (**21**). NMR interpreter: T. Raiber.

6.1.6. Establishment of Model System anti-TNT scFv-IgE 2.18 / RDX for the Analysis of Cross-Reactivities

Since TNT and RDX exhibit only a “small size and haptenic nature”, these structures are suitable as “model systems for the molecular recognition of minimal epitopes”.⁹⁶ Hence, RDX (hexogen) and TNT appeared to be particularly suitable to analyze cross-reactivities to anti-TNT antibodies by STD NMR spectroscopy. A huge in-house expertise in the field of phage display-derived anti-TNT antibodies suggested such a procedure, too.⁹⁷ RDX as ligand was drawn into consideration because it exhibits a chair confirmation similar to carbohydrates and its antibody cross-reactivity is sufficiently documented in the literature.^{98,99,100} The available anti-TNT/RDX antibodies are listed in table 3. RDX was synthesized (scheme 10) and analyzed by ¹H NMR spectroscopy (fig. 40) and X-ray crystallography (fig. 41). Its cross-reactivity against anti-TNT scFv-IgE antibodies was analyzed by a competition ELISA (fig. 42, table 4).

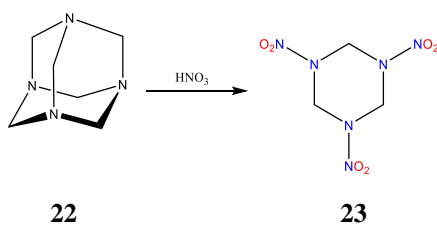
Table 3: Available ligand/receptor systems for STD NMR setup experiments.

Ligand	Receptor
TNT	scFv-IgE 4.8 and 2.18*
RDX	IgG 50518**

* Its cross-reactivity against RDX was detected by the competition ELISA shown in fig. 42 and unknown before.

** *Strategic Diagnostics Inc.*

It showed a competition of RDX with TNP-BSA if anti-TNT IgE 2.18 was used. In spite of structural resemblance (three nitro groups), there was no cross-reactivity detectable if anti-TNT IgE 4.8 was used. Obviously, the antibody 4.8 was too affine to TNP-BSA ($K_D \sim 8$ nM, reported by Michel) than to bind to solute nitro compounds. Antibody 2.18 is less affine to TNP-BSA (~ 90 nM, reported by Michel). Noticeably, the antibodies derived from selection against TNP-BSA. Hence, probably, BSA (*i.e.*, the protein proportion) makes TNP-BSA win the competition. That RDX with its non-planar geometry (fig. 41) is able to compete with TNP-BSA in a similar magnitude like the planar nitro compounds DNT and TNP-Tris indicates that the geometry plays no role for the binding mode of the 2.18 clone. Perhaps the 2.18 clone can just recognize single nitro groups and the 4.8 clone can recognize the complete TNT molecule. Based on these results, RDX/2.18 and TNT/4.8 were suggested as most suited model systems to study cross-reactivities (*e.g.*, by STD NMR spectroscopy).



Scheme 10: Synthesis of RDX (**23**) by nitric acid nitrification of hexamethylene tetraamine (**22**).

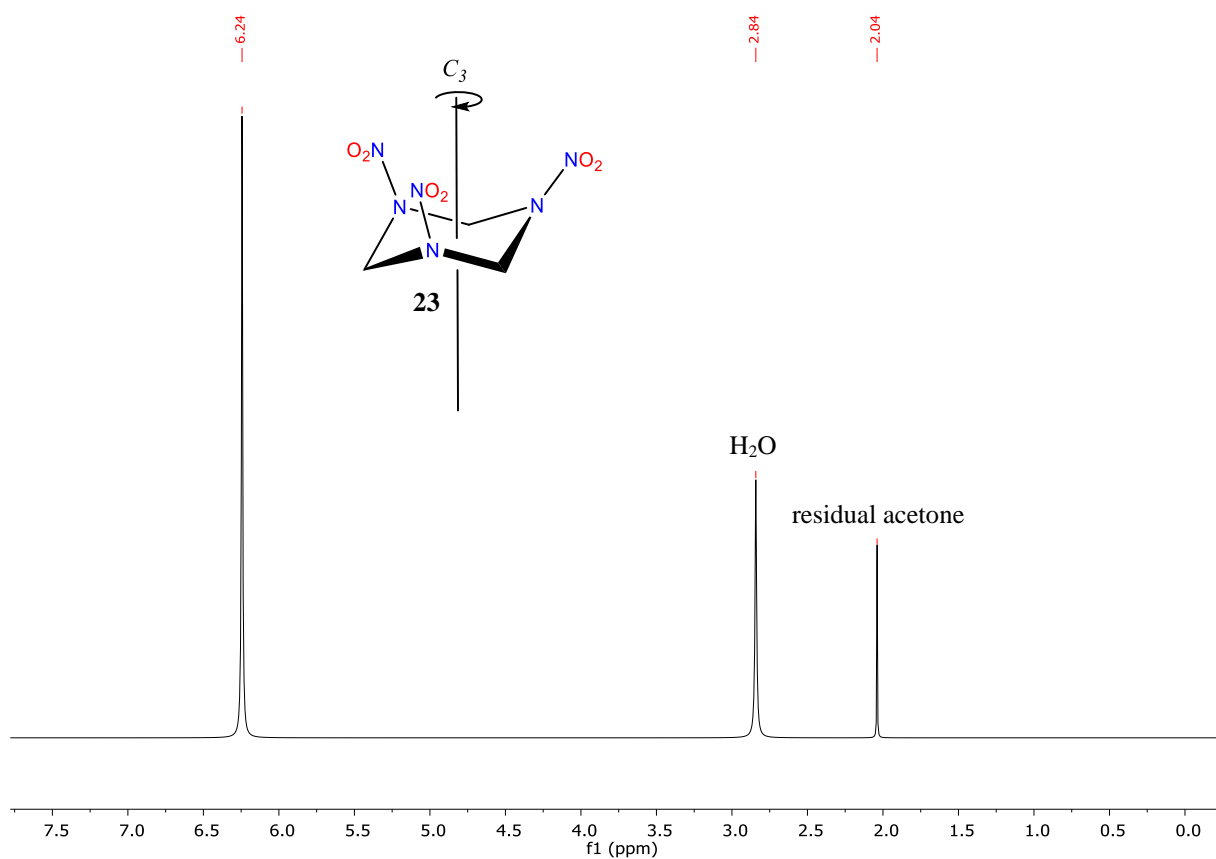


Fig. 40: The ^1H NMR spectrum of RDX (**23**) consists of a singlet at 6.24 ppm with reference to the residual acetone signal (2.04 ppm).¹⁰¹ The singlet “can be accounted for either by a planar ring or a rapid interconversion of two or more cyclic structures” (Filhol, 1971) and indicates a C_3 symmetry. The ^{13}C spectrum shows a resonance line at 62.1 ppm with reference to acetone- d_6 (data not shown). NMR interpreter: T. Raiber.

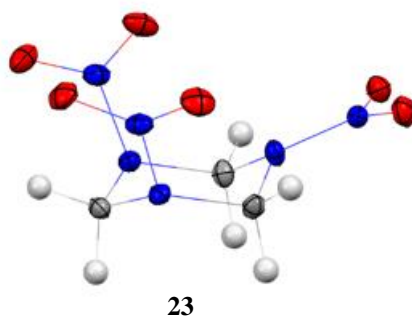


Fig. 41: Visualization of the crystal structure of RDX (**23**). Noticeably, in contrast to TNT, RDX is a non-planar nitro compound. XRD operator: I. Nevoigt, visualization (Mercury): T. Raiber.

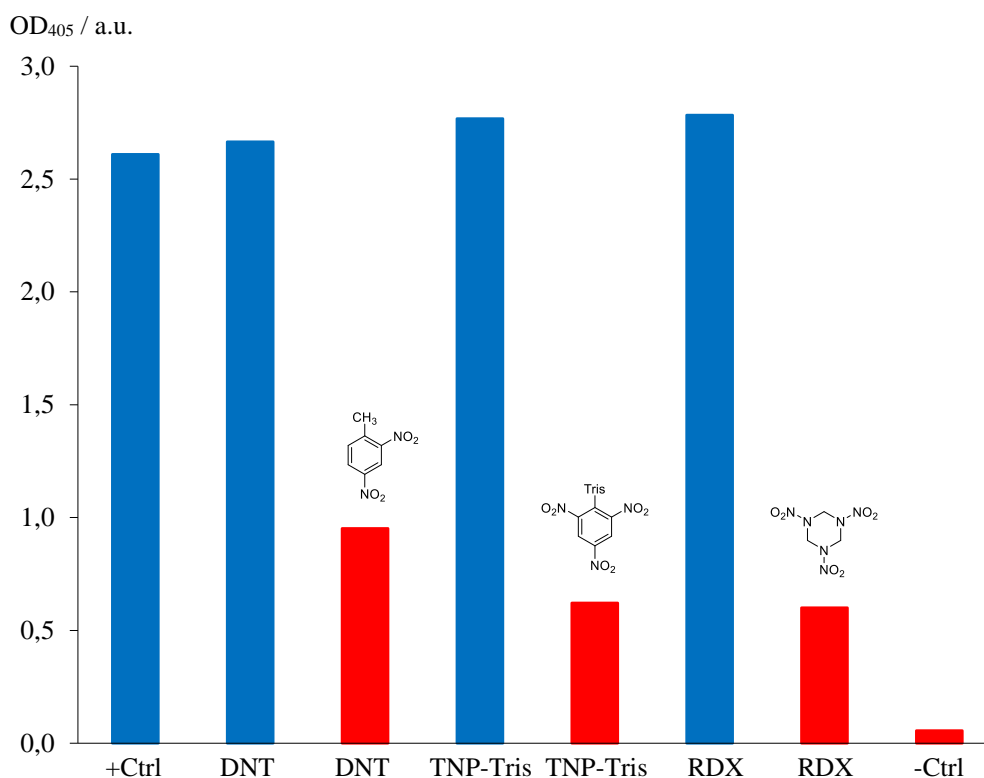


Fig. 42: Competition ELISA of TNP-BSA (coated) against different nitro compounds in solution (2,4-DNT and RDX pre-dissolved in acetonitrile, TNBS pre-dissolved in Tris buffer, pH 9). Supernatants of TNT-specific monoclonal antibodies 4.8 (blue) and 2.18 (red) were pre-incubated with nitro compounds (1 h, 450 rpm, r.t.). The supernatant of antibody 4.8 was diluted 1:2 to retard signals. The positive control is a pre-incubation without competitor. As negative control BSA was coated instead of TNP-BSA (to exclude unspecific binding). Incubation time: 1 h, r.t. The ELISA was detected with monoclonal anti-human IgE antibody conjugated to alkaline phosphatase and pNPP as chromogen substrate at 405 nm. All tested nitro compounds revealed as competitors if antibody 2.18 was used but lost completely their competitiveness if antibody 4.8 was used. Pipetting scheme: fig. 115. The monoclonal TNT-“specific” IgE antibodies were kindly provided by Y. Michel.

Table 4: Competition ELISA of TNP-BSA against different nitro compounds in solution (see fig. 42).

OD ₄₀₅ / a.u.							
+Ctrl (4.8 w/o competitor)	4.8 with DNT	2.18 with DNT	4.8 with TNP-Tris	2.18 with TNP-Tris	4.8 with RDX	2.18 with RDX	-Ctrl (BSA coated, 2.18 w/o competitor)
2.6095	2.6652	0.9517	2.7678	0.6215	2.7833	0.6003	0.0558

6.2. Analysis of the Interaction between Honeybee Venom CCD Fragments and Phage Display-Derived Monoclonal Anti-HRP Antibodies

6.2.1. STD NMR Spectroscopy

In 1986, Nowotny *et al.* showed that antigenic determinants “coincide with surface regions accessible to large probes”, such as antibody domains.¹⁰² This so-called Mollweide projection maps the surface of *entire* antigen molecules. In 1987, Arata used spin diffusion for the analysis of antigen-antibody interactions and was able to map the *contact positions* of an antigen fragment with an antibody.¹⁰³ With this ¹H NMR method, the Mollweide projection could be validated. The application of Arata’s method to fragment-based drug discovery by Peters and Meyer in 1998 was of great impact. Technically, STD NMR spectroscopy emerged from NOE and spin diffusion experiments (fig. 43).

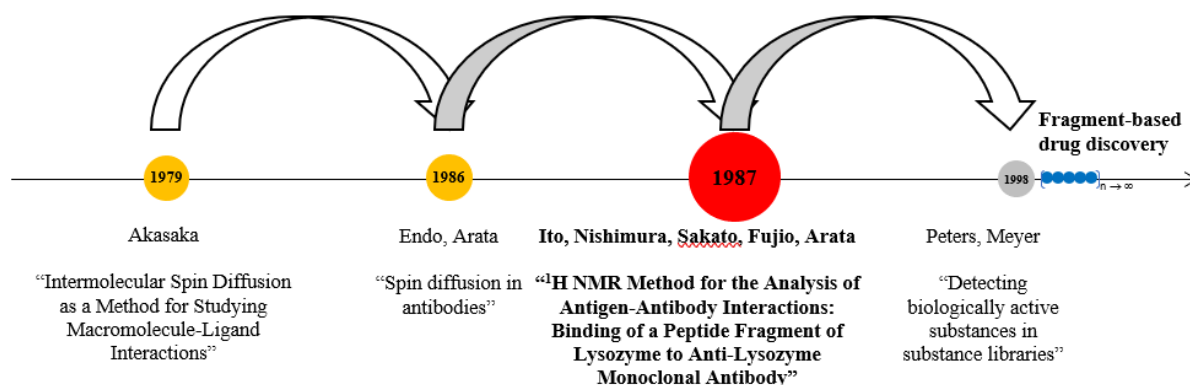


Fig. 43: Development of STD NMR spectroscopy. The STD NMR experiment by Arata in 1987 built on spin diffusion experiments on macromolecules (Akasaka, 1979). Color code: red: Historic break-throughs; yellow: contributions of guidance and orientation; blue: contributions of consolidative or establishing character; patent. Notably, the impulse character of the break-throughs (blue arrows). Remarkably, the patent by Peters and Meyer in 1998 was of great impact on fragment-based drug discovery, probably due to a commercial non-availability of Arata’s method as pulse program. NMR spectroscopy in fragment-based drug discovery was reviewed by Meyer and Peters in 2003.¹⁰⁴

6.2.1.1. Spin Diffusion Experiments with Antibodies Prepared Way to STD NMR Spectroscopy

The benefit of spin diffusion to study macromolecule-ligand interactions was described by Akasaka in 1979.¹⁰⁵ For antibodies, which are of interest in the present study, spin diffusion was first described by Arata in 1985.¹⁰⁶ In 1987, Arata described STD NMR spectroscopy at the example of a lysozyme fragment binding to an anti-lysozyme antibody (“In the present study, we used monoclonal antibody Hyb.Q (6) that recognizes one of the antigenic sites of hen egg-white lysozyme (HEL). A peptide fragment of HEL, P₁₇’, corresponding to this antigenic

site was obtained by limited pepsin digestion. When spin diffusion is prevalent, the nuclear Overhauser effect (NOE) becomes completely non-specific: the effect of saturation by continuous irradiation of any one of the protons in the rigid parts of large molecules, such as immunoglobulins, spreads over the entire molecule. We will show how the effect of saturation is transmitted through the antigen binding site to the P_{17'} peptide. On the basis of the intermolecular NOE data, we will describe how the P_{17'} peptide interacts with the Hyb.Cl antibody.”) The STD NMR spectrum is shown in fig. 44 and its epitope map in fig. 45.

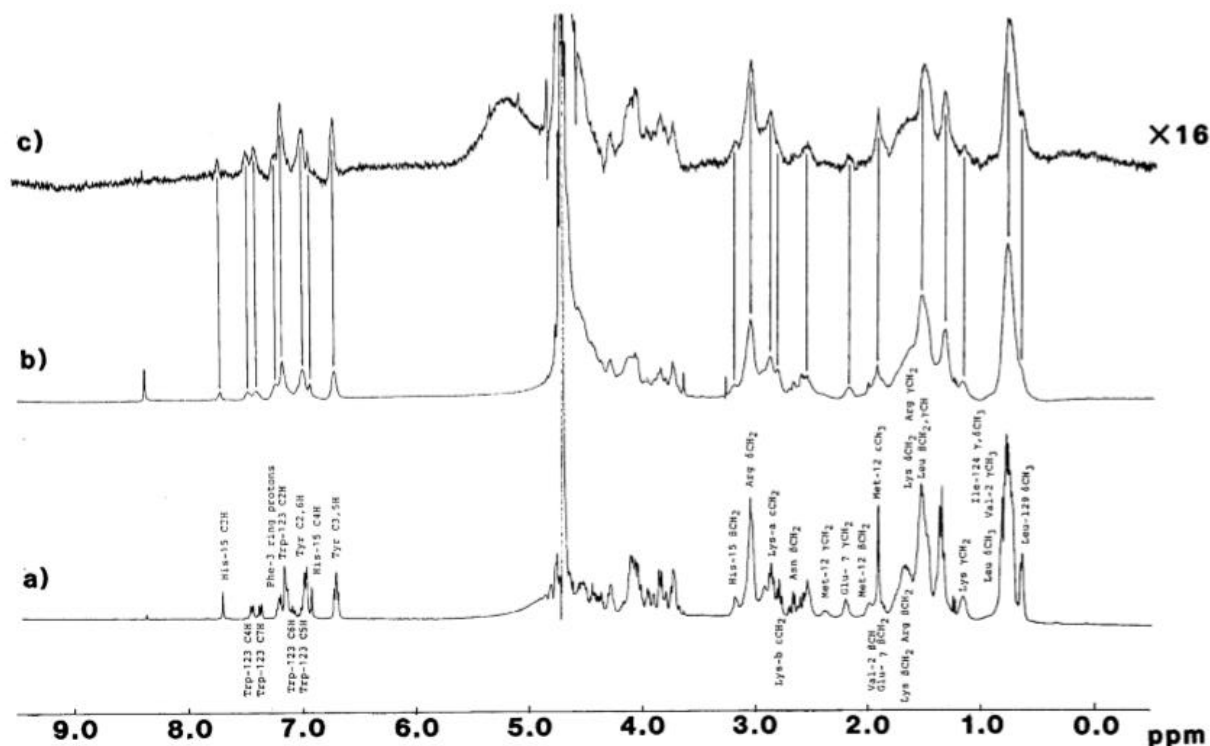


Fig. 44: In 1987, Ito *et al.* carried out history’s first STD NMR experiment: “The 400 MHz ¹H NMR spectra of P_{17'} (1 mg/0.4 mL) in the absence (a) and presence (b) of antibody. A mixture with a ratio of P_{17'} to 2 Hyb.Cl. of 16:1 was used to observe the NOE difference spectrum (c), where the vertical amplitude was expanded 16 times. Irradiation was for 1 s at 5.2 ppm.” “The free induction decay was recorded with 8K data points and a spectral width of +2,500 Hz. A total of 2,000 transients was acquired and a line broadening of 0.5 Hz was applied prior to Fourier transformation. The probe temperature was 23 °C.”

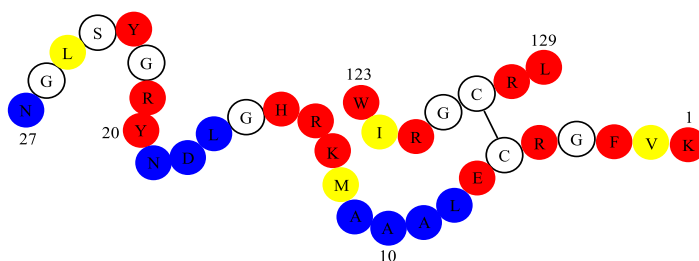


Fig. 45: History’s first epitope map based on STD effects: „NOE mapping for P_{17'} drawn on the basis of the experiments shown in“ fig. 44. Color code: red “strong”, yellow “medium” and blue “weak” magnitudes of NOE, white “no information on NOE was available due to the complexity of the observed signals.” “The side chains of aromatic residues, Trp, Tyr, and His, and of ionic residues, especially Arg, Lys, and Glu, are suggested to be important in the antigen-antibody interaction.” Illustration adapted from Arata (1987).

6.2.1.2. Application of STD NMR Spectroscopy to Fragment-Based Drug Discovery

In fragment-based drug discovery, the low binding affinities of the fragments pose significant challenges for screening. Biophysical techniques, which are sensitive enough to detect fragments with low binding affinity, are necessarily required. In **1998**, Peters and Meyer applied STD NMR spectroscopy to fragment-based drug discovery and made an optimized pulse sequence commercially available.¹⁰⁷ The method has become a standard method to identify weak binders. Even a binder in an extract or in the presence of impurities can be identified because the signals of the non-binding substances are eliminated by subtracting on- and off-spectra. Various pulse sequences are available. The invention was of great impact.^{108,109,110,111}

6.2.1.3. Fundamental Principles of STD NMR Spectroscopy

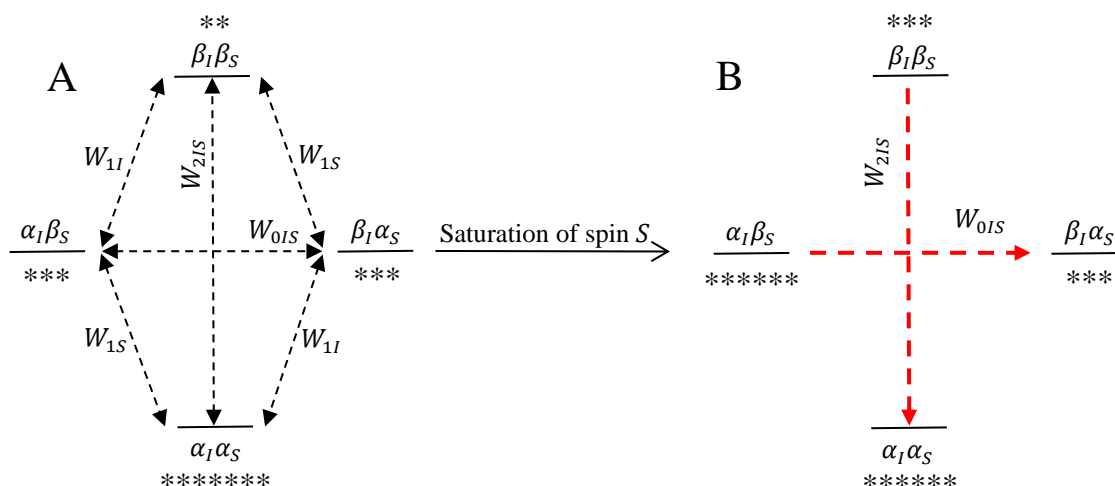
6.2.1.3.1. Nuclear Overhauser Effect

STD NMR spectroscopy is based on the nuclear Overhauser effect (*NOE*), *i.e.*, the change in intensity of one resonance when the spin transitions of another are perturbed from their equilibrium populations. According to eq. 5, the magnitude of this effect is expressed as a relative intensity change between the equilibrium intensity and that in the presence of the *NOE*.

$$NOE = f_I\{S\} = \frac{I - I_0}{I_0} \quad \text{eq. 5}$$

with f_I = fractional change in the signal intensity upon irradiation for spin I when spin S is perturbed
 I = intensity in the presence of the *NOE*
 I_0 = equilibrium intensity

A rigid molecule with two spin $\frac{1}{2}$ nuclei, I and S , which do not share a scalar coupling but are sufficiently close ($< 5 \text{ \AA}$) will share a dipolar coupling (*i.e.*, a direct, through-space magnetic interaction between the two spins). The transitions $\alpha\alpha\text{-}\alpha\beta$, $\alpha\alpha\text{-}\beta\alpha$, $\alpha\beta\text{-}\beta\beta$ and $\beta\alpha\text{-}\beta\beta$ involve just one inversion either of S or I spin, whereas the two transitions $\alpha\beta\text{-}\beta\alpha$ and $\alpha\alpha\text{-}\beta\beta$ involve the simultaneous inversion of both S and I spins (scheme 11). The latter two transitions are able to act as relaxation pathways and only these give rise to the *NOE*. Saturation of the S resonance will equalize the population differences across the S transitions and the system will alter its spin populations in order to return to its equilibrium.



Scheme 11: Energy diagram for a two homonuclear spin system, A: equilibrium state; B: saturation state. To return to equilibrium, the relaxation pathways W_{2IS} and W_{0IS} are active. The asterisks represent the spin populations.

Both W_2 and W_0 compete with each other with the dominant pathway determining the sign of the *NOE* (eq. 6).

$$f_I\{S\} = \frac{\gamma_S}{\gamma_I} \left[\frac{W_2 - W_0}{W_0 + 2W_1^I + W_2} \right] \quad \text{eq. 6}$$

with γ_S = magnetogyric ratio of spin S

γ_I = magnetogyric ratio of spin I

Which one of these two pathways will dominate, depends on rotation frequency ω of the molecule in solution (eq. 7). A maximum spectral density is reached at $\omega = 0$. If $\omega\tau_c \ll 1$, which is the case for small molecules with fast rotation, W_2 is the dominant pathway and the *NOE* is positive. This is because the probability of generating higher frequencies increases for rapid tumbling molecules. If $\omega\tau_c \gg 1$, which is the case for large molecules with slow rotation, W_0 is the dominant pathway and the *NOE* is negative. This is because slow tumbling molecules have a small probability to generate oscillating fields. If $\omega\tau_c \approx 1$, which is the case for molecules of intermediate size, the *NOE* is approximately zero. This case occurs for molecules of intermediate size and depends on the central frequency of the spectrometer.

$$J(\omega) = \frac{2\tau_c}{1 + \omega^2\tau_c^2} \quad \text{eq. 7}$$

with $J(\omega)$ = spectral density

τ_c = correlation time

ω = rotation frequency

In STD NMR spectroscopy, the Overhauser effect is generated between spin states of ligand and receptor during a binding event (fig. 46).

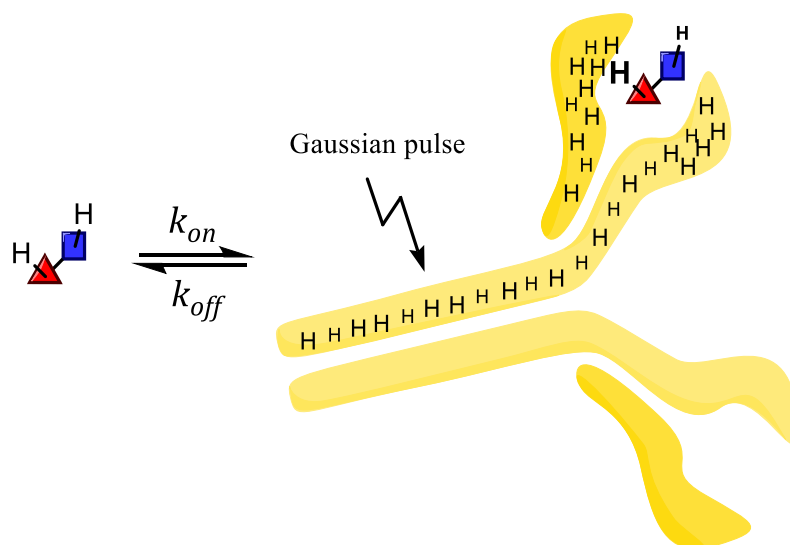


Fig. 46: Ligand exchange at a receptor saturated by a r.f. pulse which initiates spin diffusion and saturation transfer to the ligand. Spin diffusion in antibodies was first described by Endo and Arata in **1986**.

This binding is characterized by an on- and off-rate, and its corresponding thermodynamic equilibrium dissociation constant (eq. 8).

$$K_D = \frac{k_{off}}{k_{on}} \quad \text{eq. 8}$$

with K_D = dissociation constant

k_{off} = off-rate

k_{on} = on-rate

The ligand exchange takes place during saturation time. The higher the ligand concentration and the longer the saturation time the more saturation is transferred from one receptor molecule to a multitude of ligand molecules, provided that $[L] \gg [P]$ (eq. 9). This allows the application of diluted protein solutions in the μmolar range. For a given system, the ligand-to-protein ratio and the saturation time have to be selected in a STD build-up experiment according to the expected K_D . For high-affinity ligands ($0.01 \text{ s} < k_{off} < 0.1 \text{ s}$), the saturation cannot be transferred effectively to the solution because the lifetime of the complex ($1/k_{off}$) is longer than the saturation time ($1/k_{off} > t_{sat}$). For low-affinity ligands, the on-rate is that low that no saturation is transferred within the saturation time. Thus, a saturation is only transferred if the K_D is within the range of 10^{-8} mol/L and 10^{-3} mol/L .

$$A_{STD} = \frac{I_0 - I_{sat}}{I_0} \frac{[L]}{[P]} = \frac{I_{STD}}{I_0} \frac{[L]}{[P]} \quad \text{eq. 9}$$

with A_{STD} = STD amplification factor
 I_0 = off-resonance spectrum
 I_{sat} = on-resonance spectrum
 $[L]$ = ligand concentration
 $[P]$ = protein concentration

At the maximum ligand turnover, the STD amplification factor achieves its maximum, *i.e.*, the binding site is saturated with ligand (eq. 10). Then, with yet higher ligand concentrations, the STD amplification factor decreases because $I_0 \sim [L]$ (fig. 47). Notably, high ligand concentrations and high ligand-to-protein ratios employed in the STD NMR experiments favor non-specific binding. Non-specific binding ligands also contribute to STD effects.

$$A_{STD} = \frac{\alpha_{STD} [L]}{K_D + [L]} \quad \text{eq. 10}$$

with A_{STD} = STD amplification factor
 α_{STD} = maximum STD amplification factor
 $[L]$ = ligand concentration
 K_D = dissociation constant

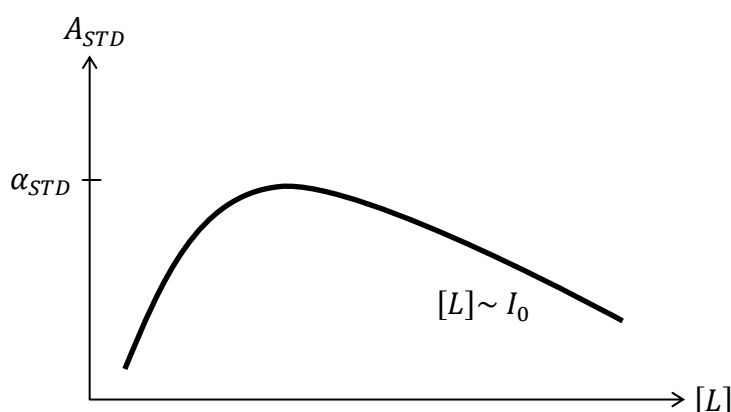


Fig. 47: STD amplification factor as a function of the ligand concentration.

6.2.1.3.2. Spin Diffusion

Spin diffusion in macromolecules was studied by Akasaka and was utilized by Arata for saturation transfer experiments. Saturation is magnetization rotating in the zx or zy plane, respectively (*i.e.*, it generates incoherent magnetization, which is undetectable). This is why in STD NMR spectroscopy a blank subtraction is required to visualize the STD effects. Depending on the size of a molecule, saturation may lead to a phenomenon called spin diffusion, which is an indirect transfer of magnetization between two nuclei *via* a third. In case of spin diffusion, it is not possible to trace back the origin of the magnetization. The spin-spin relaxation is faster

than the spin lattice relaxation (*i.e.*, before energy can be transferred to the lattice, it is spread from nuclei to nuclei over the whole molecule). Thus, with increasing molecular weight, the shorter T_2 and the more effective the spin diffusion is (*e.g.*, a large protein like myosin (470 kDa) is almost invisible due to its molecular weight and its resulting very short spin-spin relaxation time) (fig. 48).

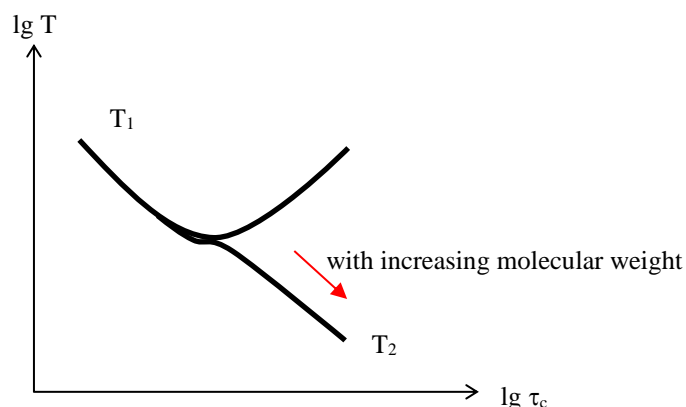


Fig. 48: Decadic logarithm of relaxation time T as a function of the decadic logarithm of correlation time τ_c .

6.2.1.3.3. Pulse Sequence

The STD NMR experiment is a pseudo-2D experiment with two rows (on- and off-resonance spectra) on F2 (fig. 49). After a relaxation delay ($D1$) of approximately 4 s, a cascade of selective Gaussian pulses with a bandwidth of approximately 40 Hz and a duration of 50 ms saturates the protein in the sample until a 'saturation time' of 1 to 2 s is achieved, typically 2 s. By so-called *spin diffusion* - happening in a time range of 50 to 200 ms - all protein protons become saturated. If binding takes place, saturation is transferred to the ligand. With high k_{diss} the saturated ligand is transferred to the solution. Thus, the higher k_{diss} is, the stronger this effect becomes. If the ligand is in high excess, a lot of molecules will be saturated. After a delay of approximately 1 s, an observation pulse of approximately 10 μs bandwidth turns the magnetization into the x-y-plane where it is kept by a so-called *spin-lock* $T_{1\rho}$ with a bandwidth of approximately 11.5 kHz and a duration of 10 to 20 ms. By this turn, the magnetization generates a signal in the receiver coil (y). The generated FID signal is transferred to frequency domain by FT as usual. Since this experiment is repeated in the same way but with a Gaussian train irradiated at a position without protein signals (*e.g.*, +40 ppm), power is transferred to the sample in order to keep the experimental conditions the same but no saturation is transferred to the protein. Then, by subtraction of on- and off-resonance spectra, the resonances will

extinguish each other in the absence of a ligand or will result in signals (STD effects) in the presence of a ligand.

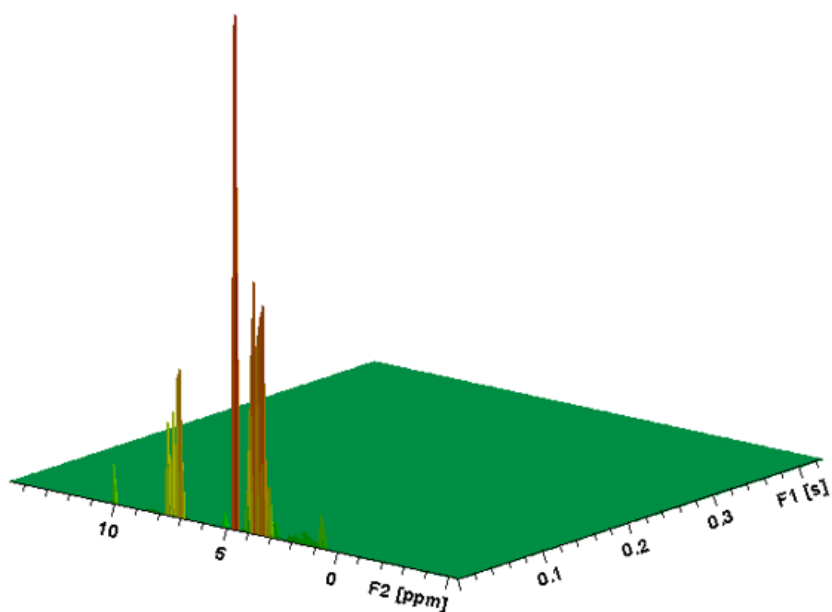


Fig. 49: STD NMR experiment as pseudo-2D experiment in the oblique mode display (TopSpin) with the two rows (on- and off-resonance ^1H spectra) on F2.

6.2.1.4. STD NMR Results

Since the serum allegedly showed immune reactivity against the disaccharide as tested by STD NMR spectroscopy, a selection against the disaccharide was skipped. Thus, the biopanning excluded the disaccharide but included HRP and MUXF as targets and delivered after three rounds two monoclonal antibodies (HHH1 and HMM5).¹¹² In contrast to the disaccharide, the trisaccharide $\text{Fuc}\alpha 1\text{-}3(\text{Fuc}\alpha 1\text{-}6)\text{GlcNAc}$ showed non-binding properties in STD-NMR experiments. For testing the hypothesis 'HMM5 is inactive', an activity ELISA was carried out (fig. 50, table 5), falsifying this hypothesis. Subsequently, a negative control STD NMR experiment revealed artefacts. SPR experiments showed no binding properties, too.

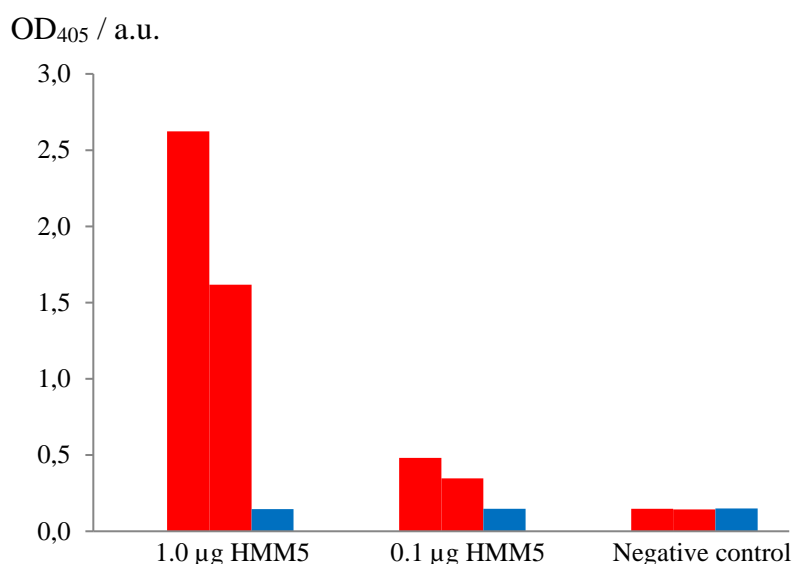


Fig. 50: Activity ELISA for falsification of hypothesis 'HMM5 is inactive' (no STD effects for the trisaccharide **18**, fig. 52). The double determination shows the retardation of pipetting the AP detection solution (containing the chromogen substrate) for the second row. Color code: see table 5; pipetting scheme: see fig. 114.

Table 5: Activity ELISA for falsification of hypothesis 'HMM5 is inactive' (see fig. 50).

Row	Positive control (supernatant)	OD ₄₀₅ / a.u. for masses of HMM5 antibody			Negative control (culture medium)
		10.0 µg	1.0 µg	0.1 µg	
Coated with HRP	Over	Over	2.6225	0.4820	0.1471
Coated with HRP	Over	Over	1.6163	0.3468	0.1435
Not coated	0.1476	0.1610	0.1463	0.1466	0.1498

6.2.1.4.1. Persisting False-Positive STD NMR Results

An epitope map for Fuc α 1-3GlcNAc in interaction with polyclonal anti-HRP IgG was obtained on an AVIII 600 MHz spectrometer (fig. 51A). The magnitude of the STD effects is similar to that obtained for a nonasaccharide in the presence of a monoclonal anti-HRP antibody (HMM5 Fab). Based on this finding, the panning step in the phage display procedure was skipped and, instead, the interaction of Fuc α 1-3GlcNAc with monoclonal anti-HRP antibodies has been analyzed resulting in epitope maps (fig. 50 B and C) and K_D values (fig.s 55-57). Then the interaction between monoclonal anti-HRP antibodies and different glycan substructures has been analyzed by STD NMR spectroscopy, first on a 700 MHz and then, in the intention to exclude unspecific binding effects, on a 600 MHz spectrometer with an AVIII console for a better performance. In order to find crucial structural elements on which a recognition may depend on, substructures with manipulated features have been synthesized and their interaction analyzed (fig.s 53 and 54).

6.2.1.4.2. Negative Control Revealed Fatal Error

The finding that the extended motif $\text{Fuc}\alpha 1\text{-}3(\text{Fuc}\alpha 1\text{-}6)\text{GlcNAc}$ showed no STD effects in contrast to $\text{Fuc}\alpha 1\text{-}3\text{GlcNAc}$, gave rise to skepticism (fig. 52). Discrepancies in repetitive K_D determinations (table 6) and generation of epitope maps for the manipulated substructures $\text{Fuc}\beta 1\text{-}3\text{GlcNAc}$ (fig. 53) and $\text{DFuc}\alpha 1\text{-}3\text{GlcNAc}$ (fig. 54), supported this skepticism. In fact, all results have later been rated as false positives due to the presence of artefacts revealed by a negative control (fig. 68). Re-evaluation of the data showed tiny STD effects for $\text{Fuc}\alpha 1\text{-}3\text{GlcNAc}$ ring protons in interaction with polyclonal anti-HRP IgG (fig.s 63 A-D) and no STD effects with HMM5 (fig.s 64 A-D); the same applies to the β -anomer (fig.s 65 A-C). For comparison, the STD NMR spectra of a nonasaccharide in the presence of polyclonal anti-HRP IgG and HMM5 are shown (fig.s 69 and 70). A double check of the STD NMR experiment with $\text{Fuc}\alpha 1\text{-}3\text{GlcNAc}$ showed no STD effects, not even by sweeping the irradiation frequency (table 17), and was free of artefacts (fig. 67). In retrospect, the cause of the artefacts may be traced back to a power spill-over of radio frequency irradiation to the ligand. Different parameterizations of STD NMR experiments for $\alpha 1\text{-}3$ and $\beta 1\text{-}3$ fucose may have led to a presence of artefacts in case of $\alpha 1\text{-}3$ and $\beta 1\text{-}3$ fucose and absence of artefacts in case of $\text{Fuc}\alpha 1\text{-}3(\text{Fuc}\alpha 1\text{-}6)\text{GlcNAc}$. A binding of the $\text{Fuc}\alpha 1\text{-}3\text{GlcNAc}$ substructure and all other synthesized glycan substructures to anti-HRP antibodies is clearly ruled out. Due to alleged technical reasons, STD experiments with anti- Le^x rat IgM (positive control) could not be carried out (fig. 66). The positive control (AAL / $\text{Fuc}\alpha 1\text{-}3\text{GlcNAc}$, data not shown) resulted in a difference spectrum with very low STD effects, though SPR spectroscopy resulted in an affinity of 50 nM (fig. 86). Since later, the alleged STD effects will be revealed as pure artefacts, the alleged binding isotherms (fig.s 55-62) show the behaviour of the artefacts with increasing ligand concentrations and α_{STD} may be interpreted as the limit of capacity to absorb a power spill-over. Therefore, the discrepancy between the artificial K_D values determined at two different spectrometers can be traced back to technical reasons. STD data at the example of HSA / Trp give a good impression how true STD effects should look like (fig.s 71 A-D). An impression of a proper K_D determination by STD NMR spectroscopy was given by Angulo *et al.* in 2010.¹¹³

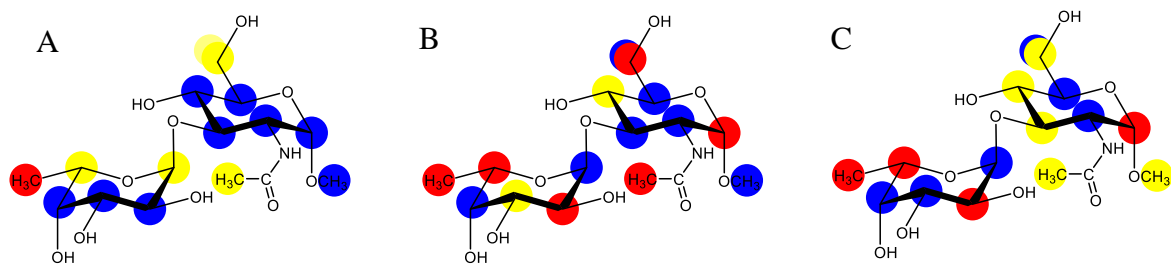


Fig. 51: True-positive but statistically insignificant epitope map of Fuc α 1-3GlcNAc α 1-OMe (**11**) with polyclonal anti-HRP rabbit IgG (**A**; NMR operator: T. Hackl, NMR interpreter: M. Kötzler). Deceptively realistic but false-positive epitope maps of disaccharide **11** with HHH1 (**B**; NMR operator and interpreter: M. Fölsing) and HMM5 (**C**; NMR operator and interpreter: M. Fölsing). Epitope map **A** results from a test of immune reactivity in the forefront of antibody phage display. The complete mapping enhanced the impression of a *true* fingerprint of the antibody. Color code: blue 0-30 %, yellow 30-70 %, red 70-100 % with the strongest STD effects set 100 %.

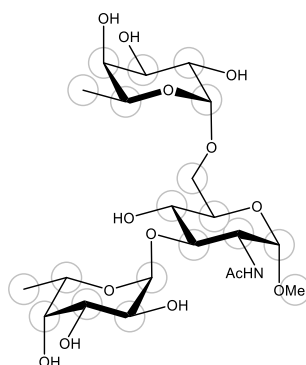


Fig. 52: Although the disaccharide **11** (fig. 51) and the nonasaccharide GlcNAc β 1-4Man α 1-3(GlcNAc β 1-4Man α 1-6)Man β 1-4GlcNAc β 1-4[Fuc α 1-3(Fuc α 1-6)]GlcNAc β 1-NHAc (M. Kötzler) allegedly showed STD signals, the trisaccharide Fuc α 1-3(Fuc α 1-6)GlcNAc α 1-OMe (**18**) showed no STD signals. This contradiction was resolved later.

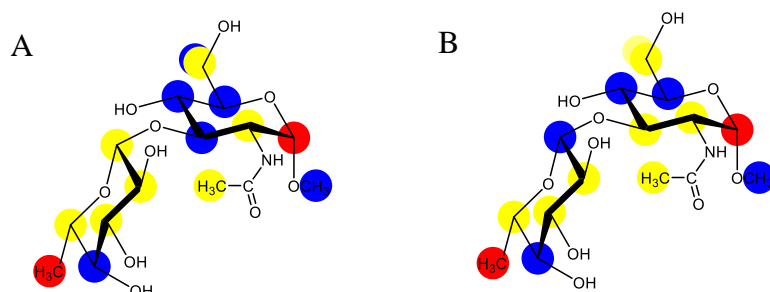


Fig. 53: False-positive epitope maps. Fuc β 1-3GlcNAc α 1-OMe (**21**) with monoclonal antibodies HHH1 (**A**; NMR operator and interpreter: M. Fölsing) and HMM5 (**B**; NMR operator and interpreter: M. Fölsing). Color code: see fig. 51).

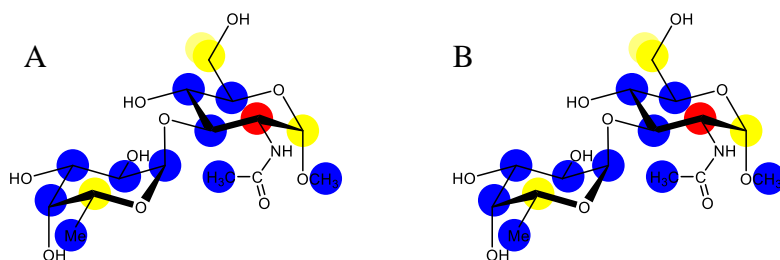


Fig. 54: False-positive epitope maps. dFuc α 1-3GlcNAc α 1-OMe with monoclonal antibody HHH1 (**A**; NMR operator and interpreter: M. Fölsing) and HMM5 (**B**; NMR operator and interpreter: M. Fölsing). Color code: see fig. 51).

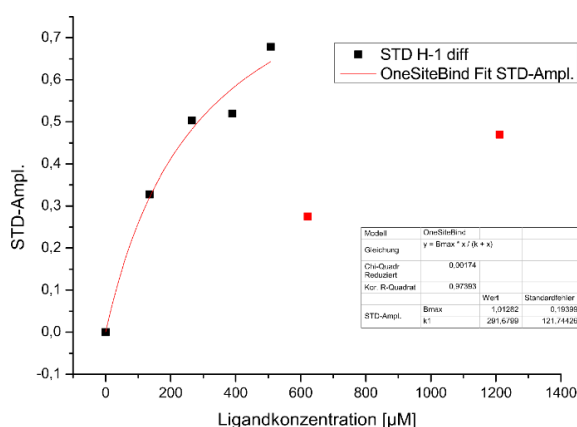
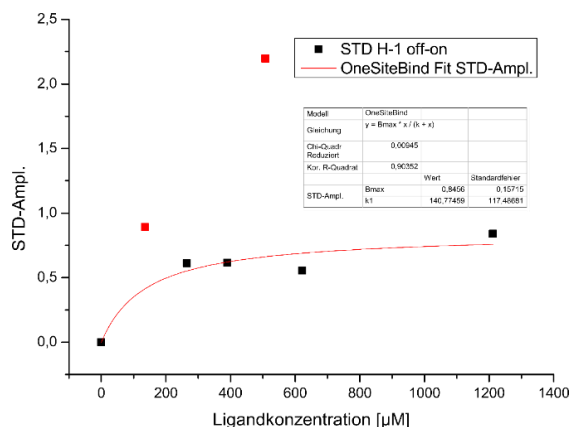


Fig. 55: K_D Determination of HMM5 by titration with Fuc α 1-3GlcNAc (H-1) against the STD amplification. The values of the first and the second analysis deviate strongly: (A) $K_D = 140.8 \mu\text{M} \pm 117.5 \mu\text{M}$, (B) $291.7 \mu\text{M} \pm 121.7 \mu\text{M}$. Fatally, titration points 2 and 5 (A) and 6 and 7 (B) were excluded, seemingly for no statistical reason. However, note that the measured values are affected by a large measuring error and the measuring system no longer meets the stated specifications. NMR operator and interpreter: M. Fölsing.

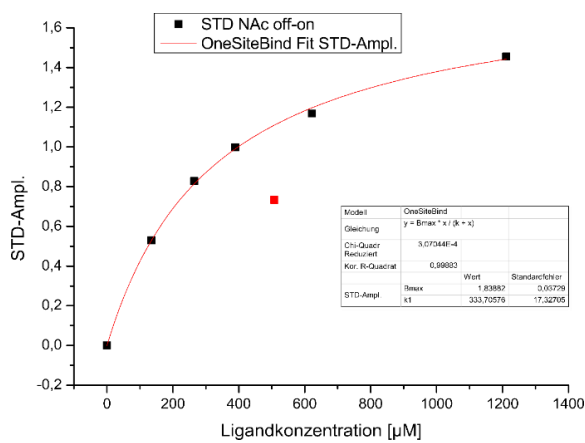
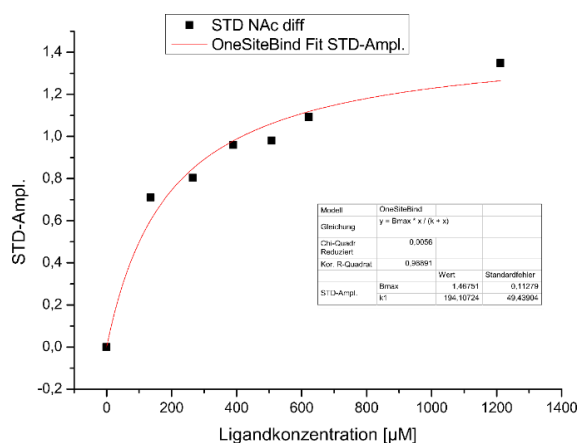


Fig. 56: K_D Determination of HMM5 by titration with Fuc α 1-3GlcNAc (NHAc) against the STD amplification (700 MHz spectrometer). The values of the first and the second analysis deviate strongly: (A) $K_D = 194.1 \mu\text{M} \pm 49.4 \mu\text{M}$, (B) $333.7 \mu\text{M} \pm 17.3 \mu\text{M}$. NMR operator and interpreter: M. Fölsing.

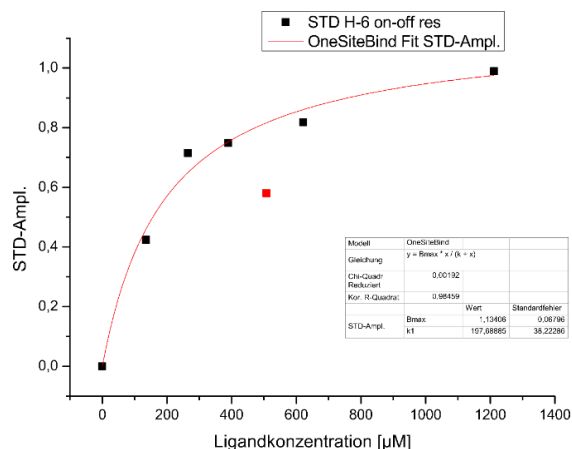
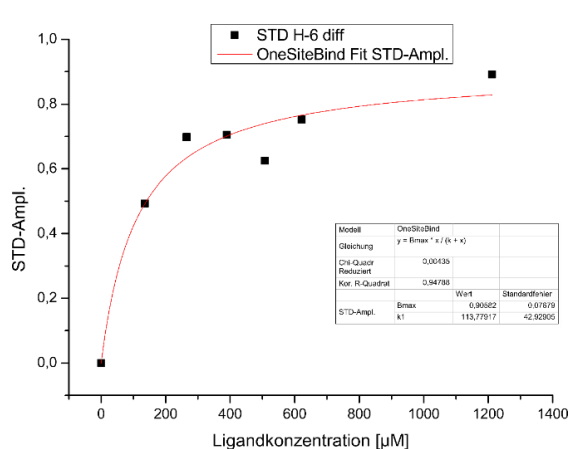


Fig. 57: K_D Determination of HMM5 by titration with Fuc α 1-3GlcNAc (H-6) against the STD amplification (700 MHz spectrometer). The values of the first and the second analysis deviate strongly: (A) $K_D = 113.8 \mu\text{M} \pm 42.9 \mu\text{M}$, (B) $197.7 \mu\text{M} \pm 38.2 \mu\text{M}$. NMR operator and interpreter: M. Fölsing.

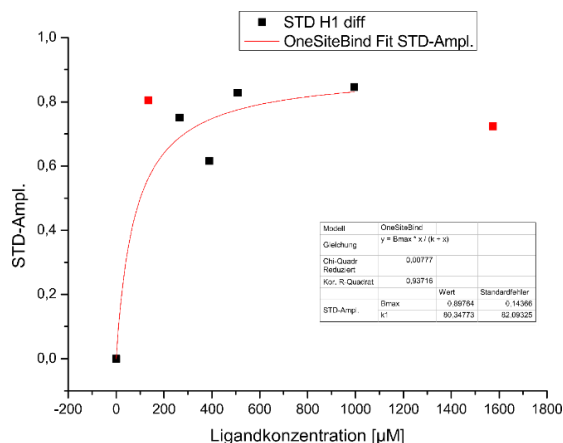
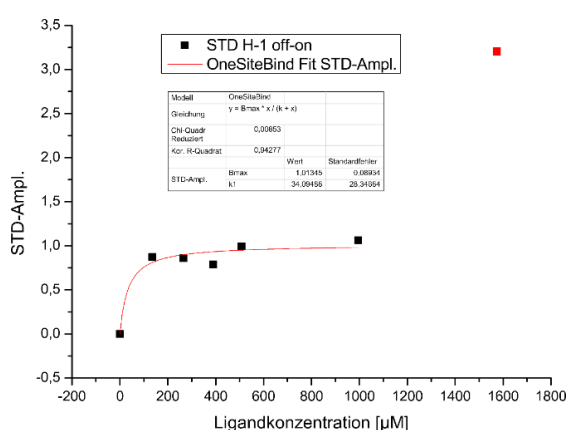


Fig. 58: K_D Determination of HMM5 by titration with Fuc β 1-3GlcNAc (H-1) against the STD amplification. The values of the first and the second analysis deviate strongly: (A) $K_D = 34.1 \mu\text{M} \pm 28.3 \mu\text{M}$, (B) $K_D = 80.3 \mu\text{M} \pm 82.1 \mu\text{M}$. Fatally, titration point 7 (A) was excluded, seemingly for no statistical reason. NMR operator and interpreter: M. Fölsing.

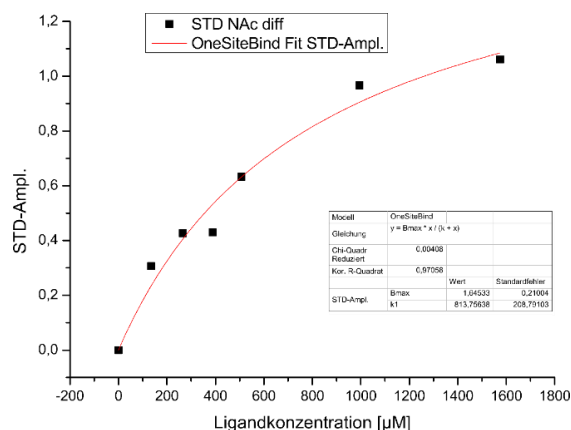
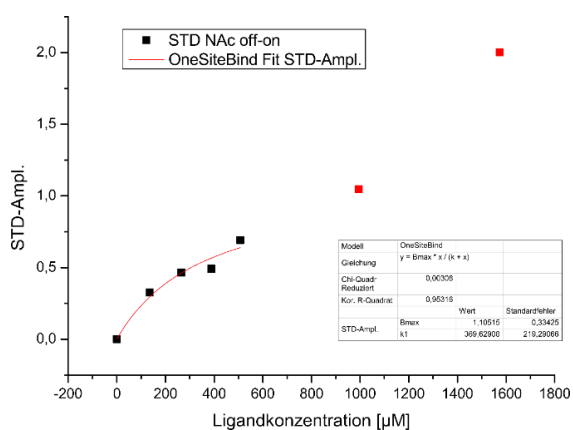


Fig. 59: K_D Determination of HMM5 by titration with Fuc β 1-3GlcNAc (NHAc) against the STD amplification (700 MHz spectrometer). The values of the first and the second analysis deviate strongly: (A) $K_D = 369.6 \mu\text{M} \pm 219.3 \mu\text{M}$, (B) $K_D = 813.8 \mu\text{M} \pm 208.8 \mu\text{M}$. (A) The titration curve shows a linearity but fatally, the K_D value was calculated by exclusion of titration points 6 and 7, seemingly for no statistical reason. NMR operator and interpreter: M. Fölsing.

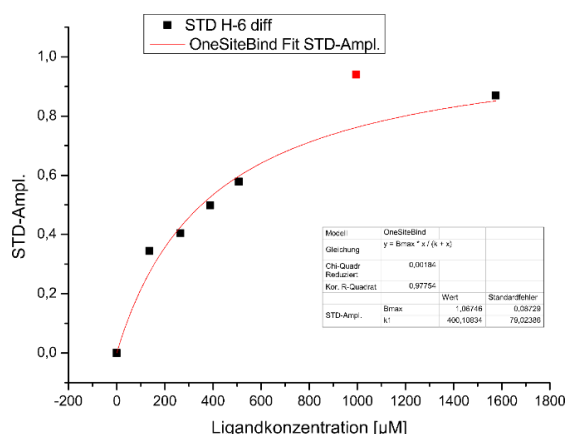
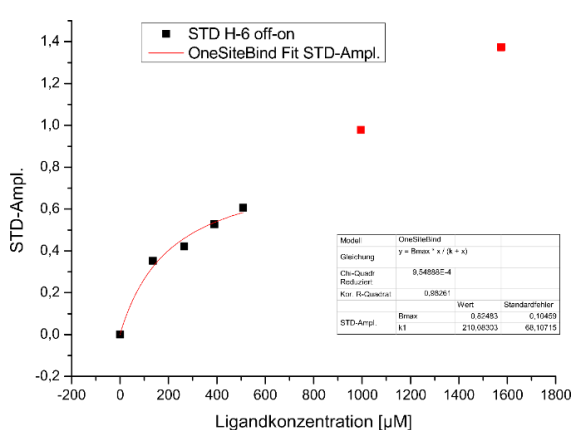


Fig. 60: K_D Determination of HMM5 by titration with Fuc β 1-3GlcNAc (H-6) against the STD amplification (700 MHz spectrometer). (A) $K_D = 210.1 \mu\text{M} \pm 68.1 \mu\text{M}$, (B) $K_D = 400.1 \mu\text{M} \pm 79.0 \mu\text{M}$. (A) The titration curve shows a linearity but fatally, the K_D value was calculated by exclusion of titration points 6 and 7, seemingly for no statistical reason. NMR operator and interpreter: M. Fölsing.

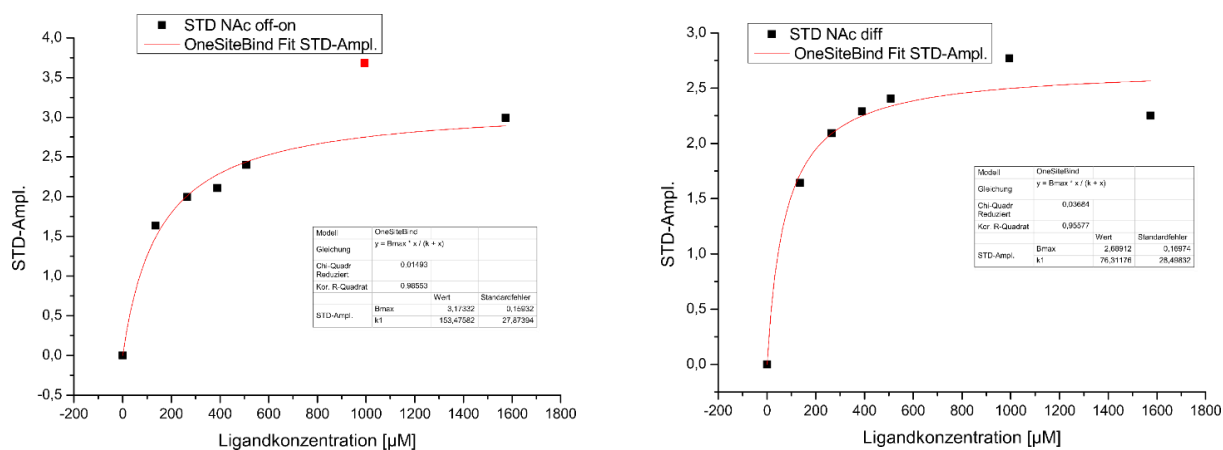


Fig. 61: K_D Determination of HMM5 by titration with dFuc α 1-3GlcNAc (NHAc) against the STD amplification (700 MHz spectrometer). The values of the first and the second analysis deviate strongly: (A) $K_D = 153.5 \mu\text{M} \pm 27.9 \mu\text{M}$, (B) $K_D = 76.3 \mu\text{M} \pm 28.5 \mu\text{M}$. NMR operator and interpreter: M. Fölsing.

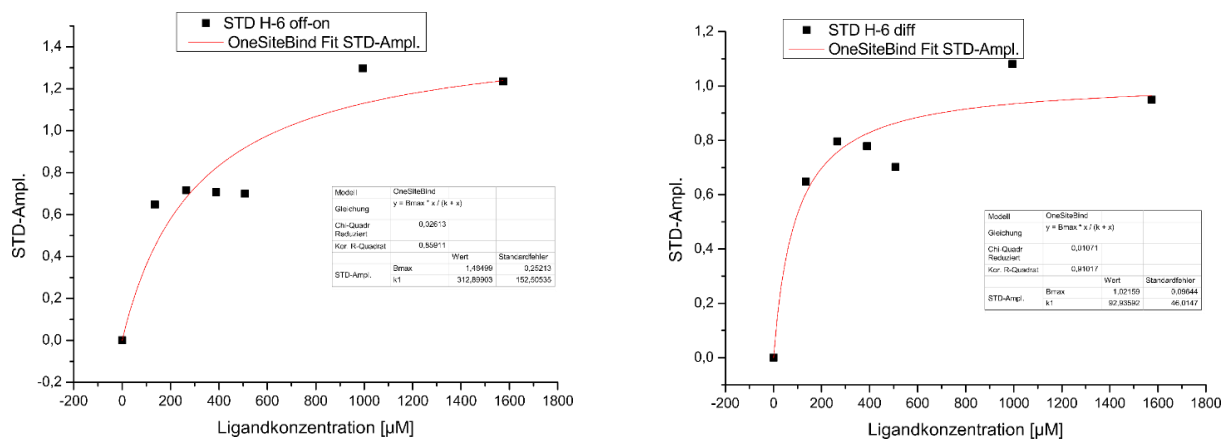


Fig. 62: K_D Determination of HMM5 by titration with dFuc α 1-3GlcNAc (H-6) against the STD amplification (700 MHz spectrometer). The values of the first and the second analysis deviate strongly: (A) $K_D = 312.9 \mu\text{M} \pm 152.5 \mu\text{M}$, (B) $K_D = 92.9 \mu\text{M} \pm 46.0 \mu\text{M}$. NMR operator and interpreter: M. Fölsing.

Table 6: False-positive K_D values of Fuc α 1-3GlcNAc α 1-OMe and Fuc β 1-3GlcNAc α 1-OMe in interaction with HMM5. For the trisaccharide Fuc α 1-3(Fuc α 1-6)GlcNAc α 1-OMe no STD effects were detected (true-negative). The lowest K_D value was chosen as allegedly best representation.

Ligand	K_D / mmol/L (700 MHz)	K_D / mmol/L (600 MHz)
Fuc α 1-3GlcNAc α 1-OMe	113.8 \pm 42.9 (H-6)	1.3 \pm 1.1 (H-5')
	197.7 \pm 38.2 (H-6)	1.8 \pm 0.3 (NHCOCH ₃)
Fuc β 1-3GlcNAc α 1-OMe	34.1 \pm 28.3 (H-1)	1.6 \pm 0.5 (NHCOCH ₃)
	80.3 \pm 82.1 (H-1)	
dFuc α 1-3GlcNAc α 1-OMe	312.9 \pm 152.5 (H-6)	n.d.
	92.9 \pm 46.0 (H-6)	

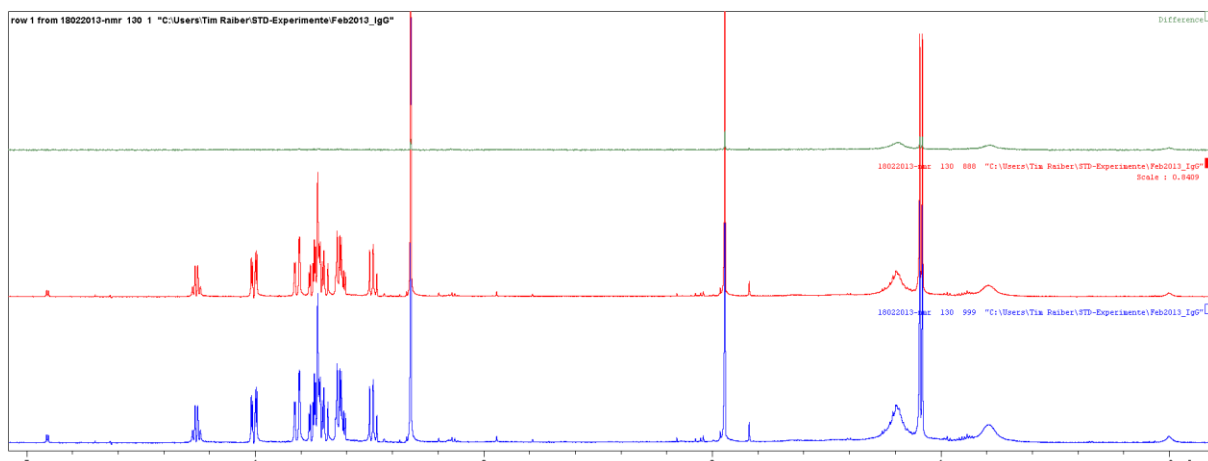


Fig. 63A: Stack plot of off (blue), on (red) and difference spectrum (green) showing polyclonal anti-rabbit IgG in interaction with Fucc α 1-3GlcNAc α 1-OMe. NMR operator: T. Hackl, NMR interpreter (re-evaluation, this fig.): T. Raiber.

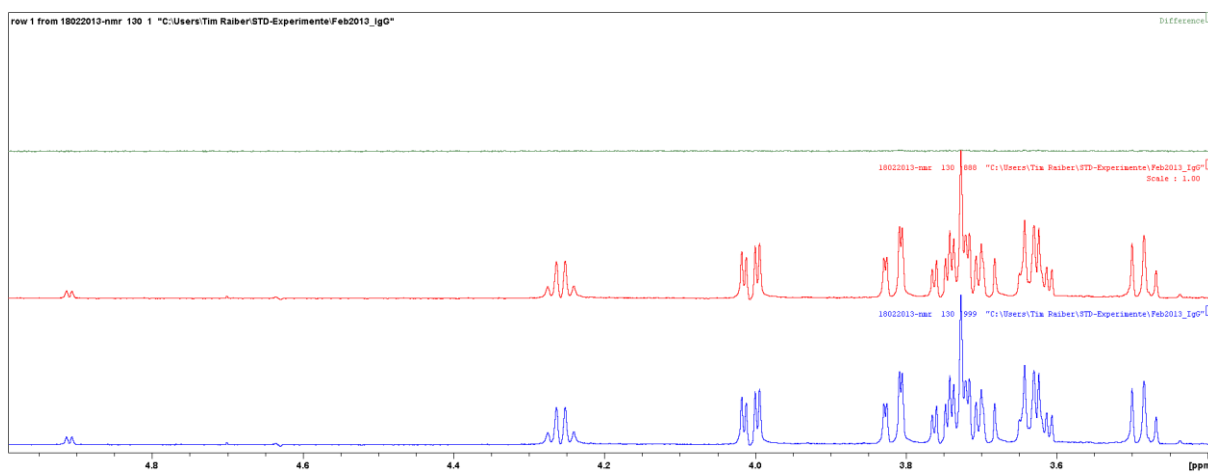


Fig. 63B: Expanded region of fig. 63A.

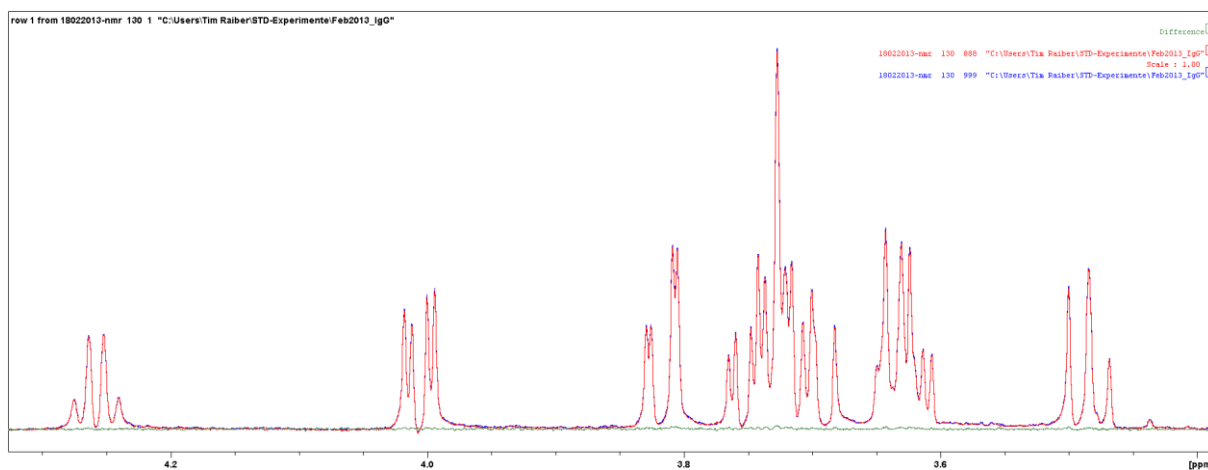


Fig. 63C: Overlay plot of off (blue), on (red) and difference (green) spectrum of fig. 63A showing the ring proton region.

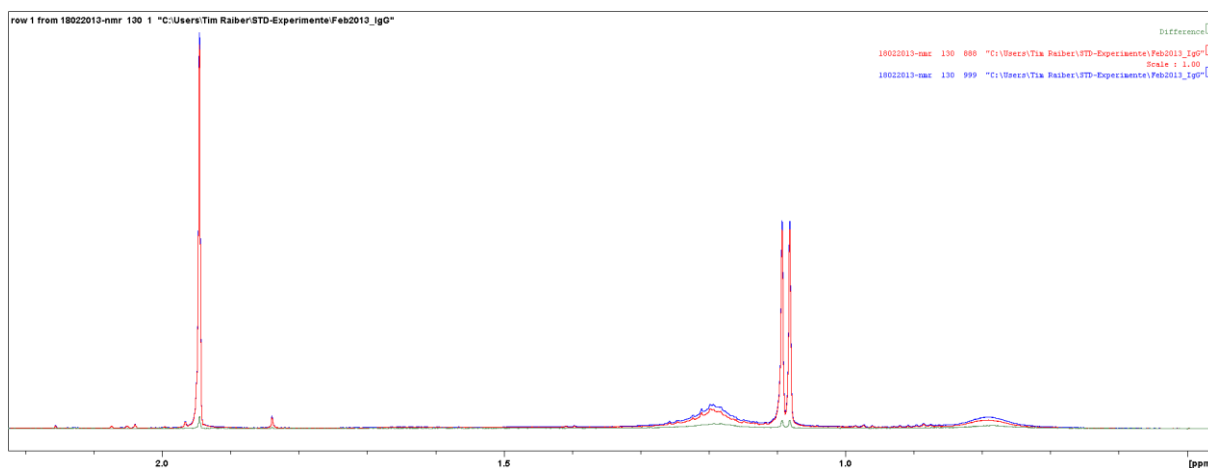


Fig. 63D: Overlay plot of off (blue), on (red) and difference (green) spectrum of fig. 63A showing NHC(O)CH_3 , H-6' and the protein signals.

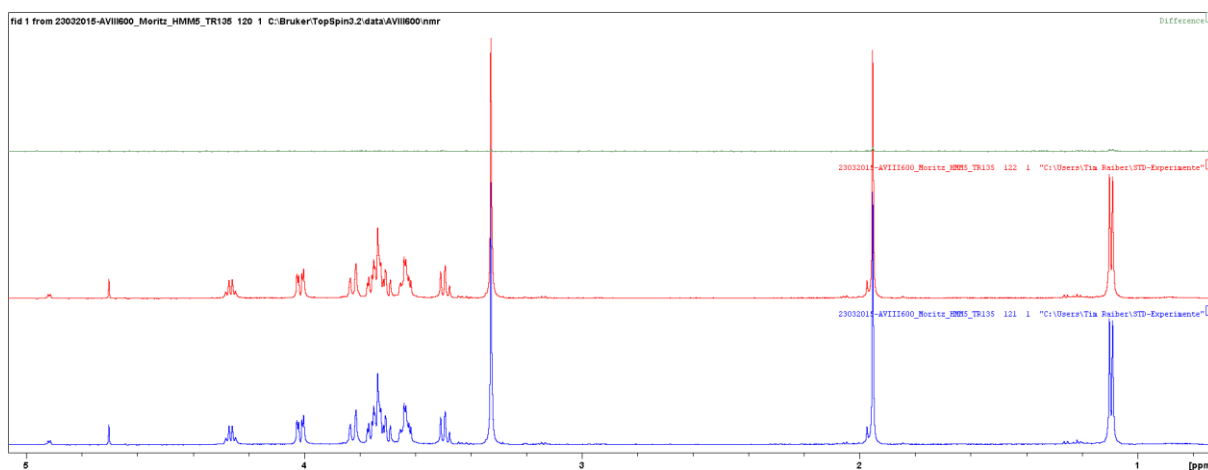


Fig. 64A: Stack plot of off (blue), on (red) and difference spectrum (green) showing HMM5 in no interaction with $\text{Fuc}\alpha 1\text{-3GlcNAc}\alpha 1\text{-OMe}$. NMR operator and interpreter (epitope map): M. Fölsing, NMR interpreter (re-evaluation, this fig.): T. Raiber.

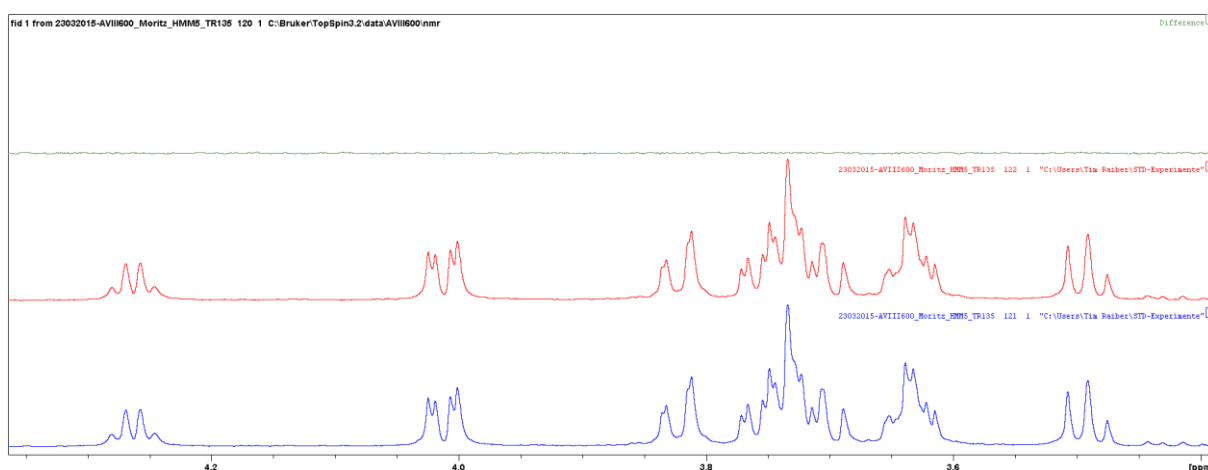


Fig. 64B: Expanded region of fig. 64A.

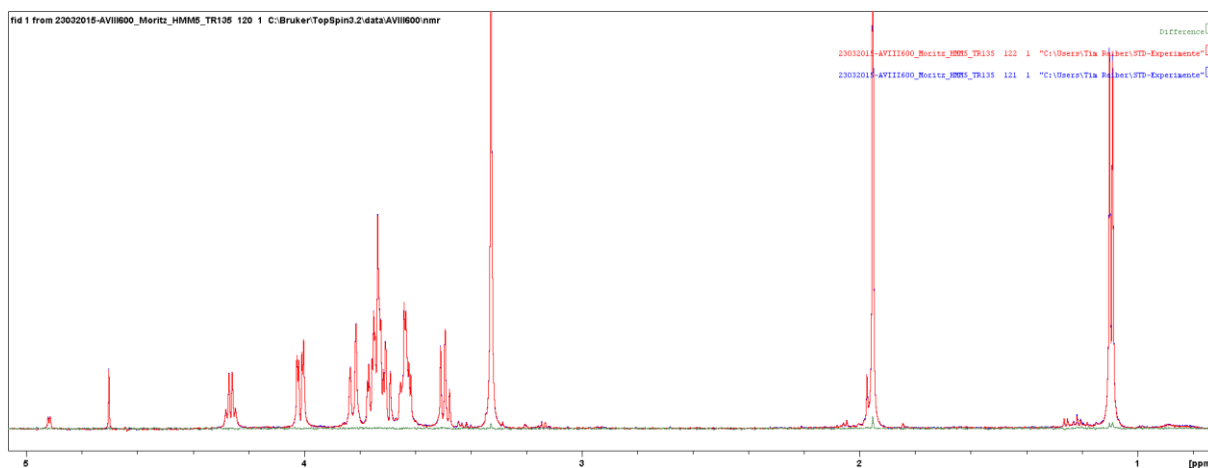


Fig. 64C: Overlay plot of the spectra shown in fig. 64A.

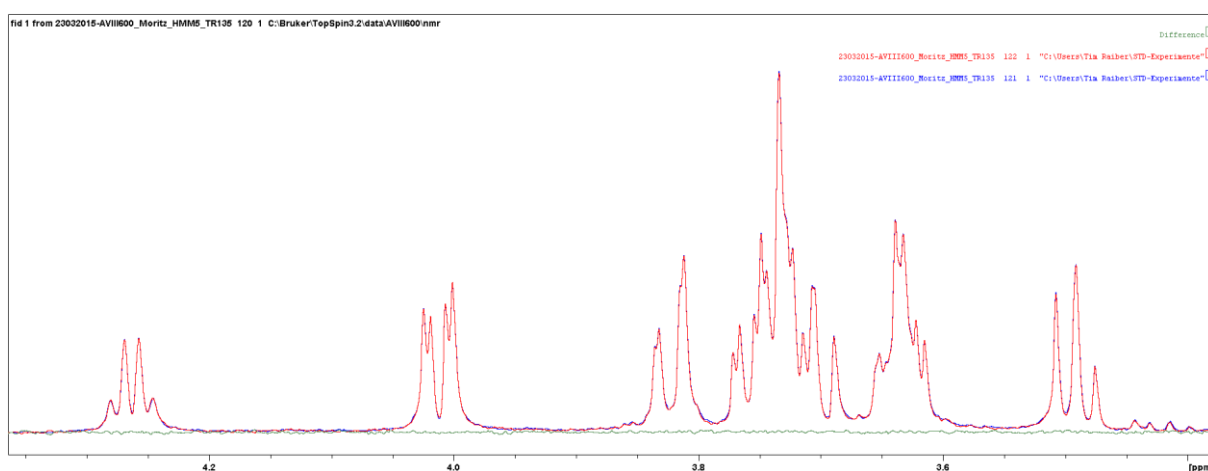


Fig. 64D: Expanded region of the overlay plot shown in fig. 64C.

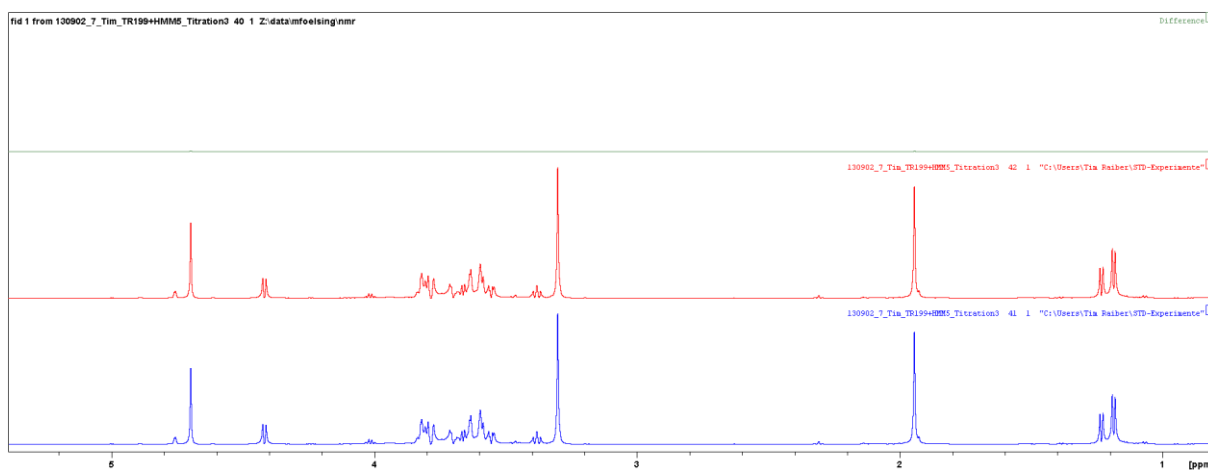


Fig. 65A: Stack plot of off (blue), on (red) and difference spectrum (green) showing Fucβ1-3GlcNAcα1-OME in no interaction with HMM5. NMR operator and interpreter (epitope map): M. Fölsing, NMR interpreter (re-evaluation, this fig.): T. Raiber.

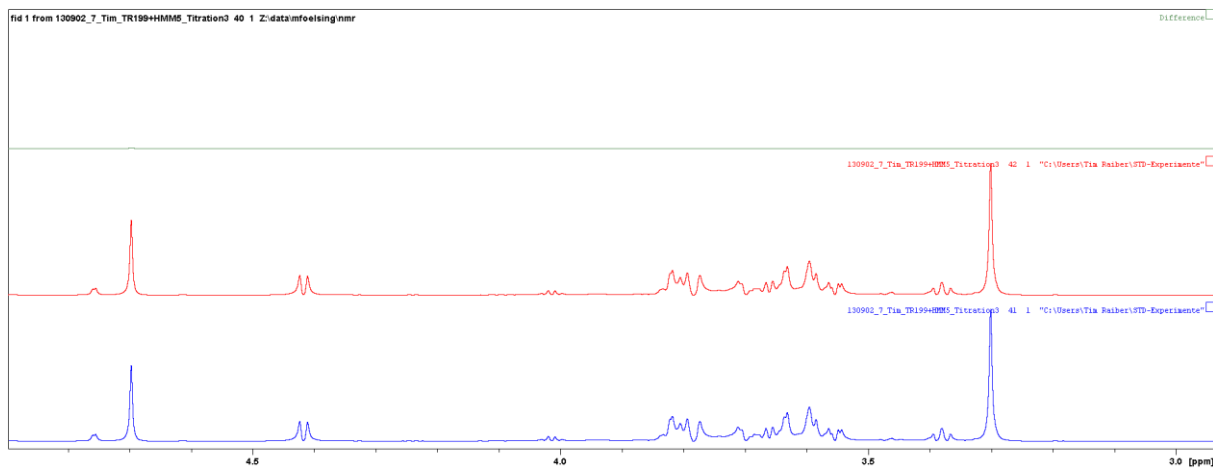


Fig. 65B: Expanded region of the stack plot shown in fig. 65A.

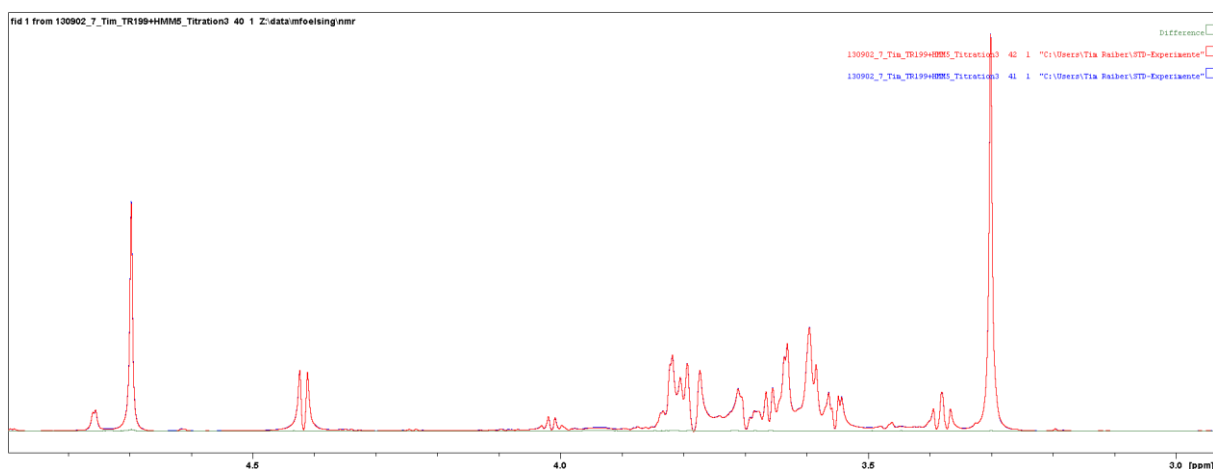


Fig. 65C: Overlay plot of the same expanded region as shown in fig. 65B.

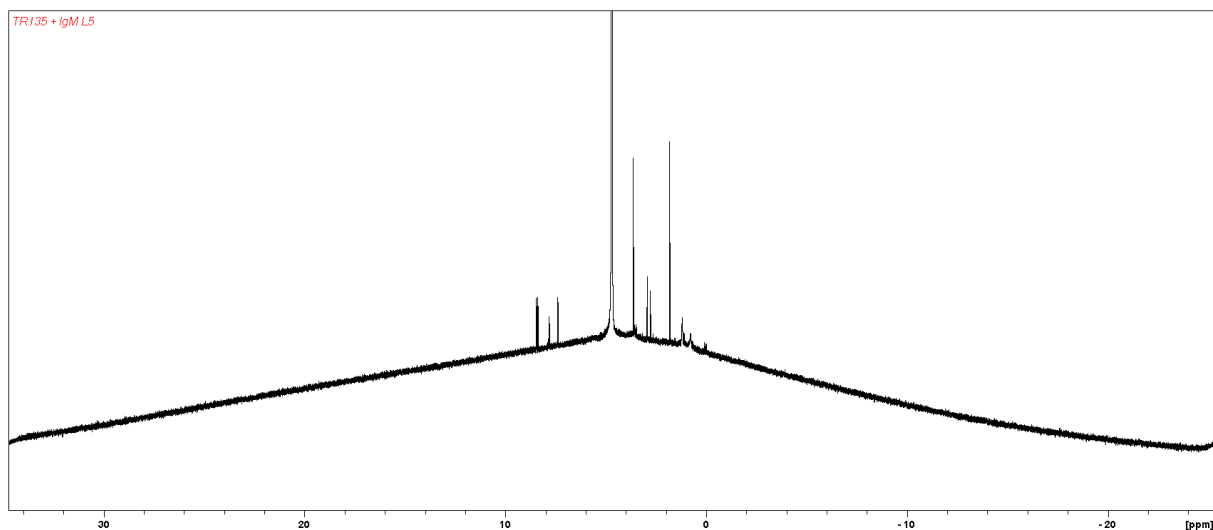


Fig. 66: ^1H spectrum of the mixture Fuca1-3GlcNAc1-OMe and the anti-Le^x rat IgM L5 (MW = 900 kDa). Due to the baseline artefact and presence of protein signals, a STD NMR experiment was not carried out (NMR operator: T. Hackl). The larger the protein the better the T1 ρ filter should actually function but due to unknown reasons the protein signals still appeared. Unnecessarily, the spectral window was set very large. NMR interpreter: T. Raiber.

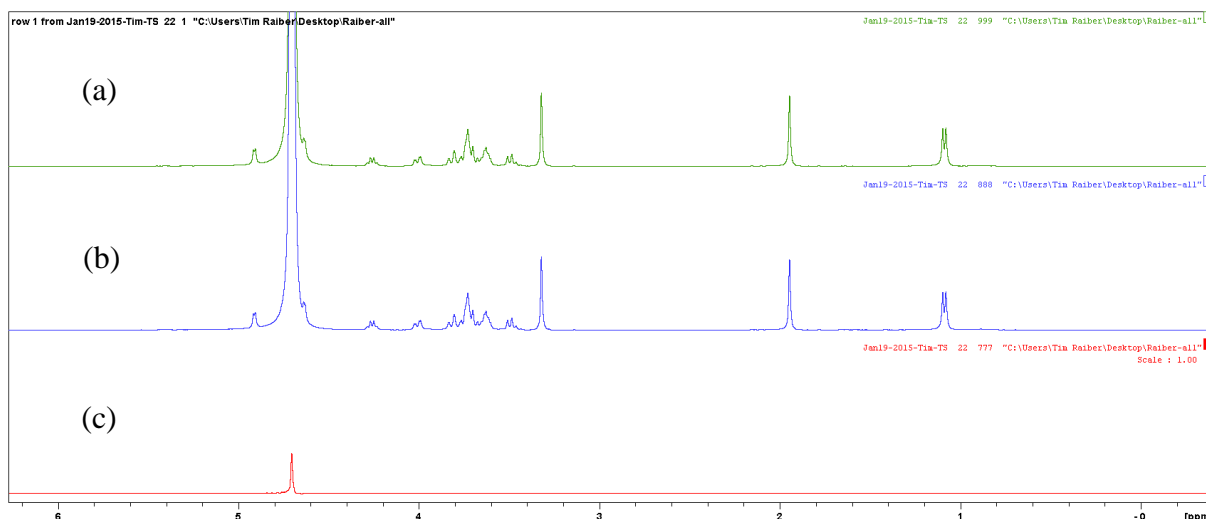


Fig. 67: STD NMR experiment of Fuc α 1-3GlcNAc α 1-OME in the presence of HMM5 antibody (double-check). Saturation with an attenuation of 40 dB and a total saturation time of 2 s. (a) on: +7.25 ppm, (b) off: -25 ppm. The difference spectrum (c) shows no STD effects. 400 MHz spectrometer (Bruker), NMR interpreter: T. Raiber.

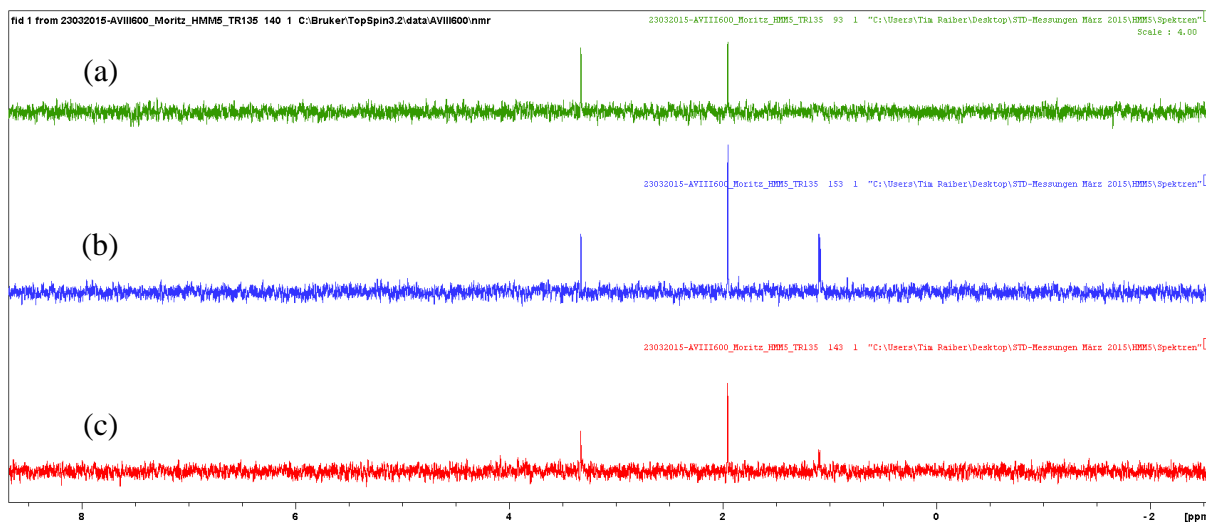


Fig. 68: STD NMR negative control (Fuc α 1-3GlcNAc without receptor). At all chosen irradiation positions, artefacts were detected: (a) difference spectrum (green), +7.35 ppm, 4 s; (b) difference spectrum (blue), -0.5 ppm, 4 s; (c) -1.5 ppm, 2 s (red). NMR operator: M. Fölsing, NMR interpreter (re-evaluation, this fig.): T. Raiber.

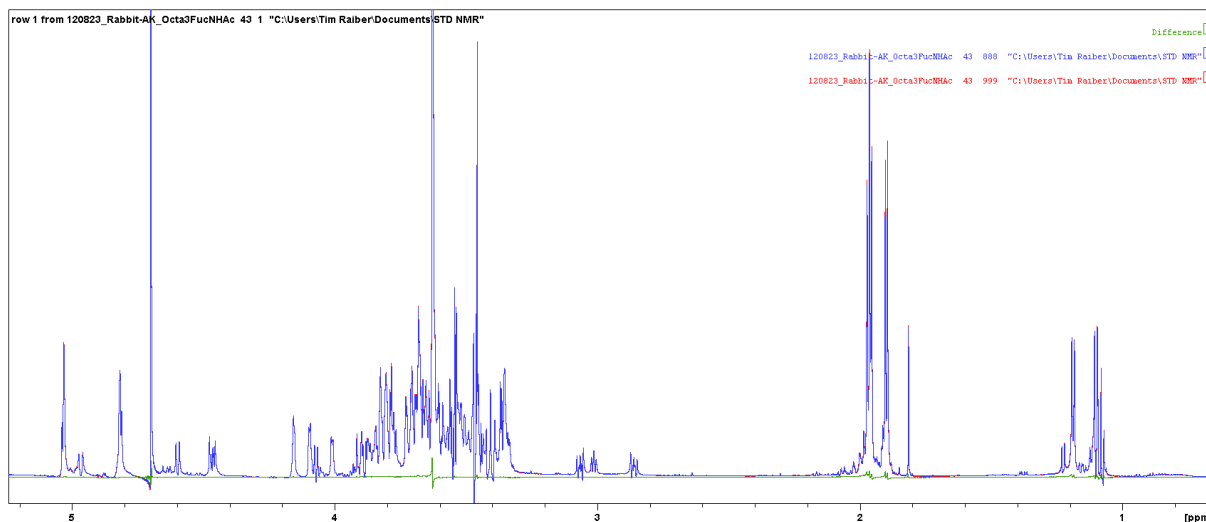


Fig. 69: STD NMR spectrum (green) of nonasaccharide (~1.0 mM) and anti-HRP rabbit IgG (~3.0 mg/mL). Off- (red) and on- (blue) resonance spectra are superimposed. Based on these data, an interaction is highly questionable. NMR operator and interpreter (epitope map): M. Kötzler, NMR interpreter (re-evaluation, this fig.). T. Raiber.

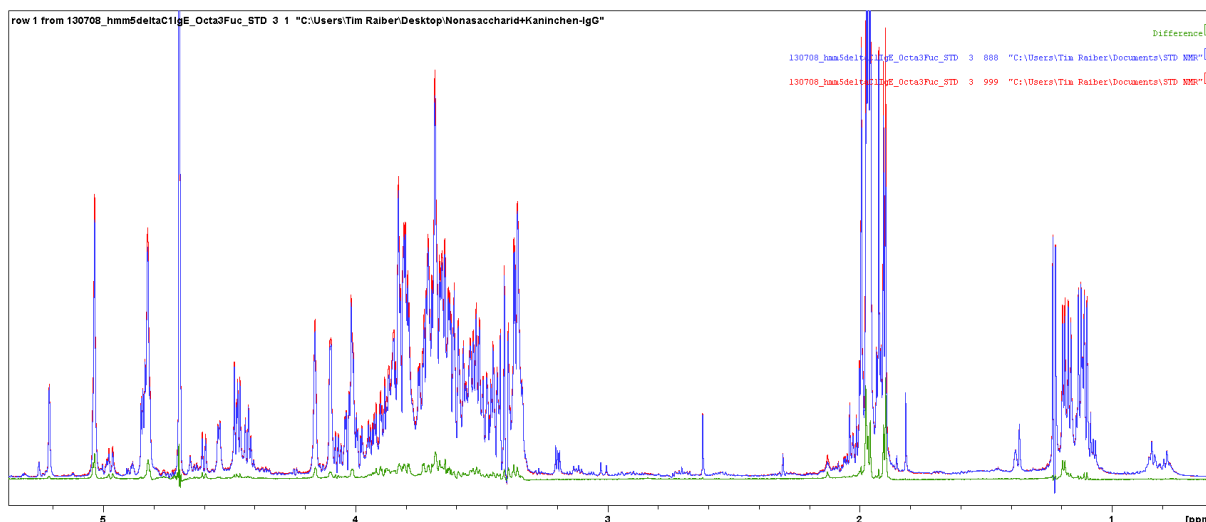


Fig. 70: STD NMR spectrum (green) of nonasaccharide (0.8 mM) and HMM5 Δ C1IgE antibody (1 mg) showing STD effects. Off- (red) and on- (blue) resonance spectra are superimposed. NMR operator and interpreter (epitope map): M. Kötzler, NMR interpreter (re-evaluation, this fig.): T. Raiber.

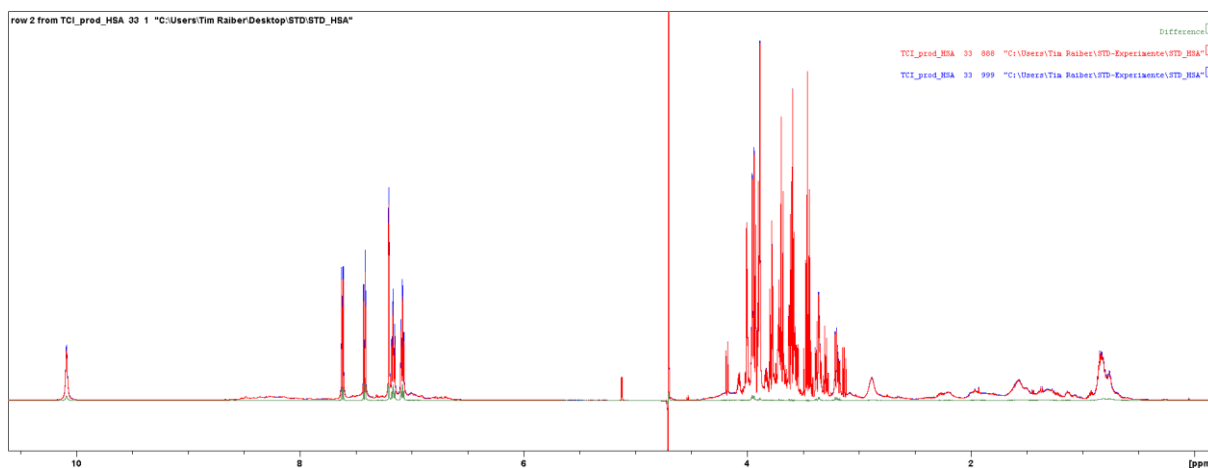


Fig. 71A: Overlay plot of off (blue), on (red) and difference (green) spectra as extracted from STD NMR data set of Trp in clear interaction with HSA. The carbohydrate (4.0 - 3.5 ppm) is not binding. NMR data were kindly provided by F. Schumann (*Bruker BioSpin*); NMR interpreter: T. Raiber.

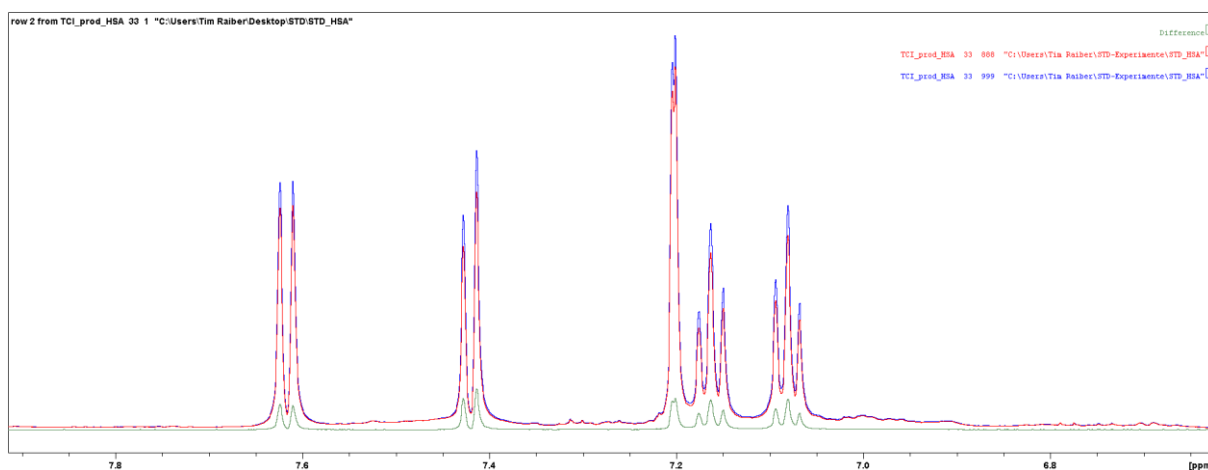


Fig. 71B: Expanded region of the overlay plot shown in fig. 71A. Clear STD effects are observable.

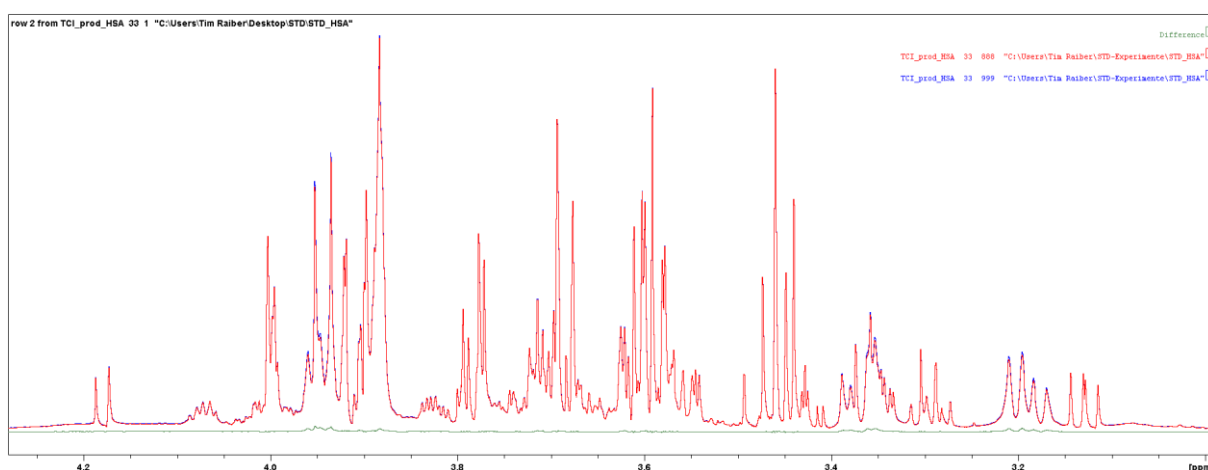


Fig. 71C: Expanded region of the overlay plot shown in fig. 71A. The carbohydrate (sucrose) is not binding. Only very weak negligible artefacts are observable.

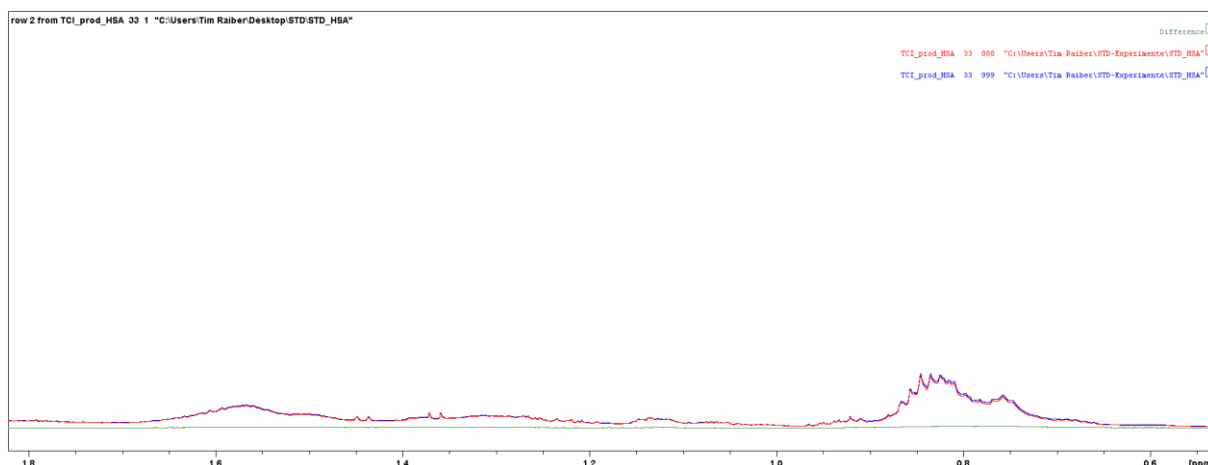


Fig. 71D: Expanded region of the overlay plot shown in fig. 71A. The protein signals are quite congruent and thus its difference almost zero. The congruence of the protein signals is a very good indicator for the stability of the system.

6.2.1.4.3. STD Effects of CCD Fragments Statistically Insignificant

The misinterpretation of the STD NMR data generated in this study demonstrates the necessity of control experiments. In addition, STD NMR data need be validated by a statistical method. As a first approach, a *limit of detection* (LOD) and a *limit of quantification* (LOQ), as introduced by Currie in 1968, are suggested (eq. 11 and 12, fig. 72).^{114, 115, 116, 117, 118}

$$\mathbf{LOD} = \mathbf{y_B} + \mathbf{3.3} \sigma_B \quad (\text{eq. 11})$$

$$\mathbf{LOQ} = \mathbf{y_B} + \mathbf{10} \sigma_B \quad (\text{eq. 12})$$

with y_B = average of the background signal

σ_B = standard deviation of the background signal

An important criterion for accurate integrations (notably, epitope mapping is based on peak integrations) is the signal to noise ratio (S/N). In NMR experiments, the number of scans (ns) directly influences the signal to noise ratio: $S/N \sim \sqrt{ns}$ (*i.e.*, four times more scans double the signal to noise ratio). As generally known, a spectrum should have an S/N of at least 250:1 for the smallest peak to be integrated. Because the noise can be described as an oscillation around an average, the average of the background signal (y_B) may be set to zero. Hence, the error of a resonance signal is the standard deviation of the noise and may be approximated as half the noise amplitude. Consequently, with $y_B = 0$ and $\sigma_B \approx \frac{1}{2} (N_{pp})$, the limit of detection of an STD effect is suggested by eq. 13.

$$\mathbf{LOD} (\mathbf{A_{STD}}) \approx \mathbf{3.3} \cdot \frac{\mathbf{1}}{\mathbf{2}} (\mathbf{N_{pp}}) \quad (\text{eq. 13})$$

Since STD effects shall be quantified for epitope mapping and K_D determination, such values need to be statistically validated by the limit of quantification (LOQ) as suggested by eq. 14.

$$\text{LOQ (A}_{\text{STD}}) \approx 10 \cdot \frac{1}{2} (\text{N}_{\text{pp}}) \quad (\text{eq. 14})$$

Eq. 14 was applied to STD data provided by *Bruker BioSpin* (fig.s 73 A and B) and then to all STD NMR spectra of this study (fig.s 74-76).

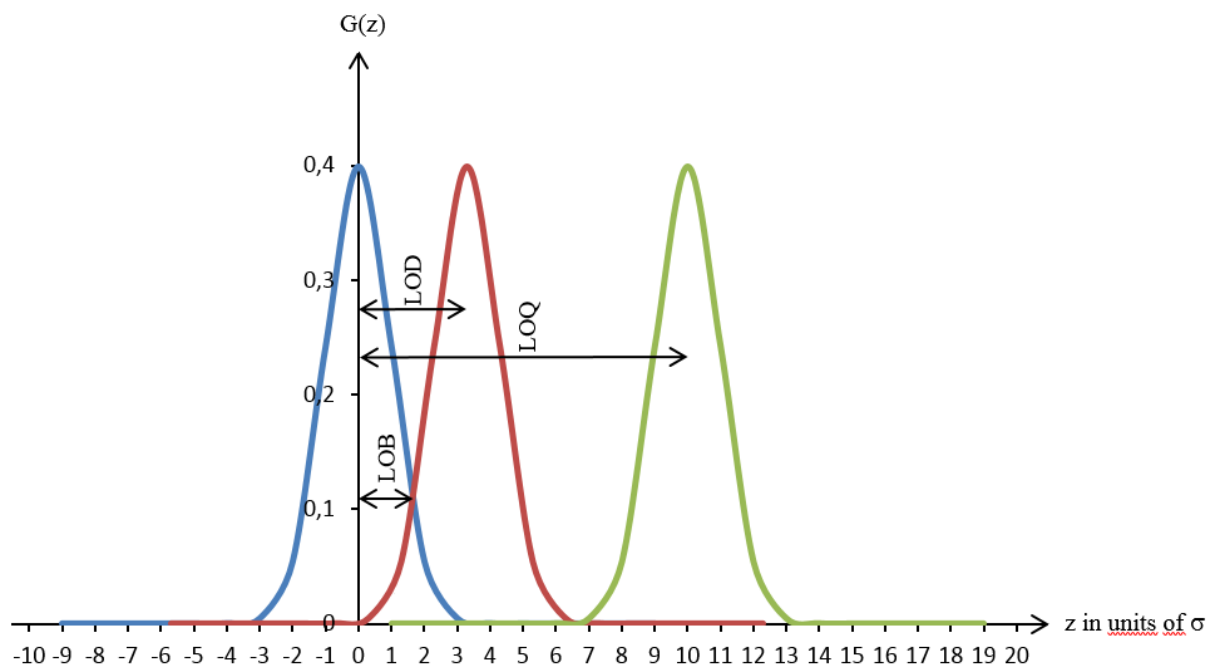


Fig. 72: Limits for detection (LOD) and determination (LOQ) with $G =$ Gaussian distribution and $\sigma =$ standard deviation. The limit of blank (LOB) is estimated by measuring replicates of a blank sample and calculating the standard deviation. Assuming a Gaussian distribution, it represents 95 % of the observed values. The remaining 5 % of blank values represent a response that could actually be generated by a sample containing a very low concentration of analyte. Statistically, this false positivity is known as type I error.

The STD effects assigned to the ring protons of the CCD fragments are smaller than $10 \sigma_B$ and therefore statistically insignificant. Hence, all epitope maps and K_D values determined for the CCD fragments must be rated as false positives. Remarkably, this rejection is independent of the presence of artefacts, which affect mostly singlet signals and signals nearby the on-resonance irradiation. Obviously, the signal to noise ratio plays a key role in the significance of STD NMR data. Thus, in case of doubt, an increase of the number of scans may be indicated. However, applying the limit of quantification on STD effects should help to place STD NMR interpretations on statistically firm ground. It has not escaped notice that signals may fall below the LOQ or even vanish into the noise due to H,H-coupling. Therefore, an “instant homonuclear broadband decoupling” according to Zangger is to be suggested, “which leads to a collapse of ^1H signals into singlets” and improves the sensitivity of STD NMR spectroscopy by a multiple.¹¹⁹ To decouple the direct dimension, the acquisition is interrupted approximately every $1/3 \ ^3J_{\text{H,H}}$ to send in a ZS-decoupling block. Recently, Aguilar *et al.* have shown that H,H-

decoupling results in an increase of sensitivity comparable with a conventional ^1H NMR experiment measured at 5 GHz.¹²⁰

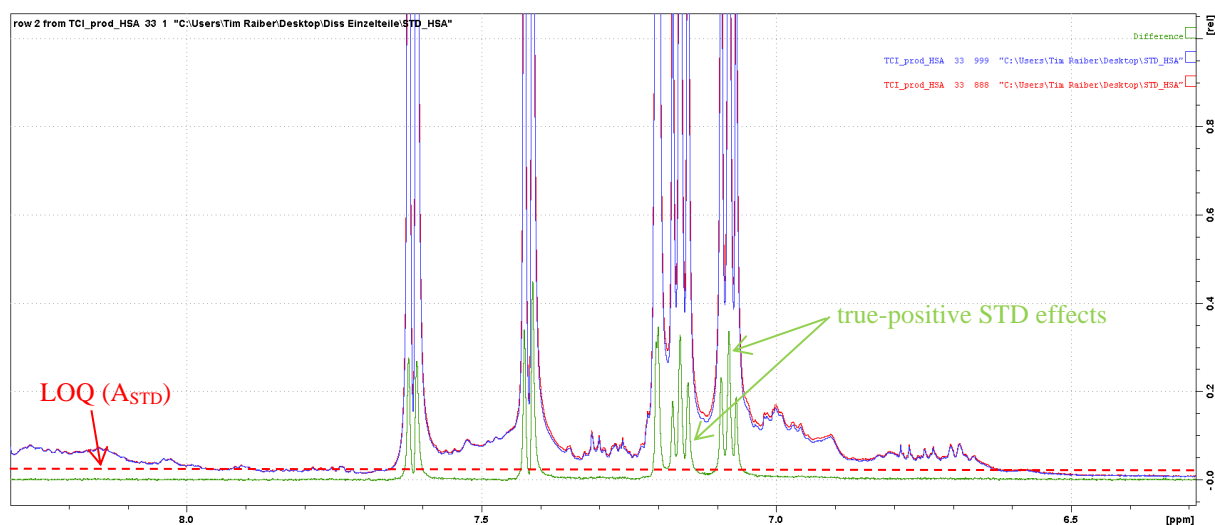


Fig. 73A: Suggested LOQ for STD effects (red dashed line) at the example of HSA/Trp (600 MHz, on: -1.0 ppm, off: -40 ppm, 36 dB, 2 s, $T_{1\rho} = 30$ ms). The limit was calculated according to eq. 14. The difference signals exceed the LOQ and are thus significant STD effects. NMR data were kindly provided by F. Schumann (*Bruker BioSpin*), NMR interpreter: T. Raiber.

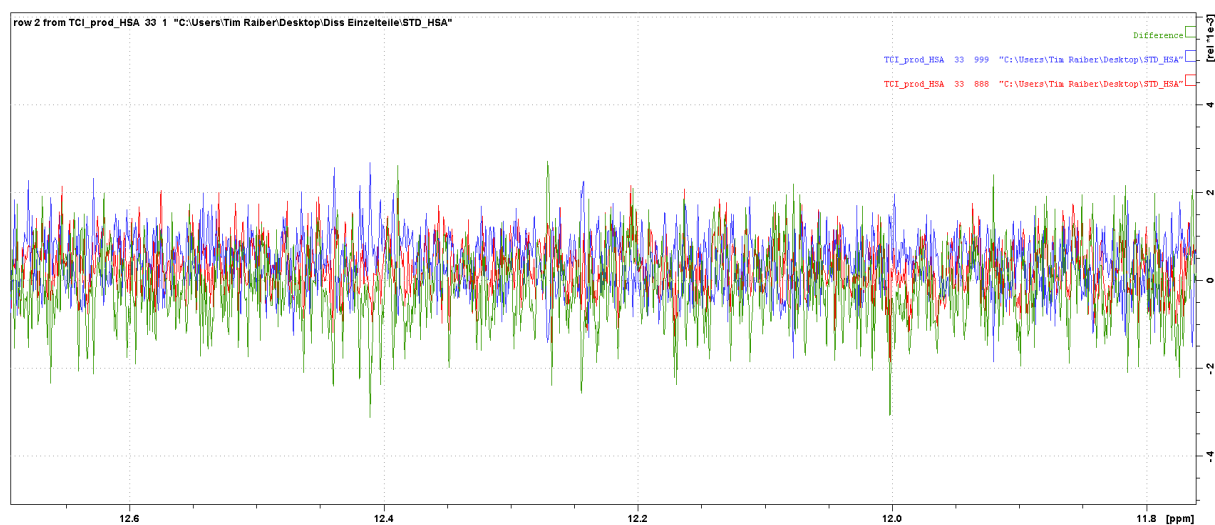


Fig. 73B: Determination of N_{pp} for the STD NMR difference spectrum of HSA / Trp ($N_{pp} \approx 0.005$, $LOQ \approx 0.025$). NMR data were kindly provided by F. Schumann (*Bruker BioSpin*), NMR interpreter: T. Raiber.

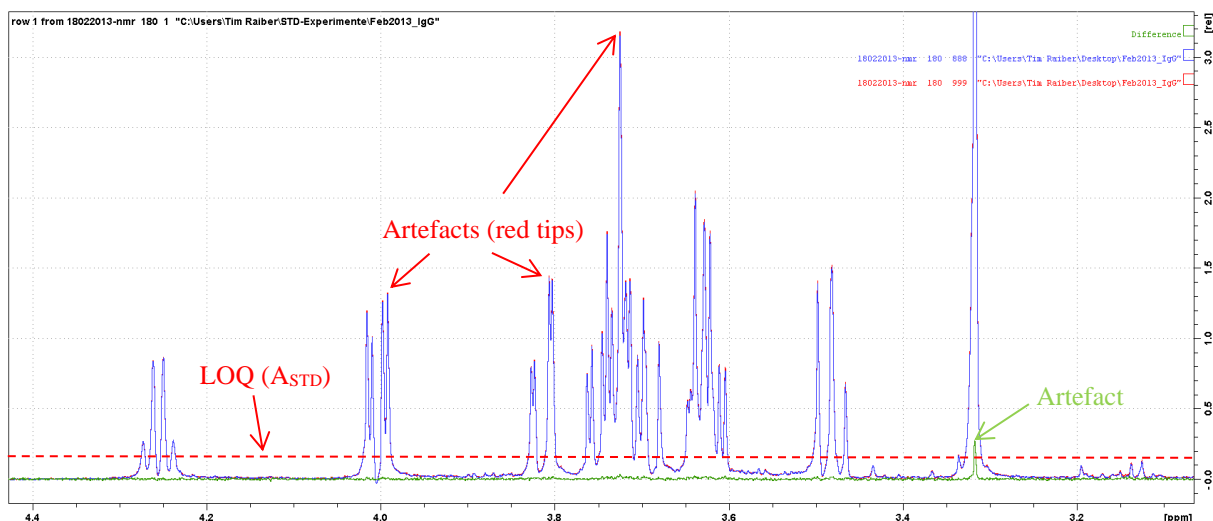


Fig. 74A: Suggested LOQ for STD effects (red dashed line) at the example of polyclonal anti-HRP rabbit IgG / Fuc α 1-3GlcNAc. The limit was calculated according to eq. 14. The difference of the carbohydrate ring proton signals falls below the LOQ and does not permit an epitope mapping. NMR operator (T. Hackl), NMR interpreter (epitope map): M. Kötzer, NMR interpreter (re-evaluation, this fig.): T. Raiber.

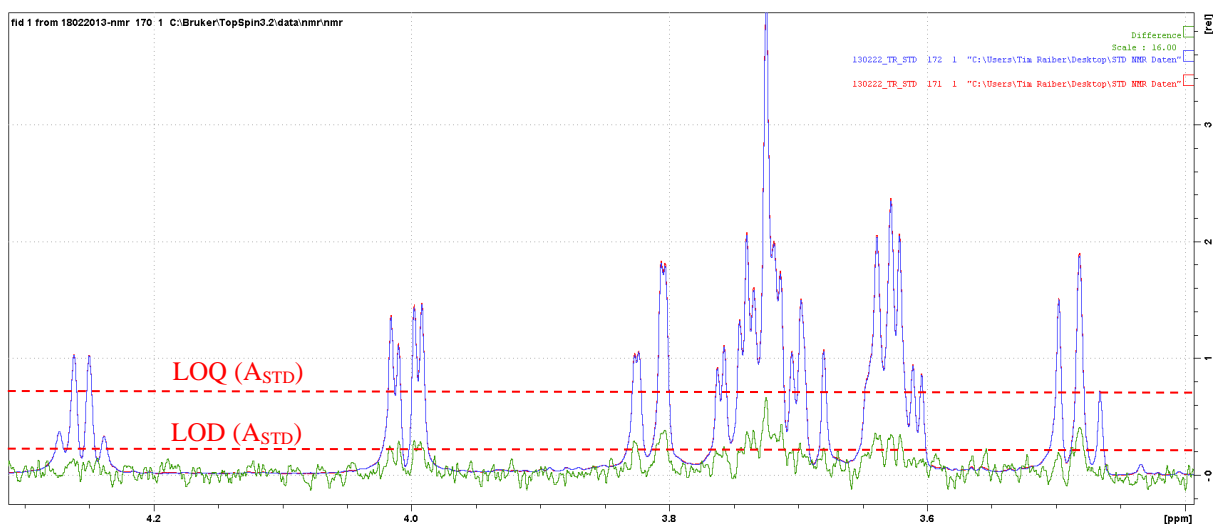


Fig. 74B: Suggested LOQ for STD effects (red dashed line) at the example of polyclonal rabbit IgG / Fuc α 1-3GlcNAc (600 MHz, on: -1.0 ppm, off: +67 ppm, 20 dB, *i.e.*, far outside the recommended range). The limits were calculated according to eq.s 13 and 14. The difference of the carbohydrate ring proton signals is 16-fold upscaled. It falls below the LOQ and does not allow an epitope mapping. But it exceeds the LOD and thus there are in fact statistically significant, albeit very weak STD effects. NMR operator T. Hackl, NMR interpreter (epitope map): M. Kötzer, NMR interpreter (re-evaluation, this fig.): T. Raiber.

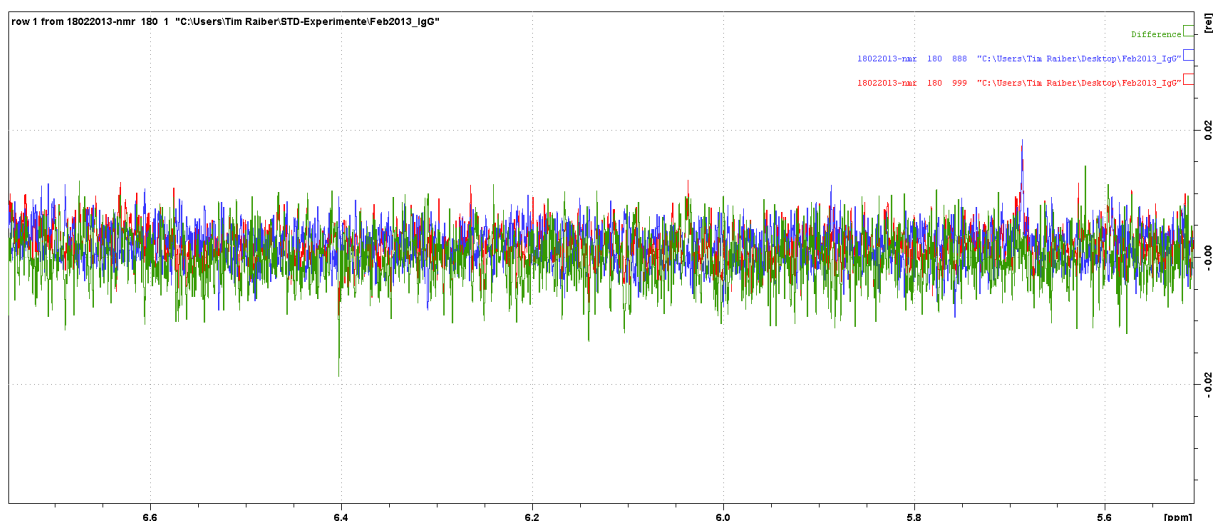


Fig. 74C: Determination of N_{pp} for the STD NMR difference spectrum of polyclonal rabbit IgG / Fuc α 1-3GlcNAc. ($N_{pp} \approx 0.03$, $LOQ \approx 0.15$). NMR operator: T. Hackl, NMR interpreter (epitope map): M. Kötler, NMR interpreter (re-evaluation, this fig.): T. Raiber.

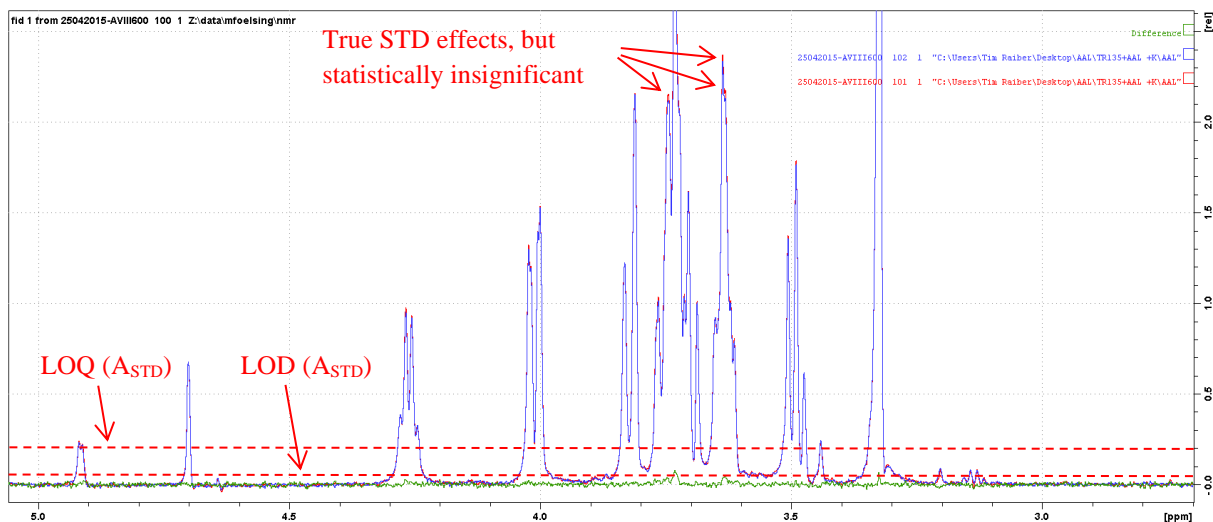


Fig. 75A Suggested LOQ for STD effects (red dashed line) at the example of AAL / Fuc α 1-3GlcNAc. The limit was calculated according to eq. 14. The difference of the carbohydrate ring proton signals falls below the LOQ and does not permit an epitope mapping. AAL was originally intended to serve as positive control but even the LOD is not exceeded and thus the STD effects, which are visible in the overlay plot are in fact statistically insignificant. Seen retrospectively, CCL2 from *Coprinopsis cinerea* might be a better positive control because it is known to recognize the trisaccharide GlcNAc β 1-4(Fuc α 1-3)GlcNAc. NMR operator: M. Fölsing, NMR interpreter (re-evaluation, this fig.): T. Raiber.

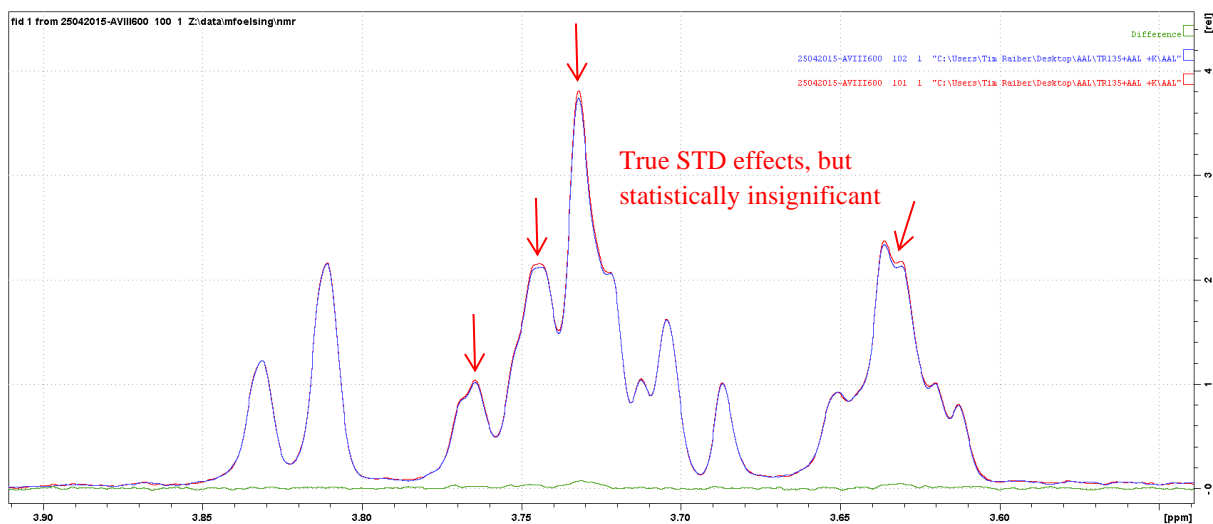


Fig. 75B: Section of the STD NMR spectrum of AAL / Fuc α 1-3GlcNAc (fig. 75A). The STD effects, which are visible in the overlay plot are true but statistically insignificant.

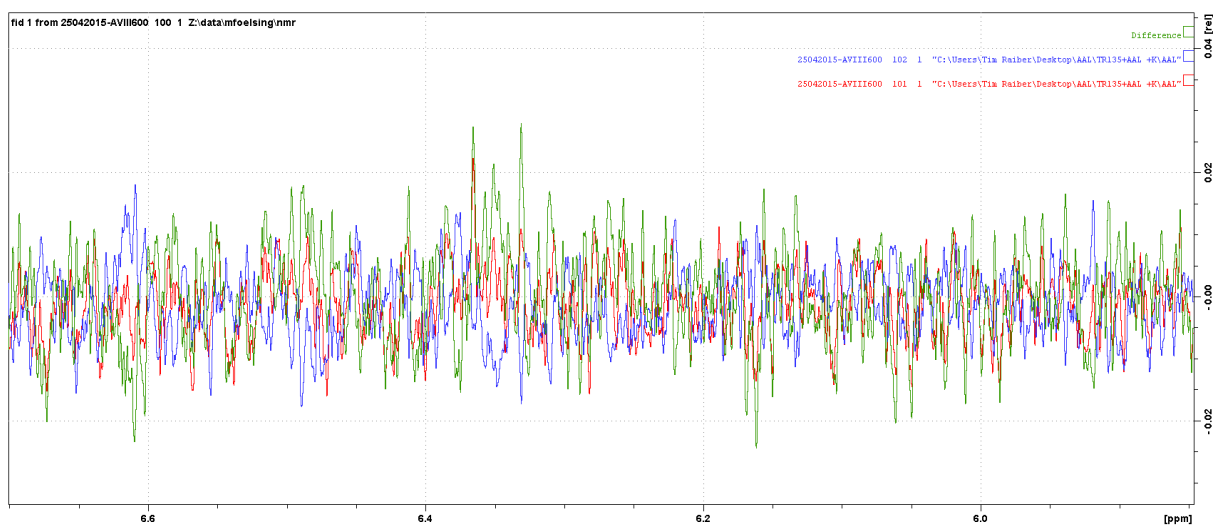


Fig. 75C: Determination of N_{pp} for the STD NMR difference spectrum of AAL / Fuc α 1-3GlcNAc ($N_{pp} \approx 0.04$, $LOQ \approx 0.20$). NMR operator and interpreter (epitope map): M. Fölsing, NMR interpreter (re-evaluation, this fig.): T. Raiber.

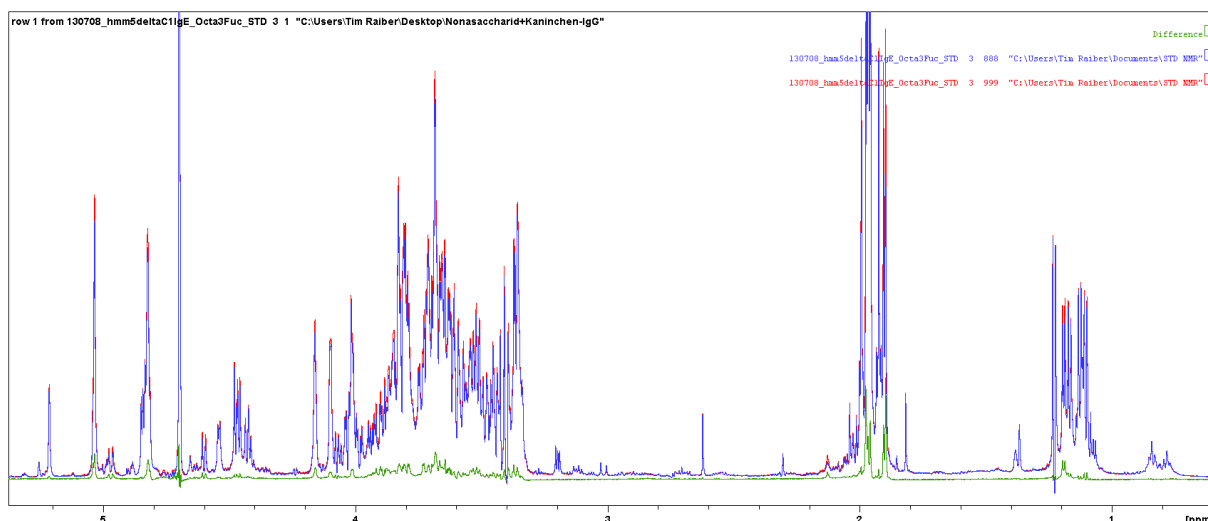


Fig. 76A: STD NMR spectrum (green) of HMM5 Δ C1IgE antibody (1 mg) and nonasaccharide (0.8 mM) showing weak STD effects. Off- (red) and on- (blue) resonance spectra are superimposed. NMR operator: T. Hackl, NMR interpreter (epitope map): M. Kötler, NMR interpreter (re-evaluation, this fig.): T. Raiber.

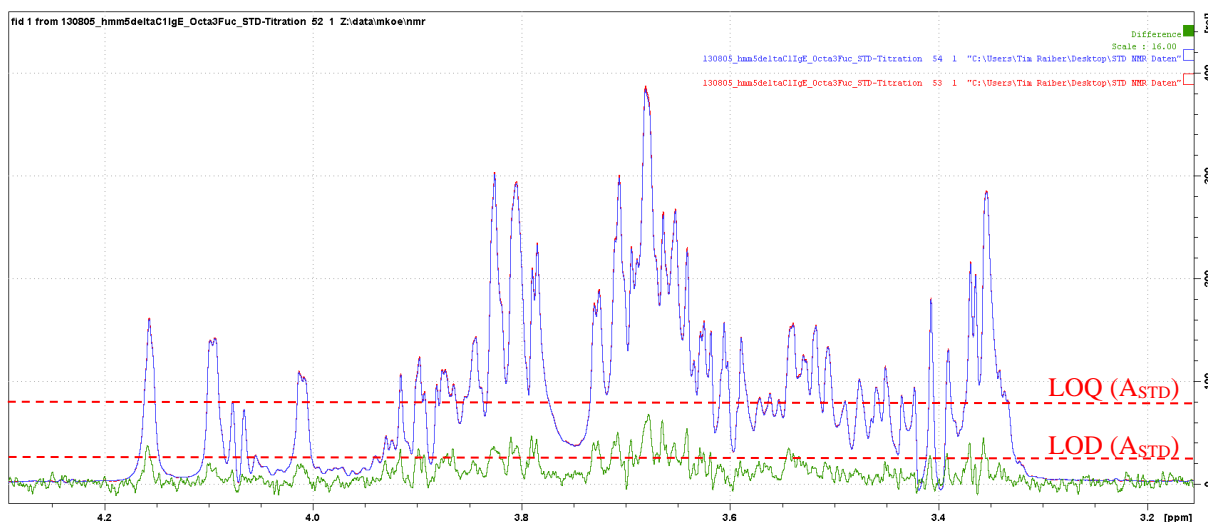


Fig. 76B: Suggested LOQ for STD effects (red dashed line) at the example of HMM5 / nonasaccharide. The limits were calculated according to eq.s 13 and 14. The difference of the carbohydrate ring proton signals is 16-fold upscaled. It falls below the LOQ and does not allow an epitope mapping. It exceeds the LOD and thus there are in fact statistically significant, albeit very weak STD effects. NMR operator and interpreter (epitope map): M. Kötler, NMR interpreter (re-evaluation, this fig.): T. Raiber.

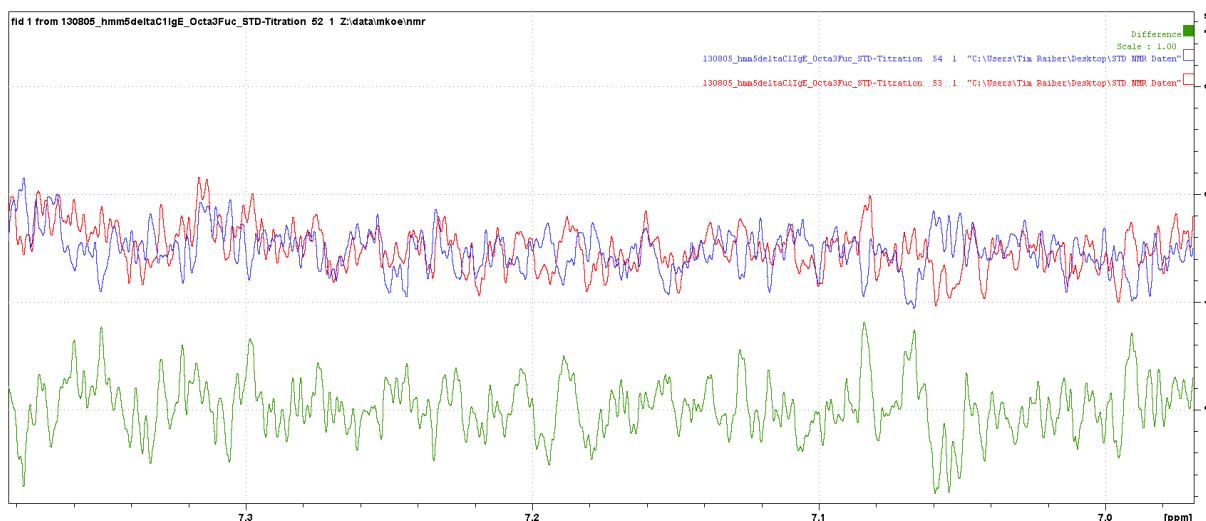


Fig. 76C: Determination of N_{pp} for the STD NMR difference spectrum of HMM5 / nonasaccharide ($N_{pp} \approx 1.0$, $LOQ \approx 5.0$). NMR operator and interpreter (epitope map): M. Kötzler, NMR interpreter (re-evaluation, this fig.): T. Raiber.

Another statistical approach is to evaluate the STD data by a paired t -test where off- and on-resonance signals are considered as *pairs of observation*, investigating if the STD effect is likely.¹²¹ This test has two competing hypotheses, the null hypothesis and the alternative hypothesis. The null hypothesis (H_0) assumes that the true mean difference (σ_d) is equal to zero. The two-sided alternative hypothesis (H_1) assumes that μ_d is not equal to zero. The goal is to determine the hypothesis with which the data are more consistent. The mathematical representations of the null and alternative hypotheses are defined below:

$$H_0: \mu_0 = 0 \quad \text{eq. 15}$$

$$H_1: \mu_0 \neq 0 \quad (\text{two-sided}) \quad \text{eq. 16}$$

The STD data of HSA/Trp and polyclonal anti-HRP/Fuc α 1-3GlcNAc were chosen to apply such a test (fig.s 77-78). The resonances were integrated after calibration on the internal standard (Bruker sample: anomeric proton of sucrose). Since an internal standard was not present in the antibody sample, the on-resonance signal of H-5' was calibrated to 10.00 (*i.e.*, 1.00×10). Off- and on-resonance spectra were processed simultaneously to avoid integration errors. The integrals were represented by a box-whisker plot (fig. 79). In none of the cases, outliers occurred. The significance level α was set 0.05 prior to the test. The expected difference μ_0 was set 0. The t -value was calculated according to the eq. 17.

$$t = \sqrt{n} \frac{\bar{d} - \mu_0}{\sigma_d} \quad \text{eq. 17}$$

where n represents the number of protons surveyed and \bar{d} is the mean of the differences with the standard deviation σ_d . If the t -value is in the 95 % critical value accepted range, H_0 is accepted (*i.e.*, statistically *insignificant* difference). If H_0 is true, the p -value is the probability of getting the t -value or a more extreme t -value. If the p -value is less than the chosen significant level, then H_0 is rejected (*i.e.*, the sample gives reasonable evidence to support H_1). The larger the p -value the more it supports H_0 . The choice of significance level at which H_0 is rejected is arbitrary (*i.e.*, a pre-chosen probability; conventionally $p < 0.05$, *i.e.*, less than 5 % error probability). If H_0 is true but rejected, this is a type I error. If H_0 is false but accepted, this is a type II error.

The Bruker sample showed statistically *significant* STD effects (fig. 77, table 7). **H_0 hypothesis:** Since p -value $< \alpha$, H_0 is rejected. The average of the off- minus on-integral is considered to be not equal to μ_0 . In other words, the difference between the average of the off- minus on-integral and μ_0 is big enough to be statistically significant. **p -value:** The p -value equals 0.000597042, ($p(x \leq t) = 0.000298521$). This means that the chance of type I error (rejecting a correct H_0) is small (0.060 %). The smaller the p -value the more it supports H_1 . **3. Statistics:** The test statistic t equals -9.844923 and is not in the 95 % critical value accepted range: [-2.7764 ; 2.7764]. The mean of the differences (-1.29) is not in the 95 % accepted range [-0.3600 ; 0.3600].

Conversely, the antibody sample showed statistically *insignificant* STD effects (fig. 78, table 8). **H_0 hypothesis:** Since p -value $> \alpha$, H_0 is accepted. The average of the differences is considered to be equal to the μ_0 . In other words, the difference between the average of the off- minus on-integral and μ_0 is not big enough to be statistically significant. **p -value:** p -value equals 0.0615708, ($p(x \leq t) = 0.0307854$). This means that if H_0 would be rejected, the chance of type I error (rejecting a correct H_0) would be too high (6.2 %). The larger the p -value the more it supports H_0 . **Statistics:** The test statistic t equals -2.918502 and is in the 95 % critical value accepted range: [-3.1824 ; 3.1824]. The mean of the differences is in the 95 % accepted range: [-0.3700 ; 0.3700].

TCI_prod_HSA.33.888.1r

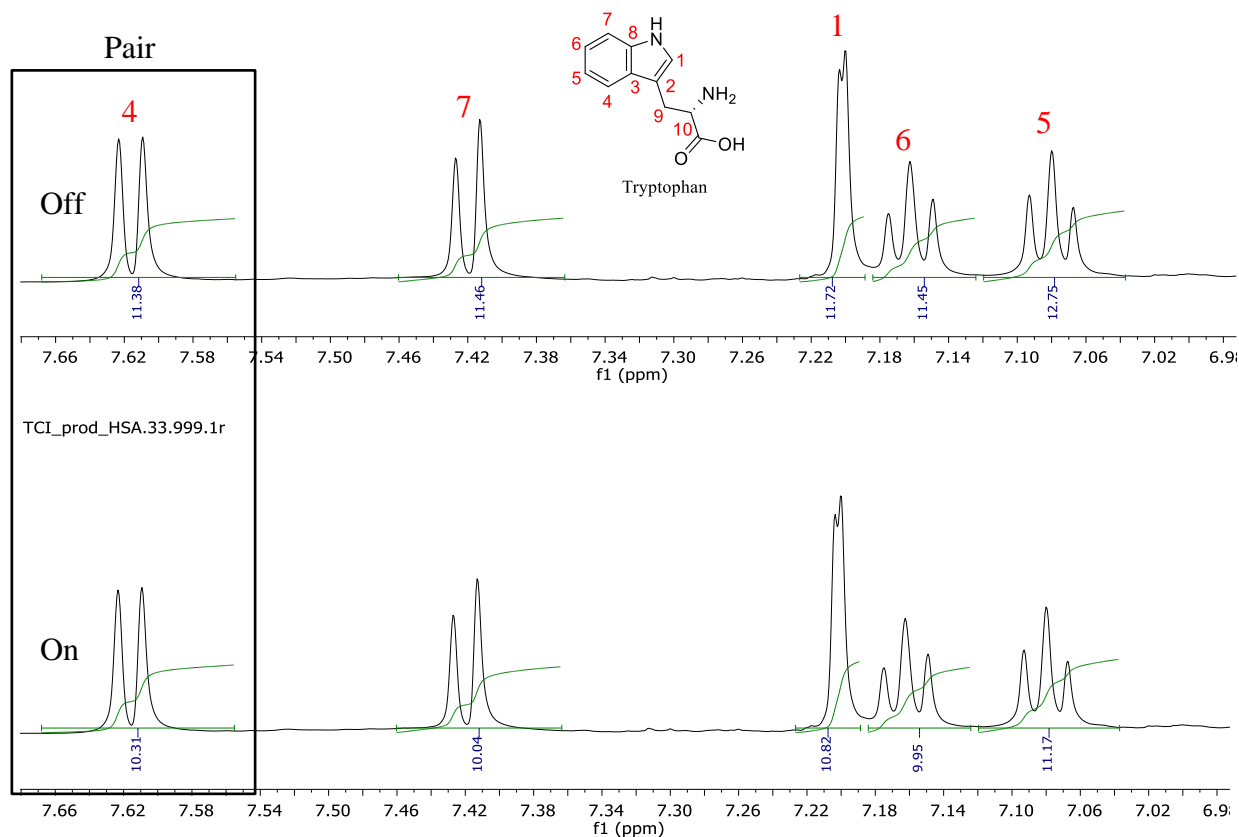
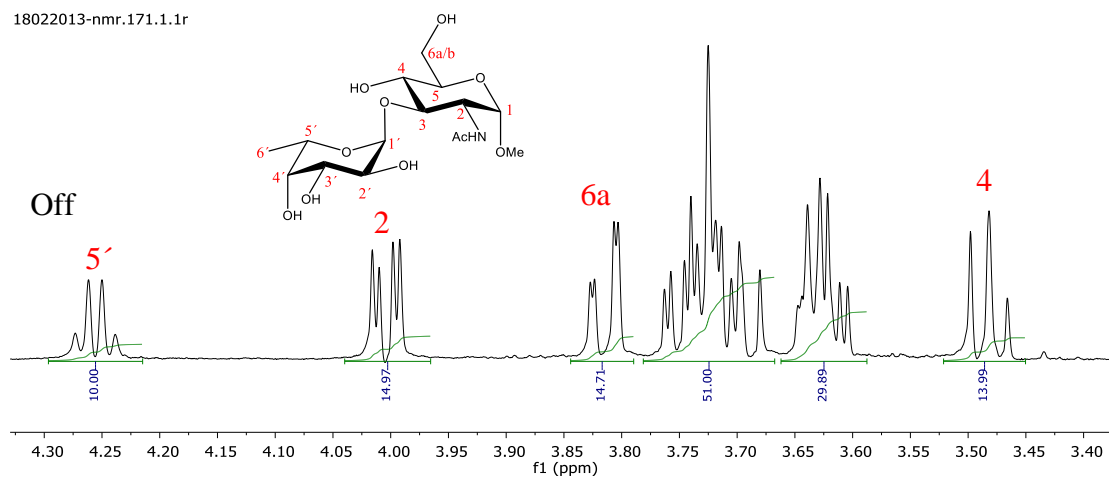


Fig. 77: Integrations of off- and on-resonance signals (HSA/Trp). The integration was calibrated on the anomeric proton of sucrose (internal standard). Both spectra were processed simultaneously.

Table 7: Paired sample *t*-test for the STD NMR experiment HSA/Trp. The integrals were calibrated on the anomeric proton of sucrose (internal negative control). Signals for H-9 (~3 ppm) and H-10 (~4 ppm) were excluded from the *t*-test due to interferences with signals of sucrose.

Proton	4	7	1	6	5
Off-integral	11.38	11.46	11.72	11.45	12.75
On-integral	10.31	10.04	10.82	9.95	11.17
<i>d</i>	1.07	1.42	0.90	1.50	1.58
Abs. %	9.4	12.4	7.7	13.1	12.4
\bar{d}	-1.294000				
σ_d	0.293905				
<i>n</i>	5				
<i>t</i>	-9.844923				
<i>p</i>	0.000597042				

18022013-nmr.171.1.1r



18022013-nmr.172.1.1r

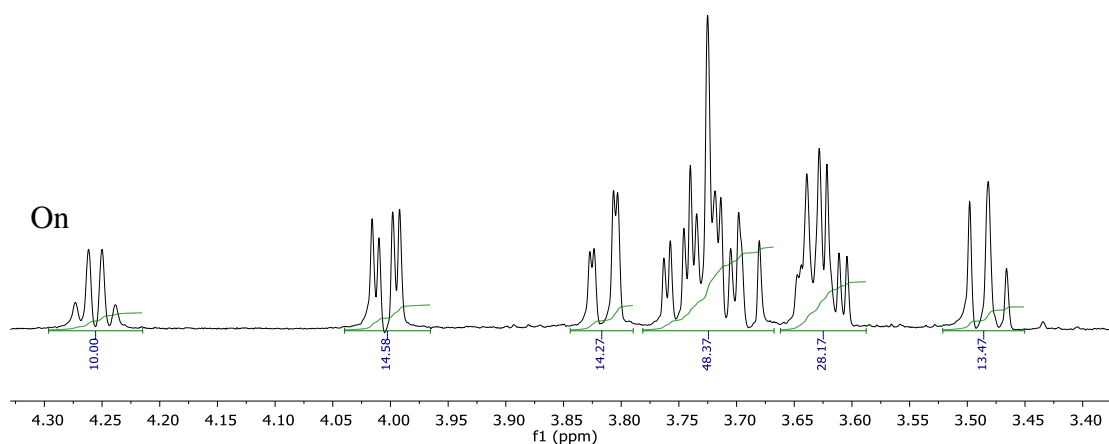


Fig 78: Integrations of off- and on-resonance signals. The integration was calibrated on H-5' and multiplied by 10 to generate the same number of significant digits as for the *t*-test for HSA/Trp.

Table 8: Paired sample *t*-test for the STD NMR experiment polyclonal anti-HRP antibodies / Fuc α 1-3GlcNAc. Due to the absence of an internal standard, the integrals were calibrated on H-5' and multiplied by 10 to generate the same number of significant digits as for HSA / Trp. The multiplets between 3.77 and 3.60 ppm were excluded.

Proton	5'	2	6a	4
Off-integral	10.00	14.97	14.71	13.99
On-integral	10.00	14.58	14.27	13.47
<i>d</i>	0.00	0.39	0.44	0.52
Abs. %	0	2.6	3.0	3.7
\bar{d}	-0.337500			
σ_d	0.231283			
<i>n</i>	4			
<i>t</i>	-2.918502			
<i>p</i>	0.0615708			

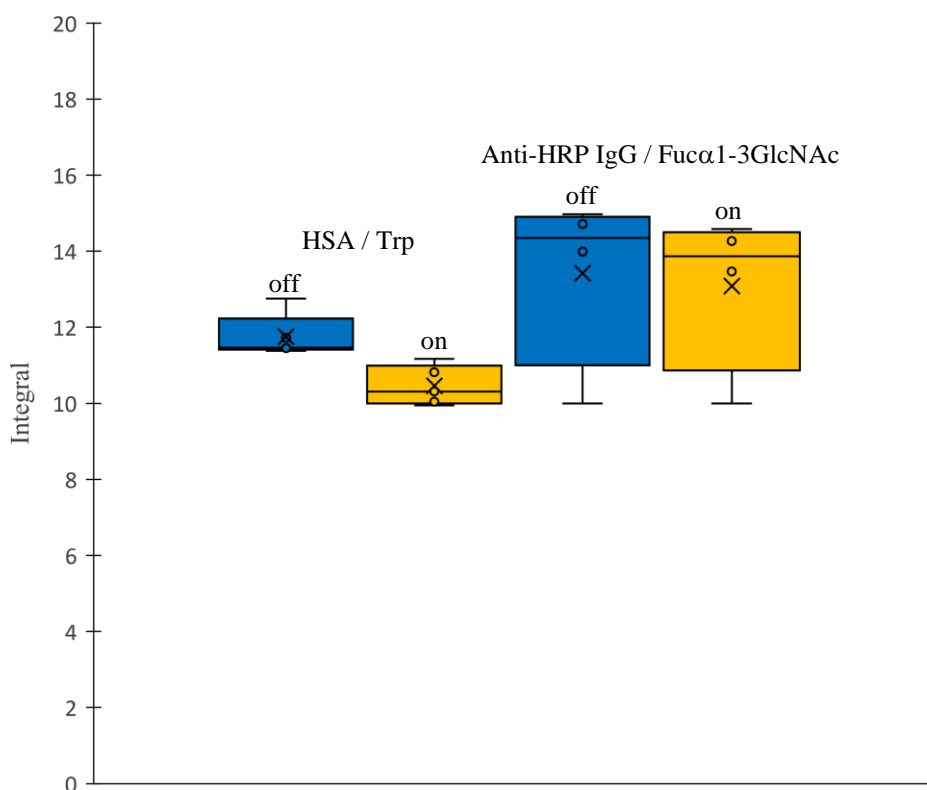


Fig. 79: Box-whisker plot of the off- (blue) and on- (orange) resonance integrals. The plot indicates that there is a significant difference between off- and on-signals in the case of HSA/Trp but not in the case of anti-HRP IgG / Fuc α 1-3GlcNAc. Diagram: T. Raiber.

6.2.1.4.4. STD Artefacts Probably Caused by Power Spill-Over due to Non-Calibrated Gaussian Pulse

For an explanation what may have caused the artefacts, Xia *et al.* are instructive. To eliminate artefacts, they developed so-called Clean STD NMR experiments.¹²² For this, two STD-NMR spectra are acquired “with the on-resonance irradiations at high- and downfield ends, respectively”, and “the left half part of the first STD-NMR and the right half part of the second STD-NMR” are concatenated “forming a Clean STD-NMR spectrum, free of the power spill-over or the false positives”. Such a spill-over should actually be avoided by the application of a long-shaped pulse.¹²³ Long shaped pulses (ms) at low power will selectively excite a small region (single peak) of the NMR spectrum, in contrast to short pulses (μ s) at high power, which simultaneously excite the entire NMR spectrum. A 10 μ s hard pulse, for example, results in a 25 kHz excitation profile ($1/(4 \times 10 \mu$ s)). In STD NMR spectroscopy, a saturation pulse is shaped to limit its excitation profile and prevent an accidental excitation of the ligand. To test the hypothesis ‘Saturation pulse too broad’, the negative control experiments at different

saturation positions were re-evaluated. The artefacts particularly appear at CH₃ groups (NHCOCH₃, OCH₃, Fuc H-6). Their behavior, especially intensity, varies depending on the position of the on-resonance irradiation (fig. 82, table 9). One striking feature is that with irradiation at +7.37 ppm there appears no artefact at 1.2 ppm (Fuc H6) but with irradiation at -0.5 ppm (strong) and -1.5 ppm (weak). Furthermore, the artefact intensity of the methyl aglycon at 3.4 ppm is almost equal with the irradiation at -0.5 ppm (10 a.u.) and +7.37 ppm (11 a.u.). Thus, due to the almost equal distances from 3.4 ppm to 7.37 ppm and 3.4 ppm to -0.5 ppm of around 4 ppm, here the flank of the Gaussian pulse is probably positioned. This information leads to the trace of the origin of the STD artefacts (fig. 80): At a rough estimate, the Gaussian pulse is ± 4.5 ppm broad, maybe due to side lobes. The excitation profile of a 2.5 ms Gaussian pulse delivered continually as a train of pulses for 2 s at 14.1 T (600 MHz ¹H) is approximately ± 1.5 ppm broad. A 5.0 ms Gaussian pulse is approximately ± 1.0 ppm broad. For comparison, the Gaussian pulse in the STD NMR experiment on the 400 MHz spectrometer is approximately ± 0.85 ppm broad - determined by shifting the irradiation position - what is in good accordance with the literature (fig. 81). The question remains why artefacts of the ring protons do not appear. A trivial and plausible explanation is that the artefacts of the ring protons (methine groups) are in principle there but just do not exceed the noise because their integrals are just one third of methyl groups and their signal heights are diminished due to their multiplicity. Hence, artefacts of the ring protons should exceed noise with longer acquisition time according to $S/N \sim \sqrt{ns}$. Ley *et al.* maximized the saturation transfer by optimizing selective excitation pulses (fig. 81).¹²⁴ Another potential cause of artefacts in STD NMR spectra are Bloch-Siegert shifts.^{125,126,127} A Bloch-Siegert shift is a shift of a signal from its usual frequency caused by nearby irradiation. It results in a difference spectrum with *dispersed* signal shapes because the misalignment causes negative phases. A relative offset of 0.015 Hz between the same two datasets is sufficient. Therefore, the irradiated and control (with irradiation away from any signals) spectra have to be acquired simultaneously or interleaved to avoid shifting. But Bloch-Siegert shifts could be ruled out because the artefacts show a *Lorentzian*, and not a dispersive, shape.

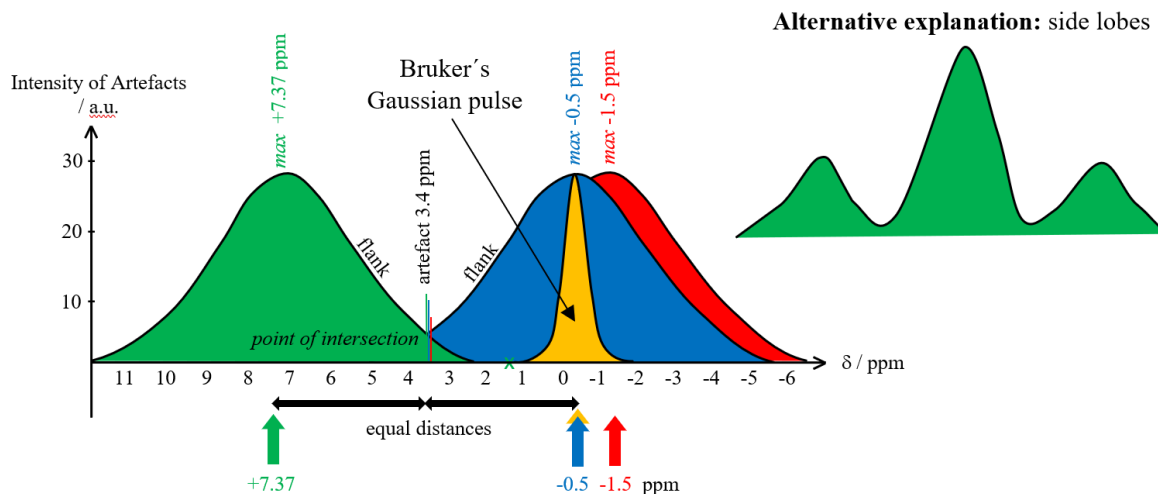


Fig. 80: Gaussian pulse shapes roughly estimated from spectra shown in fig. 82. The Gaussian pulses applied in this study revealed as non-calibrated or fatally manipulated (green, blue, red). Its broadness of ± 4.5 ppm results in an unselective saturation. For comparison, the Gaussian pulse used in the STD NMR experiment on the 400 MHz spectrometer was determined to be ± 0.85 ppm broad (yellow). The similar artefact intensities at 3.4 ppm (10 and 11 a.u.) with irradiation at +7.37 ppm (see table 9) indicated a point of intersection of the Gaussian pulse shapes. That there is no artefact with irradiation at +7.37 ppm is a pointer to the fact that there the Gaussian pulse shape approaches zero. Also, broad side lobes would explain the artefacts (top right). Diagram: T. Raiber

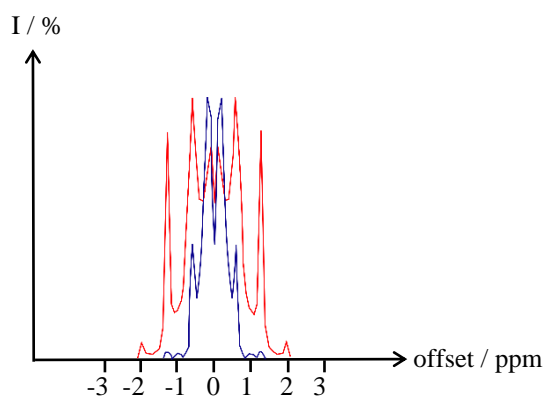


Fig. 81: Excitation profiles of 2.5 ms (red line) and 5 ms (blue line). “Gaussian pulses delivered continually as a train of pulses for 2 s at 14.1 T (600 MHz ^1H).” At large offsets from the pulse, the excitation levels are low. Diagram adapted from Ley *et al.* (2014).

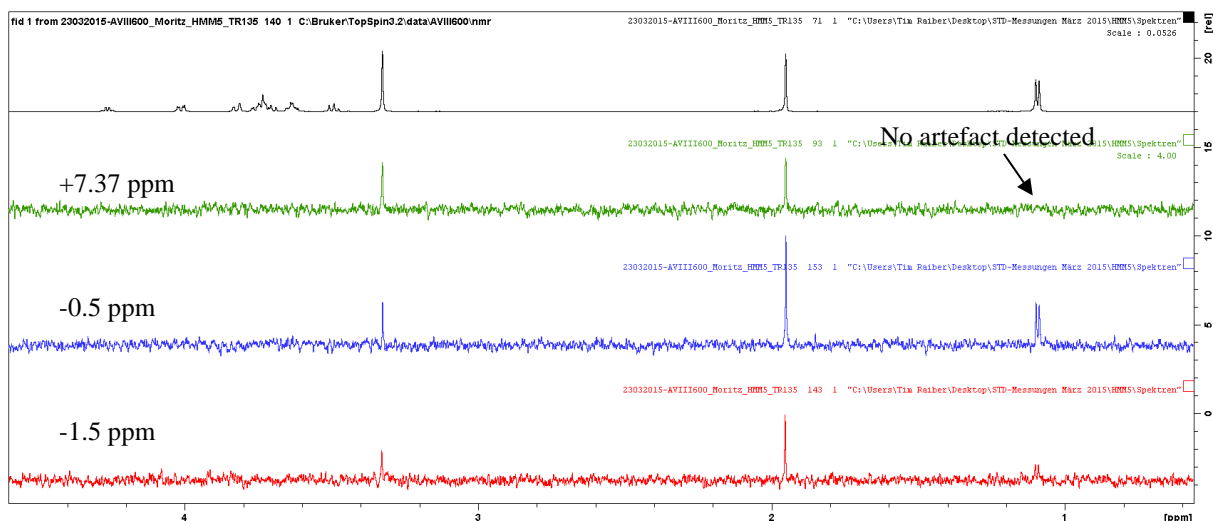


Fig. 82: STD NMR difference spectrum of HMM5/Fuc α 1-3GlcNAc. The appearance of the artefact is traced back to an uncalibrated Gaussian pulse, giving rise to undesired power spill-over to the ligand. NMR operator: M. Fölsing, NMR interpreter (re-evaluation, this fig.): T. Raiber.

Table 9: Intensities of the artefacts (fig. 82) as a function of different irradiation positions. The artefacts of the ring protons are obviously hidden in the noise.

Irradiation positions / ppm	Intensities at artefact positions / a.u.		
	3.4 ppm	2.0 ppm	1.2 ppm
+7.37	11	12	0
-0.5	10	25	10
-1.5	7	15	3

6.2.2. SPR Spectroscopy

6.2.2.1. Fundamental Principles of SPR Spectroscopy

Surface plasmon resonance (SPR) spectroscopy is an optical method to measure adsorption processes on metal surfaces. The physical principle was described by Turbadar in **1959** and refined by Otto and Kretschmann in **1968**.^{128,129,130} In **1991**, the Swedish company *Biacore* developed a commercial system, which facilitates SPR measurements in biological contexts without huge effort.¹³¹ SPR is a resonant oscillation of conduction electrons at the interface between a negative and positive permittivity material stimulated by incident light. A surface plasmon is a non-radiative electromagnetic surface wave that propagates in a direction parallel to the negative permittivity material interface. Since the wave is on the boundary of the conductor and the external medium with an evanescent field protruding into the external medium (buffer), these oscillations are very sensitive to any change of this boundary, such as adsorption of molecules on the conducting surface. Typical methods that support surface plasmons are silver and gold. When using light to excite surface plasmon waves, there are two setups possible. In the Otto setup, the light illuminates the wall of a glass block, typically a prism, and is totally internally reflected. A thin film, for example gold, is positioned close enough to the prism wall so that an evanescent wave can interact with the plasma waves at the surface and hence excite the plasmons. In the Kretschmann setup, the metal film is evaporated onto the glass block. The light again illuminates the glass block, and an evanescent wave penetrates through the metal film. The plasmons are excited at the outer side of the film. This setup is used in most practical applications. Binding makes the reflection angle change (fig. 83). As molecules from the injected sample bind to the immobilized molecules, this results in an alteration in refractive index of the sensor surface that is proportional to the change in mass concentration. These changes are detected in real time and displayed as a sensorgram (fig. 84). A SPR sensor chip with coated gold layer and a beamline through a prism for detection of binding events is illustrated in fig. 85. In this system, a sensor chip consists of a glass carrier coated with a thin gold layer as an optical thicker medium on which a matrix with suitable terminated functional groups is coupled by thiol anchors. To measure interactions, one of the interaction partners is immobilized on the chip (*e.g.*, by activation with EDC/NHS and coupling *via* an amino function). The optical thinner medium is a flow cell in which an analyte dissolved in buffer streams across the cell. By comparison with a reference cell, a difference sensorgram is obtained. The measurements are controlled by a software and automatized. A typical sensorgram is shown in fig. 84. The response (RU = response units) increases with the flow of

analyte buffer solution through the flow cell (*i.e.*, association) until an equilibrium is reached (*i.e.*, association rate is equal to dissociation rate). Afterwards, the flow cell is rinsed with buffer dissociating the analyte. By washing, the initial conditions are reconditioned. As a rough approximation, a response of 1 RU is equivalent to change in a surface concentration of about 1 pg/mm^2 (for proteins on a sensor chip CM5). This equation is used to determine surface coverage.

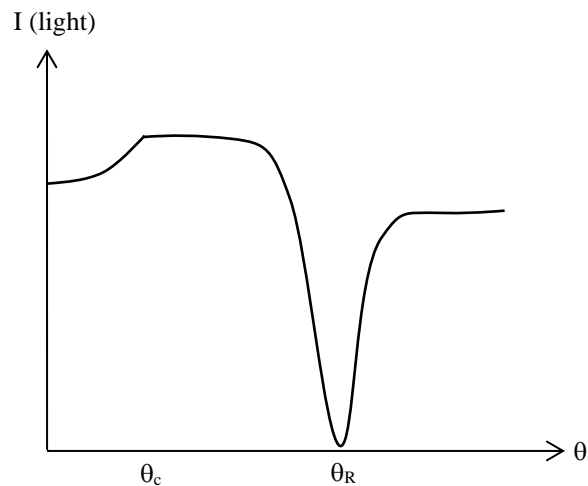


Fig. 83: During transition of light from an optical thicker (glass) to an optical thinner medium (buffer) total reflection occurs at passage of a critical angle, θ_c (*i.e.*, the intensity of the reflecting light beam is equivalent to the intensity of the incident light beam). But if the glass is coated by a thin layer of a noble metal, surface plasma is excited to oscillate around its atomic cores. This resonance attenuates the intensity of total reflection, esp. at θ_R . Due to the plasma oscillation, an evanescent electric field occurs which penetrates the optical thinner medium. The penetration deepness depends on the refraction index of the medium and the incident angle. Hence, the resonance angle, θ_R , is influenced by changes on the surface of the metallic medium.

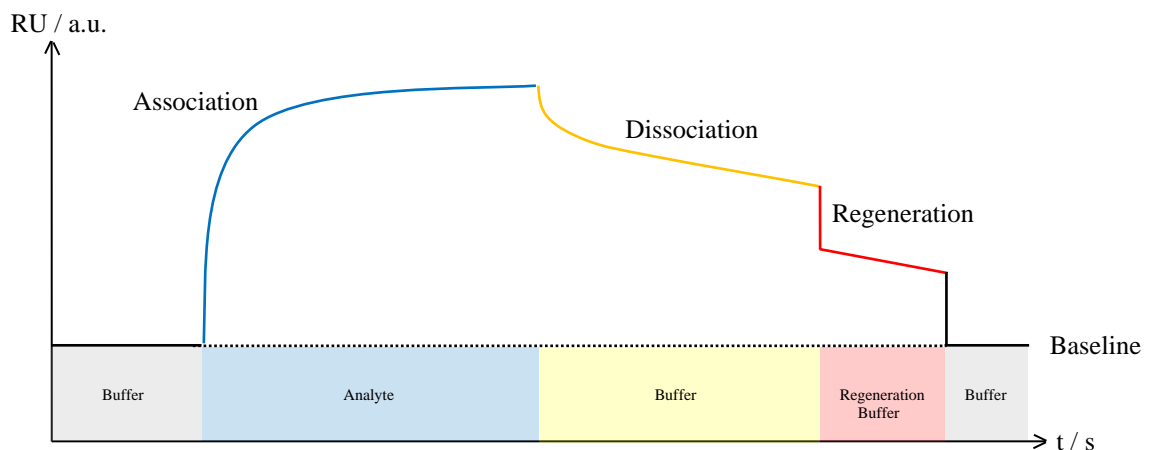


Fig. 84: SPR response plotted against time (sensorgram). The analyte associates to the surface when analyte buffer solution flows through the chip. When the chip is then subjected to a flow of buffer, the analyte dissociates. To complete dissociation, a regeneration buffer is injected.

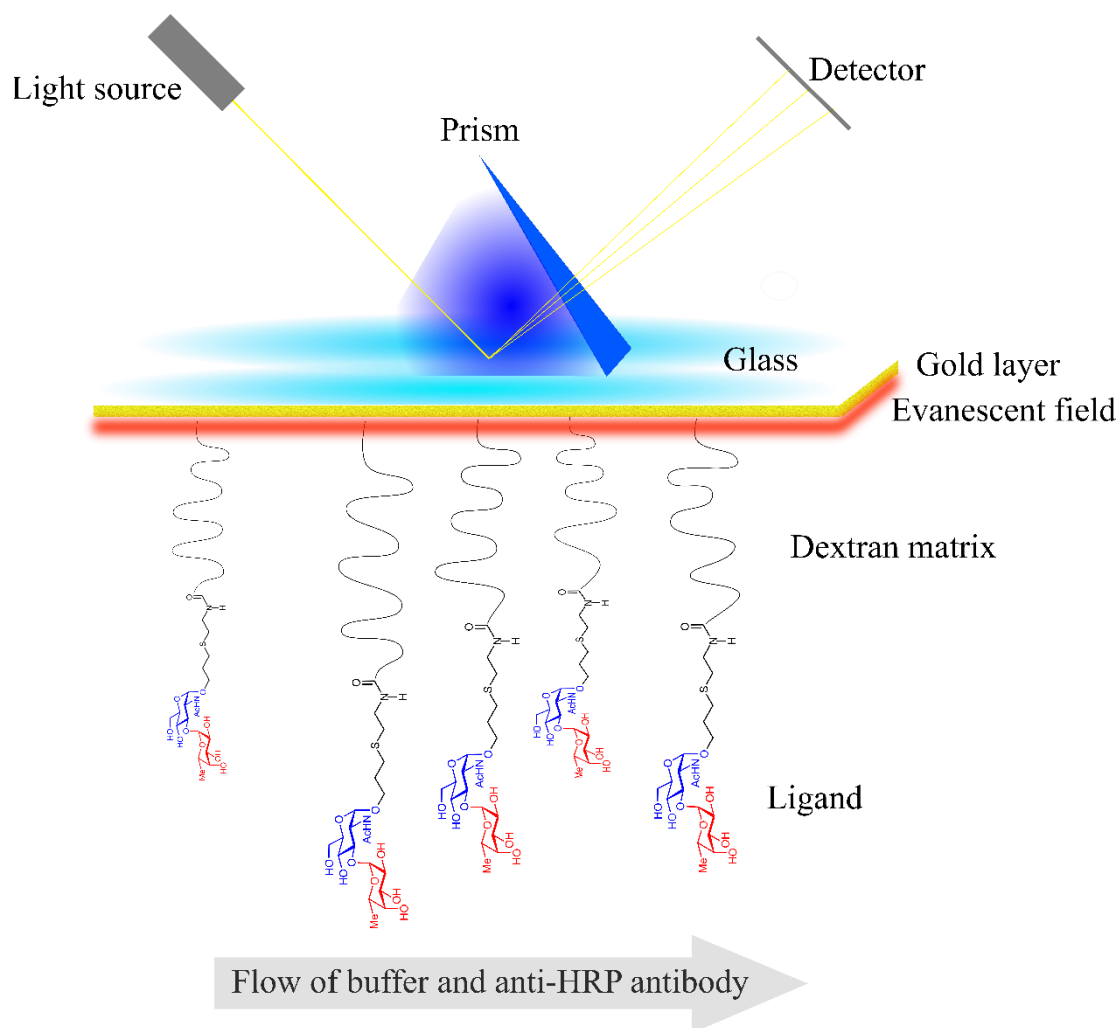


Fig. 85: CM5 chip with immobilized carbohydrate **15**. The ligand was immobilized by activation with EDC/NHS. The resonance angle is influenced by changes on the surface of the gold layer.

6.2.2.2. SPR Results

The disaccharide **15** was immobilized on a CM5 chip by activation with EDC/NHS. The immobilization of the ligand was controlled with AAL as receptor ($K_D = 50$ nM, fig.s 86-87). The activity of AAL was controlled with immobilized HRP ($K_D = 85$ nM, fig. 88). The monoclonal antibody HMM5 showed no binding (data not shown). The result was interpreted in a fatal way: The disaccharide might be *sterically hindered* by its immobilization. Based on this interpretation, the STD NMR measurements should be repeated a third time. The main information of this SPR experiment has unfortunately not been considered relevant: It was *negative*. Therefore, an STD NMR experiment was carried out on another spectrometer, showing that HMM5 is not binding the disaccharide Fuc α 1-3GlcNAc at all (fig. 67).

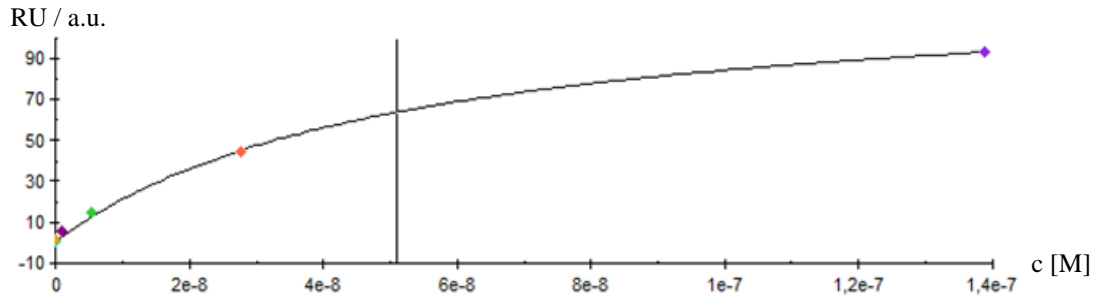


Fig. 86: Binding kinetics of AAL on immobilized Fuc α 1-3GlcNAc (Fc 2-1; Fit: 1. steady state affinity). $K_D = 50$ nM ($\chi^2 = 0.806$ RU 2). SPR operators: T. Raiber, M. Plum, SPR interpreter: T. Raiber.

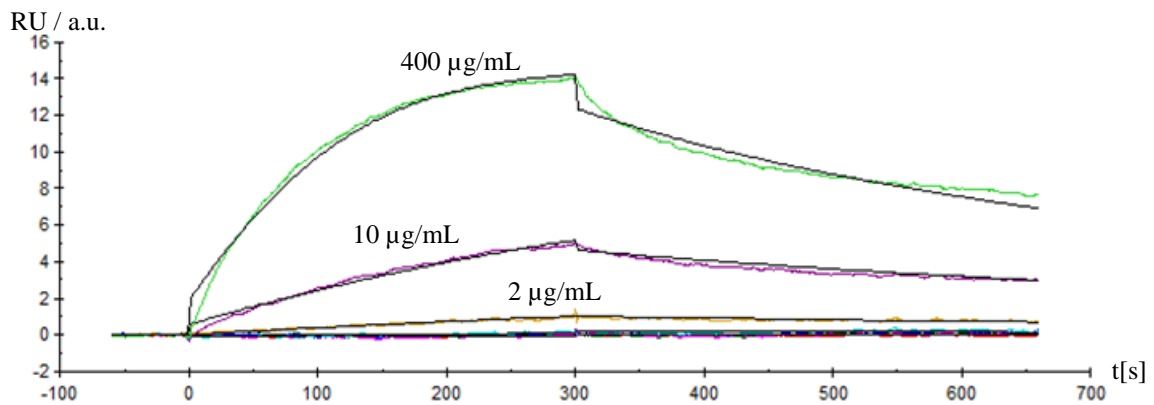


Fig. 87: Subtracted sensorgrams (Fc 4-1, AAL concentrations: 0-10 μ g/mL, flow 25 μ L/min, contact time 300 μ s, dissociation time 360 s). SPR operators: T. Raiber, M. Plum, SPR interpreter: T. Raiber.

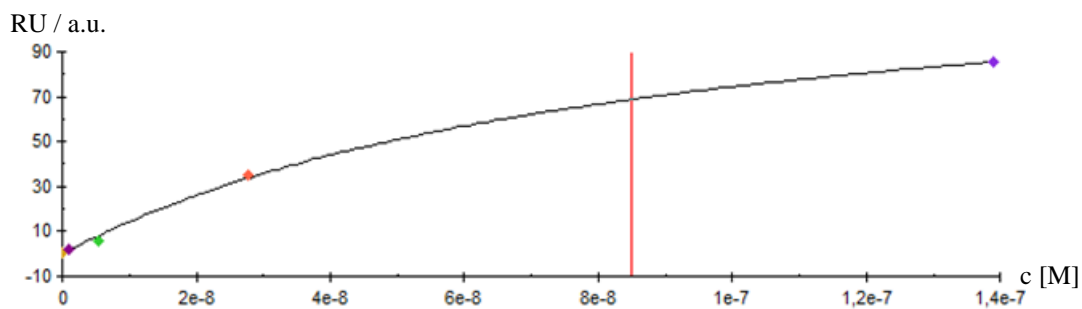


Fig. 88: Binding kinetics of AAL on immobilized HRP (Fc 4-1). $K_D = 85$ nM ($\chi^2 = 1.14$ RU 2). SPR operators: T. Raiber, M. Plum, SPR interpreter: T. Raiber.

6.2.3. X-Ray Crystallography of Co-Crystals

6.2.3.1. Fundamental Principles of X-Ray Crystallography

Crystal structures of proteins began to be solved in the late **1950s**, beginning with the structure of sperm whale myoglobin by Kendrew (Noble Prize in **1962**).¹³² Based on PDB statistics (**2018**), over 131000 X-ray crystal structures have been determined. For comparison, the nearest competing method in terms of structures analyzed is NMR spectroscopy, which has resolved over 12000 chemical structures. Moreover, crystallography can solve structures of arbitrarily large molecules, whereas solution-state NMR is restricted to relatively small ones (less than 70 kDa). X-ray crystallography is a form of elastic scattering. A typical wavelength used for crystallography is 1 Å, which is on the scale of covalent chemical bonds and the radius of a single atom. Longer-wavelength photons (such as ultraviolet radiation) would not have sufficient resolution to determine the atomic positions. At the other extreme, shorter wavelength photons, such as γ -rays, are difficult to produce large numbers, difficult to focus, and interact too strongly with matter, producing particle-antiparticle pairs. In practice, a crystal is mounted on a so-called goniometer (Anc. Gr.: $\gamma\omicron\nu\iota\alpha$ = angle; $\mu\epsilon\tau\rho\omicron\nu$ = measure) so that it may be held in the X-ray beam and rotated (fig. 89). The rotations about each of the four angles ϕ , κ , ω and 2θ leave the crystal within the X-ray beam but change the crystal orientation. The protein crystals are scooped up by a loop and then flash-frozen with liquid nitrogen to reduce the radiation damage of the X-rays, as well as the noise in the Bragg peaks due to thermal motion (the Debye-Waller effect). However, untreated protein crystals often crack if flash-frozen; therefore, they are generally pre-soaked in a cryoprotectant solution like buffer with 10 % (v/v) DMSO before freezing. The crystal is illuminated with a monochromatic X-ray beam, producing a diffraction pattern. The three-dimensional images taken at different orientations are converted into a three-dimensional model of the electron density using Fourier transforms. Hence, the main goal of X-ray crystallography is to determine the density of electrons $f(r)$ throughout the crystal, where r represents the three-dimensional position vector within the crystal. To do this, X-ray scattering is used to collect data about its Fourier transform $F(q)$, which is inverted mathematically to obtain the density defined in real space, using the formula

$$f(r) = \frac{1}{(2\pi)^3} \int F(q)e^{iqr} dq \quad \text{eq. 18}$$

where the integral is taken over all values of q . The three-dimensional real vector q represents a point in reciprocal space, that is, to a particular oscillation in the electron density as one moves in the direction in which q points.

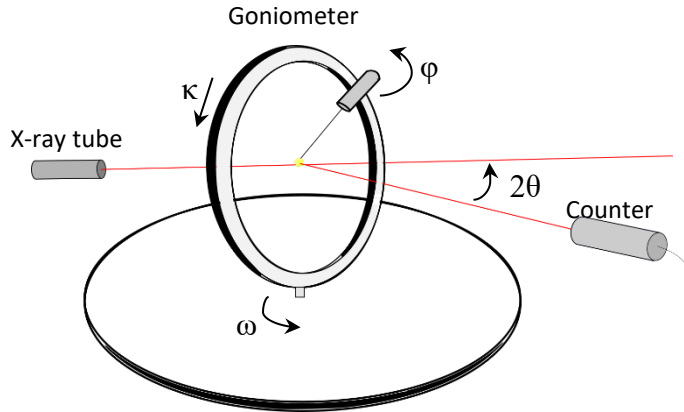


Fig. 89: Beamline of a 4-circle single-crystal x-ray diffractometer consisting of an X-ray tube, a sample holder (goniometer) and an X-ray detector. Electrons are boiled off a cathode and accelerated through a strong electric potential of ~50 kV, collide with a metal plate, emitting bremsstrahlung and some strong spectral lines corresponding to the excitation of inner-shell electrons of the metal. The most common metal used is copper, which can be kept cool easily due to its high thermal conductivity, and which produces strong K_α and K_β lines. The K_β line is sometimes suppressed with a thin (~10 μm) nickel foil. The X-rays are collimated and directed onto the sample. When the X-rays satisfy the Bragg equation, constructive interference occurs. A detector records this X-ray signal and converts it to a count rate.

The length q corresponds to 2 divided by the wavelength of the oscillation. The corresponding formula for a Fourier transform will be used below

$$F(q) = \int f(r)e^{-iqr} dr \quad \text{eq. 19}$$

where the integral is summed over all possible values of the position vector r within the crystal. The Fourier transform $F(q)$ is generally a complex number, and therefore has a magnitude $|F(q)|$ but not the phases. To obtain the phases, full sets of reflections are collected with known alterations to the scattering, either by modulating the wavelength past a certain absorption edge or by adding strongly scattering (*i.e.*, electron dense) metal atoms, such as mercury. Combining the magnitudes and phases yields the Fourier transform $F(q)$, which may be inverted to obtain the electron density $f(r)$.

$$F(q) = |F(q)|e^{i\phi q} \quad \text{eq. 20}$$

One diffraction pattern is insufficient to reconstruct the whole crystal; it represents only a small slice of the full FT. To collect all the necessary information, the crystal must be rotated step by step (0.5 to 2°) through 180°, with an image recorded at every step; actually, slightly more than 180° is required to cover reciprocal space due to the curvature of the Ewald sphere. A full data set may consist of hundreds of separate images taken at different orientations of the crystal. The first step is to merge and scale these various images, that is, to identify which peaks appear in two or more images and to scale the relative images so that they have a consistent intensity

scale. Optimizing the intensity scale is critical because the relative intensity of the peaks is the key information from which the structure is determined. The repetitive technique of crystallographic data collection and the often-high symmetry of crystalline materials cause the diffractometer to record many symmetry-equivalent reflections multiple times. This allows calculating the symmetry-related R-factor, a reliability index based upon how similar the measured intensities of symmetry-equivalent reflections are, thus assessing the quality of the data. The data processing begins with indexing the reflections, generally accomplished using an auto-indexing routine. This means identifying the dimensions of the unit cell and which image peak corresponds to which position in reciprocal space. Since reflection symmetries cannot be observed in chiral molecules, only 65 space groups of 230 possible are allowed for protein molecules. Having obtained initial phases, an initial model can be built. This model can be used to refine the phases, leading to an improved model. Given a model of some atomic positions, these positions and their respective Debye-Waller factors (or B-factors, accounting for the thermal motions of the atom) can be refined to fit the observed diffraction data, ideally yielding a better set of phases. A new model can then be fit to the new electron density map and a further round of refinement is carried out. This continues until the correlation between the diffraction data and the model is maximized. The agreement is measured by an R-factor. A similar quality criterion is R_{free} which is calculated from a subset (~10 %) of reflections that were not included in the structure refinement. The file format, which is used in molecular graphics to store electron density as a three-dimensional grid of voxels each with a value corresponding to electron density, is referred to as *ccp4*.

6.2.3.2. Evaluation of Co-Crystal Data

In order to gain insight into the molecular interaction between α 1-3 core fucose and an anti-HRP antibody, the ligand Fuc α 1-3GlcNAc α 1-OMe was co-crystallized by L. Tjerrild in **2015** with HMM5 Fab fragment (fig. 90).¹³³ The resolution is lower than 1 Å (table 10) and there are only 6 outliers in the Ramachandran plot (fig. 91, table 12). The presence of the ligand is proven by an electron density map (fig. 92). The HMM5 Fab fragment is build-up of two characteristic β -barrels as top domains consisting of four antiparallel β -strands each. The barrels are stabilized by 5 disulfide bridges (table 11). At the top of these two barrels, CDR peptide loops form an antigen recognizing interface. In order to bind to carbohydrates, these loops must be able to form specific hydrogen bonds. The β -sheets maintain integrity of the hydrophobic core. The α 1-3 core fucose appears in contact with the loops of a heavy chain domain (table 13, fig.s 93-

95). Remarkably, the light chain is not involved in the binding mode. Asparagine N32 (heavy chain) seems to play an important role in binding α 1-3 core fucose. Its side chain forms a hydrogen bond to the fucose ring oxygen and to fucose 4-OH. Furthermore, the side chains of Y31 (heavy chain) and Y99 (heavy chain) seem to form a hydrophobic pocket. That carbohydrates are stabilized by aromatic residues in the binding site was already described by Fernández-Alonso *et al.* in **2005** at the example of influenza virus hemagglutinin stabilizing 2,3-sialyllactose and lectin II from *Ulex europaeus* stabilizing galactose.¹³⁴ Tyrosine Y31 interacts with NH-CO-CH₃ and tyrosine Y99 with fucose C-6. The methyl aglycon points into the bulk water indicating its low importance. In contrast to the fucose unit, the GlcNAc unit is not stabilized by hydrogen bonds. Thus, a structural anchor and spacer function directing α 1-3 core fucose into its pocket, seems to be more likely than a role as an important glycan valence itself.

Table 10: Crystallographic parameters of the co-crystal HMM5 Fab with Fuc α 1-3GlcNAc α 1-OMe. Values for the outer shell are given in parentheses.

λ / Å	0.8726
Space group	P2 ₁ 2 ₁ 2 ₁
α , β , γ / °	90, 90, 90
Resolution / Å	1.8
Total number of reflections	273313
Number of unique reflections	41512 (3833)
Completeness / %	99.97 (100)
Redundancy	6.594
$I/\sigma(I)$	9.05 (1.72)
R_{merge}	0.17 (0.982)
Wilson B-factor	16.14

Table 11: Localization of disulfide bridges in the HMM5 Fab fragment.

Disulfide bridges				Function
H	C21	H	C93	Stabilization of top domain
H	C143	H	C199	Stabilization of bottom domain
H	C219	L	C217	Cross-linking heavy and light chain
L	C23	L	C90	Stabilization of top domain
L	C137	L	C197	Stabilization of bottom domain
H	C29*	-	-	-

* unreduced cysteine; in scFv-HMM5, C29 (TGT) is replaced by S29 (AGT).



Fig. 90: Co-crystal structure of Fuc α 1-3GlcNAc α 1-OMe and HMM5 Fab fragment visualized as cartoon (PyMOL). Each sub domain is stabilized by a disulfide bridge. The bottom subdomains of heavy and light chain are crosslinked by a disulfide group while the attachment of the top domains is obviously mediated by van der Waals forces. Color code: *blue* heavy chain, *magenta* light chain, *yellow* ligand Fuc α 1-3GlcNAc. Co-crystallization: L. Tjerrild (University of Aarhus), determination of the crystal structure: G. R. Andersen (University of Aarhus), visualization (PyMOL): T. Raiber

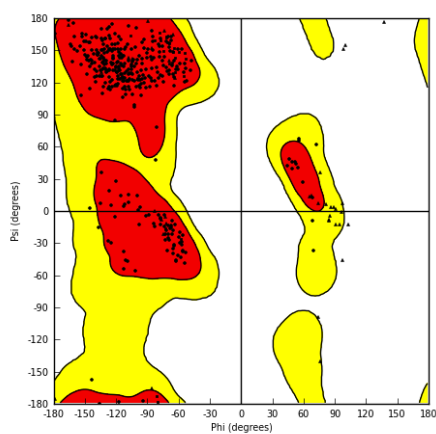


Fig. 91: Ramachandran plot of co-crystal HMM5 / Fuc α 1-3GlcNAc α 1-OMe. In total, 6 outliers (table 12).

Table 12: Outliers of Ramachandran plot (Fig. 96).

Chain	Amino acid	$\Phi / ^\circ$	$\Psi / ^\circ$
L	G68	137.0	176.4
L	G104	100.1	154.9
H	G109	98.4	151.3
H	G7	103.0	-12.6
H	G64	97.4	-46.0
L	G70	73.9	-99.4

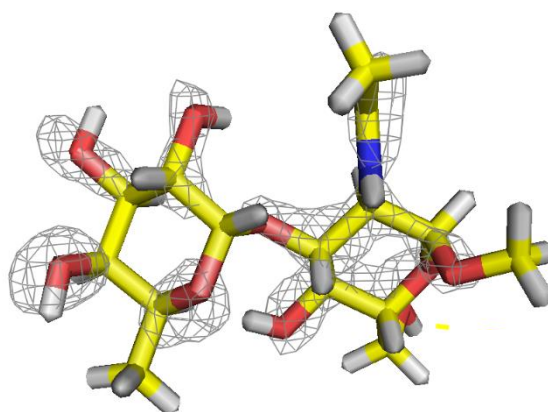


Fig. 92: Electron density map (level 3.0) of Fuc α 1-3GlcNAc α 1-OMe in the co-crystal. The mesh encloses the region in which the electron density exceeds the given threshold. Noticeably, structural elements with higher degree of freedom are missing electron density (*i.e.*, Fuc C-6, GlcNAc C-6, -NHCOCH₃, -OMe). The *ccp4* file was kindly provided by G. R. Andersen (University of Aarhus); visualization (PyMOL): T. Raiber.

Table 13: Contacts between ligand Fuc α 1-3GlcNAc α 1-OMe and HMM5 Fab.

Structural element of Fuc α 1-3GlcNAc	Amino acid of HMM5 Fab	Distance / Å	Type of interaction
Fuc 2-O <u>H</u>	H T30 (backbone C <u>O</u>)	< 3*	Polar
-NH-CO-C <u>H</u> ₃	H Y31 (aromatic ring)	5.1, 4.9, 4.7, 4.1, 3.9, 3.6	Hydrophobic
Fuc ring oxygen	H N32 (side chain -CO-N <u>H</u> ₂)	2.2	Polar
Fuc 4-O <u>H</u>	H N32 (side chain -C <u>O</u> -NH ₂)	2.5	Polar
Fuc 4-O <u>H</u>	H T52 (backbone N <u>H</u>)	2.5	Polar
-N <u>H</u> -CO-CH ₃	H F97 (backbone C <u>O</u>)	1.7	Polar
Fuc C-6	H Y99 (aromatic ring)	4.4, 4.4, 3.9, 3.9, 3.4, 3.2	Hydrophobic

H = heavy chain. * The orientation of the Fuc 2-OH proton does not allow an accurate distance measurement.

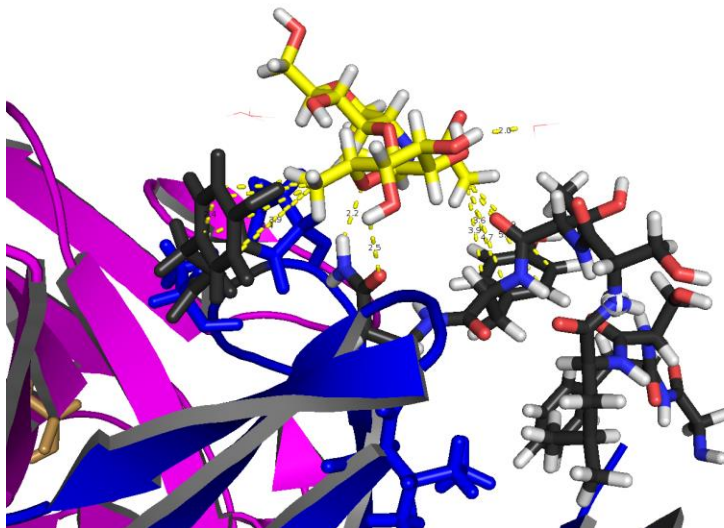


Fig. 93: Extension of the antigen recognizing interface of the HMM5 Fab fragment. Interaction of α 1-3 core fucose with the heavy chain of HMM5 Fab fragment. Color code: *blue* heavy chain, *magenta* light chain, *yellow* ligand Fuc α 1-3GlcNAc. Visualization (PyMOL): T. Raiber.

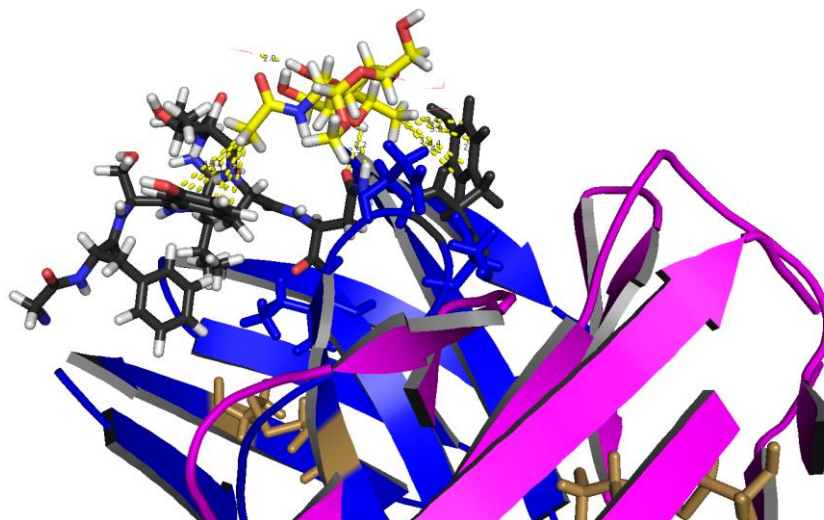


Fig. 94: Extension of the antigen recognizing interface of the HMM5 Fab fragment. Color code: *blue* heavy chain, *magenta* light chain, *yellow* ligand Fuc α 1-3GlcNAc. Visualization (PyMOL): T. Raiber.

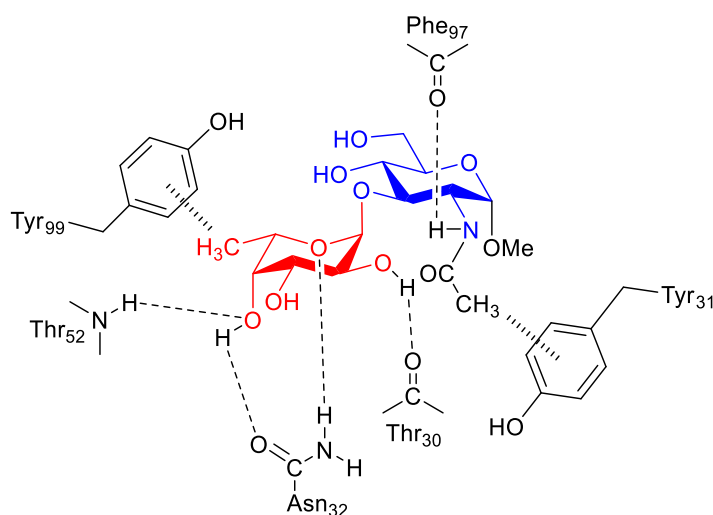
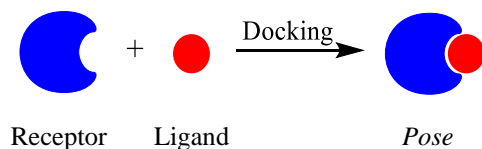


Fig. 95: Simplified illustration of the interaction of the α 1-3 core fucose and the amino acids of the HMM5 Fab.

6.2.4. Molecular Modeling

6.2.4.1. Fundamental Principles of Molecular Modeling

In the field of molecular modeling, docking is a method which predicts the preferred binding conformation of a candidate ligand to an appropriate binding site of a receptor forming a stable complex. Its result is a so-called *pose* (*i.e.*, a candidate binding mode; scheme 12).



Scheme 12: Illustration of the docking process resulting in a candidate binding mode called *pose*.

Molecular docking is a computational simulation of a candidate ligand binding to a receptor and may be defined as an optimization problem, which would describe the best fit orientation of a ligand that binds to a particular receptor of interest. However, since both the ligand and the protein are flexible, a *hand-in-glove* analogy is more appropriate than lock-and-key. During the course of the docking process, the ligand and the protein adjust their conformation to achieve an overall best-fit and this kind of conformational adjustment resulting in the overall binding is referred to as induced-fit. For molecular docking, a structure of the receptor of interest is necessarily required. Usually, the structure has been determined by x-ray crystallography, NMR spectroscopy or homology modeling. This receptor structure and a database of potential ligands serve as inputs to a docking program. The success of a docking procedure depends on the search algorithm and the scoring function. The search space consists of all possible orientation and conformations of the protein paired with the ligand. However, in practice it is impossible to exhaustively explore the search space. Most docking programs in use account for the whole conformational space of the ligand, and some attempt to model a flexible receptor. Searching the conformational space for docking is realized by either shape complementarity methods, molecular dynamics simulations or genetic algorithms and includes an appropriate force field, which consists of energy terms accounting for covalent bonds, van der Waals and electrostatic forces (eq. 21) yielding all-atom, united-atom or coarse-grained force fields.

$$E_{pot} = E_{bonded} + E_{non-bonded} \quad \text{eq. 21}$$

with $E_{non-bonded}$ = van der Waals and electrostatic forces

For energy minimizing, different force fields have been developed for different purposes. UFF (Universal Force Field) was developed at *Colorado State University* and is a general force field

with parameters for the full periodic table including the actinoids.¹³⁵ Structure builders, such as ChemDraw, use CFF (consistent force field), which was developed by S. Lifson and Warshel in **1968**, for geometry cleanup.¹³⁶ MM2 was developed by Allinger mainly for conformational analysis of hydrocarbons and other small organic molecules. It precisely reproduces covalent geometry and is updated for many different classes of organic compounds (MM3, MM4).^{137,138} AMBER (Assisted Model Building and Energy Refinement) was developed by Kollman *et al.* in **1995** and is widely used for proteins and DNA.¹³⁹ CHARMM (Chemistry at Harvard Molecular Mechanics) is widely used for both small molecules and macromolecules. OPLS (Optimized Potential for Liquid Simulations) was developed by Jorgensen and is implemented in Maestro.^{140,141,142}

The docking programs vary in regard of the algorithm from incremental construction approaches (FlexX) to shape based algorithms (DOCK), genetic algorithms (GOLD), Monte Carlo simulations (LigandFit) and systematic search techniques (GLIDE).^{143,144,145,146} GLIDE (Grid-based Ligand Docking with Energetics) uses hierarchical series of filters to search for possible locations of the ligand in the active-site region of the receptor (fig. 96). It is able to act in three modes: SP (Standard Precision), HTVS (High-Throughput Virtual Screening) and XP (eXtra Precision). HTVS reduces the number of intermediate conformations throughout the docking funnel, and also reduces the thoroughness of the final torsional refinement and sampling. The algorithm is the same as in the case of SP. XP is a different algorithm and includes more extensive sampling: SP sampling and after it its own anchor-and-grow procedure. XP includes a harder scoring with greater requirements for ligand-receptor shape complementarity. This weeds out false-positives that SP lets through.

The site-point search generates a grid of site points in the binding site and a ligand center-ligand surface. In this step, the site point-receptor surface is compared with the ligand center-ligand surface histogram. If there is a good enough match, GLIDE positions the ligand center at the site point. The diameter test checks steric clashes of atom near ligand diameter for different orientations of the ligand diameter. Then, subset test rotates about the ligand diameter and scores atoms capable of making H-bonds and ligand-metal interactions. If the score is good enough, all interactions are scored, so-called greedy scoring (*i.e.*, all atom positions $\pm 1 \text{ \AA}$ in x, y, z directions).

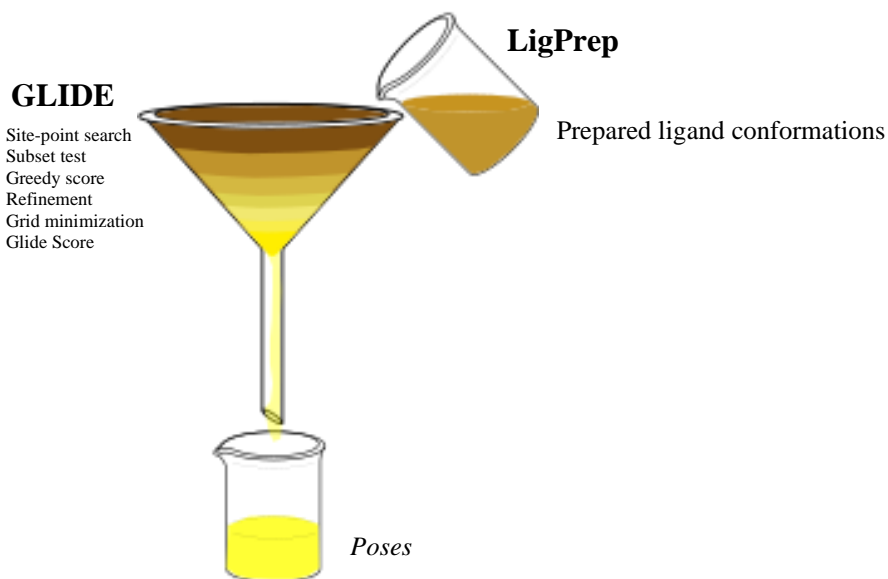


Fig. 96: Hierarchical filters of GLIDE. Filters 1 to 3 predict the position and orientation of a ligand relative to the receptor (*pose*). The filters 4-6 estimate the tightness of the receptor-ligand interactions (*scoring*).

In the refinement step, the whole ligand $\pm 1 \text{ \AA}$ is moved in x, y, z directions and is re-scored. The number of poses for energy minimization is reduced, so only a small number of the best refined poses (100-400) is passed to the energy minimization step. The energy minimization is carried out on the pre-computed OPLS van der Waals and electrostatic grids for the receptor. When doing flexible docking, also torsional angles are optimized. Using Monte Carlo moves, nearby torsional minima for a small number of low-energy poses are explored. These minimized poses are re-scored using Schrödinger's proprietary GlideScore scoring function. The choice of best-docked structure for each ligand is made using a model energy score (Emodel). Emodel is a scoring function composited of GlideScore (binding affinity), MM interaction energy (OPLS-AA) and ligand strain. In addition to the GlideScore, a docking score is reported, which is the GlideScore supplemented by Epik state penalties, if used, and strain corrections, if used. Epik is a program for the prediction of the pK_a values of the ionizable groups in ligands, and for the generation of the probable ionized and tautomerized structures within a given pH range. To predict the binding affinity, scoring functions may be used.¹⁴⁷ Scoring is a process of evaluating a particular pose by counting the number of favorable intermolecular interactions, such as hydrogen bonds and hydrophobic contacts.

6.2.4.2. Molecular Docking Reproduced Co-Crystal

In order to understand the data inconsistencies and, at best, to resolve them, molecular modeling appeared to be an effective remedy. For that purpose, the ligand $\text{Fu}\alpha\text{1-3GlcNAc}\alpha\text{1-OMe}$ was prepared using *LigPrep* with flexible ligand sampling and docked to the antibody crystal structure using *GLIDE*. The docked structure reproduced the pose of the co-crystal structure very well (fig.s 97-99) but with a low pose score (-4.07), indicating low affinity. For comparison, affine ligands are docked with a score of -8 to -15. Keeping both flexible, the glyco structures and the variable antibody domains exceeded the computational power even of a ‘gaming notebook’ (CPU: Intel Core i7-6500U, 2.5 GHz; graphics processor: NVIDIA GeForce 940M).

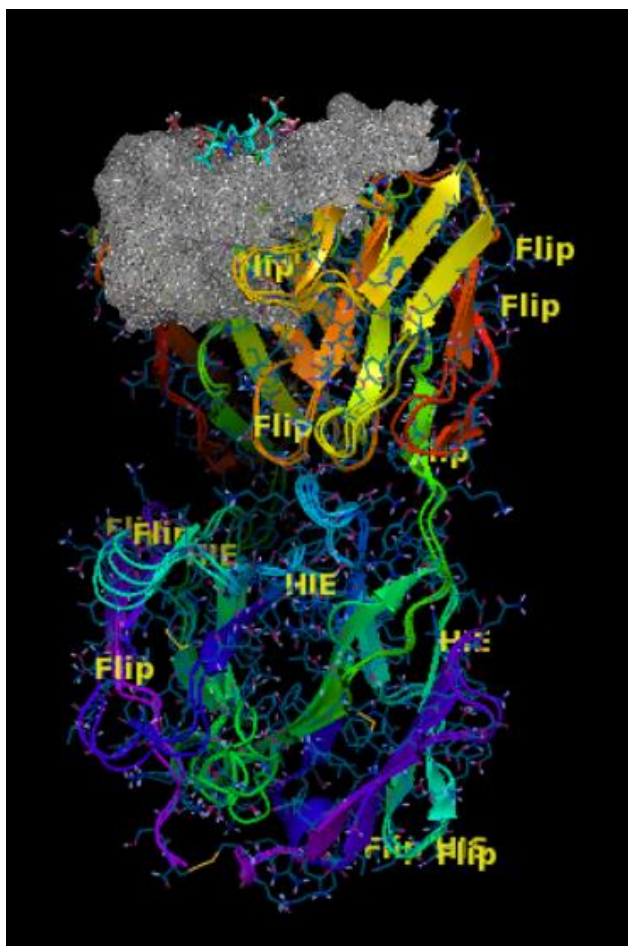


Fig. 97: HMM5 Fab docked to ligand $\text{Fu}\alpha\text{1-3GlcNAc}\alpha\text{1-OMe}$ (overview). The ligand is docked to the heavy chain. Crystal data: G. R. Andersen (University of Aarhus), Maestro user: T. Raiber.

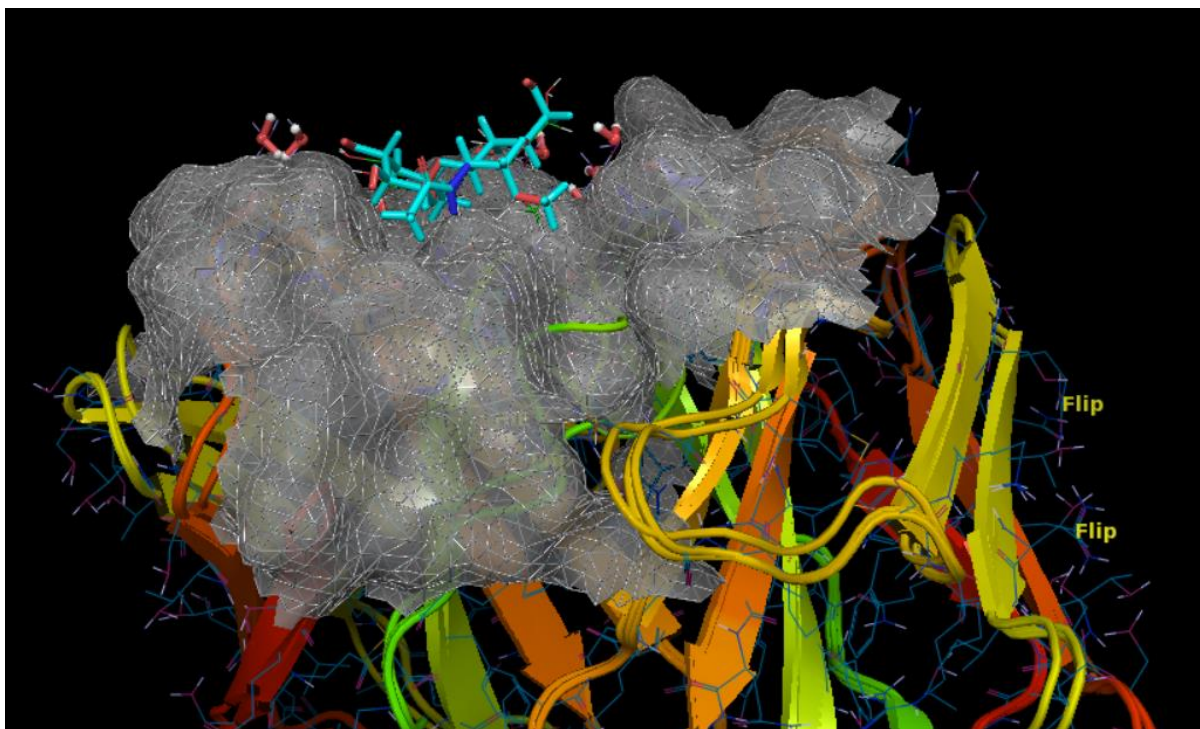


Fig. 98: Paratope of HMM5 Fab docked to ligand Fuc α 1-3GlcNAc. Crystal data: G. R. Andersen (University of Aarhus), Maestro user: T. Raiber.

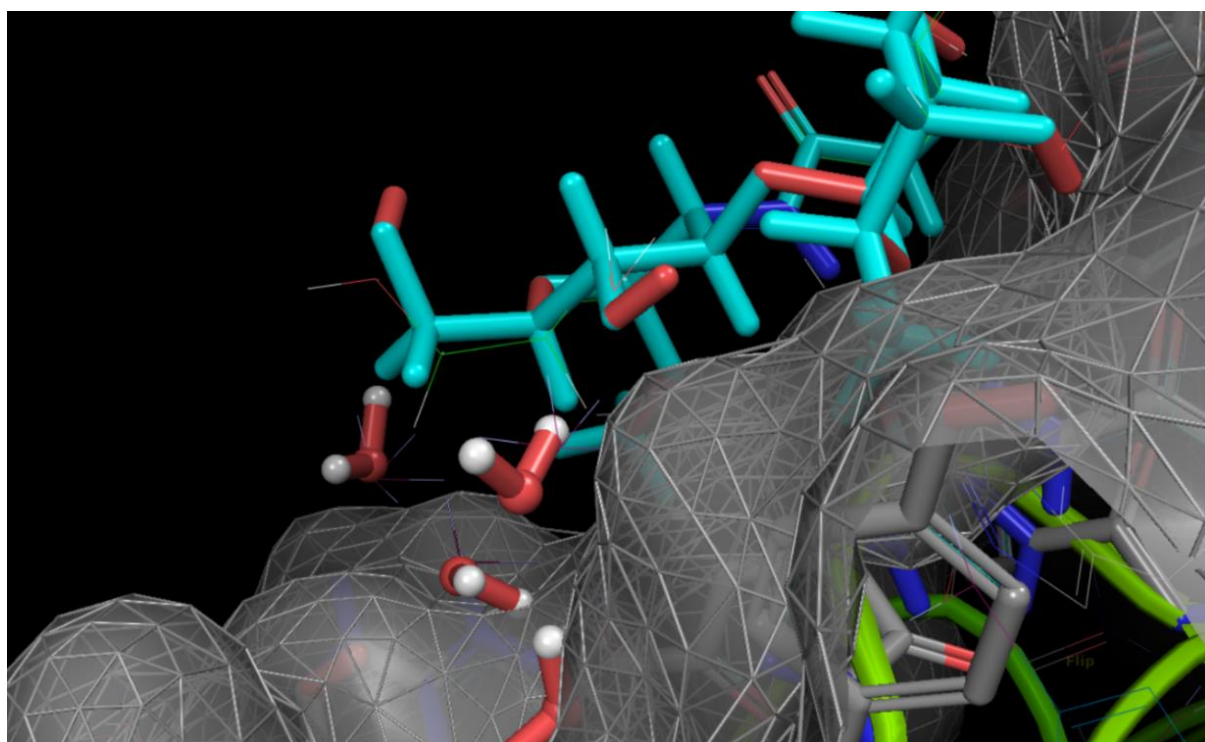


Fig. 99 Paratope of HMM5 Fab docked to ligand Fuc α 1-3GlcNAc. The interaction of the methyl group of fucose with Y99 (heavy chain) is reproduced very well. Crystal data: G. R. Andersen (University of Aarhus), Maestro user: T. Raiber.

6.2.4.3. Man α 1-6 Constitutes an Important Fragment of the Epitope

For the ligand which was co-crystallized with HMM5 Fab, a score of -4.07 was found. This is in the magnitude of the score calculated for sucrose (table 14). Docking experiments with extended carbohydrate chains revealed that the mannosyl branch significantly contributes to the binding. Especially when Man α 1-6 is missing, the score is of the same magnitude as that of the disaccharide. Hence, the Man α 1-6 substituent, and *not* Man α 1-3, is involved in the binding. Another finding is that substitution of Fuc α 1-3 by Fuc α 1-6 significantly improves the score from -6.53 to -8.45 (table 14). Thus, the valence combination Fuc α 1-6 and Man α 1-3, and not Fuc α 1-3 and Man α 1-6, was identified to be necessary for binding. It might be noted that the target structures were not checked for purity or glycosylation heterogeneity. Maybe, the phage display selections have amplified Fuc α 1-6-specific antibodies what can be referred to as a *selection artefact* (*i.e.*, an assignment of specificity to an antibody due to target structures expected but not *de facto* presented to the selected antibody). The MUXF conjugate (MUXF-HSA) was a gift by Altmann who describes the preparation of Fuc α 1-6 containing glycoconjugates in his patent.¹⁴⁸ A review of selection strategies was given by Eldridge *et al.* in 2015.¹⁴⁹ Furthermore, the presence of a β 1-2Xyl substituent results in non-binding properties of the ligand. Maybe, the spacer Man β 1-4GlcNAc β 1-4GlcNAc needs to be an unsubstituted chain, which just connects the two glyco valences with each other (*i.e.*, Man α 1-6 and Fuc α 1-3 in case of the native anti-HRP antibodies). The poor binding property of HMM5 against MUXF in ELISA experiments was traced back to the low quality of the MUXF preparation. If this is the case, the co-crystal HMM5/Fuc α 1-3GlcNAc α 1-OMe shows this selection artefact, too. This would mean that the co-crystal was forced by co-crystallization conditions like PEG and high ligand concentration. This effect is generally known from buffer substances, such as TEA and HEPES, which often become involved into binding modes. The finding of a selection artefact confirms the generally known fact that evolution has certain tendencies but *no goal*.

Table 14: Docking scores for differently extended ligands.

Ligand	GScore
Sucrose (-Ctrl)	-3.45
Free fucose	-4.85
Fuc α 1-3GlcNAc α 1-OMe	-4.07
Man α 1-3(Man α 1-6)Man β 1-4GlcNAc β 1-4(Fuc α 1-3)GlcNAc α 1-OMe	-5.40
Man α 1-3Man β 1-4GlcNAc β 1-4(Fuc α 1-3)GlcNAc α 1-OMe	-4.63
Man α 1-6Man β 1-4GlcNAc β 1-4(Fuc α 1-3)GlcNAc α 1-OMe	-3.99
Man α 1-3(Man α 1-6)Man β 1-4GlcNAc β 1-4(Fuc α 1-3)GlcNAc β 1-NHAc	-6.53
Man α 1-3(Man α 1-6)Man β 1-4GlcNAc β 1-4(Fuc α 1-6)GlcNAc β 1-NHAc	-8.45
Man α 1-3(Man α 1-6)(Xyl β 1-2)Man β 1-4GlcNAc β 1-4(Fuc α 1-6)GlcNAc β 1-NHAc	~100

6.2.4.4. V_H and V_L Domains Internally Cross-Linked by the Two Glyco Valences Fuc α 1-3 and Man α 1-6

Even though the docking experiments indicate HMM5 specificity to be a selection artefact, it is worth to inspect the binding mode because actually it should be still very similar to that of polyclonal anti-HRP antibodies. The interaction maps (fig.s 100-103) show that Fuc α 1-3 and Fuc α 1-6 interact with amino acid residues of the V_H chain, especially the amino acids T30, N32, T52 and F97 are involved (fig. 100). The subunit Man α 1-6 interacts with amino acid residues of the V_L chain (N95, G96, fig. 101). Thus, the glycan seems to be clamped by the V_H and V_L chain what is a plausible mode for binding two necessary glycan valences (fig.s 104-107). The distance between both chains is about 21 Å. A main uncertainty of the presented docking results is that the antibody was kept rigid. In contrast to the antibody, the carbohydrate was allowed to change its conformation. Thus, if an induced fit mechanism plays a significant role (*e.g.*, a conformational change of the loops), this could not be modeled. Such a simulation would need a lot of computational power. That is why the glycan was allowed to be flexible. The largest degree of freedom glycans show are the *dihedral* angles and this was sufficiently accounted.

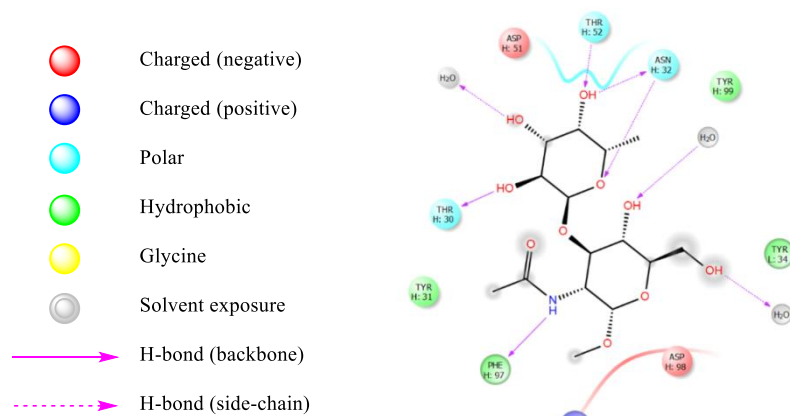


Fig. 100: Interaction map of Fuc α 1-3GlcNAc α 1-OME in simulated interaction with HMM5 Fab. The Fuc α 1-3 valence interacts with the V_H chain (T30, N32, T52, F97). Maestro user: T. Raiber.

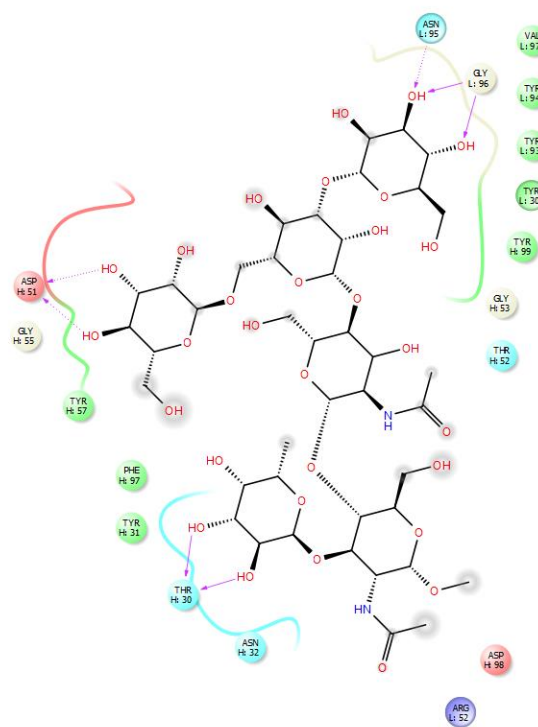


Fig. 101: Interaction map of Man α 1-3(Man α 1-6)Man β 1-4GlcNAc β 1-4(Fuc α 1-3)GlcNAc α 1-OME in simulated interaction with HMM5 Fab. The Fuc α 1-3 valence interacts with the V_H chain (T30) whereas the Man α 1-3 valence interacts with the V_L chain (N95, G96). Maestro user: T. Raiber

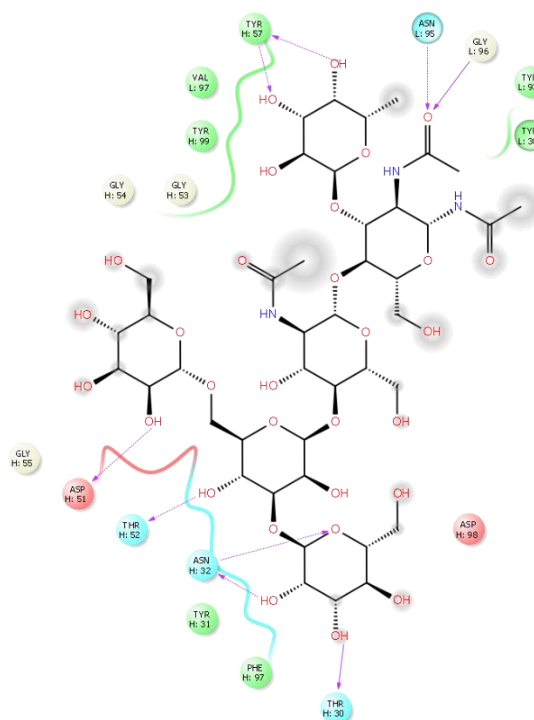


Fig. 102: Interaction map of Man α 1-3(Man α 1-6)Man β 1-4GlcNAc β 1-4(Fuc α 1-3)GlcNAc β 1-NHAc in simulated interaction with HMM5 Fab. In this docking experiment, the glyco moiety interacts with the V_H chain whereas the peptide moiety – represented by β 1-NHCOCH₃ – interacts with the V_L chain. Maestro user: T. Raiber.

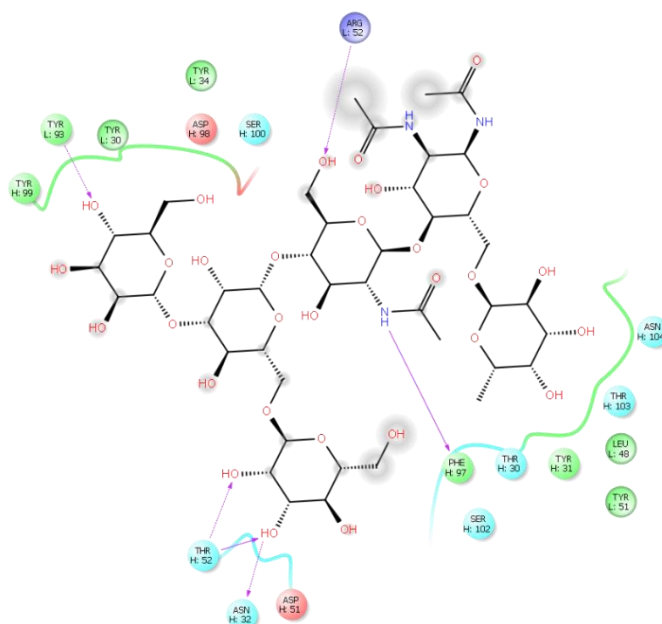


Fig. 103: Interaction map of Man α 1-3(Man α 1-6)Man β 1-4GlcNAc β 1-4(Fuc α 1-6)GlcNAc β 1-NHAc in simulated interaction with HMM5 Fab. The fucose moiety is stabilized by F97 of the heavy chain in the way that the ring protons of the fucose are directed towards the aromatic plane. The Man α 1-6 moiety is stabilized by T52 and N32 of the heavy chain, whereas the Man α 1-3 moiety is stabilized by Y93 of the light chain. Thus, in this simulation, Fuc α 1-6 and Man α 1-3 cross-link V_H with V_L chain. Maestro user: T. Raiber

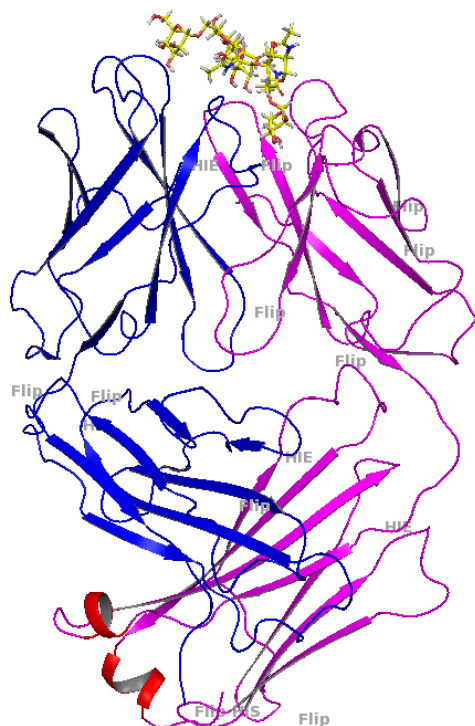


Fig. 104: Cartoon of the hexasaccharide $\text{Man}\alpha 1\text{-}3(\text{Man}\alpha 1\text{-}6)\text{Man}\beta 1\text{-}4\text{GlcNAc}\beta 1\text{-}4(\text{Fuc}\alpha 1\text{-}6)\text{GlcNAc}\beta 1\text{-NHAc}$. It shows the interaction of the $\text{Man}\alpha 1\text{-}6$ moiety (top left) and $\text{Fuc}\alpha 1\text{-}6$ moiety (bottom right) with the heavy chain (blue). The $\text{Man}\alpha 1\text{-}3$ moiety interacts with the light chain. The following pictures (fig.s 105-107) show the interactions in detail. Crystal data: G. R. Andersen (University of Aarhus), Maestro user: T. Raiber.

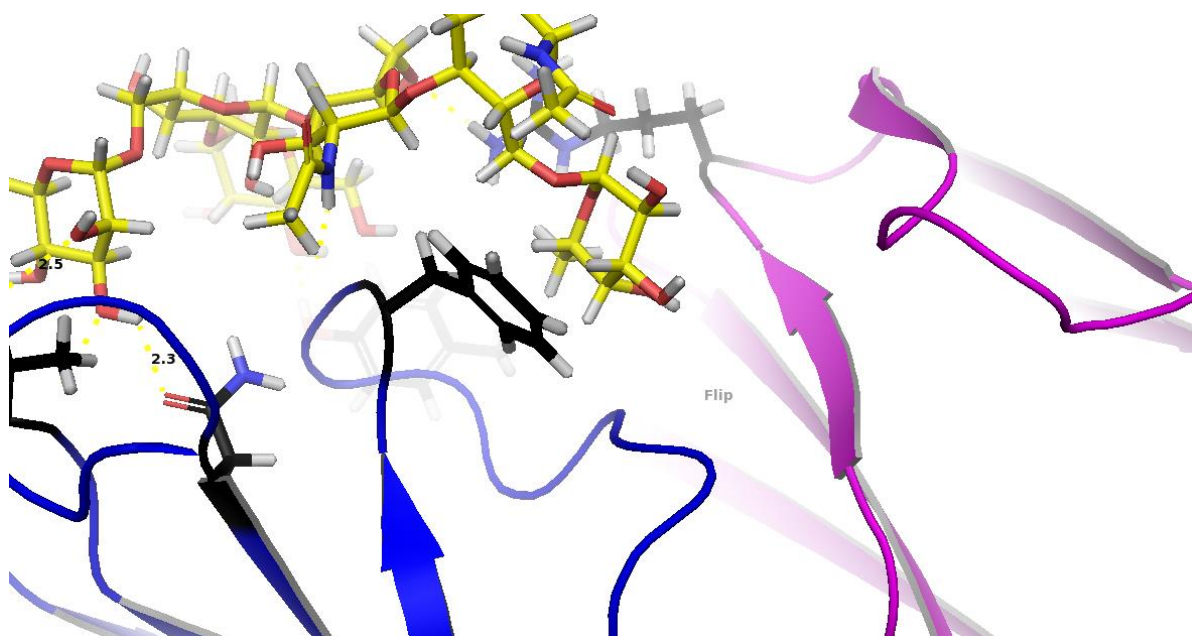


Fig. 105: F97 of the heavy chain interacts with ring protons of $\text{Fuc}\alpha 1\text{-}6$ (center of the picture).

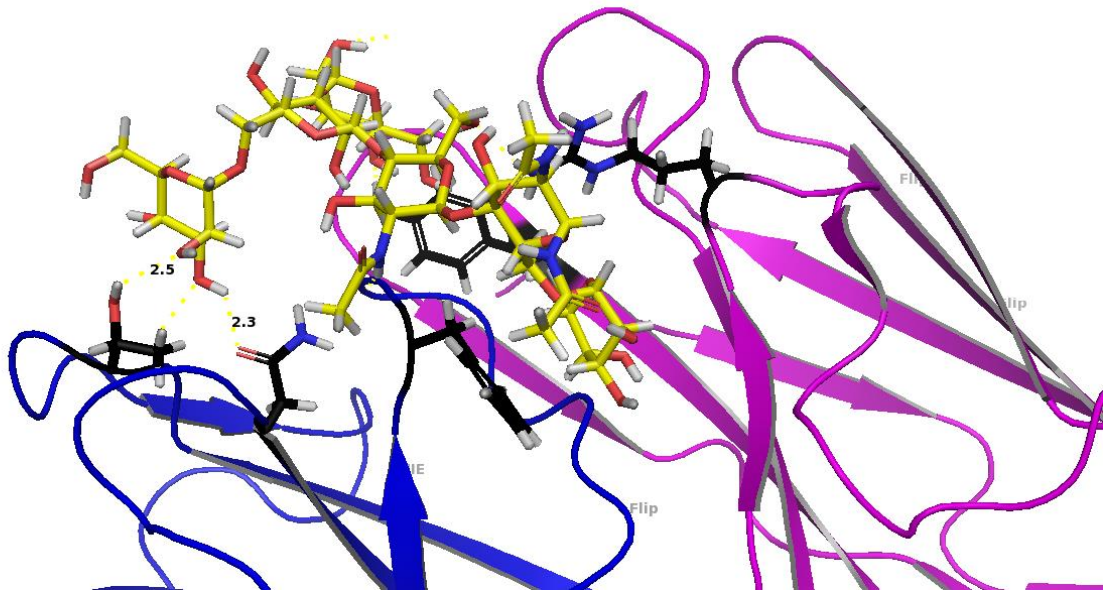


Fig. 106: N32 and T52 of the heavy chain (blue) interact with Man α 1-6 (top left of the picture).

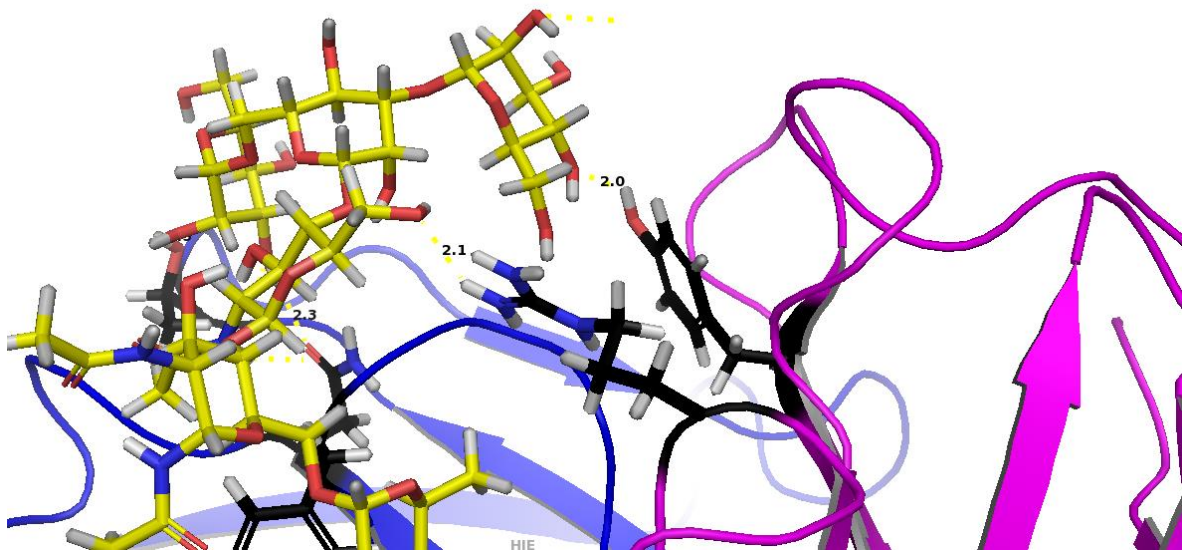


Fig. 107: Y93 of the light chain (magenta) interacts with Man α 1-3 (center of the picture).

7. Discussion

7.1. Trapped in the Quicksand of STD NMR Artefacts

7.1.1. STD NMR Spectroscopy Ended up Building Edifices on Sand

The aim of the present study was to analyze the cross-reactivity of carbohydrate determinants responsible for false-positive results allergy diagnostics. Ironically, false-positive STD NMR results hampered to achieve this aim. Faced with such NMR misinformation, it makes sense to take a closer look at the nature of these STD NMR artefacts in order to draw lessons for the future.

7.1.2. An Artefact is an Incorrect Rejection of the Null Hypothesis

According to the Oxford Dictionary, an artefact (from Lat. *arte factum* = made by using art) is “s.th. observed in a scientific investigation or experiment which is not naturally present but occurs as a result of the preparative or investigative procedure. `Researchers need to question whether the phenomena observed are real or an artefact of the experimental methodology used.`
`This is a flash artifact and is observed also when the flash is ignited in the empty spectrometer.”¹⁵⁰ This definition relates to the fact that artefacts are caused by the measuring instrument not following the main logic of the measuring principle but being influenced by an undesired side effect.

In statistics, an artefact is an incorrect rejection of the null hypothesis. A null hypothesis is a statement that says that there is *no* relationship or effect. For instance, probands treated with a drug will *not* show changes that differ from the control group. The basic result of a hypothesis test is that the results are statistically significant or insignificant. If the researcher incorrectly rejects the null hypothesis, this is called artefact or false positive (*i.e.*, the results appear to support the hypothesis but were only due to chance). For instance, an *ineffective* treatment appeared effective because the scores in one group differed from another by chance. For the sake of completeness, a false negative is an incorrectly accepted null hypothesis. That is, due to sampling error, the results appear to show no difference between the treatment and control conditions when the treatment actually is *effective*. This kind of artefact could be revealed by subjecting the STD NMR data to paired *t*-tests as well as setting detection limits.

The statistics have already been sufficiently discussed. Only the technical origin of the STD NMR artefacts shall therefore be investigated in greater detail.

7.1.3. Phage Display Study Misguided by STD NMR Artefacts

To observe interactions, the respective system must be positioned into an artificial environment, either *in vitro* or *in silico*. As a consequence, all observables become influenced artificially. Thus, artefacts must be taken into account when interpreting the acquired data. Often, they are already well known and described in literature and ways of correction are available (Xia *et al.*, 2010).¹⁰³ Routinely, positive and negative controls should reveal them and keep under control. If studies are carried out without this accuracy, artefacts may remain unrecognized and lead to fatal conclusions. The present study is an example of such misguidance by unrecognized artefacts. The STD NMR artefacts have been of such a magnitude that spurious epitope mappings and K_D determinations were carried out based on pure artefacts. In not a single case, a synthesized CCD substructure bound to a phage display-derived monoclonal antibody. However, the conclusions could be corrected and the importance to consider artefacts could be outlined. This STD NMR study contributes towards avoiding such misguidances in the future.

7.1.4. STD NMR Artefacts Caused by Irradiation Anomalies

The immune reactivity of polyclonal anti-HRP rabbit IgG against the disaccharide Fuc α 1-3GlcNAc was tested false-positive. Efforts to find the cause of STD NMR artefacts affecting this study have not yet carried out. However, inspection of the literature revealed four principle causes of STD NMR artefacts:

- i. Unspecific binding
- ii. Bloch-Siegert shifts
- iii. Power spill-over
- iv. any instability of the spectrometer (*e.g.*, vibrations, uncalibrated r.f. pulses)

Since the STD experiments have been repeated on another spectrometer without any appearance of artefacts, unspecific binding as a cause of the artefacts in this study can be ruled out because this type of artefact just depends on the nature of the receptor ligand system and should therefore appear independently of spectrometers. Subtraction of the on- and off- resonance with involved Bloch-Siegert shifts results in a difference spectrum with dispersed signal shapes. Hence, this cause is also ruled out. By exclusion of these two causes, power spill-over and spectrometer instability are the most likely causes of the STD NMR artefacts appearing in this study. The cause of the artefacts misleading the present phage display study may be traced back to a power spill-over of radio frequency irradiation to the ligand in the way that a strong radio frequency

partially saturates some resonances of the ligand. STD NMR artefacts are typically favored by the parameterization of the saturation pulse. Power spill-over is favored in three possible ways:

- i. Increasing the amplitude of the Gaussian pulse
- ii. Decreasing the Gaussian pulse width (*i.e.*, increasing the bandwidth of excitation)
- iii. Moving the irradiation position close to ligand resonances

Typically, the artefacts from power spill-over occurred close to the on-resonance irradiation position. Another origin of artefacts might be the processing of both spectra with unsuitable LB value, which not allows precise subtractions. Finally, epitope maps based on overlay plots of on- and off- spectra with a difference spectrum showing no STD effects should be treated as questionable results. The artefact signals show a Lorentzian line shape and thus are no typical Bloch-Siegert artefacts, which are characterized by a dispersive signal shape. The STD NMR artefacts may arise rather from unspecific binding since OMe, NHAc and CH₃ (H-6', C-6') are hydrophobic groups or, they are caused by power spill-over. That their intensities vary independently from each other but dependent on parameterization is a pointer to power spill-over as a technical cause. It is not excluded that they are of another origin, especially an electronic cause which affects the subtraction of on- and off- spectra is suggestable. However, these artefacts are not of a magnitude that should actually irritate and are insufficient to map an epitope. Questions regarding the cause of the STD NMR artefacts and the way of processing the STD NMR data resulting to false-positive epitope maps and K_D values remain yet open. The artefact intensities resulted from irradiation at different chemical shifts strongly indicated that the Gaussian pulse is approximately ± 4.5 ppm broad and thus unsuitable for a selective saturation of an antibody. Phages with potential affinity to core-3 fucose without a mannosyl branch were not secured or amplified by the selection strategy carried out in this study. As expected, the phage display-derived antibodies did not bind to Fuca1-3GlcNAc. Collot *et al.* have already shown that mannosyl residues are necessary for a binding. Reactivity phage ELISA data confirm this finding, too (Eckenberger, **2012**). From the insights described above, a guideline for STD NMR experiments has been formulated.

7.1.5. Method Validation Guidelines

In the course of the study, the following guidelines have proven to ensure the confidence in the integrity of STD NMR data.

- i. To ensure sample quality, the check sheet attached (*¹H-Check*) may be helpful.
- ii. The *stability* of the spectrometer (vibrations, temperature, gauge of the spinner, calibration of Gaussian pulses, saturation of the lock signal) should be checked.
- iii. To analyze cross-reactivities, it is advisable to exercise with a cheap and well-characterized model system (e.g., anti-TNP/RDX) beforehand.
- iv. *STD build-up* experiments reveal the optimal parameterization conditions for the given receptor-ligand structure (*i.e.*, maximum STD effects, minimum artefacts). Here, a *check sheet* would provide several benefits (*e.g.*, to eliminate mistakes, to reduce decision fatigue and to drive consistency). In particular, the attenuation of the selective saturation pulse (SPW9) should be 40 to 60 dB, the saturation time (D20) 0.25 to 5 s and the spin-lock time $T_{1\rho}$ (D29) 10 to 50 ms. The longer the saturation pulse the higher is the degree of selectivity, typically it is 50 ms. The STD experiment should be optimized for the values for on-resonance in the frequency list. The frequency list consists of on-resonance (-3 to 0 ppm, very upfield methyl groups) and off-resonance (± 30 to 40 ppm).
- v. STD effects should always be calculated by *subtracting* on from off-resonance, *not* by estimation from overlays, and quantified with *absolute* instead of relative values. The reason to favor subtraction of on- from off-resonance spectra over calculation from overlays is obvious immediately: The difference is *adjusted for any kind of instability*, because instabilities influence on- and off-traces in the same way and to the same degree, such as noise is generated on both traces ($N_{\text{off}} - N_{\text{on}} \approx 0$), and thus the differences give far less rise to false positives.
- vi. Any STD NMR experiment should be validated by *control experiments*. The off-resonance spectrum is an *insufficient* negative control experiment. A negative control is ligand without receptor. A non-binding solute (*e.g.*, sucrose or maleic acid) is a recommended internal negative control.
- vii. To determine the *reproducibility* of the test method, a round robin test is advisable.
- viii. The STD effects need to be *statistically significant*.

7.2. Study Suffered from Confirmation Bias

A confirmation bias is the tendency to search for or interpret information in a way that confirms preexisting beliefs, expectations, or a hypothesis in hand.¹⁵¹ In addition, individuals discredit information that does not support their view. Even scientists can be susceptible to confirmation bias.^{152,153,154} In this study, the preexisting hypothesis can be represented by the title of a publication, which was aware to all participants: “Fucose α 1,3-linked to the core region of glycoprotein N-glycans creates an important epitope for IgE from honeybee venom allergic individuals.” (Tretter *et al.*, **1993**). Probably, this statement was interpreted in the way that the α 1-3 fucose is necessary and sufficient to be recognized and bound by anti-honeybee venom IgE antibodies (*i.e.*, fucose is bound if it is “ α 1,3-linked”). Probably, less importance was attributed to the addition “to the core region of glycoprotein N-glycans”. Now the misinterpretation (*i.e.*, the origin of the confirmation bias) can be identified: The core region of such glycoproteins is referred to as *core C*, which is a *pentasaccharide* (fig. 7). The saccharide tested in this study was Fuc α 1-3GlcNAc, wherein GlcNAc is just a small fragment of the core C. The possibility that a second valence (provided by the core C) could be necessary for a binding has therefore never taken into consideration. The confirmation bias prevented a hypothesis that a terminal mannose might be necessary to facilitate a binding. It subconsciously influenced decisions and interpretations in a fatal way: An antibody selection against Fuc α 1-3GlcNAc was skipped. False-positive epitope maps were adapted to the preexisting hypothesis (fig. 108). A non-binding event of Fuc α 1-3GlcNAc in an SPR experiment was explained by “steric hindrance”, what means that the explanation was adapted to the preexisting hypothesis, too. The overlay method was identified as the *root cause* of false-positive epitope maps: It is *too error-prone* to be used to calculate STD effects. But it is suitable to control congruence between on- and off-spectrum. That STD differences of ring protons equaling zero have been calculated from overlays of on- and off-spectra in disregard of incongruent baselines, gives rise to the suspicion that other STD NMR studies are affected by false-positives, too. At this point, the question arises why the previous study (Plum *et al.*, **2011**) was not suffering from confirmation bias: The α -Gal epitope is *monovalent*.¹⁵⁵ Furthermore, K. Wallach included control experiments in the STD NMR experiments. Fortunately, the epitope maps of the study at hand were challenged by a measurement on another NMR spectrometer.

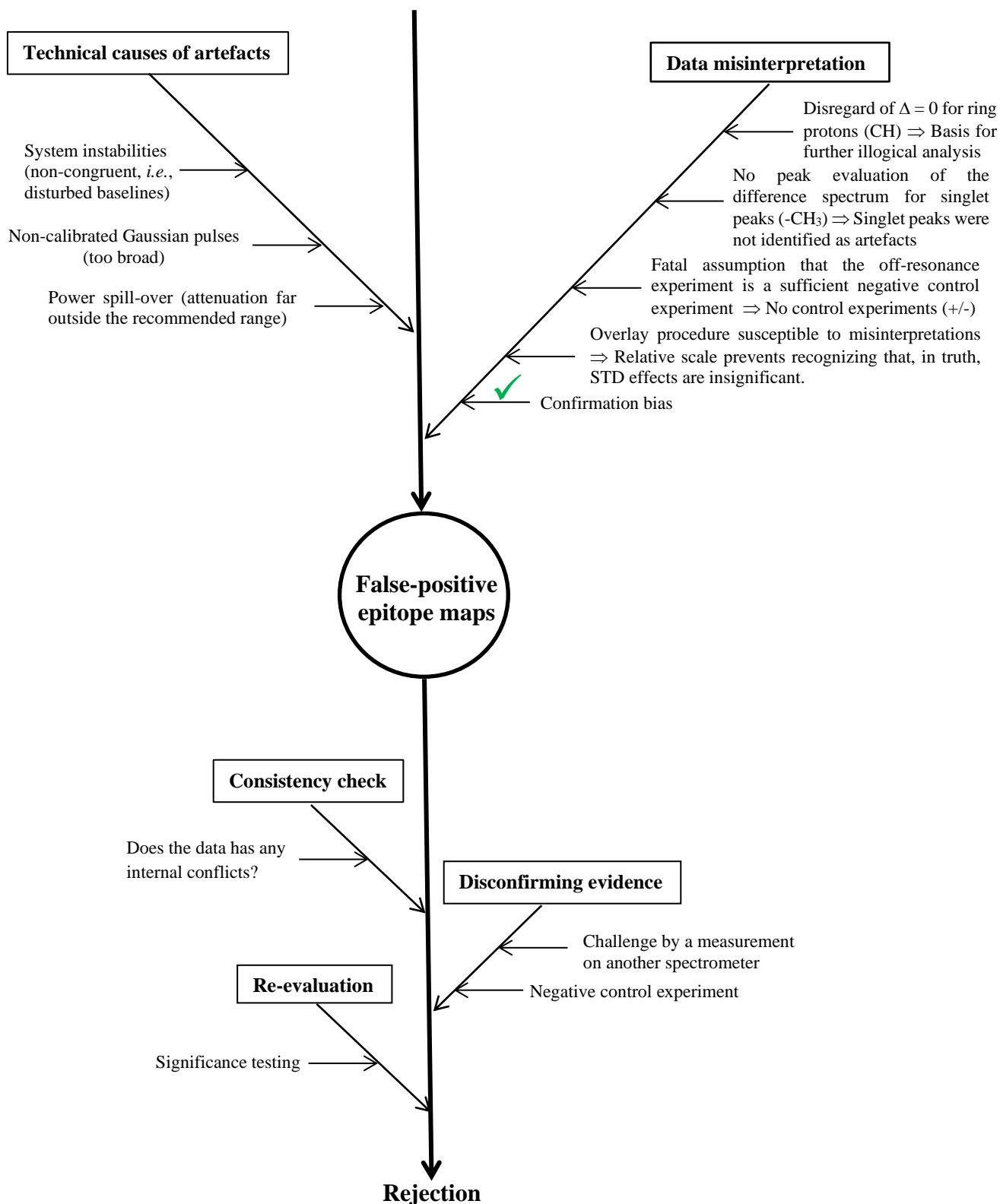


Fig. 108: Fishbone diagram showing generation and falsification of the epitope maps. STD artefacts fed into STD data and remained unrecognized. The applied procedure to analyze STD data was not able to identify artefacts. The epitope maps were wrongly confirmed by a confirmation bias. The green hook shall symbolize this fatal confirmation. The consistency check was the initial point of questioning the data. A measurement on another NMR spectrometer was necessary to provide a disconfirming evidence and to rate the maps as false positives. A viable quality assurance procedure, by which the STD data could be re-evaluated, was developed.

7.3. A Co-Crystal with Questionable Information Value

7.3.1. Missing Crossroad Between Phage Display and Synthesis of CCD Substructures

The study was conceptualized as two ways crossing at a biopanning step (*i.e.*, antibody selection against CCD substructures). Biopanning is the first *in vitro* interaction and therefore the key step to generate affine antibodies. Unfortunately, this step was skipped. The reason for this may be explained by STD NMR testing polyclonal anti-HRP rabbit IgG false-positive for immune reactivity against Fuc α 1-3GlcNAc. Here, artefacts played an irritating role. To guard against confusion, an SPR experiment was carried out to validate the binding of Fuc α 1-3GlcNAc to monoclonal anti-HRP antibodies. Fortunately, the target compound was already available because it was originally intended to immobilize for phage selection and binding detection by ELISA (fig.s 22 and 24). The immobilized disaccharide **15** could be detected by AAL (+Ctrl), but the monoclonal antibodies HHH1 and HMM5 showed no binding. From a technical point of view, a possible reason the selected anti-HRP antibodies do not bind Fuc α 1-3GlcNAc is that the targets differ considerably in size and shape (HRP: 44 kDa; Fuc α 1-3GlcNAc: 0.4 kDa).

7.3.2. Docking Confirms Co-Crystal Data and Identifies Fuc α 1-3GlcNAc as a Weak Binder

Surprisingly, in contrast to STD NMR and SPR results, the binding of Fuc α 1-3GlcNAc could be shown by co-crystallization with HMM5. That the disaccharide in the co-crystal might be an artefact, too, could be ruled out because the ligand is attached to the CDR loops (heavy chain) and shows sufficient electron density validated by ccp4 data. The docked structure reproduced the pose of the co-crystal structure very well but with low score (-4.07), indicating a low affinity. This result also suggests that the co-crystal was generated under extreme and unphysiological conditions, meaning that the disaccharide was probably forced to co-crystallize with HMM5 Fab under extreme conditions (high concentrations of PEG and disaccharide).

7.4. Postulate of a Two-Glyco-Valences Binding Model

7.4.1. Findings of this Study in Harmony with Findings of a Previous Study by Hypothesis of a Two-Glyco-Valences Binding Model

At first glance, all results seemed to be contradictory. But molecular modeling reproduced the binding shown by co-crystallization data very well and identified Fuc α 1-3GlcNAc as a very weakly binding ligand (low score but well reproduced pose). The low ELISA signal of anti-HRP antiserum binding GlcNAc β 1-4(Fuc α 1-3)GlcNAc (fig. 18) corresponds to the true-positive but statistically insignificant STD effects of anti-HRP antiserum binding Fuc α 1-3GlcNAc (fig. 78B). The monoclonal antibodies HHH1 and HMM5 have obviously lost this low binding activity (fig. 67). Immobilized CCD fragments (MUX, MMX, F³ and F³F⁶ core fragment) show extremely low or even no ELISA binding signals with anti-bee venom serum and patient sera (Collot *et al.*, 2011). Remarkably, MUX fragment and F³ core fragment would show no binding, while BSA-MUXF³ (*i.e.*, the *composite* of both fragments) was used as *positive control* (U = unoccupied, *i.e.*, α 1-3Man is *missing*). This finding indicates that *two glyco valences* are necessary for binding anti-bee venom antiserum. Besides, both valences must be linked since a mixture of Man α 1-6Man and Fuc α 1-3GlcNAc shows no binding in STD NMR experiments. This means that the STD effects depicted in fig. 51A *do not* represent the fingerprints of the main fucose-specific anti-HRP fraction, but rather originate from a tiny anti-CCD antibody fraction, which is able to bind α 1-3 core fucose as a *single glyco valence*. In contrast to the anti-HRP antiserum, HHH1 and HMM5 have probably lost the *single glyco valence* binding activity completely, presumably because the antibodies which use the *two-glyco-valences* binding mode were *amplified* during the panning process, whereas the tiny fraction of single valence binding antibodies was washed away. The two valences must be α 1-6Man and α 1-3Fuc, bridged by Man β 1-4GlcNAc β 1-4GlcNAc (*i.e.*, Man α 1-6Man β 1-4GlcNAc β 1-4(Fuc α 1-3)GlcNAc; fig.s 109A and 110A).

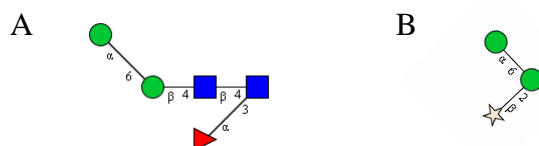


Fig. 109: Postulated minimal motifs with Fuc α 1-3 and Man α 1-6 (**A**) and Xyl β 1-2 and Man α 1-6 (**B**) as binding glyco valences. With this postulation, the binding signals of the literature can be explained. If one of the two glyco valences is missing, the binding will collapse, which can be seen in the literature data (fig. 18) and is sufficiently shown in the present study under the guise of no binding signals (*e.g.*, STD NMR experiment with a mixture of Fuc α 1-3GlcNAc and Man α 1-3/6Man). Obviously, an induced fit mechanism is underlying.

Because the co-crystal data show that only the V_H domain binds fucose (table 13), it is logical that the V_L domain becomes involved to bind the other glyco valence ($\text{Man}\alpha 1-6$). Such an internal cross-linking of V_H and V_L domain is suggested by molecular docking, too (see above). Simultaneous binding of both valences supposedly results in an *induced fit* as the typical binding mode of antibodies (fig. 19). Hence, the *glyco rack*, itself unreactive, consists of $\text{Man}\beta 1-4\text{GlcNA}\beta 1-4\text{GlcNAc}$. It just connects the two valences over a distance of around 21 Å. The same applies to $\text{Xyl}\beta 1-2$ and $\text{Man}\alpha 1-6$ (*not* $\text{Man}\alpha 1-3$) (fig.s 109B and 110B). Since $\text{Xyl}\beta 1-2$ is not binding HMM5 (table 14), anti-xylose antibodies must be an extra fraction. $\text{Xyl}\beta 1-2$ seems to play an inferior role at all. In 2015, Brzezicka *et al.* have shown that „core xylose markedly reduced or completely abolished binding [...] to DC-SIGN [...]”. The reason given was that “core xylose distorts the conformation of the unsubstituted glycan, with important implications for the immunogenicity and protein binding properties of complex N-glycans” (for more on this topic, see chapter 7.4.5.).¹⁵⁶

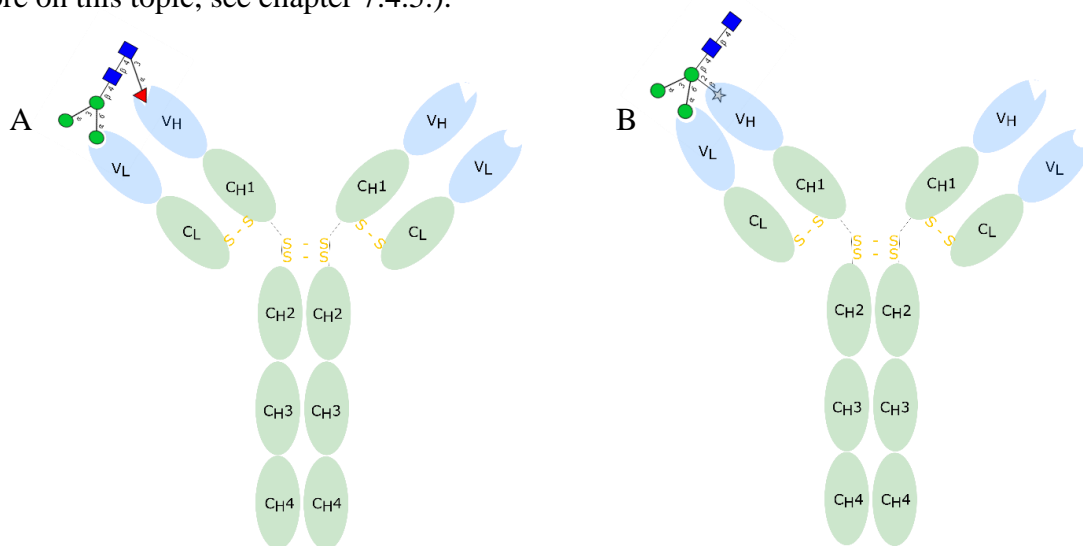


Fig. 110: Illustration of a two-glyco-valences binding hypothesis for two anti-CCD antibody fractions. **A:** Binding of $\text{Fuc}\alpha 1-3$ by the V_H and $\text{Man}\alpha 1-6$ by the V_L domain results in an induced fit (polyclonal anti-HRP rabbit IgG; polyclonal anti-CCD IgE of allergy patients). The same binding principle was applied to the xylose-specific fraction (**B**): Binding of $\text{Xyl}\beta 1-2$ by the V_H and $\text{Man}\alpha 1-6$ by the V_L domain. The postulated minimal motif $\text{Xyl}\beta 1-2(\text{Man}\alpha 1-6)\text{Man}$ with binding glyco valences underlined and a bridging mannose rack gives rise to strong ELISA signals (fig. 18). The depicted antibodies represent distinct fractions.

The additional $\text{Man}\alpha 1-3$ subunit *just slightly* improves the binding affinity of anti-HRP serum to $\text{Xyl}\beta 1-2(\text{Man}\alpha 1-6)\text{Man}$ (fig. 18). Obviously, anti-CCD antibodies behave logically. The two-glyco-valences binding model is likely the reason why the SPR and STD experiments showed no binding events, but co-crystal and molecular docking showed bindings due to *complementarity*. Based on these conclusions, even for the postulated second valence, $\text{Man}\alpha 1-6$, a co-crystal structure should be obtained as likely as for the first valence, $\text{Fuc}\alpha 1-3$. Despite

misguidance by STD NMR false-positive results, the double-valence binding model harmonizes all obtained data, including true-positive, statistically insignificant (anti-HRP) as well as true-negative (HHH1, HMM5) STD NMR, true-negative SPR (HHH1, HMM5) and true-positive crystallographic (HMM5) results.

7.4.2 Hypothesis II. Two-Glyco-Valences Recognition is a Logical Consequence of Self-Tolerance to Le^x and sLe^x

Sialyl Lewis^x (sLe^x, CD15s, fig. 111B) is known to play a vital role in cell-to-cell recognition processes. In case of an infection, lymphocytes (effector T cells and neutrophils) migrate from the blood to the site of inflammation and use a selectin-mediated rolling mechanism for adhesion to endothelial cells, which present sLe^x as an adhesion molecule.¹⁵⁷ Both sLe^x and Le^x (fig. 111) are important blood group antigens. They are attached to the terminus of glycolipids on the cell surface of granulocytes and monocytes and mediate inflammatory extravasation of these cells. These examples show that the fragment Fuc α 1-3GlcNAc is present in the blood in *large amounts*.

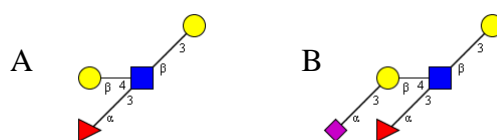


Fig. 111: Le^x (A) and sLe^x (B) are mammalian adhesion molecules and contain Fuc α 1-3GlcNAc. The adhesion to sLe^x on endothelial cells and platelets is mediated by selectins on the surface of lymphocytes. sLe^x is displayed by endothelial cells and platelets at the site of inflammation. Both carbohydrates are displayed by granulocytes and monocytes. An anti-CCD antibody must *distinguish* self- from non-self Fuc α 1-3GlcNAc.

Hence, anti-CCD antibodies with a specificity against α 1-3 core fucose as a *single valence* would induce an *autoimmune* response (type II hypersensitivity) resulting in a collapse of the *whole* immune system. This consideration shows that anti-CCD antibodies *must distinguish between self and non-self-carbohydrates*. The two-glyco-valences binding hypothesis gives a plausible suggestion of how they do it. It is a *principle* of the adaptive immunity to rely on *two* signals (co-stimulation), for instance, naïve T cells are activated by dendritic cells, which present an MHC/antigenic peptide complex (first signal) and CD80/86 (second signal). CD80/86 is expressed when the dendritic cell has recognized a *pathogen-associated pattern* (LPS, bacterial carbohydrates). That such principles are applied for recognition of glyco patterns was shown at the example of human anti-Neu5Gc antibodies against the Hanganutziu-Deicher antigen (requirement of two adjacent Neu5Gc, fig. 1). In **1992**, Lund-Johansen *et al.* indirectly supported the two-glyco-valence hypothesis by describing that sLe^x and Le^x (CD15) mediate phagocytosis: The carbohydrate antigens displayed by granulocytes and monocytes are

cross-linked by anti-CD15 and anti-CD15s antibodies. Hence, they are “receptors capable of signal transduction”.¹⁵⁸ This signal induces degranulation and oxidative burst. Though it is a dogma of immunology that tolerance to self-antigens is to be realized by *negative selection* in the thymus, the function of the mechanism described by Lund-Johansen *et al.* could be that CD15 and CD15s provide *autoantibody clearance*. This would also support the two-glycovalence binding hypothesis: Anti-CCD antibodies are *unable* to bind Le^x. If there is generated an antibody with specificity to α 1-3 core fucose as a *single* glyco valence, it is cleared by adsorption. The same may apply to AB0 blood groups.

7.4.3. Hypothesis III. Blood Groups are Natural Vaccination Gaps in the Population, which Break the Vicious Circle of the Red Queen Effect

The hypothesis of ‘clearance by adsorption’ would explain why antibodies against other blood groups persist in the blood (speculations): They are *not cleared*. In contrary, antibodies against the blood group (self) are *cleared* (self-tolerance). The benefit of this is that pathogenic *mimicry* of blood groups would be neutralized by IgG antibodies (antibody-dependent cellular cytotoxicity or complement-mediated antibody cytotoxicity).¹⁵⁹ Pathogenic mimicry of blood group A is eliminated by individuals with blood group B or 0. The best protectors of a population are individuals with blood group 0 (anti-A and anti-B antibodies). This hypothesis would mean that the individual immune systems *cooperate* at the level of a population. A blood group *distribution* in a population guards against *adaptive* mimicry by pathogens. Such ‘social side-effects’ are already known from vaccinations (*e.g.*, herd immunity).¹⁶⁰ This comparison once again shows that the *antibodies* against the blood groups provide the protection. These are generated due to exposition of the baby to bacterial and food antigens, which are similar enough to cause *cross-reactions*.¹⁶¹ IgM antibodies generated in the first 6 months of life *perform* antibodies against blood group antigens. This is a *natural vaccination*. The blood group distribution creates vaccination gaps in the population (*e.g.*, an individual with blood group A is not vaccinated against pathogenic mimicry of A but B). These gaps might ‘hide’ selection pressure on pathogenic mimicry and in this way break the vicious circle of the Red Queen effect (fig. 6), what means that the glycan conflict was ‘appeased’. However, the α 1-3 fucosylated core C (parasites, insect venoms) is immunogenic (in contrast to α 1-6 core fucose of mammals), and to distinguish it from Fuc α 1-3GlcNAc occurring in *self*-antigens, such as Le^x and sLe^x, a second valence, a ‘co-valence’, is necessary. According to the two-glyco-valences binding hypothesis, this valence is delivered by the core C (Man α 1-6). On the time scale of the human

evolution, the migrations of *H. sapiens* 50 to 60 thousand years ago are associated with the confrontation with new bacterial and food antigens. As a consequence of this, the human immune system was under selection pressure by parasites mimicking the human adhesion molecules and created a way to arrange with its new pathogenic environment by *using* the new bacterial antigens as natural vaccines and *distributing* blood groups as ‘strategic’ vaccination gaps. In this way, the ‘glycan war’ was tackled at the level of the early human populations. But a distinction between self- and non-self carbohydrates was still mandatory, which is best carried out by ‘check points’ on cell surfaces in tissue boundaries between body and pathogenic environment: A receptor against *non-self* Le^x was necessary.

7.4.4. Hypothesis IV: Two-Glyco-Valences Binding Model Explains Self-Tolerance to Blood Group 0

The anti- α -Gal IgG antibody (human natural antibody, 1 % of circulating IgG) does not bind to the blood group B antigen because Fuc α 1-2 sterically prevents a binding. Removal of Fuc α 1-2 converts the B antigen into the α -Gal-epitope and results in binding of anti- α -Gal antibodies.¹⁶² Anti-A and anti-B antibodies “require the complete blood group structure for binding”.¹⁶³ In the same time, they are not allowed to bind blood group 0 (self-tolerance). Following the two-glyco-valences binding model, anti-A antibodies require Fuc α 1-2 and GalNAc α 1-3, while anti-B antibodies require Fuc α 1-2 and Gal α 1-3 (table 15). In **2014**, Makeneni *et al.* have docked blood group A to an anti-A scFv antibody and demonstrated that one single amino acid (His^{L49} stabilizing the NHAc moiety of GalNAc) is able to induce a fit of three groups of amino acids (group 1 for GalNAc: His^{L49}, Tyr^{L50}, Asn^{L34}; group 2 for α -GalNAc: Trp^{H100}, Trp^{L96}; group 3 for Fuc: Gly^{L91}, Asn^{L92}), resulting in affinity.¹⁶⁴ In case of α -Gal (B-antigen), this fit is *not* induced due to the missing NHAc moiety, resulting in a *loss* of affinity. Generally speaking, a strong interaction with a first (non-self) glyco valence (α -GalNAc or α -Gal) results in an induced fit involving a second (self) glyco valence (Fuc α 1-2). Consequently, when the first glyco valence is missing (*e.g.*, blood group 0), there is no binding (fig. 112). This principle applied to anti-HRP antibodies means that an induced fit mechanism initiated by the first glyco valence (*i.e.*, Xyl β 1-2 or Fuc α 1-3) results in a fit to the second glyco valence (*i.e.*, Man α 1-6).

Table 15: Application of the two-glyco-valences binding model to anti-A and anti-B antibodies. The terminal sugar (*i.e.*, α -Gal or α -GalNAc) initiates an induced fit to the core sugar (*i.e.*, Fuc α 1-2). This mechanism prevents an autoimmune response against blood group 0.

Blood group		IgG Antibodies against	
0		A B	α -GalNAc, Fuc α 1-2 α -Gal, Fuc α 1-2
A		B	α -Gal, Fuc α 1-2
B		A	α -GalNAc, Fuc α 1-2
AB		Neither anti-A nor anti-B antibodies	-
α -Gal		Anti-Gal (always present)	Gal α 1-3

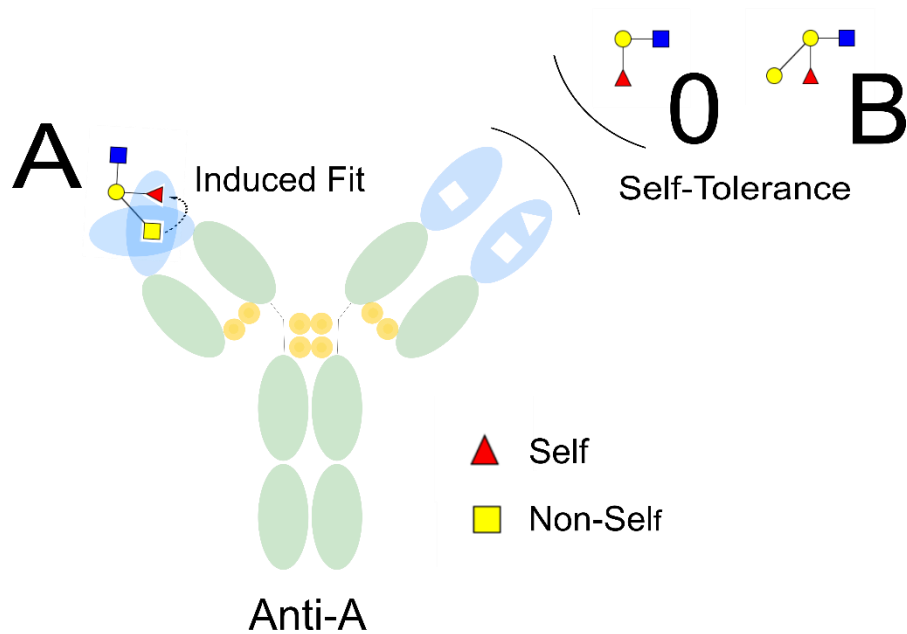


Fig. 112: Application of the two-glyco-valences binding model to blood groups. In any case, Fuc α 1-2 is self. Only an initial interaction with a non-self-glyco-valence (here: GalNAc) involves it in a binding (induced fit). In case of blood group 0, there is no trigger to involve Fuc α 1-2 in a binding (self-tolerance). Illustration adapted to Makeneni *et al.*, 2014.

7.4.5. Hypothesis V. Anti-CCD Antibodies are a Logical Consequence of Antigen Capture by the Innate Immune Receptor DC-SIGN

The examples mentioned above show that mammals have developed sLe^x and Le^x for communication between immune and other somatic cells. In 2010, van Die and Cummings described “*glycan gimmickry by parasitic helminths*” as a “*strategy for modulating the host immune response*” with Le^x playing a key role. It has not escaped notice that mammalian wounds show a *gradient* of Le^x (self), which might have played a key role in the development of glycan gimmickry: Wounds invaded by granulocytes and monocytes show a concentration gradient of Le^x because both types of phagocytes use their Le^x molecules to pass the endothelium but then change their habitus from round to dendritic. Besides, phagocytes seem to be an unsuitable nutrition for pathogens. Hence, a mimicry was perhaps the most efficient way to escape these immune cells. Wounds seem to be predestined to act as natural ‘pans’ for the evolution of glycan gimmickry. Due to mimicry, the mammalian immune system had to develop an immune receptor to detect parasite-associated Le^x. This receptor is DC-SIGN (CD209; fig. 113). It is a balancing act to *defend* against a parasite-associated ‘self’-antigen (Le^x as a decoy) *and* to maintain *self-tolerance* to this self-antigen. It is generally known that APCs are not able to distinguish self from non-self in the preparation of peptides (12-25 amino acids, 1-3 kDa) and that the phagocytosis generates peptide fragments quite arbitrarily. But the APCs can recognize the parasite-associated molecular patterns with their PRRs (*e.g.*, DC-SIGN) and in this way control the T cell response. The parasite-associated antigens certainly reveal their self by imperfections (LDNF *vs.* Le^x, high epitope density). DC-SIGN takes them

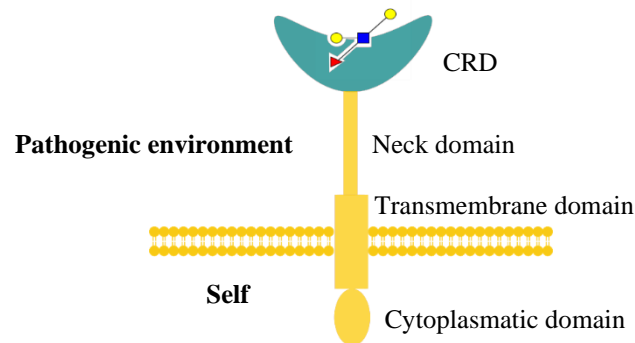


Fig. 113: DC-SIGN captures *non-self* Le^x by its carbohydrate recognition domain (CRD). The immune system must distinguish between self-Le^x on the surface of somatic cells and pathogenic mimicry-derived non-self Le^x. The migrations of *H. sapiens* 50 to 60 thousand years ago were probably associated with a confrontation with new pathogenic and food antigens. The study presented here hypothesizes that the generation of an anti-Le^x CRD and a blood group distribution tackled the new pathogenic environment. Nowadays, uptake of antigens, which are cross-reactive to Le^x (*e.g.*, insect venoms, plant glycoproteins) gives rise to type I hypersensitivities (T_H2 pathway). According to the hygiene hypothesis, an uptake of bacteria (LPS) in a *rural* environment (stables, manure) favors the T_H1 pathway with IL-2 inhibiting type I hypersensitivities. LPS is taken up by TLR4 on the surface of the DCs. DC-SIGN cannot recognize Xylβ1-2.

up for a 'sequence check' by T_H0 cells. Indeed, literature data give evidence that DC-SIGN is *specific* for "mannose- and fucose-containing glycans" (e.g., HIV gp120 and Le^x).¹⁶⁵ Hence, the specificity of DC-SIGN to both glyco valences is *predisposed in the genes* of the innate immune system and is associated with parasites (*S. mansoni* soluble egg antigens Le^x and LDNF).¹⁶⁶ This clarifies that type I hypersensitivities are a misfiring of a defense against parasites due to *cross-reactions*. Schistosome Fuc α 1-3- and Xyl β 1-2-containing N-glycans are strong inducers of T_H2 responses.¹⁶⁷ Presentation of antigen fragments to T_H0 cells is followed by a release of IL-4 resulting in a differentiation of T_H0 into T_H2 cells. The B cells present antigen fragments to the T_H2 cells. The T_H2 cells only recognize *sequences*. The sequence seems to be an 'objective' criterion whether the fragments presented by B cells correspond to the ones presented by APCs and to distinguish between self- and non-self. When the T_H2 cells recognize the sequence, they stimulate the B cells to differentiate into antibody producing plasma cells (*i.e.*, to initialize an antibody response). The antibodies recognize the *conformation* of the glycosylated epitope under resort to their *own* genetic repertoire what opens up a high degree of freedom (table 2). The idea behind it is to avoid limitations in the recognition of the antigen. When both glyco valences are bound, an induced fit increases the affinity, and a conformation change will conduct the signal through the Fc domain into the inside of a mast or basophilic cell to release inflammation mediators for 'defense'. Overall, type I hypersensitivities to CCDs are echo and smoke of an ancient glycan war, which was brought under control of DC-SIGN. But here and there it is still smoldering.

8. Outlook

8.1. Test of Binding Hypothesis

Based on molecular docking experiments, a binding model was postulated harmonizing contradictory results derived from interaction experiments. It has already proven its value by explaining the ELISA data published by Collot *et al.* in **2011**. In the future, this binding hypothesis should be tested involving co-crystallization of Man α 1-6 and HMM5 Fab antibody to verify that Man α 1-6 interacts with the V_L chain *exclusively*. Such data then might be verified by molecular docking in an analogous way as the co-crystal data of Fuc α 1-3/HMM5 Fab. An advanced molecular modeling approach might be carried out involving Man α 1-6/V_L and Fuc α 1-3/V_H with the variable domain keeping *flexible*, the same approach applies to Xyl β 1-2/V_H. In **1999**, van Die *et al.* found that “core α 1 \rightarrow 3-fucose is a common modification of N-glycans in parasitic helminths and constitutes an important epitope for IgE from *Haemonchus contortus* infected sheep.”¹⁶⁸ Thus, ruminant anti-*H. contortus* sera of animals infected by other parasites should be tested if they bind HRP and its CCD fragments to gain deeper insight into the recognition of parasite-associated glyco patterns. In this context, it would be worth exploring whether glycans are suitable vaccines against parasites and type I hypersensitivities.

8.2 Subjection of STD NMR Spectroscopy to Quality Assurance

The present study encountered a severe quality assurance issue in the analysis of epitopes by STD NMR spectroscopy. The insights into the STD artefacts indicated that also other STD NMR studies are affected in a hitherto unknown extend. Future research calls for more accurate determination of STD effects and elimination of artefacts. The list of possible causes of STD artefacts given in the present study might serve as a check list to subject STD NMR data to a quality assurance. Significance testing has proven its value as a feasible statistical tool to tackle and evaluate vast amounts of STD NMR data. Its application on STD NMR data is strongly recommended to all customers of STD NMR experiments. Anyway, statistics have an important role to play in the research process. Due to the low S/N ratio visible in many STD NMR spectra, H,H broadband decoupling should be implemented in the pulse sequence. Classical negative control STD NMR experiments have to be implemented into a standard operating procedure. Furthermore, it is advisable to take part in round robin tests.

9. Experimental Section

9.1. Materials and Methods

Chemical glycosylations were carried out with standard Schlenk technique. Chemical reactions were monitored by TLC on silica gel 60 F₂₅₄ plates (*Macherey-Nagel*). Protected saccharides were purified by normal phase column chromatography on silica gel 60 (*VWR*). Deprotected saccharides were purified by size-exclusion chromatography on biogel P-2 (fine, *Bio-Rad Laboratories*). All reagents and solvents were purchased from commercial suppliers, in particular, L-Fucose (*Carbosynth*), mannobioses, horseradish peroxidase type II (*Sigma-Aldrich*) and polyclonal anti-HRP serum (*BioGenes*). NMR spectra were recorded by the NMR service (Department of Chemistry, University of Hamburg) on a *DRX 500* NMR spectrometer (*Bruker*) equipped with a 5 mm BBI probe, an *AVI 400* NMR spectrometer (*Bruker*) equipped with a 5 mm BBO probe or an *AVII 400* NMR spectrometer (*Bruker*) equipped with a 5 mm BBI probe. ESI MS spectra were recorded by the MS service (Department of Chemistry, University of Hamburg) on a *MAT 95XL* spectrometer (*Finnigan*). Specific rotations were measured with a *P8000* polarimeter (*Krüess Optronic*) at 589 nm in a 1 dm cuvette. SPR sensorgrams were recorded on a *T200* SPR spectrometer (*Biacore*). Proteins were re-buffered using *Amicon Ultra-4* membranes (MWCO = 50 kDa). Protein concentrations were determined photometrically on the spectrophotometer *NanoDrop* (*Thermo Scientific*). The absorption coefficients of the phage display-derived monoclonal antibodies HHH1 and HMM5 were calculated on the basis of their sequences (<https://www.expasy.org/protparam>). SDS-PAGE and Coomassie/silver stainings were carried out according to established laboratory protocols.¹⁶⁹ ELISA plates were measured on the ELISA reader *GENios* (*Tecan*). Molecular docking experiments were carried out using *Maestro 10.2* (*Schrödinger*) according to the GLIDE user manual.

9.2. Rabbit Immunization Experiment

The immunization experiments were carried out by *BioGenes* (table 16). Two rabbits (animal numbers 7439 and 7440) have been inoculated with HRP (isotype and glycoform unknown) as antigen and a modified Freund's adjuvant. Pre-immune sera and anti-HRP sera (final bleedings 7439 and 7440) of unknown anti-HRP antibody titer were delivered as crude material (whole blood).

Table 16: Immunization schedule.*

Date	Procedure
21.12.2010	First immunization (300 µg HRP)
04.01.2011	Boost (100 µg HRP)
11.01.2011	Boost (100 µg HRP)
18.01.2011	Boost (100 µg HRP), bleeding (20 mL / animal)
01.02.2011	Boost (100 µg HRP)
08.02.2011	Final bleeding (60 mL / animal)
February 2011	Euthanasia of both animals, preparation of the spleens

*The immunization schedule was kindly provided by K. Krusemark (*BioGenes*).

9.3. STD NMR Experiments

9.3.1. Set-up of a Typical STD NMR Experiment

STD-NMR experiments were performed by the NMR service at 298 K on an *AV III 600* MHz spectrometer (*Bruker*) equipped with a 5 mm TBI probe head. The PBS NMR buffer (100 mM NaCl, 40 mM Na₂HPO₄, 10 mM NaH₂PO₄ in D₂O) was adjusted to pH 7.4. Saturation was achieved by a Gaussian pulse train of 50 ms, yielding a total saturation time of 0.25 to 5 s with an attenuation of 40-60 db (on-resonance: -1.5, -1.0 or -0.5 ppm; off-resonance: +40 ppm). For suppression of protein background, a T_{1ρ} filter was used, applying a field strength of 11.5 kHz and a duration of 10 to 50 ms. Each experiment was performed with a total of 1024 scans. Protein/ligand ratios of 1:200 (6.5 µM antibodies with 1.3 mM saccharide) were used. The spectra were acquired with a spectral width of 8000 Hz and TD = 64000, and two transients using a pseudo-two-dimensional pulse sequence (*stdiffesgp.3*). The main parameters of the most important STD NMR experiments are listed in table 17.

Table 17: Parameterization of STD NMR experiments.

Parameters	Anti-HRP pAb	HMM5	HMM5	HSA
	Fuc α 1-3	Nonasaccharide	Fuc α 1-3	Trp
	(600 MHz)	(Kötzler)	(double check)**	(Bruker)
On / ppm	-1.0	-0.5	+7.25	-1.0
Off / ppm	+67	+40	-25	-40
D20 / s	2	4	2	2
D29 / ms	40	10	30	30
Attenuation* / dB	20	20	40	36

*Conversion formula: $-10 \times \lg(\text{attenuation in W}) = \text{attenuation in dB}$ (e.g., $0.01 \text{ W} \triangleq 20 \text{ dB}$). **The Gaussian pulse used in the double check was shown to be ± 0.85 ppm broad (i.e., 1.7 ppm) by shifting the irradiation position towards a resonance signal of the ligand.

9.3.2. Preparation of STD NMR Samples

The antibodies were re-buffered with an Amicon tube to D₂O based PBS. PBS (20 mL) was lyophilized and D₂O (20 mL) added. An *Amicon Ultra-4* (MWCO = 50 kDa) was washed with NaOH solution (0.1 M, 4 mL; removal of glycerine) and distilled water (4 mL, 3000 g, 30 min, removal of NaOH). Disaccharide Fuc α 1-3GlcNAc α 1-OMe (1.0 mg, M = 381 g/mol) was dissolved in D₂O (100 μ L; i.e. 0.1 mg correspond to 10 μ L). The NMR tube contained 0.1 mg / 200 μ L disaccharide (i.e., $2.6 \cdot 10^{-4}$ mmol / 200 μ L, 1.3 mM disaccharide). Protein samples were kept on ice. Their purity was controlled by SDS-PAGE (20 μ L protein sample, 3 to 5 μ g protein / gel pocket, 4 μ L 5x sample buffer ad 20 μ L PBS, denaturation: 95 °C, 10 min) and ¹H NMR spectroscopy (check sheet attached as supplementary information).

Preparation of anti-HRP polyclonal rabbit IgG antibody: After affinity purification of anti-HRP polyclonal rabbit IgG with bromelain as target the concentration was determined photometrically at 280 nm (MW = 160 kDa, $\epsilon = 210000 \text{ mol}^{-1} \text{ cm}^{-1}$, $c = 0.18 \text{ mg/mL}$). An aliquot (1.96 mL) was centrifuged (4000 rpm) until a volume of approximately 50 μ L and PBS buffer (D₂O) was added (4 mL). The solution was centrifuged again until a volume of approximately 50 μ L, PBS buffer was added again and the solution was centrifuged until a volume of approximately 200 μ L. The concentration of this solution was determined photometrically at 280 nm (2.99 mg/mL). Since the receptor/ligand ratio should be 1:200, the antibody in the NMR tube should amount 1.3×10^{-9} mol (1.3 mmol / L). With 1.3×10^{-9} mol \times 150 000 g/mol, an amount of approximately 0.2 mg polyclonal IgG was transferred to the NMR tube (6.5 μ M polyclonal IgG).

Preparation of monoclonal antibodies: Anti-Le^x rat IgM antibody **L5**: MW pentamer = 970 kDa, MW monomer = 180 kDa, $\epsilon = 114000 \text{ mol}^{-1} \text{ cm}^{-1}$. A concentration of 4.10 mg / mL was measured for the antibody in the original vessel. An aliquot of 98 μL (0.4 mg) was re-buffered as described above to obtain a concentrate (96 μL , 35 mg/mL). 1:1000 = 1:(200 \times 5), *i.e.*, 1.3 μM IgM. HHH1: MW = 105 kDa, $\epsilon = 177.45$, $c = 4.8 \text{ mg/mL}$, 200 μL 1 mg/mL, $1.3 \cdot 10^{-9} \text{ mol} \times 105000 \text{ g/mol} = 0.14 \text{ mg}$. HMM5: MW = 125 kDa, $\epsilon = 186.45$, $1.39 \cdot 10^{-9} \text{ mol} \times 125000 \text{ g/mol} \approx 0.16 \text{ mg}$, *NanoDrop*: 1.0 mg/mL, 0.16 mg HMM5 in the NMR tube (163 μL), + 27 μL PBS.

Purification of HHH1 and HMM5 human IgG ΔC1 antibody. Supernatant (50 mL in a falcon) of cracked HEK cells was centrifuged (30 min, 5000 rpm, centrifuge 5804R) and filtered (0.45 or 0.8 μm). The filtrate was transferred to a new falcon and Ni matrix (1 to 2 mL) was added. The falcon was sealed with parafilm and rolled at 4 °C overnight. The suspension was centrifuged (100 g, 30 min), washed eight times with PBS (pH 8, 500 mM NaCl) at r.t. for 15 to 30 min. The supernatant was discarded and PBS with imidazole (< 100 mM) was added. The suspension was rolled at r.t. overnight. The supernatant (~ 2 mL) was transferred to an Eppendorf tube, centrifuged (300 g) and the antibody concentration was determined photometrically at 280 nm.

9.4. SPR Experiments

SPR measurements were performed using a *Biacore T200* at 25 °C with PBS as running buffer. The interaction between HHH1 (analyte) and Fuc α 1-3GlcNAc (ligand) was analyzed. As positive controls AAL (analyte) and HRP (ligand) were applied. The proteins were re-buffered to PBS pH 7.4 (0.22 μM) using 3k Amicon Ultra-4000 tubes (round bucket 3608, 2000 g, 20 min). Note: The commercial AAL preparation contains 39 % salts which have to be considered weighing the lyophilizate (1.2 mg lyophilizate – 0.47 mg salts = 0.7 mg protein; dissolved in 1.0 mL PBS; 3 μg / 4.3 μL protein were mixed with 6.5 μL 4 \times PP and 15.2 μL PBS for SDS-PAGE) and HHH1 is re-buffered due to presence of imidazole. The protein concentrations were determined by photometry (HHH1: $\epsilon = 177.45$, MW = 105 kDa; AAL: Abs = 1 mg/mL mode; $\lambda = 280 \text{ nm}$). Immobilization with EDC/NHS. The contact time was set to 120 s (58 μL). Compound 15 (4 mg) was dissolved in ddH₂O (1000 μL) and diluted 1:1000 to obtain a concentration of 4 $\mu\text{g/mL}$. This dilution was diluted 1:200 with Biacore acetate buffer (500 μL acetate buffer + 2.5 μL) to obtain 20 ng/mL. The CM5 chip was equilibrated to r.t. and injected.

Rack (R1) positions: D1 GnF³ (20 ng/500 μ L, *i.e.*, 10 μ g/mL); D2 HRP; E1 EDC/NHS (250 μ L EDC + 250 μ L NHS). Activation of the chip with EDC/NHS for 480 s (118 μ L) and a flow rate of 10 μ L/s. Fc3 was injected with D1 (2 x 20 μ L = 2 x 120 s; 48 RU) and Fc4 with D2 (120s + 240 s; 330 RU). The activated dextran layers were deactivated by ethanol amine hydrochloride (1.0 M, pH 8.5, D3) with a contact time of 600 s. AAL (1 μ g/mL, position R1D1, 500 μ L) was injected with a contact time of 600 s and a flow rate of 25 μ L / s (Fc3: ~30 RU, *i.e.*, ~30 pg/mm²; Fc4 80 RU, *i.e.*, ~80 pg/mm², note: binding curve is immediately in saturation and is stabilized at 3 RU). Due to the high binding affinity to HRP, a mild regeneration with fucose (R1D2, 1 μ g / mL, 300 s, 25 μ L/s) was inefficient (Fc3: 2.6 RU residual, Fc4: 2.6 RU residual). A regeneration with Tris/glycine buffer seemed too rigid. Thus, a regeneration with HRP (10 μ g/mL in PBS, not: in acetate, contact time 300 s, D3) was preferred but revealed as dysfunctional, too. This is why the flow cells were subjected to pH shifts (pH 11, 60 s \rightarrow pH 1, 60 s). In case of Fc4, the regeneration worked but at Fc3 after pH 1 treatment a negative response of -15 RU was detected. The procedure was repeated and the effect occurring in Fc3 was reproduced (-5 RU). Fc2 was activated with EDC/NHS as described, coated with GnF³ (330 RU) and capped as described above (11 RU \rightarrow -59 RU). A Binding of AAL could be regenerated by treatment with pH 11, a binding of HHH1 and HMM5 could be regenerated treatment with HRP as described above. A new run (Testlauf2.blr) was carried out with AAL (0.64 mg/mL stock solution \rightarrow 10 μ g/mL, 500 μ L), HHH1 (1.0 mg/mL stock solution \rightarrow 50 μ g/mL, 500 μ L) and HMM5 (1.0 mg/mL stock solution \rightarrow 50 μ g/mL, 500 μ L) as analytes. Regeneration was performed in a combined mode applying first pH 11 (60 s \rightarrow 60 s \rightarrow 120 s, E4) and then fucose (1 mg/mL, 120 s, E5) over all flow cells. This treatment worked to remove AAL from GnF³, but HRP could not be regenerated completely. For removal of binders from HRP, first pH 11 (60 s) and then pH 1 (60 s) was applied. For Fc2, a sequence of pH 11 (60 s) followed by fucose (120 s) worked perfectly. A serial dilution for AAL was prepared (10 μ g/mL, 5 μ g/mL, 1 μ g/mL, 0.1 μ g/mL and 0.05 μ g/mL). Regeneration conditions for Fc2 were set as follows: pH 11 (120 s) followed by fucose (120 s); for Fc4: pH 11 (60 s) followed by pH 1 (60 s). Contact time 300 s, dissociation time 300 s, regeneration 1: Tris-HCl pH 11 (120 s) with a flow rate of 25 μ L/s; regeneration 2: fucose (1 mg/mL, 120 s) with a flow rate of 25 μ L/s. The data were stored in the file *AAL-GnF3-Kinetik.blr*. Relevant subtractions are Fc3-1 (30 RU) and Fc2-1 (90 RU; $K_D = 5 \cdot 10^{-8}$ M). Additionally, the file Testlauf2.blr is informative. Relevant subtractions are Fc4-1 and Fc2-1.

9.5. Sitting Drop Vapor Diffusion Crystallization

The co-crystallization was carried out by L. Tjerrild (*Department of Engineering, University of Aarhus*). Sitting drops (0.3 μL) and reservoir solutions (60 μL) were set up in MR 2 crystallization trays (*SWISSCI*) by an *Oryx4* robot (*Douglas Instruments*). HMM5 Fab crystals were let grown by vapor diffusion (19 $^{\circ}\text{C}$) and used as seeds. Streak seeding was carried out using a cat whisker which dislodged seeds from a crystal and passed them through drops of different buffer compositions. Crystals of HMM5 Fab grew in the presence of 200 x molar excess of Fuc α 1-3GlcNAc α 1-OMe under optimized conditions (15-25 mM LiSO $_4$, 15-26.5 % (w/v) PEG 3350, 0.1 M Tris or HEPES pH 7.0-8.5), were cryoprotected (30 % w/v PEG 3350, 20 mM NaCl, 75 mM HEPES pH 5.5), fished, frozen in liquid nitrogen and measured at the *European Synchrotron Radiation Facility* in Grenoble. The X-ray diffraction images were processed with XDS by G. R. Andersen (*Department of Engineering, University of Aarhus*).

9.6. ELISA Experiments

9.6.1. Activity ELISA of HMM5 against HRP

A 96 well plate (Gre 96 ft) was coated with HRP (50 $\mu\text{g}/\text{mL}$ in PBS, at 4 $^{\circ}\text{C}$ overnight or at r.t. for 2 h), washed three times with TPBS (300 μL) and three times with PBS (300 μL). In order to avoid wash artefacts, a stepper was used and the plate was turned. All wells were blocked with MPBS (4 %, 300 μL , 30 min, r.t.). Antibody samples (supernatant as positive control, medium as negative control, dilution serial of HMM5 antibody) were added (100 μL) without washing the wells before. The plate was kept at 4 $^{\circ}\text{C}$ overnight, washed with TPBS and PBS like described above. As a second antibody, an anti-IgE AP direct conjugate (“ αE ”, 1:2000 in 2 % MPBS) was added (100 $\mu\text{L}/\text{well}$) and incubated (r.t., 1 h). The plate was washed with TPBS and PBS like described above and AP detection solution (5 mg/mL pNPP in AP detection buffer) was added (100 μL). The plate was measured at 405 nm (nr = 10, measurement mode: absorbance).

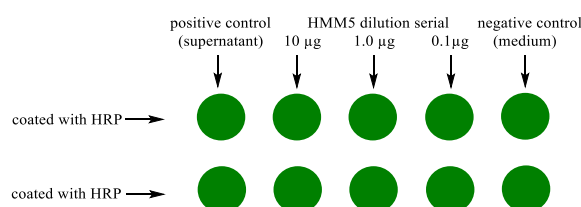


Fig. 114: ELISA preparation testing HMM5 activity after failed STD NMR spectroscopy. Color code: green = coated.

9.6.2. Competition ELISA of Solute Nitro Compounds against TNP-BSA

A 96 well plate (Gre 384 fb) was coated with TNP-BSA (2 % in PBS, 30 μ L; one well with BSA) at 4 °C overnight. The antigen was removed with a pipette to recycle TNP-BSA. The well plate was blocked with BSA PBS (2 %, 100 μ L, 30 min, r.t.). Monoclonal anti-TNT scFv-IgE antibodies 4.8 and 2.18 (original supernatant concentrations < 50 μ g/mL; 1:2 diluted to retard signals) were pre-incubated with different nitro compounds (1 h, 450 rpm, r.t.; 49 μ L supernatant either 4.8 or 2.18 supernatant mixed with 1 μ L pre-dissolved nitro compound either 2,4-DNT (2.6 mg/mL acetonitrile) or RDX (10 mg/mL DMSO) or TNBS-Tris (0.36 mg TNBS / mL Tris buffer, pH 9). BSA-PBS was discarded and the pre-incubated supernatants was added to the wells. Antibody 4.8 (50 μ L, pre-incubated without any competitor) served as a positive control. As a negative control, BSA (BSA PBS, 2 %, 30 μ L) was coated instead of TNP-BSA. The plate was kept at r.t. for 1 h, was washed with PBS three times (100 μ L) and AP detection solution (5 mg/mL pNPP in detection buffer) was added (100 μ L). The plate was measured at 405 nm (nr = 10, measurement mode: absorbance).

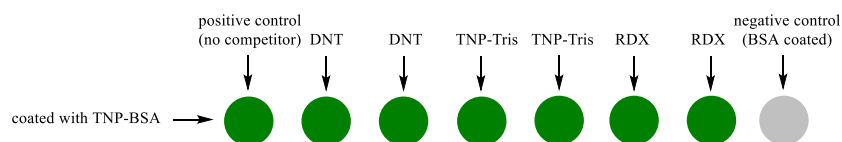
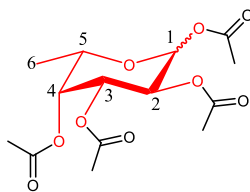


Fig. 115: ELISA preparation testing the cross-reactivity against RDX to the monoclonal anti-TNT scFv-IgE antibodies 4.8 and 2.18. Color code: green = coated with TNP-BSA; grey = coated with BSA.

9.7. Access to Honeybee Venom CCD Fragments

Synthesis of 1,2,3,4-tetra-*O*-acetyl- α/β -L-fucopyranose-acetate (2). L-Fucose (1) (5.00 g, 30.5 mmol) was dissolved in pyridine/acetanhydride (2:1, 80 mL) at 0-5 °C, then stirred at r.t. overnight. The reaction progress was monitored by TLC on silica gel 60 F₂₅₄ (PE/EA 2:1 v/v, R_f 0.23). Upon completion, the reaction mixture was evaporated under reduced pressure. The residue was co-distilled with toluene three times and purified by column chromatography on silica gel 60 with PE/EA (2:1 v/v) as mobile phase yielding compound **2** as a colorless oil (8.80 g, 26.5 mmol, 86 %, α/β 5:3).



Exact Mass: 332,11
Molecular Weight: 332,31

NMR data and assignments:

Table 18: ¹H Assignments of 1,2,3,4-tetra-*O*-acetyl- α/β -L-fucopyranose (**2**) (CDCl₃, τ g30, 400.13 MHz).

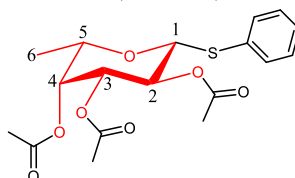
¹ H Assignment	¹ H δ / ppm ^a	J _{H,H} / Hz	Multiplicity
1 α	6.34	J _{1,2} 2.5	d
1 β	5.69	J _{1,2} 8.0	d
2 α	5.36-5.29	J _{2,3} n.r.	m
2 β			m
3 α	5.08	J _{3,4} 3.5	dd
3 β	5.36-5.29		m
4 α	5.36-5.29	J _{4,5} <1	m
4 β	5.27		dd
5 α	4.27	J _{5,6} 6.5	dq~q
5 β	3.96		dq~q
6 α	1.17		d
6 β	1.23		d
4 x COCH ₃ α	2.18, 2.15, 2.02, 2.00	-	s
4 x COCH ₃ β	2.19, 2.11., 2.04, 1.99	-	s

^a The spectrum was calibrated on the solvent residual peak (7.260 ppm, ref.: *J. Org. Chem.* **1997**, 62, 7512-7515).

Table 19: ¹³C Assignments of 1,2,3,4-tetra-*O*-acetyl- α/β -L-fucopyranose (**2**) (CDCl₃, *jmod*, 100.61 MHz).

¹³ C Assignment	¹³ C δ / ppm
1	83.7
2	66.4
3	72.8
4	70.5
5	73.6
6	16.9
4 x COCH ₃	170.7, 170.2, 169.8, 168.9
4 x COCH ₃	20.8, 20.6, 20.5, 20.3

Synthesis of phenyl 1-thio-2,3,4-tri-*O*-acetyl- β -L-fucopyranoside (3). Compound **2** (10 g, 30 mmol) was dissolved in anhydrous DCM, thiophenol (3.72 g, 3.5 mL, 30 mmol) and BF₃-Et₂O were added. The progress of the reaction was monitored by TLC on silica gel 60 F₂₅₄ (EA/MeOH 30:1 v/v, R_f 0.33). Detection was achieved by UV absorption (245 nm) and dipping the plate into 10 % (v/v) sulfuric acid in ethanol followed by charring at ~120 °C. Upon completion, the lilac reaction mixture was neutralized by saturated sodium hydrogen carbonate solution and the organic layer was evaporated. The syrupy residue was purified by column chromatography on silica gel 60 with PE/EA (4:1 v/v) as mobile phase yielding compound **3** (6.98 g, 18.2 mmol, 61 %).



Exact Mass: 382,11
Molecular Weight: 382,43

Polarimetry (*P8000*, Krüss Optronic, 589 nm, 1 dm cuvette): $[\alpha]_D^{20} = -9.0^\circ$ (*c* 0.2, CHCl₃);
ref. 170: $[\alpha]_D = -3.0^\circ$ (*c* 0.9, CHCl₃).

NMR data and assignments:

Table 20: ¹H Assignments of phenyl 2,3,4-tri-*O*-acetyl-1-thio β -L-fucopyranoside (**3**) (CDCl₃, *zg30*, 400.13 MHz).

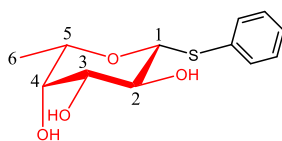
¹ H Assignment	¹ H δ / ppm ^a	<i>J</i> _{H,H} / Hz	Multiplicity
1	4.70	<i>J</i> _{1,2} 9.9	d
2	5.22	<i>J</i> _{2,3} 9.9	dd~vt
3	5.05	<i>J</i> _{3,4} 3.3	dd
4	5.26	<i>J</i> _{4,5} 0.7	dd
5	3.82	<i>J</i> _{5,6} 6.3	dq~q
6	1.23		d
SPh	7.52-7.49 (2H)	n.r.	m
	7.34-7.27 (3H)	n.r.	m
3 x COCH ₃	2.13, 2.07, 1.96	-	s

^aThe spectrum was calibrated on the solvent residual peak (7.260 ppm, ref.: *J. Org. Chem.* **1997**, 62, 7512-7515).

Table 21: ¹³C Assignments of phenyl 2,3,4-tri-*O*-acetyl-1-thio β -L-fucopyranoside (**3**) (CDCl₃, *jmod*, 100.61 MHz).

¹³ C Assignment	¹³ C δ / ppm
1	86.5
2	67.4
3	72.4
4	70.3
5	73.2
6	16.5
SPh	132.3, 128.9, 127.9
3 x COCH ₃	20.9, 20.7, 20.6
3 x COCH ₃	170.6, 170.1, 169.5

Synthesis of phenyl 1-thio- β -L-fucopyranoside (4). Compound **3** (6.98 g, 18.2 mmol) was dissolved in abs. MeOH (50 mL) and catalytic amounts of NaOMe were added (0 °C \rightarrow r.t., pH \approx 9) and the reaction mixture was left to stir. The progress of the reaction was monitored by TLC on silica gel 60 F₂₅₄ with PE/EA (1:1 v/v) as mobile phase (R_f 0.66). Detection was achieved by UV absorption (245 nm) and dipping the plate into 10 % (v/v) sulfuric acid in ethanol followed by charring at \sim 120 °C. Upon completion, the reaction mixture was neutralized with Amberlite IR-120 [H⁺] and filtered. The filtrate was evaporated under reduced pressure and the residue was purified by column chromatography on silica gel 60 with EA/MeOH (30:1 v/v) as mobile phase. The product containing fractions were pooled and evaporated under diminished pressure yielding compound **4** as a colorless powder (3.49 g, 13.6 mmol, 75 %).



Exact Mass: 256,08
Molecular Weight: 256,32

Polarimetry: (P8000, Krüss Optronic, 589 nm, 1 dm cuvette): $[\alpha]_D^{20} = +65^\circ$ (c 0.2, MeOH);
ref. 170: $[\alpha]_D^{20} = +68^\circ$ (c 0.6, MeOH).

NMR data and assignments:

Table 22: ¹H Assignments of phenyl-1-thio β -L-fucopyranoside (**4**) (MeOD, ζ g30, 400.13 MHz).

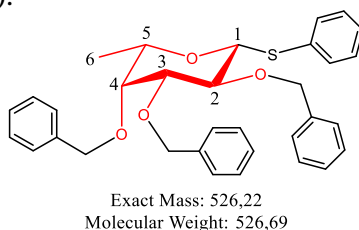
¹ H Assignment	¹ H δ / ppm ^a	$J_{H,H}$ / Hz	Multiplicity
1	4.56	$J_{1,2}$ 9.6	d
2	3.58	$J_{2,3}$ 9.4	dd~vt
3	3.68	$J_{3,4}$ 3.3	m
4	3.52	$J_{4,5}$ n.r.	dd
5	3.68	$J_{5,6}$ 6.4	dq~m
6	1.28		d
SPh	7.59-7.45 (2H)	n.r.	m
	7.30-7.18 (3H)	n.r.	m

^a The spectrum was calibrated on the solvent residual peak (3.310 ppm, ref.: *J. Org. Chem.* **1997**, 62, 7512-7515).

Table 23: ¹³C Assignments of phenyl-1-thio β -L-fucopyranoside (**4**) (MeOD, ζ gpg30, 100.61 MHz).

¹³ C Assignment	¹³ C δ / ppm
1	90.0
2	70.8
3	76.9
4	76.5
5	73.1
6	17.0
SPh	132.2, 129.9, 129.8, 128.0

Synthesis of phenyl 1-thio-2,3,4-tri-*O*-benzyl- β -L-fucopyranoside (5). Compound **4** (2.70 g, 10.5 mmol) was dissolved in dried DMF (80 mL) and the solution was cooled at 4 °C. NaH suspension (60 %, 3.75 g, 94.0 mmol), TBAI (585 mg, 1.58 mmol, 15 %) and benzyl bromide (22.2 mL, 188 mmol) were added. The reaction mixture was left to stir at r.t. The progress of the reaction was monitored by TLC on silica gel 60 F₂₅₄ with PE/EA (1:1 v/v) as mobile phase (*R_f* 0.84). Detection was achieved by UV absorption (245 nm) and dipping the plate into 10 % (v/v) sulfuric acid in ethanol followed by charring at ~120 °C. Upon completion, the reaction was quenched by addition of methanol, the mixture was concentrated under diminished pressure at a rotary evaporator with cold finger condenser, the residue was triturated with diethyl ether and washed with water and brine. The organic layer was dried over sodium sulfate, filtered and concentrated under diminished pressure. The residue was purified by column chromatography on silica gel 60 with PE/EA (10:1 v/v) as mobile phase to yield compound **5** as a colorless powder (4.60 g, 8.74 mmol, 83 %).



Polarimetry (*P8000*, Krüss Optronic, 589 nm, 1 dm cuvette): $[\alpha]_D^{20} = -3.0^\circ$ (*c* 0.2, CHCl₃), ref.
170: $[\alpha]_D^{20} = -14.0^\circ$ (*c* 0.7, CHCl₃).

NMR data and assignments:

Table 24: ¹H Assignments of phenyl 2,3,4-tri-*O*-benzyl-1-thio- β -L-fucopyranoside (**5**) (DMSO-d₆, ζ g30, 400.13 MHz).

¹ H Assignment	¹ H δ / ppm ^a	<i>J</i> _{H,H} / Hz	Multiplicity
1	4.79	<i>J</i> _{1,2} 9.4	d
2	3.67	<i>J</i> _{2,3} 9.4	dd~vt
3	3.74	<i>J</i> _{3,4} 2.4	dd
4	3.91	<i>J</i> _{4,5} < 1	dd~d
5	3.74	<i>J</i> _{5,6} 6.3	dq~q
6	1.18		d
3 x OCH ₂ Ph	4.87, 4.80	² <i>J</i> 11.5, 12.4	2 x d
	4.67, 4.66, 4.63, 4.61	n.r.	m
SPh, 3 x OCH ₂ Ph	7.52-7.20	-	m

^a The spectrum was calibrated on the solvent residual peak (2.500 ppm, ref.: *J. Org. Chem.* **1997**, 62, 7512-7515).

Table 25: ^{13}C Assignments of phenyl 2,3,4-tri-*O*-benzyl-1-thio- β -L-fucopyranoside (**5**) (DMSO- d_6 , APT, 100.61 MHz).

^{13}C Assignment	^{13}C δ / ppm
1	85.4
2	76.5
3	83.2
4	76.3
5	73.5
6	16.9
OCH ₂ Ph	74.4, 74.2, 71.1
C _{arom.}	129.9, 128.9, 128.2(3), 128.1(5), 128.0(5), 127.,7, 127.5, 127.4, 127.3 126.6
C _{arom.} quarternary	139.0, 138.5, 138.4, 134.3

X-ray crystallography:

Crystals were grown by slow evaporation of a DMF solution (table 26, fig. 116).

Table 26: Crystal parameters of phenyl 2,3,4-tri-*O*-benzyl-1-thio- β -L-fucopyranoside (**5**) (Bruker, AXS SMART APEX, three circle single crystal diffractometer with molybdenum X-ray tube, $\lambda_{\text{Mo K}\alpha} = 0.71073 \text{ \AA}$, T = 100 K.)

Compound	Phenyl 2,3,4-tri- <i>O</i> -benzyl-1-thio- β -L-fucopyranoside
Habitus	Colorless needle
Crystal size	0.07 x 0.12 x 0.36 mm
Crystal system	primitive orthorhombic ($P2_12_12_1$)
Symmetry	identity (x, y, z) three 2-fold screw axes ($1/2-x, -y, 1/2+z$; $1/2+x, 1/2-y, -z$; $-x, 1/2+y, 1/2-z$)
A	9.7640(4) \AA
B	11.7242(5) \AA
C	23.8375(10) \AA
α	
β	90 $^\circ$
γ	
R ₁	3.94 %
Chair conformation	$^1\text{C}_4$

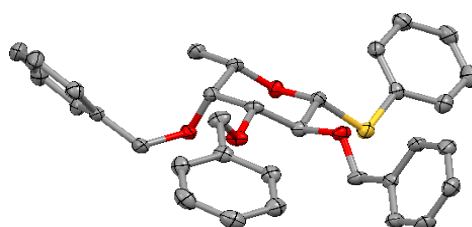
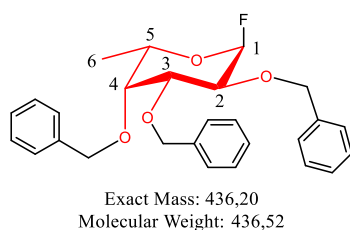


Fig. 116: Visualized crystal structure of compound **5**.¹⁰

Synthesis of 2,3,4-tri-*O*-benzyl- α -L-fucopyranosyl fluoride (6). Compound **5** (200 mg, 0.38 mmol) was dissolved in dried dichloromethane (4 mL) and the solution was cooled on ice. DAST (149 μ L, 0.18 g, 1.12 mmol, 3 eq.) and NBS (104 mg, 0.58 mmol, 1.5 eq.) were added and the reaction mixture was stirred (r.t., 5 h), cooled on ice and diluted with dichloromethane (25 mL). The solution was washed with sodium hydrogen carbonate solution (5 %, 50 mL) and brine (50 mL), dried over sodium sulfate, filtered and diminished under reduced pressure to yield a yellow oil. The crude product was kept in high vacuum overnight and may either be directly used for chemical fucosylation to avoid decomposition or purified by column chromatography on silica gel 60 with PE/EA (10:1 v/v \rightarrow 4:1 v/v) as mobile phase to yield compound **6** as a colorless oil (120 mg, 0.28 mmol, 73 %, α/β 5:1). Due to its decomposition sensitivity, a specific rotation was not determined.



ESI-TOF-MS (Agilent 6224, positive mode): $m/z = 459.194(8)$ $[M+Na]^+$.

NMR data and assignments:

Table 27: ^1H Assignments of 2,3,4-tri-*O*-benzyl- α -L-fucopyranosyl fluoride (**6**) (CDCl_3 , $\zeta g 30$, 400.13 MHz).^a

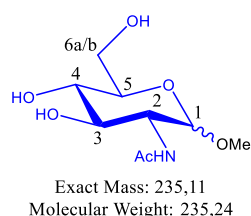
^1H Assignment	^1H δ / ppm ^b	$J_{\text{H,H}}$ / Hz	Multiplicity
1	5.23	$J_{1,2}$ 3.5	d
2	4.08	$J_{2,3}$ 9.3	dd
3	3.99	$J_{3,4}$ 2.5	dd
4	3.66	$J_{4,5} < 1$	dd~s
5	4.21	$J_{5,6}$ 6.5	dq~q
6	1.00		d
3 x OCH_2Ph	4.97-4.61 (6H)	2J 11.3, 12.1, 10.9, 11.8, 11.4, 10.7	6 x d
3 x OCH_2Ph	7.4-7.1	n.r.	m

^a Decomposition can be observed in the NMR tube. ^b The spectrum was calibrated on the solvent residual peak (7.260 ppm, ref.: *J. Org. Chem.* **1997**, 62, 7512-7515).

Table 28: ^{13}C Assignments of 2,3,4-tri-*O*-benzyl- α -L-fucopyranosyl fluoride (**6**) (CDCl_3 , *jmod*, 100.61 MHz).

^{13}C Assignment	^{13}C δ / ppm
1	94.0
2	76.3
3	79.2
4	77.7
5	66.8
6	16.6
3 x $\text{O}\overline{\text{C}}\text{H}_2\text{Ph}$	77.3, 77.0, 76.7, 74.9, 73.0, 72.8
3 x $\text{OCH}_2\overline{\text{P}}\text{h}$	128.3, 128.2(4), 128.1(6), 127.5, 127.4, 127.3

Synthesis of methyl 2-acetamido-2-deoxy- α/β -D-glucopyranoside (8). To a solution of 2-acetamido-2-deoxy- α/β -D-glucopyranose (7) (50.0 g, 0.22 mmol) in MeOH (50 ml) was added a catalytic amount of Amberlite IR-120 [H⁺] resin and the mixture was heated for 3 days. The progress of the reaction was monitored by TLC on silica gel 60 F₂₅₄ with dichloromethane/methanol (4:1 v/v) as mobile phase (R_f 0.35). Detection was achieved by UV absorption (245 nm) and dipping the plate into 10 % (v/v) sulfuric acid in ethanol followed by charring at ~120 °C. Upon completion, the reaction mixture was filtered and the filtrate was evaporated under diminished pressure. The crude product was purified by column chromatography on silica gel 60 with CHCl₂/MeOH (5:1 v/v) as mobile phase to yield compound **8** as a colorless powder (35.3 g, 0.15 mmol, 70 %, α/β 5:1).



NMR data and assignments:

Table 29: ¹H Assignments of methyl 2-acetamido-2-deoxy- α/β -D-glucopyranoside (**8**) (D₂O, zg30, 400.13 MHz).

¹ H Assignment	¹ H δ / ppm ^a	J _{H,H} / Hz	Multiplicity
1 α	4.78	J _{1α,2α} < 7 ^b	d
1 β	4.47	J _{1β,2β} 8.5	d
2 α	3.95	J _{2α,3α} n.r.	dd~m
2 β	3.72	J _{2β,3β} n.r.	dd~m
3 α	3.75	J _{3α,4α} 9.3	dd~m
3 β	3.56	J _{3β,4β} n.r.	dd~m
4 α	3.50	J _{4α,5α} 9.3	dd~vt
4 β	3.47	J _{4β,5β} n.r.	dd~m
5 α	3.70	J _{5α,6aα} 2.1	ddd~m
		J _{5α,6bα} 5.4	
5 β	3.47	J _{5β,6aβ} n.r.	ddd~m
		J _{5β,6bβ} n.r.	
6a	3.91	J _{6aα,6bα} 12.3 ^c	2 x dd
6b	3.81		
OMe α	3.41	-	s
OMe β	3.53	-	s
NHCOCH ₃	2.06	-	s

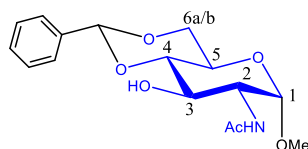
^a The spectrum was calibrated on the solvent residual peak (4.790 ppm, ref.: *J. Org. Chem.* **1997**, 62, 7512-7515). Apodization: exponential -0.60 Hz, Gaussian +0.30 Hz. ^b Deconvolution (*line fitting* under Mnova) revealed J_{1 α ,2 α} 4.2 Hz). ^c A distinction between α and β at 6-position is not necessary since the influence of the anomeric conformation on the chemical shift of the external 6-position is negligibly small. Even the 4-position and NHCOCH₃ are almost not influenced in GlcNAc systems.

Table 30: ^{13}C Assignments of methyl 2-acetamido-2-deoxy- α/β -D-glucopyranoside (**8**) (D_2O , *jmod*, 100.61 MHz).

^{13}C Assignment	^{13}C δ / ppm
1 α	98.1
1 β	101.9
2 α	53.6
2 β	55.5
3 α	71.1
3 β	74.0
4 α	70.0
4 β	69.9
5 α	71.7
5 β	75.9
6 α	60.6
6 β	60.8
OMe α	55.1
OMe β	57.0
NHCOCH $_3\alpha$	21.9
NHCOCH $_3\beta$	22.2
NHC <u>O</u> CH $_3\alpha$	174.4
NHC <u>O</u> CH $_3\beta$	174.7

Synthesis of methyl 2-acetamido-4,6-*O*-benzylidene-2-deoxy- α -D-glucopyranoside (**9**).

Compound **8** (5.50 g, 23.4 mmol) was dissolved in acetonitrile, benzaldehyde dimethyl acetal (7.1 mL, 7.24 g, 47.6 mmol) and campher-10-sulfonic acid (272 mg, 1.17 mmol, 5 mol %) were added and the reaction mixture was stirred under reflux for 20 min. The progress of the reaction was monitored by TLC on silica gel 60 F₂₅₄ with dichloromethane/methanol (4:1 v/v) as mobile phase (R_f 0.79). Detection was achieved by UV absorption (245 nm) and dipping the plate into 10 % (v/v) sulfuric acid in ethanol followed by charring at ~120 °C. Upon completion, the reaction mixture was neutralized with TEA and concentrated under diminished pressure. The crude product was purified by column chromatography on silica gel 60 with dichloromethane/methanol (100:1 v/v \rightarrow 10:1 v/v) as mobile phase. The product containing fractions were pooled and evaporated under reduced pressure to yield compound **9** as a colorless powder (5.27 g, 16.3 mmol, 70 %).



Exact Mass: 323,14
Molecular Weight: 323,35

Polarimetry (*P8000*, Krüss Optronic, 589 nm, 1 dm cuvette): $[\alpha]_D^{20} = +45.5^\circ$ (c 0.2, CHCl₃),
ref. 171: $[\alpha]_D^{20} = +40^\circ$ (c 1.5, CHCl₃).

ESI-TOF-MS (*Agilent 6224*, positive mode): $m/z = 346.124(1)$ [M+Na]⁺, 669.262(6) [2M+Na]⁺.

NMR data and assignments:

Table 31: ^1H Assignments of methyl 2-acetamido-4,6-*O*-benzylidene-2-deoxy- α -D-glucopyranoside (**9**) (DMSO- d_6 , $\tau g30$, 400.13 MHz).

^1H Assignment	^1H δ / ppm ^a	$J_{\text{H,H}}$ / Hz	Multiplicity
OMe	3.30	-	s
1	4.62	$J_{1,2}$ 3.6	d
2	3.86	$J_{2,3}$ 10.2	d
NHCOCH ₃	1.85	-	s
NHCOCH ₃	7.89	$J_{\text{NH,H-2}}$ 8.4	d
3	3.66	$J_{3,4}$ 9.2	dd
3-OH ^b	5.16	$J_{3\text{-OH, H-3}}$ 5.8	d
4	3.50	$J_{4,5}$ 9.2	dd~vt
5	3.62	$J_{5,6a}$ 5.0 $J_{5,6b}$ 10.1	ddd~m
6a	4.17	$J_{6a,6b}$ 10.1	dd
6b	3.74		dd~t
PhCHO	5.61	-	s
H _{arom.}	7.46	n.r.	m
	7.38	n.r.	m

^aThe spectrum was calibrated on the solvent residual peak (2.500 ppm, ref.: *J. Org. Chem.* **1997**, *62*, 7512-7515).

^bAdditionally, in the H,H-COSY spectrum, 3-OH shows a coupling to residual H₂O (at 3.36 ppm) confirming the assignment of the signal at 5.16 ppm to a hydroxyl group.

Table 32: ^{13}C Assignments of methyl 2-acetamido-4,6-*O*-benzylidene-2-deoxy- α -D-glucopyranoside (**9**) (DMSO- d_6 , $jmod$, 100.61 MHz).

^{13}C Assignment	^{13}C δ / ppm
OMe	54.4
1	99.1
2	54.1
NHCOCH ₃	169.5
NHCOCH ₃	22.7
3	67.3
4	82.3
5	62.8
6	68.2
PhCHO	101.6
C _{arom.} -H	128.9, 126.4, 128.0
C _{arom.} quaternary	137.8

X-ray crystallography:

Crystals were grown by slow evaporation of a chloroform solution (table 33, fig. 117).

Table 33: Crystal parameters of methyl 2-acetamido-4,6-*O*-benzylidene-2-deoxy- α -D-glucopyranoside (**9**) (Oxford Diffraction, SuperNova, four circle single crystal diffractometer with copper X-ray tube, $\lambda_{\text{Cu K}\alpha} = 1.54184 \text{ \AA}$, $T = 100 \text{ K}$). The packing is strongly affected by the formation of hydrogen bonds between 3-OH and H₂O and NH---O=C bridges.

Compound	Methyl 2-acetamido-4,6- <i>O</i> -benzylidene-2-deoxy- α -D-glucopyranoside
Habitus	Colorless needle
Crystal size	0.07 x 0.10 x 0.32 mm
Crystal system	primitive orthorhombic ($P2_12_12_1$)
	identity (x, y, z)
Symmetry	three 2-fold screw axes
	($1/2-x, -y, 1/2+z$; $1/2+x, 1/2-y, -z$; $-x, 1/2+y, 1/2-z$)
a	4.83459(4) \AA
b	14.75860(10) \AA
c	23.05893(15) \AA
α	
β	90 °
γ	
R_1	3.7 %
Chair conformation	4C_1

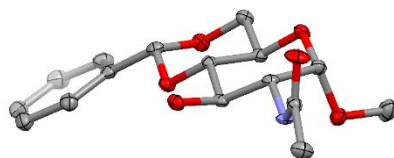
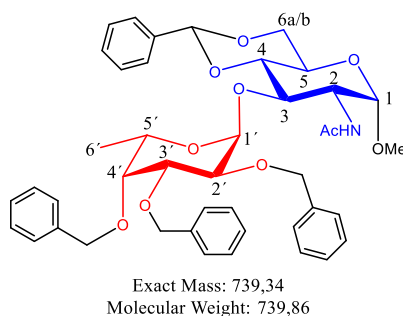


Fig. 117: Visualized crystal structure of compound **9**.

Synthesis of methyl 2-acetamido-4,6-*O*-benzylidene-2-deoxy-3-*O*-(2,3,4-tri-*O*-benzyl- α -L-fucopyranosyl)- α -D-glucopyranoside (10**).** Donor **6** (83 mg, 0.19 mmol), acceptor **9** (61 mg, 0.19 mmol), lithium perchlorate (1.18 g, 10.9 mmol), cesium fluoride (29 mg, 0.19 mmol) as acid scavenger and activated molecular sieve (4 Å) were suspended in dried dichloromethane and left to stir under argon atmosphere at r.t. for 24 h. The progress of the reaction was monitored by TLC on silica gel 60 F₂₅₄ with EE as mobile phase (*R*_f 0.29). Detection was achieved by UV absorption and dipping the plate into 10 % (v/v) sulfuric acid in ethanol followed by charring at ~120 °C. Upon completion, the mixture was diluted with dichloromethane, filtered and the filtrate was washed once with distilled water, dried over sodium sulfate and concentrated under diminished pressure. The crude product was purified by column chromatography on silica gel 60 with dichloromethane/methanol (100:1 v/v → 10:1 v/v) as mobile phase to yield compound **10** as a colorless powder (111 mg, 0.15 mmol, 81 %).



ESI-TOF-MS (Agilent 6224, positive mode): $m/z = m/z$ 740.343 [M+H]⁺, 762.325 [M+Na]⁺, 778.229 [M+K]⁺, 1501.657 [2M+Na]⁺.

NMR data and assignments:

Table 34: ¹H Assignments of methyl 2-acetamido-4,6-*O*-benzylidene-2-deoxy-3-*O*-(2,3,4-tri-*O*-benzyl- α -L-fucopyranosyl)- α -D-glucopyranoside (**10**) (CDCl₃, *zg30*, 600.13 MHz).

¹ H Assignment	¹ H δ / ppm ^a	<i>J</i> _{H,H} / Hz	Multiplicity
1	4.90	<i>J</i> _{1,2} 3.30	d
OMe	3.30	-	s
2	3.98	<i>J</i> _{2,3} 9.16	dd~m
NHCOCH ₃	1.47	-	s
NHCOCH ₃	6.44	<i>J</i> _{NH,H-2} 6.38	d
3	3.57	<i>J</i> _{3,4} 9.16	dd ~ vt
4	4.01	<i>J</i> _{4,5} n.r.	dd~m
5	3.78	<i>J</i> _{5,6a} 4.41 <i>J</i> _{5,6b} 9.86	ddd
6a	4.20	<i>J</i> _{6a,6b} 9.86	dd
6b	3.71	-	dd~vt
PhCHO	5.53	-	s
1'	5.18	<i>J</i> _{1',2'} 3.41	d
2'	4.01	<i>J</i> _{2',3'} 9.96	dd~m
3'	3.83	<i>J</i> _{3',4'} 2.78	dd
4'	3.57	<i>J</i> _{4',5'} n.r.	dd
5'	4.00	<i>J</i> _{5',6'} 6.50	dq~m
6'	1.00	-	d
PhCH ₂ O	4.9 ^b , 4.59 ^{b,c}	11.47	d, d
	4.69 ^d , 4.66 ^e	n.r.	m (4H)
H _{arom.}	7.50-7.46 (2H)	n.r.	m
	7.37-7.19 (18H)	n.r.	m

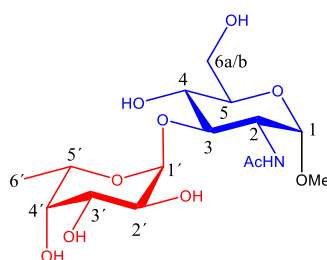
^a The spectrum was calibrated on the solvent residual peak (7.260 ppm, ref.: *J. Org. Chem.* **1997**, *62*, 7512-7515).

^b Proton is attached to carbon at 75.0 ppm. ^c Doublet at 4.59 ppm shows a roof effect. ^d Proton is attached to carbon at 74.4 ppm. ^e Proton is attached to carbon at 73.1 ppm. n.r. = not resolved due to interferences.

Table 35: ¹³C Assignments of methyl 2-acetamido-4,6-*O*-benzylidene-2-deoxy-3-*O*-(2,3,4-tri-*O*-benzyl- α -L-fucopyranosyl)- α -D-glucopyranoside (**10**) (CDCl₃, *jmod*, 150.90 MHz).

¹³ C Assignment	¹³ C δ / ppm
1	98.5
OMe	55.4
2	54.1
NHCOCH ₃	23.23
NHCOCH ₃	170.6
3	82.2
4	75.6
5	62.8
6	69.0
PhCHO	101.0
1'	99.2
2'	67.7
3'	79.9
4'	77.8
5'	68.0
6'	17.2
PhCH ₂ O	75.0, 74.4, 73.1
C _{arom.} quarternary	138.6, 138.5, 137.6, 137.4
C _{arom.} C-H	130-125

Synthesis of methyl 2-acetamido-2-deoxy-3-O- α -L-fucopyranosyl- α -D-glucopyranoside (11). Compound **10** (111 mg, 0.15 mmol) was suspended in methanol, palladium on carbon (~ 50 % H₂O) was added and the suspension was stirred under hydrogen atmosphere at normal pressure and r.t. overnight. The progress of the reaction was monitored by TLC on silica gel 60 F₂₅₄ with n-butanol/HOAc/H₂O (5:2:2 v/v/v) as mobile phase (R_f 0.43). Detection was achieved by dipping the plate into 10 % (v/v) sulfuric acid in ethanol followed by charring at ~120 °C. Upon completion, the reaction mixture was filtered, concentrated under diminished pressure and co-distilled with toluene three times. The crude product was purified by column chromatography on biogel P-2 (fine) with distilled water as eluent (1.6 mL/h, 4 mL fractions). The product containing fractions were pooled and lyophilized to yield target compound **11** as a colorless powder (65.0 mg, 0.17 mmol, 88 %).



Exact Mass: 381,16
Molecular Weight: 381,38

Polarimetry (*P8000*, Krüss Optronic, 589 nm, 1 dm cuvette): $[\alpha]_D^{20} = -27.5^\circ$ (*c* 0.2, H₂O), $[\alpha]_D^{20} = -19.5^\circ$ (*c* 0.2, MeOH), ref. 172: $[\alpha]_D^{20} = -19.8^\circ$ (*c* 0.5, MeOH).

Melting Point (*M-565*, Büchi, sample loader *M-569*): caramelization temperature: 235-236 °C, carbonization temperature: 237 °C, ref. (see above): m.p. = 276-277 °C.

ESI-TOF-MS (*Agilent 6224*, positive mode): *m/z* = 404.156(0) [M+Na]⁺.

NMR data and assignments:

Table 36: ^1H Assignments of Fuc α 1-3GlcNAc α 1-OMe (**11**). Bruker AVANCE I 400 NMR spectrometer, ^1H = 400.13 MHz, 5 mm PABBO BB probe head, zg30, AQ 3.96 s, NS 16, TD 64 k, 65 mg / 650 μL D $_2$ O, LB -0.60 Hz.

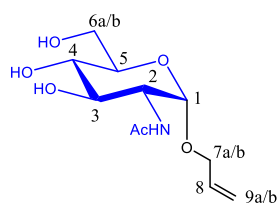
^1H Assignment	^1H δ / ppm ^a	$J_{\text{H,H}}$ / Hz	Multiplicity
1	4.73	$J_{1,2}$ 3.6	d
OMe	3.42	-	s
2	4.11	$J_{2,3}$ 10.5	dd
NHCOCH ₃	2.05	-	s
3	3.80	$J_{3,4}$ 8.9	dd~vt
4	3.58	$J_{4,5}$ 9.9	dd~vt
5	3.73	$J_{5,6a}$ 2.3 $J_{5,6b}$ n.r.	ddd
6a	3.91 (3.95-3.88)	$^2J_{6a,6b}$ 12.2	dd
6b	3.82 (3.85-3.79)		dd
1'	5.01	$J_{1',2'}$ 4.1	d
2'	3.72	$J_{2',3'}$ 10.2	dd
3'	3.85	$J_{3',4'}$ 3.3	dd
4'	3.81	$J_{4',5'} < 1$	dd~vt
5'	4.36	$J_{5',6'}$ 6.6	dq~vq
6'	1.19		d

^a The spectrum was calibrated on the solvent residual peak (4.790 ppm, *J. Org. Chem.* **1997**, 62, 7512-7515). n.r. = not resolved due to interference with the H-2' signal, typically 5 Hz (GlcNAc α 1-OMe). vt = virtual triplet, vq = virtual quartet.

Table 37: ^{13}C Assignments of Fuc α 1-3GlcNAc α 1-OMe (**11**). Bruker DRX 500 NMR spectrometer, ^{13}C = 125.76 MHz, 5 mm PABBI probe head, jmod, AQ 1.09 s, NS 320, TD 64 k, 65 mg / 650 μL D $_2$ O.

^{13}C Assignment	^{13}C δ / ppm
1	98.3
OMe	55.1
2	53.2
NHCOCH ₃	22.0
NHCOCH ₃	174.4
3	78.3
4	68.5
5	71.8
6	60.6
1'	99.8
2'	68.0
3'	69.5
4'	71.8
5'	66.8
6'	15.2

Synthesis of allyl 2-acetamido-2-deoxy- α -D-glucopyranoside (12). 2-Acetamido-2-deoxy- α / β -glucopyranose (**7**) (9.5 g, 43 mmol) was suspended in allyl alcohol (140 mL) and acetyl chloride was added (0.7 mL). The mixture was stirred under reflux (70 °C, 3 days). Upon completion (R_f 0.21, $\text{CHCl}_3/\text{MeOH}$ 10:1), the mixture was evaporated under diminished pressure. The residue was re-crystallized from acetonitrile to yield compound **12** as a colorless powder (10.5 g, 40.0 mmol, 93 %).



Exact Mass: 261,12
Molecular Weight: 261,27

$[\alpha]_D^{20} = +137.2^\circ$ (c 1.0, MeOH), ref. 173: $[\alpha]_D^{25} = +148.8^\circ$ (c 1.62, H_2O)

m.p. = 168 °C, ref. (see above): 172-174 °C

NMR data and assignments:

Table 38: ^1H Assignments of allyl 2-acetamido-2-desoxy- α -D-glucopyranoside (**12**) (MeOD, $z\theta$ 30, 400.13 MHz).

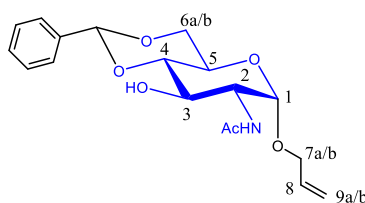
^1H Assignment	^1H δ / ppm	$J_{\text{H,H}}$ / Hz	Multiplicity
1	4.83	$J_{1,2}$ 3.3	d
2	3.90	$J_{2,3}$ 10.7	dd
3	3.70	$J_{3,4}$ n.r.	dd~m (2H)
4	3.32	$J_{4,5}$ 9.8	dd
5	3.59	$J_{5,6a}$ 2.0 $J_{5,6b}$ 5.6	ddd
6a	3.82	$J_{6a,b}$ 11.7	dd
6b	3.70		dd~m (2H)
7a	4.20	$J_{7a,8}$ 6.1	dd
7b	4.00	$J_{7b,8}$ 5.1	dd
8	5.90	$J_{8,9\text{cis}}$ 17.3 $J_{8,9\text{trans}}$ 10.4	dddd
9 _{cis} 9 _{trans}	5.33-5.24	n.r.	dd~m (2H)
NHCOCH₃	1.98	-	s

Table 39: ^{13}C Assignments of allyl 2-acetamido-2-desoxy- α -D-glucopyranoside (**12**) (MeOD, *jmod*, 100.61 MHz).

^{13}C Assignment	^{13}C δ / ppm
1	98.1
2	55.8
3	72.8
4	73.3
5	74.3
6	63.1
7	69.6
8	136.0
9	117.9
NHCOCH ₃	174.1
NHCOCH ₃	21.7

Synthesis of allyl 2-acetamido-4,6-O-benzyliden-2-deoxy- α -D-glucopyranoside (13).

Compound **12** (5.00 g, 19.1 mmol) was suspended in acetonitrile (100 mL), BADMA (5.80 mL, 38.2 mmol) and campher-10-sulfonic acid (222 mg, 1.00 mmol) were added and the reaction mixture was stirred under reflux for 20 min. The progress of the reaction was monitored by TLC on silica gel 60 F₂₅₄ with dichloromethane/methanol (4:1 v/v) as mobile phase (R_f 0.83). Detection was achieved by UV absorption (245 nm) and dipping the plate into 10 % (v/v) sulfuric acid in ethanol followed by charring at ~ 120 °C. Upon completion, the mixture was neutralized with TEA, diluted with EA and washed with water. The organic phase was dried over NaSO₄ and evaporated under diminished pressure. The residue was purified by column chromatography (dichloromethane/methanol 100 % \rightarrow 95:5) to yield compound **13** as a colorless powder (5.33 g, 15.3 mmol, 80 %).



Exact Mass: 349,15
Molecular Weight: 349,38

$[\alpha]_D^{20} = +86.5^\circ$ (c 1.0, DMSO), $+94.9^\circ$ (c 1.0, DMF), ref. 174: $+99^\circ$ (c 1.0, DMF)

m.p. = 231 °C, ref. (see above): 232-234 °C

NMR data and assignments:

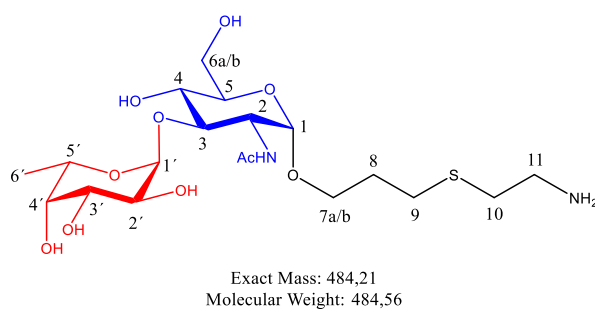
Table 40: ^1H Assignments of allyl 2-acetamido-4,6-*O*-benzylidene-2-desoxy- α -D-glucopyranoside (**12**) (MeOD, z_{g30} , 400.13 MHz).

^1H Assignment	^1H δ / ppm	$J_{\text{H,H}}$ / Hz	Multiplicity
1	4.76	$J_{1,2}$ 3.3	d
2	4.10-4.01	$J_{2,3}$ 10.7	dd~m (2H)
3	3.92	$J_{3,4}$ n.r.	dd~vt (2H)
4	3.50	$J_{4,5}$ 9.8	dd~vt
5	3.87-3.77	$J_{5,6a}$ 2.0 $J_{5,6b}$ 5.6	ddd~m (2H)
6a	4.19-4.11	$J_{6a,b}$ 11.7	dd~m (2H)
6b	3.87-3.77		dd~m (2H)
7a	4.19-4.11	$J_{7a,8}$ 6.1	dd~m (2H)
7b	4.10-4.01	$J_{7b,8}$ 5.1	dd~m (2H)
8	5.90	$J_{8,9\text{cis}}$ 17.3 $J_{8,9\text{trans}}$ 10.4	dddd
9 _{cis}	5.36	n.r.	dd~m (2H)
9 _{trans}	5.17		
PhCHO	5.63	-	s
H _{arom.}	7.47-7.37	n.r.	m (5H)
NHCOCH ₃	2.02	-	s

Table 41: ^{13}C Assignments of allyl 2-acetamido-4,6-*O*-benzylidene-2-desoxy- α -D-glucopyranoside (**12**) (MeOD, j_{mod} , 100.61 MHz).

^{13}C Assignment	^{13}C δ / ppm
1	96.8
2	54.1
3	67.2
4	82.1
5	62.7
6	67.5
7	68.0
8	137.7
9	116.8
PhCHO	109.9
C _{arom.} -H	128.8, 128.0, 126.4
C _{arom.} quarternary	134.4
NHCOCH ₃	169.4
NHCOCH ₃	22.5

Synthesis of 3-(2-aminoethylthio)propyl 2'-acetamido-2'-deoxy-3'-O- α -L-fucopyranosyl- α -D-glucopyranoside (15). Cysteamine hydrochloride (2.0 g) was dissolved in ethanol (96 %, 10 mL), the solution was heated gently and kept at 4 °C overnight. The supernatant was removed, the precipitate (29 mg, 0.38 mmol) was dissolved in distilled water (50 μ L) and compound **14** (10 mg, 25 μ mol), which was subjected to mild hydrolysis before (HOAc, reflux, 20 min, co-distilled with toluene) was added. The reaction mixture was kept at r.t. overnight. The progress of the reaction was monitored by ESI MS spectrometry. After complete conversion, the reaction mixture was lyophilized. The lyophilizate was dissolved in methanol, palladium on carbon (~ 50 % H₂O) was added and the solution was stirred under hydrogen atmosphere at normal pressure and r.t. overnight. The mixture was directly purified by column chromatography on biogel P-2 (fine) with distilled water as eluent (1.6 mL / h, 4 mL fractions). The product containing fractions were pooled and lyophilized to yield target compound **15** as a colorless powder (11 mg, 23 μ mol, 91 %).



ESI-TOF-MS: m/z 507.32 [M+Na]⁺.

NMR data and assignments:

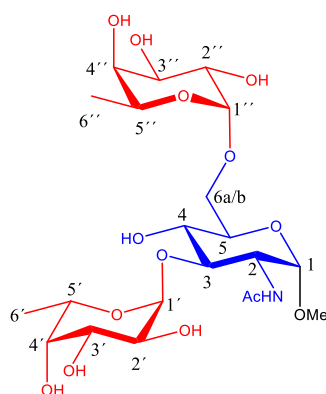
Table 42: ^1H Assignments of 3-(2-aminoethylthio)propyl 2'-acetamido-2'-deoxy-3'-*O*- α -L-fucopyranosyl- α -D-glucopyranoside (**15**).

^1H Assignment	^1H δ / ppm	$J_{\text{H,H}}$ / Hz	Multiplicity
-O-CH(a) <u>2</u> -CH ₂ -CH ₂ -S-	3.61	n.r.	dt
-O-CH(b) <u>2</u> -CH ₂ -CH ₂ -S-	3.85	13.1	dt
-O-CH ₂ -CH ₂ -CH ₂ -S-	1.95	6.9	dq
-O-CH ₂ -CH ₂ -CH ₂ -S-	2.76	7.2	t
S-CH ₂ -CH ₂ -NH ₂	2.91	6.7	t
S-CH ₂ -CH ₂ -NH ₂	3.27		t
1	4.86	$J_{1,2}$ 3.6	d
2	4.12	$J_{2,3}$ 10.5	dd
NHCOCH ₃	2.06	-	s
3	3.83	$J_{3,4}$ n.r.	dd~m
4	3.58	$J_{4,5}$ n.r.	dd~m
5	3.74	$J_{5,6a}$ n.r. $J_{5,6b}$ n.r.	ddd~m
6 _a	3.88	$J_{6a,6b}$ 11.7	dd~m
6 _b	3.80		dd~m
1'	5.04	$J_{1',2'}$ 4.2	d
2'	3.73	$J_{2',3'}$ n.r.	dd~m
3'	3.84	$J_{3',4'}$ n.r.	dd~m
4'	3.81	$J_{4',5'}$ n.r.	dd~m
5'	4.37	$J_{5',6'}$ 6.6	dq~q
6'	1.20		d

Table 43: ^{13}C Assignments of 3-(2-aminoethylthio)propyl 2'-acetamido-2'-deoxy-3'-*O*- α -L-fucopyranosyl- α -D-glucopyranoside (**15**).

^{13}C Assignment	^{13}C δ / ppm
-O-CH ₂ -CH ₂ -CH ₂ -S-	66.3
-O-CH ₂ -CH ₂ -CH ₂ -S-	28.3
-O-CH ₂ -CH ₂ -CH ₂ -S-	27.5
-S-CH ₂ -CH ₂ -NH ₂	28.1
-S-CH ₂ -CH ₂ -NH ₂	38.4
1	97.1
2	53.3
NHCOCH ₃	174.4
NHCOCH ₃	22.0
3	78.2
4	68.4
5	72.1
6	60.6
1'	99.7
2'	68.0
3'	69.6
4'	71.9
5'	66.9
6'	15.3

Synthesis of methyl 2-acetamido-2-deoxy-3-O- α -L-fucopyranosyl-(6-O- α -L-fucopyranosyl)- α -D-glucopyranoside (18). Compound **10** (50 mg, 68 μ mol) was dissolved in dichloromethane/diethyl ether (5 mL, 1:1 v/v), lithium aluminum hydride (18 mg, 476 μ mol, 7 eq.) was suspended and the mixture was heated (50 $^{\circ}$ C). Under reflux, aluminum chloride (41 mg, 306 μ mol, 4.5 eq.), dissolved in diethyl ether (10 mL), was added slowly. The reaction was stirred under reflux for 2 h, diluted with diethyl ether (50 mL) and ethyl acetate (10 mL) and quenched with water (30 mL). The aqueous phase was extracted with diethyl ether and the unified organic extracts were washed with water and brine, dried over sodium sulfate and evaporated under diminished pressure. The crude product was dissolved in dried dichloromethane and donor **6** (30 mg, 68 μ mol), lithium perchlorate (425 mg, 4.00 mmol, 60 eq.), cesium fluoride (10 mg, 68 μ mol, 1 eq.) as acid scavenger and activated molecular sieve (4 Å) were added. Upon completion, the reaction mixture was diluted with dichloromethane and washed with water, the organic layer was dried over sodium sulfate and diminished under reduced pressure. The residue was dissolved in methanol, palladium on carbon (\sim 50 % H_2O) was added and the suspension was stirred under hydrogen atmosphere at normal pressure and r.t. overnight. The progress of the reaction was monitored by TLC on silica gel 60 F₂₅₄ with n-butanol/HOAc/H₂O (5:2:2 v/v/v) as mobile phase (R_f 0.43). Detection was achieved by dipping the plate into 10 % (v/v) sulfuric acid in ethanol followed by charring at \sim 120 $^{\circ}$ C. Upon completion, the reaction mixture was filtered, concentrated under diminished pressure and co-distilled with toluene three times. The crude product was purified by column chromatography on biogel P-2 (fine) with distilled water as eluent (1.6 mL/h, 4 mL fractions). The product containing fractions were pooled and lyophilized to yield target compound **18** as a colorless powder (7.0 mg, 13 μ mol, 19 %).



Exact Mass: 527,22
Molecular Weight: 527,52

NMR data and assignments:

Table 44: ^1H NMR data of Fuc α 1-3(Fuc α 1-6)GlcNAc α 1-OMe (22).

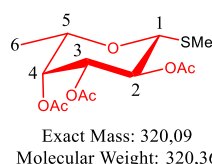
Assignment	^1H ν / ppm	$J_{\text{H,H}}$ / Hz	Multiplicity
1	4.73	$J_{1,2}$ 3.5 Hz	d
OMe	3.43	-	s
2	4.11	$J_{2,3}$ 10.4 Hz	dd
NHCOCH ₃	2.04	-	s
3	3.80	$J_{3,4}$ 10.4	dd
4	3.71	n.d. [†]	dd
5	n.d.*	n.d.*	ddd
6a	3.97	$^2J_{6a,6b}$ 9.6 Hz	dd~d
6b	3.86		m
1'	5.00	$J_{1',2'}$ 4.0 Hz	d
2'	3.71	$J_{2',3'}$ 10.4 Hz	dd
3'	3.85	n.d.**	dd
4'	3.82	$J_{3',4'}$ 9.2 Hz	dd
5'	4.33	$J_{4',5'} < 0$ Hz	dq~q
6'	1.16	$J_{5',6'}$ 6.6 Hz	dd
1''	4.95	$J_{1'',2''}$ 3.8 Hz	d
2''	3.82	n.d.**	dd
3''	3.91		dd
4''	3.82	$J_{4'',5''} < 0$ Hz	dd
5''	4.12	$J_{5'',6''}$ 6.6 Hz	dq~q
6''	1.23		dd

*3.98-3.89 (m, 2H); **3.88-3.74 (m, 7H); [†]3.72-3.64 (m, 2H).

Table 45: ^{13}C -NMR data of Fuc α 1-3(Fuc α 1-3)GlcNAc α 1-OMe (22).

^{13}C Assignment	^{13}C δ / ppm
1	98.4
OMe	55.3
2	53.2
NHCOCH ₃	22.0
NHCOCH ₃	174.4
3	78.3
4	n.d.
5	n.d.
6a	67.0
6b	67.0
1'	99.9
2'	n.d.
3'	n.d.
4'	71.9
5'	66.8
6'	15.2
1''	99.2
2''	n.d.
3''	69.5
4''	71.9
5''	66.9
6''	15.3

Synthesis of methyl 2,3,4-tri-O-acetyl-1-thio-β-L-fucopyranoside (19). Compound **2** (3.84 g, 11.6 mmol) was dissolved in dried dichloromethane (125 mL), methyl mercaptotrimethyl silane (2.00 mL, 14.1 mmol) and trimethylsilyl triflate were added (ice bath). The reaction mixture was stirred at r.t. overnight. The progress of the reaction was monitored by TLC with PE/EE (1:1 v/v) as mobile phase (R_f 0.52). The mixture was diluted with dichloromethane and washed with saturated sodium hydrogen carbonate solution and water. The organic phase was dried over sodium sulfate, filtered and concentrated under diminished pressure. The residue was co-distilled with toluene three times to yield compound **19** as a colorless powder (3.18 g, 994 μmol, 86 %).



Polarimetry (*P8000*, Krüss Optronic, 589 nm, 1 dm cuvette): $[\alpha]_D^{20} = +0.43^\circ$ (c 1.0, CHCl_3).

NMR data and assignments:

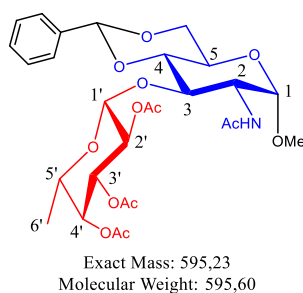
Table 46: ^1H Assignments of methyl 2,3,4-tri-O-acetyl-1-thio-β-L-fucopyranoside (**19**).

^1H Assignment	^1H δ / ppm	$J_{\text{H,H}}$ / Hz	Multiplicity
1	4.35	$J_{1,2}$ 9.8	d
2	5.23	$J_{2,3}$ 9.9	dd~vt
3	5.04	$J_{3,4}$ 3.4	dd
4	5.27	$J_{4,5}$ 1.0	dd
5	3.85	$J_{5,6}$ 6.0	dq
6	1.21		d
OCOCH ₃	2.16, 2.06, 1.97	-	s
SMe	2.18	-	s

Table 47: ^{13}C Assignments of methyl 2,3,4-tri-O-acetyl-1-thio-β-L-fucopyranoside (**19**).

^{13}C Assignment	^{13}C δ / ppm
1	83.3
2	66.8
3	72.5
4	70.7
5	73.4
6	16.3
OCOCH ₃	170.7, 170.2, 169.8
OCOCH ₃	20.9, 20.8, 20.7
SMe	11.5

Synthesis of methyl 2-acetamido-4,6-*O*-benzylidene-2-deoxy-3-*O*-(2,3,4-tri-*O*-acetyl- β -L-fucopyranosyl)- α -D-glucopyranoside (20**).** Compound **28** (500 mg, 1.55 mmol) was dissolved in dried dichloromethane (80 mL), methyl 2,3,4-tri-*O*-acetyl- α/β -L-fucopyranoside (595 mg, 1.2 eq.) and iodine (1.89 mg, 4 eq.) were added and the solution was stirred at r.t. overnight. The progress of the reaction was monitored by TLC with EE as mobile phase (R_f 0.32). Detection was achieved by UV absorption and dipping the plate into 10 % (v/v) sulfuric acid in ethanol followed by charring at ~ 120 °C. Upon completion, the mixture was neutralized with potassium carbonate, filtered, decolorized with saturated sodium thiosulfate, extracted with dichloromethane and diminished under reduced pressure. The crude product was purified by column chromatography on silica gel 60 with dichloromethane/methanol (100:1 v/v \rightarrow 50:1 v/v) as mobile phase to yield compound **20** as a colorless powder (262 mg, 0.44 mmol, 17 %).



NMR data and assignments:

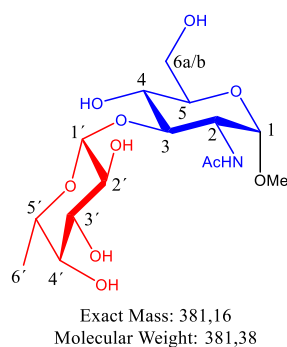
Table 48: ^1H Assignments of methyl 2-acetamido-4,6-*O*-benzylidene-2-deoxy-3-*O*-(2,3,4-tri-*O*-acetyl)- β -L-fucopyranosyl- α -D-glucopyranoside (**20**) (CDCl_3).

^1H Assignment	^1H δ / ppm*	$J_{\text{H,H}}$ / Hz	Multiplicity
OMe	3.36	-	s
1	6.17	$J_{1,2}$ 3.6	d
2	4.25	n.r.	dd~m
NHCOCH ₃ , COCH ₃ (3x)	1.99, 2.07, 2.17	-	s
3	10.02	n.r.	dd
4	4.37	n.r.	dd~m
5	4.25	n.r.	dd~m
6a	3.53	n.r.	dd~m
6b	4.08	n.r.	dd~m
PhCH ₂ OO	5.52	-	s
H _{arom.}	7.43-7.33	n.r.	m
1'	6.14	$J_{1',2'}$ 7.8	d
2'	5.71	n.r.	dd~m
3'	6.10	n.r.	dd~m
4'	5.41	n.r.	dd~m
5'	4.44	n.r.	dd~m
6'	1.26	$J_{5',6'}$ 6.5	d

Table 49: ^{13}C Assignments of methyl 2-acetamido-4,6-*O*-benzylidene-2-deoxy-3-*O*-(2,3,4-tri-*O*-acetyl)- β -L-fucopyranosyl- α -D-glucopyranoside (**20**) (CDCl_3).

^{13}C Assignment	^{13}C δ / ppm
OMe	55.4
1	103.3
2	58.1
NHCOCH ₃ , OCOCH ₃ (3x)	23.6, 21.0 (3x)
NHCOCH ₃ , OCOCH ₃ (3x)	174.6, 170.2
3	78.9
4	84.8
5	69.5
6	68.8
PhCHOO	128.6, 127.8, 126.6, 126.3
PhCHOO	108.7
1'	106.2
2'	71.0
3'	68.9
4'	70.9
5'	70.6
6'	16.7

Synthesis of methyl 2-acetamido-2-deoxy-3-O-β-L-fucopyranosyl-α-D-glucopyranoside (21). Compound **20** (262 mg, 0.44 mmol) was suspended in acetic acid (80 %, 5 mL) and stirred at 90 °C for 1 h. The reaction mixture was concentrated under diminished pressure and co-distilled with toluene three times. The residue was dissolved in methanol (5 mL), sodium methanolate was added and the reaction mixture was stirred at r.t. overnight. The reaction mixture was neutralized with IR120 H⁺ resin, filtered, concentrated under diminished pressure and co-distilled with toluene three times. The crude product was purified by column chromatography on biogel P-2 (fine) with distilled water as eluent (1.6 mL/h, 4 mL fractions) to yield target compound **21** as a colorless powder (136 mg, 0.35 mmol, 81 %).



Polarimetry (*P8000*, Krüss Optronic, 589 nm, 1 dm cuvette): $[\alpha]_D^{20} = +123$ (*c* 0.1, H₂O)

NMR data and assignments:

Table 50: ¹H Assignments of Fucβ1-3GlcNAcα1-OMe (**21**) (D₂O).

¹ H Assignment	¹ H δ / ppm	J _{H,H} / Hz	Multiplicity
OMe	3.43	-	s
1	4.89	J _{1,2} 3.0	d
2	3.96	J _{2,3} n.r.	dd~m
NHCOCH ₃	2.07	-	s
3	3.92	J _{3,4} n.r.	dd
4	3.72	J _{4,5} n.r.	dd~m
5	3.72	J _{5,6a} n.r., J _{5,6b} n.r.	ddd~m
6 _a	3.91	J _{6a,6b} n.r.	dd~m
6 _b	3.84		dd~m
1'	4.54	J _{1',2'} 7.8	d
2'	3.51	J _{2',3'} 9.9	dd
3'	3.68	J _{3',4'} 3.5	dd
4'	3.76	J _{4',5'} 1.1	dd
5'	3.78	J _{5',6'} 6.5	dd
6'	1.31		d

Table 51: ^{13}C Assignments of Fuc β 1-3GlcNAc α 1-OMe (21) (D_2O).

^{13}C Assignment	^{13}C δ / ppm
OMe	55.0
1	97.9
2	52.4
NHCOCH ₃	22.1
NHCOCH ₃	174.4
3	80.2
4	69.6
5	71.5
6	60.3
1'	104.0
2'	71.3
3'	72.8
4'	70.7
5'	71.1
6'	15.9

10. Supplemental Information

10.1. ¹H-Check Sheet for STD NMR Samples

Date: _____ **Name:** Tim Raiber **Group:** Spillner
Phone: _____ **Mobile:** _____ **Institute:** Biochemistry

¹H-Check

Name of the sample: HMM5
Experiment: STD NMR
Purpose: K_D determination
Spectrometer: AVIII 600

Properties of the sample:

Solvent: D₂O (PBS)
Mass of the ligand: 0.16 mg (Current state: without ligand)
Molecular weight of the protein: 125 kDa
Stoffmenge des Proteins: 1.3 · 10⁻⁹ mol
Agreed filling volume: 180 μL
Actual filling volume: 180 μL

The sample is to be stored on ice or in the fridge. If the sample does not meet the required criteria, do not titrate. Wait until the sample is rectified.

Questions for ¹H-check before K_D-determination.

Number	Check	Finding
1	Is the experiment running on the correct NMR spectrometer?	
2	What is the temperature? Is it stable?	
3	Is the actual filling volume equal to the agreed filling volume? (Use depth gauge or comparison tube!)	
4	Is the sample free from turbidity and precipitate?	
5	Is the sample free from contaminants? (e.g., ethanol, isopropanol, Tween 20, imidazole)	
6	Is the sample inhomogeneous? (asymmetrical HDO signal, shimming very difficult)	
7	Are protein signals detectable? (position, shape, intensity)	

Does the sample need to be rectified? Yes No

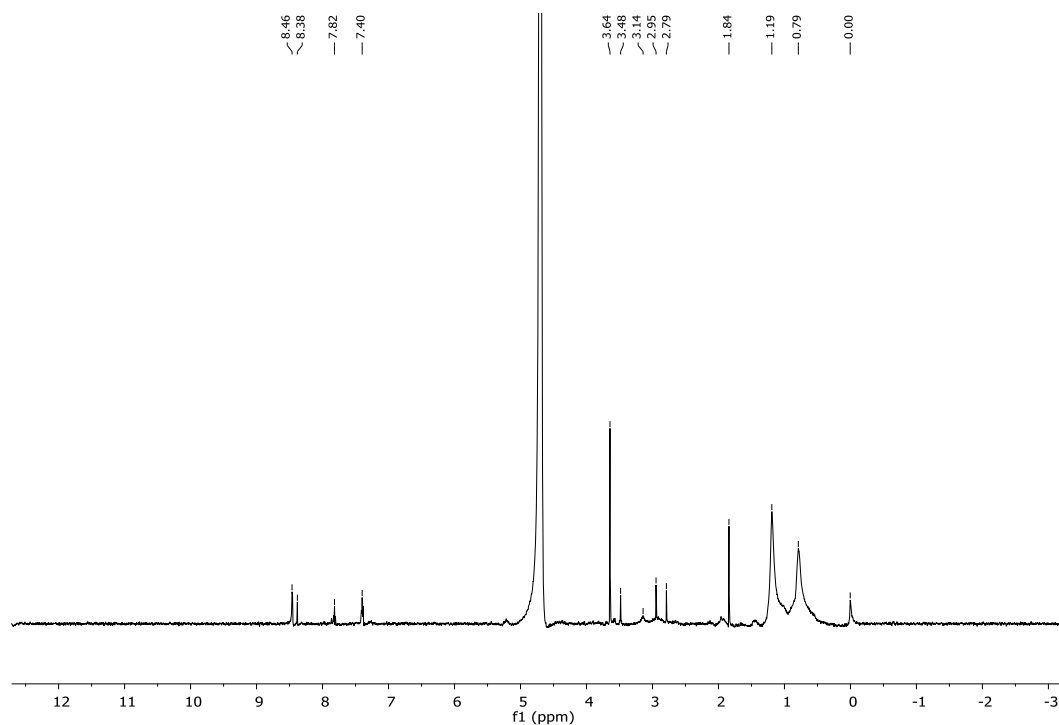


Fig. S1: ^1H NMR spectrum (quality control) of polyclonal rabbit IgG after bromelain affinity purification and re-buffering (*zg30*, 600 MHz, 5 mm, ns 256). A low pass filter according to Whittaker and an apodization with an exponential function was applied (LB 1 Hz). This is the first antibody of a serial subjected to STD NMR experiments. NMR operator: T. Hackl, NMR interpreter: T. Raiber.

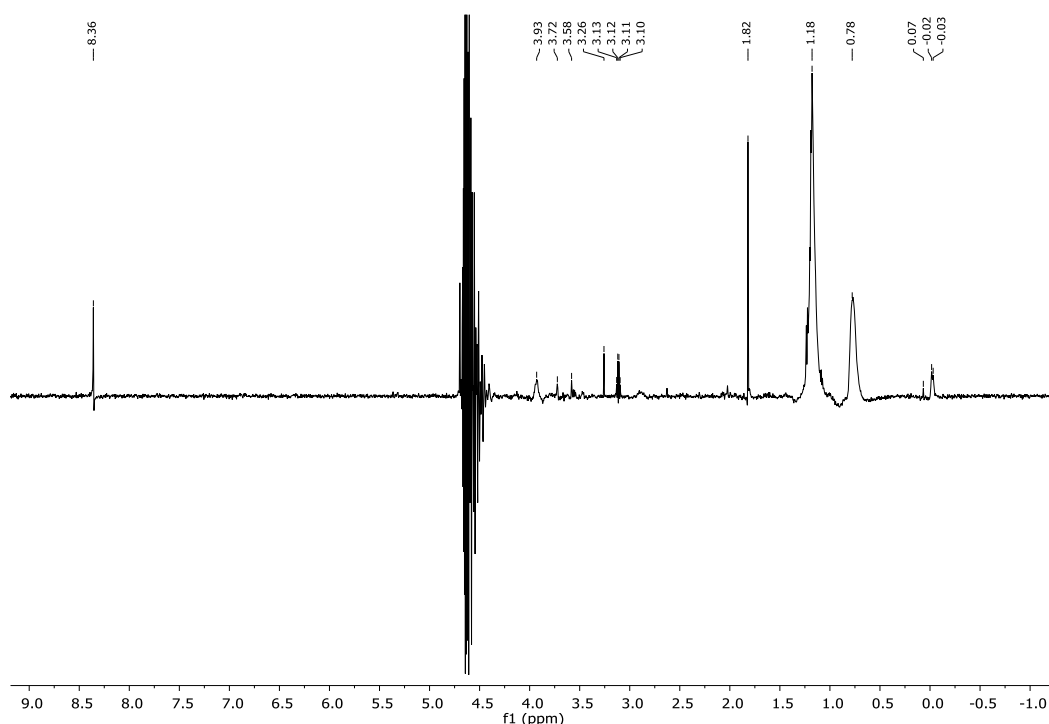


Fig. S2: ^1H NMR spectrum (quality control) of HHH1 antibody (*zgesgp*, 700.13 MHz, ns 128) manipulated with a low-pass filter according to Whittaker. A suitable filter to manipulate the disturbed water suppression could not be found. Probably, the water suppression must be optimized on the spectrometer. NMR operator: M. Fölsing, NMR interpreter: T. Raiber.

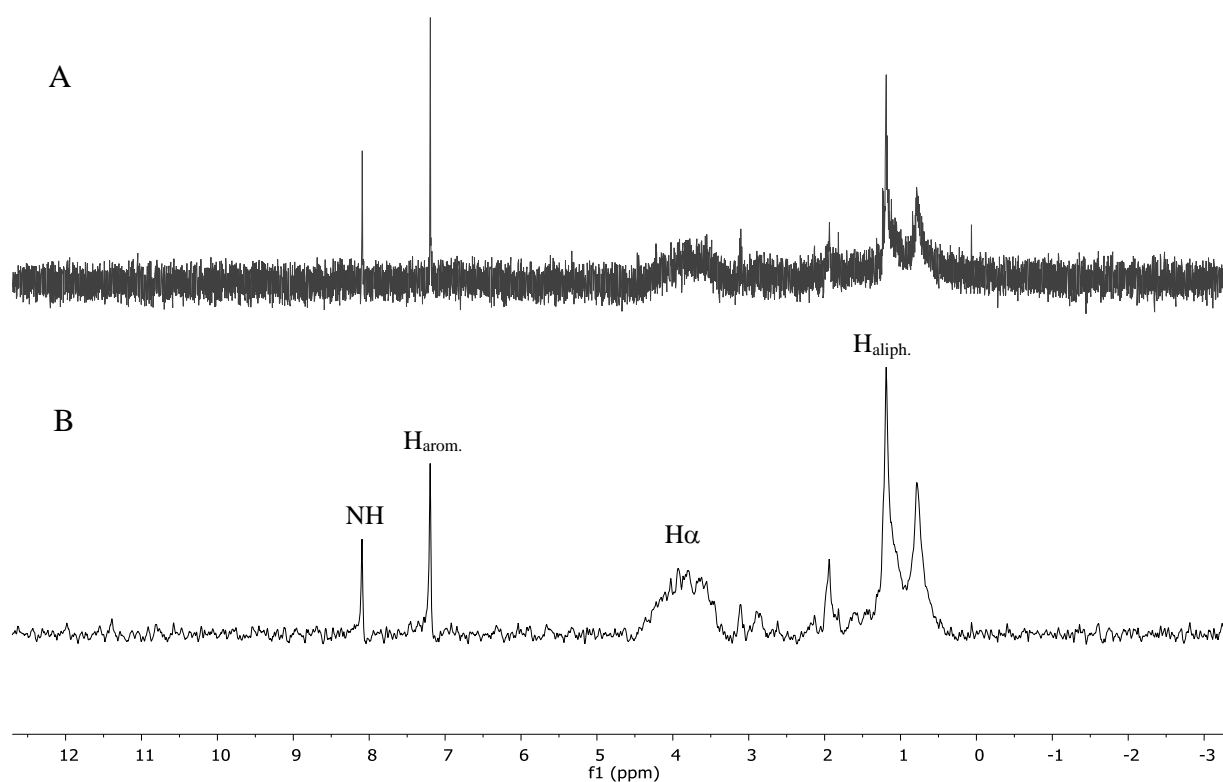


Fig. S3: ¹H NMR spectrum (quality control) of the HMM5 antibody (0.16 mg, AVIII 600 MHz, 5 mm, *zgesgp*, ns 512) after purification and re-buffering to PBS. Since the unmanipulated spectrum (A) showed protein signals massively distorted by noise, a low-pass filter according to Whittaker was applied and an apodization along t1 (exponential function, 10 Hz) favored the early parts of the FID to enhance the S/N ratio and to remove truncation artefacts (B). The signals may be assigned as follows: 8.1 ppm NH, 7.2 ppm aromatic protons, 4.5-3.3 ppm H_α, 3.3-0.5 ppm aliphatic protons. The sample seems to be absent of contaminations. NMR operator: V. Priegnitz (NMR service), NMR interpreter: T. Raiber.

10.2. DNA Sequences of Monoclonal Anti-HRP Antibodies and HRP C

Table S5: Amino acid sequence of HMM5-scFv. The first amino acid is the N-terminus. The loops forming the interface between antibody and antigen are shaded blue (heavy chain) or magenta (light chain), respectively. The linker sequence is shaded grey. The loop 72-75 is not involved in an interaction with Fuc α 1-3GlcNAc.

1	2	3	4	5	6	7	8	9	10	11	12	13	14	15	16	17	18	19	20
Q	S	L	E	E	S	G	G	R	L	V	T	P	G	T	P	L	T	L	T
21	22	23	24	25	26	27	28	29	30	31	32	33	34	35	36	37	38	39	40
C	T	V	S	G	F	S	L	C	T	Y	N	I	H	W	V	R	Q	A	P
41	42	43	44	45	46	47	48	49	50	51	52	53	54	55	56	57	58	59	60
G	K	G	L	E	W	I	G	V	I	D	T	G	G	G	T	Y	F	A	S
61	62	63	64	65	66	67	68	69	70	71	72	73	74	75	76	77	78	79	80
W	A	K	G	R	F	A	I	S	K	T	S	S	T	T	V	D	L	K	M
81	82	83	84	85	86	87	88	89	90	91	92	93	94	95	96	97	98	99	100
T	S	L	T	A	A	D	T	A	T	T	F	C	A	K	G	F	D	Y	S
101	102	103	104	105	106	107	108	109	110	111	112	113	114	115	116	117	118	119	120
A	S	T	N	L	W	G	P	G	T	L	V	T	I	S	S	G	S	G	G
121	122	123	124	125	126	127	128	129	130	131	132	133	134	135	136	137	138	139	140
S	G	G	G	G	S	G	G	G	G	S	M	E	L	D	M	T	Q	T	P
141	142	143	144	145	146	147	148	149	150	151	152	153	154	155	156	157	158	159	160
S	S	V	S	A	P	V	G	G	S	V	T	I	N	C	Q	S	S	Q	S
161	162	163	164	165	166	167	168	169	170	171	172	173	174	175	176	177	178	179	180
V	Y	G	N	N	Y	L	A	W	Y	Q	Q	K	A	G	Q	P	P	K	L
181	182	183	184	185	186	187	188	189	190	191	192	193	194	195	196	197	198	199	200
L	I	Y	R	A	S	T	L	A	S	G	A	P	S	R	F	K	G	S	G
201	202	203	204	205	206	207	208	209	210	211	212	213	214	215	216	217	218	219	220
S	G	T	Q	F	T	L	T	I	S	D	L	E	C	D	D	A	A	T	Y
221	222	223	224	225	226	227	228	229	230	231	232	233	234	235	236	237	238	239	240
Y	C	L	G	Y	Y	N	G	V	I	N	V	F	G	G	G	T	N	V	E
241	242																		
I	K																		

Table S6: Amino acid sequence of HHH1-scFv. The first amino acid is the N-terminus. The loops forming the interface between antibody and antigen are shaded blue (heavy chain) or magenta (light chain), respectively. The linker sequence is shaded grey.

1	2	3	4	5	6	7	8	9	10	11	12	13	14	15	16	17	18	19	20
Q	E	Q	L	V	E	S	G	G	G	L	V	T	P	G	G	T	L	T	L
21	22	23	24	25	26	27	28	29	30	31	32	33	34	35	36	37	38	39	40
T	C	T	A	S	G	F	T	I	S	N	Y	H	M	S	W	V	R	Q	A
41	42	43	44	45	46	47	48	49	50	51	52	53	54	55	56	57	58	59	60
P	G	K	G	L	E	W	I	G	F	I	D	T	G	G	S	A	A	Y	A
61	62	63	64	65	66	67	68	69	70	71	72	73	74	75	76	77	78	79	80
P	W	A	K	G	R	F	T	I	S	R	T	S	T	T	V	A	L	K	I
81	82	83	84	85	86	87	88	89	90	91	92	93	94	95	96	97	98	99	100
T	S	P	T	T	E	D	T	A	T	Y	F	C	A	R	G	A	P	A	W
101	102	103	104	105	106	107	108	109	110	111	112	113	114	115	116	117	118	119	120
G	T	A	N	V	W	G	Q	G	T	L	V	T	V	S	S	G	S	G	G
121	122	123	124	125	126	127	128	129	130	131	132	133	134	135	136	137	138	139	140
S	G	G	G	G	S	G	G	G	G	S	M	E	L	D	M	T	Q	T	P
141	142	143	144	145	146	147	148	149	150	151	152	153	154	155	156	157	158	159	160
A	S	V	S	A	A	V	G	G	T	V	T	I	S	C	Q	S	S	R	S
161	162	163	164	165	166	167	168	169	170	171	172	173	174	175	176	177	178	179	180
V	W	N	N	N	F	L	S	W	Y	Q	Q	K	P	G	Q	P	P	K	L
181	182	183	184	185	186	187	188	189	190	191	192	193	194	195	196	197	198	199	200
L	I	S	D	A	S	K	L	A	S	G	V	P	S	R	F	K	G	S	G
201	202	203	204	205	206	207	208	209	210	211	212	213	214	215	216	217	218	219	220
S	G	T	Q	F	T	L	T	I	S	D	L	E	C	D	D	A	A	T	Y
221	222	223	224	225	226	227	228	229	230	231	232	233	234	235	236	237	238	239	240
Y	C	A	G	D	L	S	D	W	I	H	T	F	G	G	G	T	E	V	V
241	242																		
V	K																		

Table S7: Amino acid sequence of the HMM5 Fab heavy chain. The first amino acid is the N-terminus. The amino acids forming the interface at the top domain are shaded blue. Based on the co-crystal data, the loop 72-75 is not involved in an interaction.

1	2	3	4	5	6	7	8	9	10	11	12	13	14	15	16	17	18	19	20
Q	S	L	E	E	S	G	G	R	L	V	T	P	G	T	P	L	T	L	T
21	22	23	24	25	26	27	28	29	30	31	32	33	34	35	36	37	38	39	40
C	T	V	S	G	F	S	L	C	T	Y	N	I	H	W	V	R	Q	A	P
41	42	43	44	45	46	47	48	49	50	51	52	53	54	55	56	57	58	59	60
G	K	G	L	E	W	I	G	V	I	D	T	G	G	G	T	Y	F	A	S
61	62	63	64	65	66	67	68	69	70	71	72	73	74	75	76	77	78	79	80
W	A	K	G	R	F	A	I	S	K	T	S	S	T	T	V	D	L	K	M
81	82	83	84	85	86	87	88	89	90	91	92	93	94	95	96	97	98	99	100
T	S	L	T	A	A	D	T	A	T	T	F	C	A	K	G	F	D	Y	S
101	102	103	104	105	106	107	108	109	110	111	112	113	114	115	116	117	118	119	120
A	S	T	N	L	W	G	P	G	T	L	V	T	I	S	S	A	S	T	K
121	122	123	124	125	126	127	128	129	130	131	132	133	134	135	136	137	138	139	140
G	P	S	V	F	P	L	A	P	S	S	K	S	T	S	G	G	T	A	A
141	142	143	144	145	146	147	148	149	150	151	152	153	154	155	156	157	158	159	160
L	G	C	L	V	K	D	Y	F	P	Q	P	V	T	V	S	W	M	S	G
161	162	163	164	165	166	167	168	169	170	171	172	173	174	175	176	177	178	179	180
A	L	T	S	G	V	H	T	F	P	A	V	L	Q	S	S	G	L	Y	S
181	182	183	184	185	186	187	188	189	190	191	192	193	194	195	196	197	198	199	200
L	S	S	V	V	T	V	P	S	S	S	L	G	T	Q	T	Y	I	C	N
201	202	203	204	205	206	207	208	209	210	211	212	213	214	215	216	217	218	219	
V	N	H	K	P	S	N	T	K	V	D	R	R	V	Q	P	K	S	C	

Table S8: Amino acid sequence of the HMM5 Fab light chain. The first amino acid is the N-terminus. The amino acids forming the interface at the top domain are shaded magenta. Based on the co-crystal data, the loop 69-72 would be unable to interact with an extended carbohydrate motif (With a distance of GlcNAc 4-OH to loop 69-72 of around 20 Å in principle still in reach but loop 69-72 is spatially shielded by loop 25-35).

1	2	3	4	5	6	7	8	9	10	11	12	13	14	15	16	17	18	19	20
E	L	D	M	T	Q	T	P	S	S	V	S	A	P	V	G	G	S	V	T
21	22	23	24	25	26	27	28	29	30	31	32	33	34	35	36	37	38	39	40
I	N	C	Q	S	S	Q	S	V	Y	G	N	N	Y	L	A	W	Y	Q	Q
41	42	43	44	45	46	47	48	49	50	51	52	53	54	55	56	57	58	59	60
K	A	G	Q	P	P	K	L	L	I	Y	R	A	S	T	L	A	S	G	A
61	62	63	64	65	66	67	68	69	70	71	72	73	74	75	76	77	78	79	80
P	S	R	F	K	G	S	G	S	G	T	Q	F	T	L	T	I	S	D	L
81	82	83	84	85	86	87	88	89	90	91	92	93	94	95	96	97	98	99	100
E	S	D	D	A	A	T	Y	Y	C	L	G	Y	Y	N	G	V	I	N	N
101	102	103	104	105	106	107	108	109	110	111	112	113	114	115	116	117	118	119	120
F	G	G	G	T	N	V	E	I	K	R	T	V	G	A	P	S	V	F	I
121	122	123	124	125	126	127	128	129	130	131	132	133	134	135	136	137	138	139	140
F	P	P	S	D	E	Q	L	K	S	G	T	A	S	V	V	C	L	L	N
141	142	143	144	145	146	147	148	149	150	151	152	153	154	155	156	157	158	159	160
N	F	Y	P	R	E	A	K	V	Q	W	K	V	D	N	A	L	Q	S	G
161	162	163	164	165	166	167	168	169	170	171	172	173	174	175	176	177	178	179	180
N	S	Q	E	S	V	T	E	Q	D	S	K	D	S	T	Y	S	L	S	S

Table S9: Amino acid sequence of horseradish peroxidase C. Disulfide bridges link the four pairs of residues 11-91, 44-49, 97-301; **carb** indicates the site of carbohydrate attachment.¹⁷⁵

1	2	3	4	5	6	7	8	9	10	11	12	13	14	15	16	17	18	19	20
E	L	T	P	T	F	Y	D	N	S	C	P	N	V	S	N	I	V	R	D
21	22	23	24	25	26	27	28	29	30	31	32	33	34	35	36	37	38	39	40
T	I	V	N	E	L	R	S	D	P	R	I	A	A	S	I	L	R	L	H
41	42	43	44	45	46	47	48	49	50	51	52	53	54	55	56	57	58	59	60
F	H	D	C	F	V	N	G	C	D	A	S	I	L	L	D	N	T	T	S
61	62	63	64	65	66	67	68	69	70	71	72	73	74	75	76	77	78	79	80
F	R	T	E	L	D	A	F	G	N	A	N	S	A	R	G	F	P	V	I
81	82	83	84	85	86	87	88	89	90	91	92	93	94	95	96	97	98	99	100
D	R	M	L	A	A	V	E	S	A	C	P	R	T	V	S	C	A	D	L
101	102	103	104	105	106	107	108	109	110	111	112	113	114	115	116	117	118	119	120
L	T	I	A	A	Q	Q	S	V	T	L	A	G	G	P	S	W	R	V	P
121	122	123	124	125	126	127	128	129	130	131	132	133	134	135	136	137	138	139	140
L	G	R	R	D	S	L	Q	A	F	L	D	L	A	N	A	N	L	P	A
141	142	143	144	145	146	147	148	149	150	151	152	153	154	155	156	157	158	159	160
P	F	F	T	L	P	Q	L	L	D	S	F	R	N	V	G	L	N	R	S
161	162	163	164	165	166	167	168	169	170	171	172	173	174	175	176	177	178	179	180
S	D	L	V	A	L	S	G	G	H	T	F	G	L	N	Q	C	R	F	I
181	182	183	184	185	186	187	188	189	190	191	192	193	194	195	196	197	198	199	200
M	D	L	R	Y	N	F	S	N	T	G	L	P	D	P	T	L	N	T	T
201	202	203	204	205	206	207	208	209	210	211	212	213	214	215	216	217	218	219	220
Y	L	Q	T	L	R	G	L	C	P	L	N	G	N	L	S	A	L	V	D
221	222	223	224	225	226	227	228	229	230	231	232	233	234	235	236	237	238	239	240
F	D	L	R	T	P	T	I	F	D	N	L	Y	Y	V	N	L	E	E	Q
241	242	243	244	245	246	247	248	249	250	251	252	253	254	255	256	257	258	259	260
L	G	L	I	Q	S	D	Q	E	L	F	S	S	P	N	A	T	D	T	I
261	262	263	264	265	266	267	268	269	270	271	272	273	274	275	276	277	278	279	280
P	L	V	R	S	F	A	N	S	T	Q	T	F	F	N	A	F	V	Q	A
281	282	283	284	285	286	287	288	289	290	291	292	293	294	295	296	297	298	299	300
M	D	R	M	G	N	I	T	P	L	T	G	T	Q	G	Q	I	R	L	N
301	302	303	304	305	306	307	308												
C	R	V	V	N	S	N	S												

10.3. Hazard and Precaution Statements

Chemical	CAS Registry Number	Signal Word	Hazard Pictograms	Hazard Statements	Precautionary Statements
Acetic anhydride	108-24-7	Danger		226, 302, 331, 314, 335	210, 260, 280, 303+361+353, 305+351+338, 312
Acetic acid	64-19-7	Danger		226, 290, 314	210, 280, 301+330+331, 305+351+338, 308+310
Acetone	67-64-1	Danger		225, 319, 336	210, 240, 305+351+338, 403+233
Acetonitrile	75-05-8	Danger		225, 332, 302, 312, 319	210, 240, 302+352, 305+351+338, 403+233
Acetyl chloride	75-36-5	Danger		225, 302, 314, EUH014	210, 280, 305+351+338, 310
Acryl amide	79-06-1	Danger		301, 312, 332, 315, 317, 319, 340, 350, 361f, 372	201, 280, 302+352, 304+340, 305+351+338, 308+310
Allyl alcohol	107-18-6	Danger		225, 301, 310, 330, 319, 335, 315, 400, 412	210, 280, 303+361+353, 305+351+338, 501
Ammonium persulfate	7727-54-0	Danger		372, 302, 315, 317, 319, 334, 335	220, 261, 280, 305+351+338, 342+311
Argon	7440-37-1	Warning		280	403
Benzaldehyde dimethyl acetale	1125-88-8	Warning		302	270, 264, 301+312
Benzyl alcohol	100-51-6	Warning		332, 302, 319	261, 301+312+330, 305+351+338, 305+351+338
Benzyl bromide	100-39-0	Warning		315, 319, 335	261, 305+351+338
Bortrifluoride diethyl etherate	109-63-7	Danger		226, 314, 332, 372	210, 280, 301+330+331, 305+351+338, 308+310
N-Bromosuccine imide	128-08-5	Danger		302, 314	280, 305+351+338, 310
n-Butanol	71-36-3	Danger		226, 302, 318, 315, 335, 336	210, 280, 302+352, 304+340, 305+351+338, 313
Campher-10-sulfonic acid	5872-08-2	Danger		314	280, 305+351+338, 310
Cesium fluoride	13400-13-0	Danger		301, 311, 314, 331	261, 280, 301+310, 305+351+338, 310
Chloroforme	67-66-3	Danger		302, 331, 315, 319, 351, 361d, 336, 372	261, 281, 305+351+338, 311
Dichloromethane	75-09-2	Warning		315, 319, 335, 336, 351, 373	261, 281, 305+351+338

Diethyl ether	60-29-7	Danger		224, 302, 336, EUH019, EUH066	210, 240, 403+235
N,N-Dimethyl formamide	68-12-2	Danger		226, 312, 332, 319, 360d	201, 210, 302+352, 304+340, 305+351+338, 308+313
Dimethyl sulfoxide	67-68-5	None	None required	No hazard statements apply	No precautionary statements apply
Ethanol	64-17-5	Danger		225, 319	210, 240, 305+351+338, 403+233
Ethanol amine	141-43-5	Danger		302, 312, 332, 314, 335, 412	251, 273, 301+312, 330, 303+361+353, 304+340+310, 305+351+338
Ethyl acetate	141-78-6	Danger		225, 319, 336, EUH066	210, 233, 240, 305+351+338, 403+235
Hydrogen	1333-74-0	Danger		220, 280	210, 377, 381, 403
Hydrochloric acid	7647-01-0	Danger		290, 314, 335	260, 280, 303+361+353, 304+340+310, 305+351+338
Iodine	7553-56-2	Warning		312+332, 315, 319, 335, 372, 400	273, 302+352, 305+351+338, 314
Methanol	67-56-1	Danger		225, 331, 311, 301, 370	210, 233, 280, 302+352, 304+340, 308+310, 403+235
β-Mercaptoethyl amine hydrochloride	156-57-0	Warning		302	301+312
Nitric acid	7697-37-2	Danger		272, 290, 331, 314, 318, EUH071	280, 301+330+331, 304+340, 305+351+338, 310
Petrol ether 40-60 °C	64742-49-0	Danger		225, 304, 315, 336, 361f, 373, 411	201, 210, 223, 240, 273, 280, 281, 301+310, 302+352, 304+340, 308+313, 331, 403+233, 501
Pyridine	110-86-1	Danger		225, 332, 302, 312, 319, 315	210, 280, 305+351+338
Palladium on carbon (50 % H₂O)	7440-05-3	Warning		228	210, 370+378
Silica Gel 60	7631-86-9	None	None required	No hazard statements apply	260
Silver nitrate	7761-88-8	Danger		272, 290, 314, 410	210, 220, 260, 280, 305+351+338, 370+378, 308+310
Sodium cyanoborohydride	25895-60-7	Danger		260-300-310-330-314-410, EU032	273-280-301+330+331-302+352-304+340-305+351+338-402+404
Sodium hydride	7646-69-7	Danger		228, 260, 314	210, 223, 231+232, 280, 370+378, 422
Sodium hydrogencarbonate	144-55-8	None	None required	No hazard statements apply	No precautionary statements apply

Sodium hydroxide	1310-73-2	Danger		290, 314	280, 301+330+331, 305+351+338, 308+310
Sodium methanolate	124-41-4	Danger		228, 251, 290, 302, 314, EUH014	210, 280, 310, 370+378, 305+351+338, 402+404, 406
Sodium sulfate	7757-86-6	None	None required	No hazard statements apply	No precautionary statements apply
<i>N,N,N',N'</i>- Tetramethylethylene- 1,2-diamine	110-18-9	Danger		225, 332, 302, 314	210, 280, 305+351+338, 310
Thiophenole	108-98-5	Danger		226, 300+310+330, 315, 318, 335, 361, 371, 373, 410	210, 260, 280, 301+310+330, 302+352, 304+340, 305+351+338, 310, 403+233
Toluene	108-88-3	Danger		225, 361d, 304, 373, 315, 336	210, 240, 301+310+330, 302+352, 308+313, 314, 403+233

10.4. Curriculum Vitae

Tim Raiber

Date of birth: February 22, 1980

Place of birth: Hamburg (Germany)



01/2011-05/2015 **Doctoral Thesis**

A Binding Model for Anti-Carbohydrate Antibodies

in the group of Prof. Dr. E. Spillner (University of Hamburg)

10/2010-09/2012 **Postgraduate Studies in Molecular Biology**

at the Center for Molecular Neurobiology Hamburg (ZMNH)

11/2009-04/2010 **Diploma Thesis**

Synthese von Fucosylchitobiosen als Modelle für kreuzreaktive Kohlenhydrat-Determinanten

in the group of Prof. Dr. J. Thiem (University of Hamburg)

04/2001-10/2009 **Studies in Chemistry** (University of Hamburg)

11-12/2006 **Advanced Practical Course in Biochemistry for Biochemists and Biologists**

a) RNA Interference (PD Dr. N. Piganeau)

b) Antibody Phage Display (PD Dr. E. Spillner)

06/2000 **A-Levels with Latin Proficiency at the Grammar School of Glinde**

11. References

- 1 Henle, J. (1840). *Von den Miasmen und Contagien und von den miasmatisch contagiösen Krankheiten*. In *Pathologische Untersuchungen* (p. 1-82). Berlin: Verlag von August Hirschwald.
- 2 Koch, R., *Die Ätiologie der Tuberkulose*. Berliner klinische Wochenschrift, 1884. **15**: p. 428-445.
- 3 Loeffler, F., *Untersuchung über die Bedeutung der Mikroorganismen für die Entstehung der Diphtherie beim Menschen, bei der Taube und beim Kalbe*. Mittheilungen aus dem kaiserlichen Gesundheitsamte, 1884. **2**: p. 421-499.
- 4 Yu, C., Gao, K., Zhu, L., Wang, L., Zhang, F., Liu, C., Li, M., Wormald, M. R., Rudd, P. M., Whang, J., *At least two Fc Neu5Gc residues of monoclonal antibodies are required for binding to anti-Neu5Gc antibody*. Sci. Rep., 2017. **6**(20029): p. 1-10.
- 5 Merrick, J. M., Zadarlik, K., Milgrom, F., *Characterization of the Hanganutziu-Deicher (Serum Sickness) Antigen as Gangliosides Containing N-Glycolylneuraminic Acid*. Int. Archs Allergy Appl. Immun., 1978. **57**: p. 477-480.
- 6 Locher, W. G., *Max von Pettenkofer (1818-1901) as a Pioneer of Modern Hygiene and Preventive Medicine*. Environ. Health Prev. Med., 2007. **12**: p. 238-245.
- 7 von Behring, E., Kitasato, S., *Über das Zustandekommen der Diphtherie-Immunität und der Tetanus-Immunität bei Thieren*. Deutsche medizinische Wochenschrift, 1890. **49**: p. 651-653.
- 8 Finger, J. W., Isberg, S. R., *A review of innate immune functions in crocodylians*. CAB Reviews, 2012. **7**(67): p. 1-11.
- 9 Weaver, G. H., *Serum Disease*. Arch. Intern. Med., 1909. **III**(5): p. 485-513.
- 10 Jackson, M. (2007). *Allergy: The History of Modern Malady*. London: Reaktion Books.
- 11 von Pirquet C., Schick, B. (1905). *Die Serumkrankheit*. Leipzig: Deuticke.
- 12 Daffern, P. J., Pfeifer, P. H., Ember, J. A., Hugli, T. E., *C3a Is a Chemotaxin for Human Eosinophils but Not for Neutrophils. I. C3a Stimulation of Neutrophils Is Secondary to Eosinophil Activation*. J. Exp. Med., 1995. **181**: p. 2119-2127.
- 13 von Pirquet, C. (1911). *Allergy*. In *The Archives of Internal Medicine* (p. 383-436). Chicago: American Medical Association Publishers.
- 14 von Pirquet, C. (1910). *Ergebnisse der Inneren Medizin und Kinderheilkunde: Allergie*. Berlin: Springer-Verlag.
- 15 Gell, P. G. H., Coombs, R. R. A. (1963). *The Classification of allergic reactions underlying disease*. In *Clinical Aspects of Immunology*. Oxford: Blackwell Science.
- 16 Descotes, J., Choquet-Kastylevsky, G., *Gell and Coomb's classification: is it still valid?* Toxicology, 2001. **158**: p. 43-49.
- 17 Akdis, C. A., Akdis, M., *Mechanisms of allergen-specific immunotherapy and immune tolerance to allergens*. World Allergy Organ. J., 2015. **8**(17): p. 1-12.
- 18 Emanuel, M. B., *Hay fever, a post industrial revolution epidemic: a history of its growth during the 19th century*. Clin. Allergy, 1988. **18**: p. 295-304.
- 19 Strachan, D. P., *Hay fever, hygiene, and household size*. Br. Med. J., 1989. **299**: p. 1259-1260.
- 20 Cooper, P. J., *Interactions between helminth parasites and allergy*. Curr. Opin. Allergy Clin. Immunol., 2009. **9**(1): p. 29-37.
- 21 Egner, W, Ward, C., Brown, D. L., Ewan, P. W., *The incidence and clinical significance of specific IgE to both wasp (vespula) and bee (apis) venom in the same patient*. Clin Exp Allergy, 1998. **28**:26-34.
- 22 Garratty, G., *Immune hemolytic anemia associated with drug therapy*. Blood Rev.,

-
2010. **24**: p. 143-150.
- 23 Jackson, R., *Serum sickness*. J. Cutan. Med. Surg., 2000. **4**(4): p. 223-225.
- 24 Gamarra, R. M., McGraw, S. D., Drelichman, V. S., Maas, L. C., *Serum Sickness-Like Reactions in Patients Receiving Intravenous Infliximab*. J. Emerg. Med., 2006. **30**(1): p. 41-44.
- 25 Facktor, M. A., Bernstein, R. A., Fireman, P., *Hypersensitivity to tetanus toxoid*. J. Allergy Clin. Immunol., 1973. **52**(1): p. 1-12.
- 26 Tonutti, E. Bizzaro, N., *Diagnosis and classification of celiac disease and gluten sensitivity*. Autoimmun. Rev., 2014. **13**(4-5): p. 472-476.
- 27 Portier, P., Richet, C., *De l'action anaphylactique de certains venins*. CR Seances Soc. Biol., 1902. **54**: p. 170.
- 28 Richet, C. (1913). *Anaphylaxies*. Liverpool: University Press.
- 29 Schäfer, T., *Epidemiologie der Insektengiftallergie*. Allergo J., 2009. **18**(5): p. 353-358.
- 30 Hemmer, W., *Kreuzreaktionen zwischen den Giften von Hymenopteren unterschiedlicher Familien, Gattungen und Arten*. Der Hautarzt, 2014. **9**: p. 775-779.
- 31 Mertens, M., Amler, S., Moerschbacher, B. M., Brehler, R., *Cross-reactive carbohydrate determinants strongly affect the results of the basophil activation test in hymenoptera-venom allergy*. Clin. Exp. Allergy, 2010. **40**: p. 1333-1345.
- 32 de Lima, P. R., Brochetto-Braga, M. R., *Hymenoptera venom review focussing on Apis mellifera*. J. Venom. Anim. Toxins incl. Trop. Dis. **9**(2).
- 33 R., J.-H., Chang, H.-C., Chen, J.-M., Cheng, A.-C., Khoo, K. H., *Glycan structures and intragenic variations of venom acidic phospholipases A₂ from Tropidolaemus pitvipers*. FEBS Journal, 2012. **279**: p. 2672-2682.
- 29 Aalberse, R. C., Koshte, V., Clemens, J. G. J., *Immunoglobuline E antibodies that crossreact with vegetable foods, pollen, and Hymenoptera venom*. J. Allergy Clin. Immunol., 1981. **68**(5): p. 356-364.
- 35 Allen, A. K., Desai, N. N., Neuberger, A., Creeth, J. M., *Properties of Potato Lectin and the Nature of its Glycoprotein Linkages*. Biochem. J., 1978. **171**(3): p. 665-674.
- 36 Weber, A., März, L., Altmann, F., *Characteristics of the asparagine-linked oligosaccharide from honey bee venom phospholipase A₂. Evidence for the presence of terminal N-acetyl-glucosamine and fucose in an insect glycoprotein*. Comp. Biochem. Physiol., 1986. **[83B]**: p. 321-324.
- 37 Weber, A., Schröder, H., Thalberg, K., März, L., *Specific interaction of IgE antibodies with a carbohydrate epitope of honey bee venom phospholipase A₂*. Allergy, 1987. **42**: p. 464-470.
- 38 Fujihashi, M., Peapus, D. H., Kamiya, N., Nagata, Y., Miki, K., *Crystal Structure of Fucose-Specific Lectin from Aleuria aurantia Binding Ligands at Three of Its Five Sugar Recognition Sites*. Biochemistry, 2003. **42**(38): 11093-11099.
- 39 Ishihara, H., Takahashi, N., Oguri, S., Tejima, S., *Complete structure of the carbohydrate moiety of stem bromelain*. J. Biol. Chem., 1979. **254**(21): p. 10715-10719.
- 40 Yang, B. Y., Gray, J. S. S., Montgomery, R. *The glycans of horseradish peroxidase*. Carbohydr. Res., 1996. **287**: p. 203-212.
- 41 Staudacher, E., Stepan, H., Gutternigg, M., *Protein N-glycosylation of gastropods*. Curr. Top. Biochem. Res., 2009. **11**(2): p. 29-39.
- 42 Kubelka, V., Altmann, F., Staudacher, E., Tretter, V., März, L., Hard, K., Kamerling, J. P., Vliegenthart, J. F., *Primary structures of the N-linked carbohydrate chains from honeybee venom phospholipase A₂*. Eur. J. Biochem., 1993. **213**(3): p. 1193-1204.

-
- 43 Meevissen, M. H. J., Driessen, N. N., Smits, H. H., Versteegh, R., van Vliet, S. J., van Kooyk, Y., Schramm, G., Deelder, A. M., Haas, H., Yazdanbakhsh, M., Hokke, C. H., *Specific glycan elements determine differential binding of individual egg glycoproteins of the human parasite Schistosoma mansoni by host C-type lectin receptors*. *Int. J. Parasitol.*, 2012. **42**: 269-277.
- 44 van Die, I., Cummings, R. D., *Glycan gimmickry by parasitic helminths: A strategy for modulating the host immune response?* *Glycobiology*, 2010. **20**(1): p. 2-12.
- 45 Maizels, R. M., Hewitson, J. P. (2012). *Immune Recognition of Parasite Glycans*. In Kosma, P., Müller-Loennies, S. (eds.), *Anticarbhydrate Antibodies* (p. 161-180). Wien: Springer-Verlag.
- 46 Maizels, R. M., Yazdanbakhsh, M., *Immune Regulation by Helminth Parasites: Cellular and Molecular Mechanisms*. *Nature Rev.*, 2003. **3**: p. 733-744.
- 47 Becker, D. J., Lowe, J. B., *Leukocyte adhesion deficiency type II*. *Biochim. Biophys. Acta*, 1999. **1455**(2-3): p. 193-204.
- 48 Varki, A. *et al.* (2009). *Essentials of Glycobiology*. Cold Spring Harbor: Laboratory Press.
- 49 Higashi, H., Naiki, M., Matuo, S., Okouchi, K., *Antigen of „Serum Sickness“ Type of Heterophile Antibodies in Human Sera: Identification as Gangliosides with N-glycolylneuraminic Acid*. *Biochem. Biophys. Res. Com.*, 1977. **79**(2): p. 388-395.
- 50 van Valen, L., *A new evolutionary law*. *Evol. Theory*, 1973. **1**: p. 1-30.
- 51 Carroll, L., Tenniel, J. (1871). *Through the Looking-Glass, and What Alice Found There*. London: Macmillan.
- 52 Landsteiner, K., van der Scheer, J., *On the antigens of red blood corpuscles II. Flocculation reactions with alcoholic extracts of erythrocytes*. *J. Exp. Med.*, 1925. **42**: 841-852.
- 53 Duffy, M. S., Morris, H. R., Dell, A., Appleton, J. A., Haslam, S. M., *Protein glycosylation in Parelaphostrongylus tenuis – first description of the Gal α 1-3Gal sequence in a nematode*. *Glycobiology*, 2006. **16**(9): p. 854-862.
- 54 Commins, S. P., James, H. R., Kelly, L. A., Pochan, S. L., Workman, L. J., Perzanowski, M. S.; Kocan, K. M., Fahy, J. V.; Nganga, L. W., Ronmark, E., Cooper, P. J., Platts-Mills, T. A. E., *The relevance of tick bites to the production of IgE antibodies to the mammalian oligosaccharide galactose- α -1,3-galactose*. *J. Allergy Clin. Immunol.*, 2011. **127**(5): p. 1286-1293.
- 55 Sell-Dottin, K. A., Sola, M., Caranasos, T. G., *Impact of Newly Emerging Alpha-Gal Allergies on Cardiac Surgery: A Case Series*. *Clin. Surg.*, 2017. **2**(1477): p. 1-3.
- 56 Montreuil, J., *Primary Structure of Glycoprotein Glycans Basis for the Molecular Biology of Glycoproteins*. *Adv. Carbohydr. Chem. Biochem.*, 1980. **37**: p. 157-223.
- 57 Hoorelbeke, B., Van Damme, E. J. M., Rougé, P., Schols, D., Van Laethem, K., Fouquaert, E., Balzarini, J., *Differences in the mannose oligomer specificities of the closely related lectins from Galanthus nivalis and Zea mays strongly determine their eventual anti-HIV activity*. *Retrovirology*, 2011. **8**(10): p. 1-16.
- 58 Kochibe, N., Furukawa, K., *Purification and properties of a novel fucose-specific hemagglutinin of Aleuria aurantia*. *Biochemistry*, 1980. **19**(13): p. 2841-2846.
- 59 Hoorelbeke, B., Huskens, D., Férir, G., Balzarini, J., *Actinohivin, a Broadly Neutralizing Prokaryotic Lectin, Inhibits HIV-1 Infection by Specifically Targeting High-Mannose-Type Glycans on the gp120 Envelope*. *AAC*, 2010. **54**(8): p. 3287-3301.
- 60 Chaiet, L., Wolf, F. J., *The Properties of Streptavidin, a Biotin-Binding Protein Produced by Streptomyces*. *Arch. Biochem. Biophys.*, 1964. **106**: p. 1-5.

-
- 61 Tretter, V., Altmann, F., Kubelka, V., März, L., Becker, W. M., *Fucose α 1,3-Linked to the Core Region of Glycoprotein N-Glycans Creates an Important Epitope for IgE from Honeybee Venom Allergic Individuals*. *Int. Arch. Allergy Immunol.*, 1993. **102**: p. 259-266.
- 62 Collot, M., Wilson, I. B. H., Bublin, M., Hoffmann-Sommergruber, K., Mallet, J.-M., *Synthesis of cross-reactive carbohydrate determinants fragments as tools for in vitro allergy diagnosis*. *Bioorg. Med. Chem.*, 2011. **19**: p. 1306-1320.
- 63 Porter, R. R., *Separation and isolation of fractions of rabbit gamma-globulin containing the antibody and antigenic combining sites*. *Nature*, 1958. **182**(4636): p. 670-671.
- 64 Porter, R. R. (1962). *The Structure of Gamma-Globulin and Antibodies*. In *Symposium on Basic Problems in Neoplastic Disease* (p. 177-181). New York: Columbia University Press.
- 65 Hilschmann, N., Craig, L. C., *Amino Acid Sequence Studies with Bence-Jones Proteins*. *PNAS*, 1965. **53**(6): p. 1403-1409.
- 66 ^a Edelman, G. M., Gall, W. E., *The antibody problem*. *Annu. Rev. Biochem.*, 1969. **38**: p. 415-466.
- ^b Edelman, G. M., Cunningham, B. A., Gall, W. E., Gottlieb, P. D., Rutishauser, U., Waxdal, M. J., *The covalent structure of an entire γ -immunoglobulin molecule*. *Proc. Natl. Acad. Sci. U.S.A.* **63**: p. 78-85.
- 67 Stanfield, R. L., Dooley, H., Flajnik, M. F., Wilson, I., *Crystal structure of a shark single-domain antibody V region in complex with lysozyme*. *Science*, 2004. **305**(5691): p. 1770-1773.
- 68 Burnet, F. M. (1959). *The clonal selection theory of acquired immunity*. Nashville: Vanderbilt University Press.
- 69 Smith, G. P., *Filamentous Fusion Phage: Novel Expression Vectors That Display Cloned Antigens on the Virion Surface*. *Science*, 1985. **228**: p. 1315-1317.
- 70 Altmann, F., *The role of protein glycosylation in allergy*. *Int. Arch. Allergy Immunol.*, 2007. **142**(2): p. 99-115.
- 71 ^a Weber, H., Khorana, H. G., *Total Synthesis of the Structural Gene for an Alanine Transfer Ribonucleic Acid from Yeast. Chemical Synthesis of an Icosadeoxynucleotide Corresponding to the Nucleotide Sequence 21 to 40*. *J. Mol. Biol.*, 1972. **72**: p. 219-249
- ^b Zhdanov, R. I., Zhenodarova, S. M., *Chemical Methods of Oligonucleotide Synthesis*. *Synthesis*, 1972. **4**: p. 222-245.
- 37 Deng, S., Gangadharmath, U., Chang, C. W., *Sonochemistry: A powerful way of enhancing the efficiency of carbohydrate synthesis*. *J. Org. Chem.*, 2006. **71**(14): p. 5179-5185.
- 73 ^a Zemplén, G., Kunz, A., *Über die Natriumverbindungen der Glucose und die Verseifung der acylierten Zucker*. *Eur. J. Inorg. Chem. (Ber. Dtsch. Chem. Ges., A and B series)*, 1923. **56**(7): p. 1705-1710.
- ^b Zemplén, G., Gerecs, A., Hadácsy, I., *Über die Verseifung acetylierter Kohlenhydrate*. *Eur. J. Inorg. Chem. (Ber. Dtsch. Chem. Ges., A and B series)*, 1936. **69**(8): p. 1827-1829.
- 74 Girard, C., Miramon, M. L., de Solminihac, T., Herscovici, J., *Synthesis of 3-C-(6-O-acetyl-2,3,4-tri-O-benzyl- α -D-mannopyranosyl)-1-propene: a caveat*. *Carbohydr. Res.*, 2002. **337**: p. 1769-1774.
- 75 Nicolaou, K. C., Caulfield, T. J., Kataoka, H., Stylianides, N. A., *Total Synthesis of the Tumor-Associated Le^x Family of Glycosphingolipids*. *J. Am. Chem. Soc.*, 1990. **112**(9): p. 3693-3695.

-
- 76 Allen, A. K., Davies, R. C., Neuberger, A., Morgan, D. M. L., *The separation of methyl ethers of 2-acetamido-2-deoxy-D-glucopyranosides on a strongly basic ion-exchange resin*. Carbohydr. Res., 1976. **51**(2): p. 149-155.
- 77 Demchenko, A. V., Pornsuriyasak, P., De Meo, C., *Acetal Protecting Groups in the Organic Laboratory: Synthesis of Methyl 4,6-O-Benzylidene- α -D-Glucopyranoside*. J. Chem. Educ., 2006. **83**(5): p. 782-784.
- 78 Böhm, G., Waldmann, H., *O-Glycoside Synthesis under Neutral Conditions in Concentrated Solutions of LiClO₄ in Organic Solvents Employing Benzyl-Protected Glycosyl Donors*. Liebigs. Ann., 1996. p. 613.
- 79 Heathcock, C. H., Ratcliffe, R., *A Stereoselective Total Synthesis of the Guaiazulenic Sesquiterpenoids α -Bulnesene and Bulnesol*. J. Am. Chem. Soc., 1971. **93**(7): p. 1746-1757.
- 80 Mukaiyama, T., Murai, Y., Shoda, S. Chemistry Letters, 1981. **10**: p. 431-432.
- 81 Mukaiyama, T., Hashimoto, Y., Shoda, S. Chemistry Letters, 1983. **12**: p. 935-938.
- 82 Waldmann, H., Böhm, G., Schmidt, H., Rottele, H., *O-Glycoside Syntheses under Neutral Conditions in Concentrated Solutions of LiClO₄ in Organic Solvents*. Angew. Chem. Int. Ed. Engl., 1994. **33**(19): p. 1944.
- 83 Böhm, G., Waldmann, H., *O-Glycoside Synthesis under Neutral Conditions in Concentrated Solutions of LiClO₄ in Organic Solvents Employing Benzyl-Protected Glycosyl Donors*. Liebigs. Ann., 1996. p. 613.
- 84 Edward, J. T., *Stability of glycosides to acid hydrolysis*. Chem. Ind. (London), 1955. p. 1102-1104.
- 85 Lemieux, R. U., *Effects of Unshared Pairs of Electrons and Their Solvation on Conformational Equilibria*. Pure Appl. Chem., 1971. **25**: p. 527-548.
- 86 Grieco, P. A., Cooke, R. J., Henry, K. J., Van der Roest, J. M., *Lithium Perchlorate Catalyzed Conjugate Addition of O-Silylated Ketene Acetals to Hindered α,β -Unsaturated Carbonyl Compounds at Atmosphere Pressure*. Tetrahedron Lett., 1991. **32**: p. 4665-4668.
- 87 Grieco, P. A., Nunes, J. J., Gaul, M. D., *Dramatic Rate Acceleration of Diels-Alder Reactions in 5 M Lithium Perchlorate-Diethyl Ether: The Cantharidin Problem Reexamined*. J. Am. Chem. Soc., 1990. **112**: p. 4595-4596.
- 88 Markowitz, M. M., *Lithium Salts as Solutes in Nonaqueous Media: Solubility Trends of Lithium Perchlorate*. J. Chem. Eng. Data, 1961. **6**(3): p. 325-327.
- 89 ^a Pocker, Y., Buchholz, R. F., *Electrostatic Catalysis by Ionic Aggregates. I. The Ionization and Dissociation of Trityl Chloride and Hydrogen Chloride in Lithium Perchlorate-Diethyl Ether Solutions*. J. Am. Chem. Soc., 1970. **92**(7): p. 2075-2084.
^b Pocker, Y., Buchholz, R. F., *Electrostatic Catalysis by Ionic Aggregates. II. The Reversible Elimination of HCl from *t*-Butyl Chloride and the Rearrangement of 1-Phenylallyl Chloride in Lithium Perchlorate-Diethyl Ether Solutions*. J. Am. Chem. Soc., 1970. **92**(13): p. 4033-4038.
^c Pocker, Y., Buchholz, R. F., *Electrostatic Catalysis by Ionic Aggregates. III. The Isomerization of (-)-Menthone by Hydrogen Chloride and Perchloric Acid in Lithium Perchlorate-Diethyl Ether Solutions*. J. Am. Chem. Soc., 1971. **93**(12): p. 2905-2909.
^d Pocker, Y., Buchholz, R. F., *Electrostatic Catalysis by Ionic Aggregates. IV. Rearrangement of 1-Phenyl Chloride in Lithium Perchlorate Solutions in Aprotic Solvents*. J. Am. Chem. Soc., 1977. **99**(7): p. 2276-2284.
^e Pocker, Y., Ellsworth, D. L., *Electrostatic Catalysis by Ionic Aggregates. V. Aminolysis Reaction of *p*-Nitrophenyl Acetate with Imidazole and the Proton Transfer from *p*-*

-
- Nitrophenol in Lithium Perchlorate-Diethyl Ether Solutions*. J. Am. Chem. Soc., 1977. **99**(7): p. 2284-2293.
- ^f Pocker, Y., Ciula, J. C., *Electrostatic Catalysis by Ionic Aggregates. VI. Modulation of Proton Transfer Equilibria by Lithium Perchlorate-Diethyl Ether Clusters*. J. Am. Chem. Soc., 1988. **110**: p. 2904-2909.
- ^g Pocker, Y., Ciula, J. C., *Electrostatic Catalysis by Ionic Aggregates. VII. Interactions of Dipolar Indicator Molecules with Ionic Clusters*. J. Am. Chem. Soc., 1989. **111**: p. 4728-4735.
- 90 Demchenko, A. V. (2008). *Handbook of Chemical Glycosylation: Advances in Stereoselectivity and Therapeutic Relevance*. Weinheim: Wiley-VCH.
- 91 Köbrich, G., *The Chemistry of Carbenoids and Other Thermolabile Organolithium Compounds*. Angew. Chem. Int. Ed., 1972. **11**(6): p. 473-485.
- 92 Wickleder, M. S., *Crystal Structure of LiClO₄*. Z. Anorg. Allg. Chem., 2003. **629**: p. 1466-1468.
- 93 Auzanneau, F.-J., Pinto, B. M., *Preparation of Antigens and Immunoabsorbents Corresponding to the Streptococcus Group A Cell-wall Polysaccharide*. Bioorgan. Med. Chem., 1996. **4**(11): p. 2003-2010.
- 94 Liptak, A., *Hydrogenolysis of the dioxolan type exo- and endo-benzylidene derivatives carbohydrates with LiAlH₄-AlCl₃ reagent*. Tetrahedron Lett., 1976. **39**: p. 3551-3554.
- 95 Kartha, K. P. R., Aloui, M., Field, R. A., *Iodine: A Versatile Reagent in Carbohydrate Chemistry II. Efficient Chemospecific Activation of Thiomethylglycosides*. Tetrahedron Lett., 1996. **37**: p. 5175-5178.
- 96 Michel, Y. (2012). *Structural and functional analyses of IgE epitopes and their biological relevance* (Doctoral Thesis). Hamburg: University of Hamburg.
- 97 Deckers, S., Braren, I., Greunke, K., Meyer, N., Rühl, D., Bredehorst, R., *Establishment of hapten-specific monoclonal avian IgY by conversion of antibody fragments obtained from combinatorial libraries*. Biotechnol. Appl. Biochem., 2009. **52**: p. 79-87.
- 98 Filhol, A., Clement, C., Forel, M.-T., Paviot, J., Rey-Lafon, M., *Molecular Conformation of 1,3,5-Trinitrohexahydro-s-triazine (RDX) in Solution*. J. Phys. Chem., 1971. **75**(13): p. 2056-2060.
- 99 Charles, P. T., Kusterbeck, A. W., *Trace level detection of hexahydro-1,3,5-trinitro-1,3,5-triazine (RDX) by microimmunosensor*. Biosens. Bioelectron., 1999. **14**: p. 387-396.
- 100 Bart, J. C., Judd, L. L., Hoffman, K. E., Wilkins, A. M., Kusterbeck, A. W., *Application of a Portable Immunosensor to Detect the Explosives TNT and RDX in Groundwater Samples*. Environ. Sci. Technol., 1997. **31**(5): p. 1505-1511.
- 101 Binks, P. R., Nicklin, S., Bruce, N. C., *Degradation of Hexahydro-1,3,5-Trinitro-1,3,5-Triazine (RDX) by Stenotrophomonas maltophilia PBI*. Appl. Environ. Microbiol., 1995. **61**(4): p. 1318-1322.
- 102 Notovtny, J., Handschumacher, M., Haber, E., Carlson, W. B., Fanning, D. W., Smith, J. A., Rose, G. D., *Antigenic determinants in protein coincide with surface regions accessible to large probes (antibody domains)*. Proc. Natl. Acad. Sci. USA, 1986. **83**: p. 226-230.
- 103 Ito, W., Nishimura, M., Sakato, N., Fujio, H., Arata, Y., *A ¹H NMR Method for the Analysis of Antigen-Antibody Interactions: Binding of a Peptide Fragment of Lysozyme to Anti-Lysozyme Monoclonal Antibody*. J. Biochem., 1987. **102**(3): p. 643-649.
- 104 Meyer, B., Peters, T., *NMR Spectroscopy Techniques for Screening and Identifying Ligand Binding to Protein Receptors*. Angew. Chem. Int. Ed., 2003. **42**(8): p. 864-890.

-
- 105 Akasaka, K., *Intermolecular Spin Diffusion as a Method for Studying Macromolecule-Ligand Interactions*. J. Magn. Res., 1979. **36**: p. 135-140.
- 106 Endo, S., Arata, Y., *Proton Nuclear Magnetic Resonance Study of Human Immunoglobulins G1 and Their Proteolytic Fragments: Structure of the Hinge Region and Effects of a Hinge-Region Detection on Internal Flexibility*. Biochemistry, 1985. **24**: p. 1561-1568.
- 107 Peters, T., Meyer, B., *Identification by spectroscopy of ligands in ligand libraries using receptors*. German patent: DE 19649359 (C1), 1998.
- 108 Mayer, M., Meyer, B., *Characterization of Ligand Binding by Saturation Transfer Difference NMR Spectroscopy*. Angew. Chem. Int. Ed., 1999. **38**(12): p. 1784-1788.
- 109 Möller, H., Serttas, N., Paulsen, H., Burchell, J. M., Taylor-Papadimitriou, J., *NMR-based determination of the binding epitope and conformational analysis of MUC-1 glycopeptides and peptides bound to the breast cancer-selective monoclonal antibody SM3*. Eur. J. Biochem., 2002. **269**: p. 1444-1455.
- 110 Viegas, A., Manso, J., Corvo, M. C., Marques, M. M. B., Cabrita, E. J., *Binding of Ibuprofen, Ketorolac, and Diclofenac to COX-1 and COX-2 Studied by Saturation Transfer Difference NMR*. J. Med. Chem., 2011. **54**: p. 8555-8562.
- 111 Guzzi, C., Muñoz-García, J. C., Enriquez-Navas, P. M., Rojo, J., Angulo, J., Nieto, P. M., *NMR studies on carbohydrate interactions with DC-SIGN towards a quantitative STD analysis*. Pure Appl. Chem., 2013. **85**(9): p. 1771-1787.
- 112 Eckenberger, J. (2012). *Etablierung leporider Antikörperbibliotheken und Carbohydrat-spezifischer Immunglobuline* (Master's Thesis). Hamburg: University of Hamburg.
- 113 Angulo, J., Enríquez-Navas, P. M., Nieto, P. M., *Ligand-Receptor Binding Affinities from Saturation Transfer Difference (STD) NMR Spectroscopy: The Binding Isotherm of STD Initial Growth Rates*. Chem. Eur. J., 2010. **16**: p. 7803-7812.
- 114 Currie, L. A., *Limits for qualitative detection and quantitative determination*. Anal. Chem., 1968. **40**: p. 586-593.
- 115 Currie, L. A., *Detection and quantification limits: origins and historical overview*. Analytica Chimica Acta, 1999. **391**: p. 127-134.
- 116 Carlson, J., Wysoczanski, A., Voigtmann, E., *Limits of quantitation – Yet another suggestion*. Spectrochimica Acta 2014. **Part B**: p. 69-73.
- 117 Belter, M., Sajnóg, A., Baralkiewicz, D., *Over a century of detection and quantification capabilities in analytical chemistry – Historical overview and trends*. Talanta, 2014. **129**: p. 606-616.
- 118 Armbruster, D. A., Pry, T., *Limit of Blank, Limit of Detection and Limit of Quantitation*. Clin. Biochem. Rev., 2008. **29**: p. S50-52.
- 119 Meyer, N. H., Zangger, K., *Simplifying Proton NMR Spectra by Instant Homonuclear Broadband Decoupling*. Angew. Chem. Int. Ed., 2013. **57**: p. 7143-7146.
- 120 Aguilar, J. A., Faulkner, S., Nilsson, M., Morris, G. A., *Pure Shift ¹H NMR: A Resolution of the Resolution Problem?* Angew. Chem. 2010. **122**: p. 3993–3995.
- 121 Pernet, C., *Null hypothesis significance testing: a short tutorial*. F1000Research, 2015. **4**: 621-645.
- 122 Xia, Y., Zhu, Q., Jun, K.-Y., Wang, J., Gao, X., *Clean STD-NMR spectrum for improved detection of ligand-protein interactions at low concentration of protein*. Magn. Reson. Chem., 2010. **48**: p. 918-924.
- 123 Bauer, C., Freeman, R., Frenkiel, T., Keeler, J., Shaka, A. J., *Gaussian Pulses*. J. Magn. Res., 1984. **58**: p. 442-457.
- 124 Ley, N. B., Rowe, M. L., Williamson, R. A., Howard, M. J., *Optimising selective*

-
- excitation pulses to maximise saturation transfer difference NMR spectroscopy. RSC Adv., 2014. **4**(14): p. 7347-7351.
- 125 Bloch, F., Siegert, A., *Magnetic resonance for nonrotating fields*. Phys. Rev., 1940. **57**: p. 522-527.
- 126 Abragam, A. (1961). *The Principles of Nuclear Magnetism*. London: Oxford University Press.
- 127 Mersh, J. D., Sanders, J. K. M., *The Suppression of Bloch-Siegert Shifts and Subtraction Artifacts in Double-Resonance Difference Spectroscopy*. J. Magn. Reson., 1982. **50**: p. 289.
- 128 T. Turbadar, *Complete Absorption of Light by Thin Metal Films*. Proc. Phys. Soc., 1959. **73**: p. 40-44.
- 129 A. Otto, *Excitation of Nonradiative Surface Plasma Waves in Silver by the Method of Frustrated Total Reflection*. Z. Phys., 1968. **216**: p. 398-410.
- 130 E. Kretschmann, H Raether, *Radiative Decay of Non Radiative Surface Plasmons Excited by Light*. Z. Naturforsch., A: Phys. Sci., 1968. **23**: p. 2135-2136.
- 131 U. Jönsson, L. Fägestam, B. Ivarsson, B. Johnsson, R. Karlsson, K. Lundh, S. Löfas, B. Persson, H. Roos, I. Rönnerberg, S. Sjölander, E. Stenberg, R. Stahlberg, S. Urbaniczky, H. Östlin, M. Malmqvist, Real-time biospecific interaction analysis using surface plasmon resonance and a sensor chip technology. *Biotechniques*, 1991. **11**: p. 620-627.
- 132 Kendrew, J. C., Dickerson, R. E., Strandberg, B. E., *Structure of myoglobin; A three-dimensional Fourier synthesis at 2 Å resolution*. Nature, 1960. **185**: p. 422-427.
- 133 Tjerrild, L. M. (2015). *Structural studies of Fab-antigen complexes* (Master's Thesis). Aarhus: University of Aarhus.
- 134 Fernández-Alonso, M., Canada, F. J., Jiménez-Barbero, J., Cuevas, G., *Molecular Recognition of Saccharides by Proteins. Insight on the Origin of the Carbohydrate-Aromatic Interactions*. J. Am. Chem. Soc., 2005. **127**(20): p. 7379-7386.
- 135 Rappé, A. K., Casewit, C. J., Colwell, K. S., Goddard, W. A., Skiff, W. M., *UFF, a full periodic table force field for molecular mechanics and molecular dynamics simulations*. J. Am. Chem. Soc., 1992. **114**(25): p. 10024-10035.
- 136 Lifson, S., Warshel, A., *Consistent force field for calculations of conformations, vibrational spectra, and enthalpies of cycloalkane and n-alkane molecules*. J. Chem. Phys., 1968. **49**(22): p. 5116-51129.
- 137 Allinger, N. L., *Conformational analysis. 130. MM2. A hydrocarbon interatomic potential utilizing V1 and V2 torsional terms*. J. Am. Chem. Soc., 1977. **99**(25): p. 8127-8134.
- 138 Allinger, N. L., Yuh, Y. H., Lii, J.-H., *Molecular Mechanics. The MM3 Force Field for Hydrocarbons. I*. J. Am. Chem. Soc., 1989. **111**(23): p. 8551-8565.
- 139 Cornell, W. D., Cieplak, P., Bayly, C. I., Gould, I. R., Merz, K. M., Ferguson, D. M., Spellmeyer, D. C., Fox, T., Caldwell, J. W., Kollman, P. A., *A Second Generation Force Field for the Simulation of Proteins, Nucleic Acids, and Organic Molecules*. J. Am. Chem. Soc., 1995. **117**(19): p. 5179-5197.
- 140 Jorgensen, W. L., *The OPLS potential functions for proteins, energy minimizations for crystals of cyclic peptides and crambin*. J. Am. Chem. Soc., 1988. **110**(6): p. 1657-1666.
- 141 Damm, W., Frontera, A., Tirado-Rives, J., Jorgensen, W. L., *OPLS all-atom force field for carbohydrates*. J. Comp. Chem., 1997. **18**(16): p. 1955-1970.
- 142 Harder, E., Damm, W., Maple, J., Wu, C., Reboul, M., Xiang, J. Y., Wang, L., Lupyan, D., Dahlgren, M. K., Knight, J. L., Kaus, J. W., Cerutti, D. S., Krilov, G.,

-
- Jorgensen, W. L., Abel, R., Friesner, R. A., *OPLS3: A Force Field Providing Broad Coverage of Drug-like Small Molecules and Proteins*. *J. Chem. Theory Comput.*, 2016. **12**: p. 281-296.
- 143 Metropolis, N., Ulam, S., *The Monte Carlo Method*. *J. Am. Stat. Assoc.*, 1949. **44**(247): p. 335-341.
- 144 Halgren, T. A., Murphy, R. B., Friesner, R. A., Beard, H. S., Frye, L. L., Pollard, W. T., Banks, J. L., *Glide: A New Approach for Rapid, Accurate Docking and Scoring. 2. Enrichment Factors in Database Screening*. *J. Med. Chem.*, 2004. **47**(7): p. 1750-1759.
- 145 Friesner, R. A., Murphy, R. B., Repasky, M. P., Frye, L. L., Greenwood, J. R., Halgren, T. A., Sanschagrin, P. C., Mainz, D. T., *Extra Precision Glide: Docking and Scoring Incorporating a Model of Hydrophobic Enclosure for Protein-Ligand Complexes*. *J. Med. Chem.*, 2006. **49**(21): p. 6177-6196.
- 146 Friesner, R. A., Banks, J. L., Murphy, R. B., Halgren, T. A., Klicic, J. J., Mainz, D. T., Repasky, M. P., Knoll, E. H., Shelley, M., Perry, J. K., Shaw, D. E., Francis, P., Shenkin, P. S., *Glide: A new approach for rapid, accurate docking and scoring. 1. Method and assessment of docking accuracy*. *J. Med. Chem.*, 2004. **47**(7): p. 1739-1749.
- 147 Eldridge, M. D., Murray, C. W., Auton, T. R., Paolini, G. V., Mee, R. P., *Empirical scoring functions: I. The development of a fast empirical scoring function to estimate the binding affinity of ligands in receptor complexes*. *J. Comp.-Aided Mol. Design*, 1997, **11**(5): p. 425-445.
- 148 Altmann, F., *Glycoantigenes with carbohydrate determinants*. German patent: DE201220101197 (U1), 2012.
- 149 Eldridge, G. M., Weiss, G. A., *Identifying reactive peptides from phage-displayed libraries*. *Methods Mol. Biol.*, 2015. **1248**: p. 189-199.
- 150 Simpson, J., Weiner, E. (1989). *Artefact*. In *Oxford English Dictionary*. Oxford: Oxford University Press. Retrieved from: <https://en.oxforddictionaries.com>
- 151 Wason, P., *On the failure to eliminate hypotheses in a conceptual task*. *Q. J. Exp. Psychol.*, 1960. **12**: p. 129-140.
- 152 Lee, C. J., Sugimoto, C. R., Zhang, G., Cronin, B., *Bias in peer review*. *J. Am. Soc. Inf. Sci. Tec.*, 2013. **64**: p. 2-17.
- 153 Mahoney, M. J., DeMonbreun, B. G., *Psychology of the Scientist: An Analysis of Problem-Solving Bias*. *Cognit. Ther. Res.*, 1977. **1**(3): p. 229-238.
- 154 Mitroff, I. I., *Norms and Counter-Norms in a Select Group of the Apollo Moon Scientists: A Case Study of the Ambivalence of Scientists*. *Am. Soc. Rev.*, 1974. **39**: p. 579-595.
- 155 Parker, W., Lin, S. S., Yu, P. B., Sood, A., Nakamura, Y. C., Song, A., Everett, M. L. Platt, J. L., *Naturally occurring anti- α -galactosyl antibodies: relationship to xenoreactive anti- α -galactosyl antibodies*. *Glycobiology*, 1999. **9**(9): p. 865-873.
- 156 Brzezicka, K., Echeverria, B., Serna, S., van Diepen, A., Hokke, C. H., Reichardt, N.-C., *Synthesis and Microarray-Assisted Binding Studies of Core Xylose and Fucose Containing N-Glycans*. *ACS Chem. Biol.*, 2015. **10**(5): p. 1290-1302.
- 157 Aplin, A. E., Howe, A., Alhari, S. K., Juliano, R. L., *Signal transduction and signal modulation by cell adhesion receptors: the role of integrins, cadherins, immunoglobulin-cell adhesion molecules, and selectins*. *Pharmacol. Rev.*, 1998. **50**(2): p. 197-264.
- 158 Lund-Johansen, F., Olweus, J., Horejsi, V., Skubitz, K. M., Thompson, J. S., Vilella,

-
- R., Symington, F. W., *Activation of human phagocytes through carbohydrate antigens (CD15, sialyl-CD15, CDw17, and CDw65)*. *J. Immunol.*, 1992. **148**(10): p. 3221-3229.
- 159 Westhof, C. M., Shaz, B. H. (2018). *Human Blood Group Antigens and Antibodies*. In *Hematology* (p. 1687-1701). Amsterdam: Elsevier.
- 160 Kim, T. H., Johnstone, J., Loeb, M., *Vaccine herd effect*. *Scand. J. Infect. Dis.*, 2011. **43**(9): p. 683-689.
- 161 Skripal, I. G., *ABO system of blood groups in people and their resistance to certain infectious diseases (prognosis)*. *Mikrobiol. Z.*, 1996. **58**(2): p. 102-108.
- 162 Galili, U., *Evolution and pathophysiology of the human natural anti- α -galactosyl IgG (anti-Gal) antibody*. *Springer Semin. Immunopathol.*, 1993. **15**: p. 155-171.
- 163 Galili, U., Ishida, H., Tanabe, K., Toma, H., *Anti-gal A/B, a novel anti-blood group antibody identified in recipients of ABO-incompatible kidney allografts*. *Transplantation*, 2002. **74**(11): p. 1574-1580.
- 164 Makeneni, S., Ji, Y., Watson, D. C., Young, N. M., Woods, R. J., *Predicting the Origins of Anti-Blood Group Antibody Specificity: A Case Study of the ABO A- and B-Antigens*. *Front. Immunol.*, 2014. **5**(397): p. 1-9.
- 165 van Liempt, E., Bank, C. M., Mehta, P., Garcia-Vallejo, J.J., Kawar, Z. S., Geyer R., Alvarez R. A., Cummings, R. D., Kooyk, Y., van Die, I., *Specificity of DC-SIGN for mannose- and fucose-containing glycans*. *FEBS Lett.*, 2006. **580**: p. 6123– 6131.
- 166 van Die, I., van Vliet, S. J., Nyame, A. K., Cummings, R. D., Bank, C. M. C., Appelmelk, B., Geijtenbeek, T. B. H., van Kooyk, Y., *The dendritic cell-specific C-type lectin DC-SIGN is a receptor for Schistosoma mansoni egg antigens and recognizes the glycan antigen Lewis x*. *Glycobiology*, 2003. **13**(6): p. 471-478.
- 167 Faveeuw, C., Mallevaey, T., Paschinger, K., Wilson, I. B. H., Fontaine, J., Mollicone, R., Oriol, R., Altmann, F., Lerouge, P., Capron, M., Trottein, F., *Schistosome N-glycans containing core α 3-fucose and core β 2-xylose epitopes are strong inducers of Th2 responses in mice*. *Eur. J. Immunol.*, 2003. **33**: 1271-1281.
- 168 van Die, I., Gomord, V., Kooyman, F. N. J., van den Berg, T. K., Cummings, R. D., Vervelde, L., *Core α 1 \rightarrow 3-fucose is a common modification for N-glycans in parasitic helminths and constitutes an important epitope for IgE from Haemonchus contortus infected sheep*. *FEBS Letters*, 1999. **463**: p. 189-193.
- 169 Ausubel, F. M. *et al.* (1997). *Current Protocols in Molecular Biology*. New York: John Wiley & Sons.
- 170 Komba, S., Ishida, H., Kiso, M., Hasegawa, A., *Synthesis and Biological Activities of Three Sulfated Sialyl Le^x Ganglioside Analogues for Clarifying the Real Carbohydrate Ligand Structure of L-Selectin*. *Bioorg. Med. Chem.*, 1996. **4**(11): p. 1833-1847.
- 171 Flowers, H. M., Jeanloz, R. W., *The Synthesis of a Glucosaminyl-Muramic Acid Disaccharide: Methyl 6-O-(2-Acetamido-3,4,6-tri-O-acetyl-2-deoxy- β -D-glucopyranosyl)-2-acetamido-4-O-acetyl-2-deoxy-3-O-[D-1-(methyl carboxylate)ethyl]- α -D-glucopyranoside*. *J. Org. Chem.*, 1963. **28**: p. 1564-1567.
- 172 Rana, S. S., Barlow, J. J., Matta, K. L., *Synthesis of Phenyl 2-Acetamido-2-Deoxy-3-O- α -L-Fucopyranosyl- β -D-Glucopyranoside and Related Compounds*. *Carbohydr. Res.*, 1981. p. 149-157.
- 173 Lee, R. T., Lee Y. C., *Synthesis of 3-(2-aminoethylthio)propyl glycosides*. *Carbohydr. Res.*, 1974. **37**: p. 193-201.
- 174 Warren, C. D., Jeanloz, R. W., *The synthesis of allyl 2-acetamido-3,6-di-O-benzyl-2-deoxy- α -D-glucopyranoside and of chitobiose derivatives by the oxazoline procedure*. *Carbohydr. Res.*, 1977. **53**(1): p. 67-84.

175 Welinder, K. G., *Amino Acid Sequence Studies of Horseradish Peroxidase*. Eur. J. Biochem., 1979. **96**: p. 483-502.